Semiconductor-Based Electron Lattices for Quantum Information Processing

Johannes Paul-Martin Knörzer

München 2020

Semiconductor-Based Electron Lattices for Quantum Information Processing

Johannes Paul-Martin Knörzer

Dissertation
an der Fakultät für Physik
der Ludwig–Maximilians–Universität
München

vorgelegt von
Johannes Paul-Martin Knörzer
aus Anklam

München, den 24.6.2020

Erstgutachter: Prof. J. I. Cirac
Zweitgutachter: Prof. B. Paredes
Weitere Prüfungskommissionsmitglieder: Prof. H. Weinfurter, Prof. M. Punk
Tag der mündlichen Prüfung: 22.9.2020

Abstract

Scalable physical systems that enable trapping and coherent manipulation of quantum matter lie at the heart of quantum information processing (QIP). Solid-state approaches benefit from rapidly evolving nanotechnology and provide a way towards efficient on-chip quantum devices. In this thesis we show how key ideas from quantum optics can inspire novel setups and implementations for QIP in solid-state settings. To this end, we develop strategies for the realization of well-defined lattices for electrons and other quasiparticles in semiconductors. The theoretical proposals presented in this thesis may serve as novel platforms for controlling and studying quantum many-body systems.

In an introductory passage, we provide a brief summary of goals, recent advances and future directions in quantum information science, highlighting the significant progress that has been made in related fields during the past years. The core of the thesis consists of two parts, one dedicated to quantum systems interacting with elastic waves in solids, and another related to a novel class of two-dimensional semiconductors.

In the first part, we theoretically investigate how surface acoustic waves (SAWs) may be used to create well-defined potentials for mobile electrons and other semiconductor quasiparticles. We develop an effective description of electrons coupled to SAW-driven time-dependent electromagnetic fields by modelling their dynamics within a Floquet framework. The underlying physical coupling mechanisms can be based on piezoelectric, piezomagnetic or strain fields, respectively, and we discuss the implications of each. We show that these systems bear striking similarities with atomic, molecular and optical implementations, such as trapped ions and cold neutral atoms in optical lattices. Specific to the solid-state environment are couplings to various sorts of impurities and bulk phonons, which possibly degrade the quality of SAW-based traps. We thus take into account these effects, and investigate the influence of thermal bulk phonons by deriving an effective description of the electronic motion based on quantum master equations. These results provide a recipe for a near-term realization of acoustic traps and lattices for semiconductor particles. The versatility of the presented theoretical approach allows a thorough examination of various materials, heterostructures and quasiparticles. Several case studies of suitable host materials are presented, and connections to possible future experimental work are established. With a projected lattice spacing on the scale of ~ 100nm, acoustically defined electron lattices allow for relatively large energy scales in the realization of fermionic Hubbard models, and a parameter regime very different from the one typically obtained in other systems. The ultimate prospect of entering the low-temperature, strong-interaction regime may be

crucial for a better understanding of high-temperature superconductivity.

In the second part of this thesis, we focus on realization and detection of self-assembled electron lattices in transition-metal dichalcogenides (TMDs). TMDs have remarkable mechanical, optical and electronic properties and are ideally suited for the study of quantum Wigner crystals (WCs). WCs are prime candidates for the realization of regular electron lattices under minimal requirements on external control and electronics. However, several technical challenges have prevented their detailed experimental investigation and applications to date. Based on scattering theory, we theoretically analyze the optical response of TMD-based WCs. We show that TMDs allow for minimally invasive all-optical detection schemes of charge order inherent in WCs, and that optical selection rules of TMDs provide direct access to spin measurements via Faraday rotation. Experimental signatures of WCs are presented, and disorder-induced imperfections are considered. We highlight their potential as a platform for the quantum simulation of geometrically frustrated magnetism with adjustable and self-assembled lattice structures.

Future research directions, that are related to the results presented here, are discussed at the end of the thesis.

Zusammenfassung

Kontrollierbare und skalierbare Quantensysteme bilden die Grundlage für Quanteninformationsverarbeitung. Festkörpersystemen kommt dabei eine besondere Rolle zu, da diese von industriell verfügbaren Nanofabrikationstechniken profitieren und somit einen möglichen Weg zur Bereitstellung von Chip-basierten Quantentechnologien bieten. In dieser Arbeit zeigen wir auf, wie Schlüsselkonzepte aus der Quantenoptik neuartige Implementierungen festkörperbasierter Quantensysteme ermöglichen können, die im Rahmen der Quanteninformationsverarbeitung relevant sind. Zu diesem Zweck entwickeln wir Strategien zur Realisierung wohldefinierter Fallen und Gitter zum Fangen von Elektronen und anderen Quasiteilchen in Halbleitern. Die theoretischen Ausarbeitungen in dieser Arbeit eröffnen Möglichkeiten für neue Plattformen zur Kontrolle und zum Studium von Quantenvielteilchensystemen.

In der Einleitung stellen wir eine Übersicht der Ziele, jüngsten Fortschritte und Zukunftsvisionen im Bereich der Quanteninformationswissenschaften vor. Der Hauptteil dieser Arbeit besteht aus zwei Teilen. Zuerst widmen wir uns Quantensystemen, die in Festkörpern mit akustischen Wellen wechselwirken, und danach setzen wir uns mit einer neuartigen Klasse zweidimensionaler Halbleiter auseinander.

Im ersten Teil untersuchen wir, wie akustische Oberflächenwellen wohldefinierte Potentiallandschaften für bewegliche Elektronen und andere Quasiteilchen in Halbleitern erzeugen können. Wir entwickeln eine effektive Beschreibung von Elektronen, die an akustisch getriebene, zeitabhängige elektromagnetische Felder koppeln. Hierfür modellieren wir die Dynamik der freien Ladungsträger im Rahmen eines Floquet-Formalismus. Die zu Grunde liegenden physikalischen Kopplungsmechanismen können piezoelektrischen oder piezomagnetischen Ursprungs sein oder von mechanischer Spannung herrühren. Wir zeigen, dass diese Systeme Ähnlichkeit mit atomaren, molekularen und optischen Quantensystemen haben, z. B. mit gefangenen Ionen und ultrakalten Atomen in optischen Gittern. Spezifisch für die festkörperbasierten Systeme sind Kopplungen der Elektronen an Störstellen und phononische Freiheitsgrade, welche die Funktionsweise von akustischen Fallen beeinträchtigen können. Daher berücksichtigen wir diese Effekte und untersuchen den Einfluss von thermischen Phononen auf die elektronische Bewegung auf Basis einer Quantenmastergleichung. Diese Resultate bilden die Basis für eine ausführliche Untersuchung verschiedener möglicher experimenteller Umsetzungen. Hierzu berücksichtigen wir diverse Materialien, Heterostukturen und Quasiteilchen. Verschiedene konkrete Fallbeispiele werden diskutiert. Da die Gitterkonstanten von akustischen Gittern im Bere-

ich von $\sim$ 100nm liegen können, erlauben akustisch getriebene Elektronengitter die Verwirklichung relativ großer Energieskalen in fermionischen Hubbardmodellen, und damit das Erreichen von Parameterkonstellationen, die mit anderen Systemen typischerweise nicht realisiert werden können. Damit ermöglichen uns diese Systeme gleichzeitig starke Wechselwirkungen und tiefe Temperaturen, um zum Beispiel Neues über Hochtemperatursupraleiter zu erfahren.

Im zweiten Teil beschäftigen wir uns mit der Realisierung und Detektion von selbstorganisierten Elektronengittern in zweidimensionalen Halbleitern. Die hier untersuchten Halbleiter haben beeindruckende mechanische, optische und elektronische Eigenschaften und eignen sich in besonderer Weise zur Untersuchung von Wignerkristallen. Wignerkristalle stellen Elektronengitter dar, die ohne hohe Anforderungen an externe Kontrollparameter auskommen. Allerdings haben sich diese bisher aufgrund einiger technischer Schwierigkeiten der detaillierten experimentellen Untersuchung entzogen. Aufbauend auf einer Streutheorie des Lichts untersuchen wir optische Eigenschaften von Wignerkristallen in zweidimensionalen Halbleitern. Insbesondere zeigen wir, dass diese Systeme minimalinvasive optische Detektion der Ladungsträgeranordnung in Wignerkristallen erlauben. Des Weiteren ermöglichen es die optischen Auswahlregeln dieser Halbleiter, anhand des gestreuten Lichts auch Informationen über den Spinfreiheitsgrad der Elektronen zu gewinnen. Experimentell beobachtbare Signale werden vorgestellt und Imperfektionen der Elektronengitter werden untersucht. Wir zeigen, dass sich diese Systeme auch für die Quantensimulation von frustriertem Magnetismus eignen.

Künftige Forschungsfragen, die im Zusammenhang mit dieser Arbeit stehen, werden im abschließenden Kapitel diskutiert.

List of Publications

Publications Related to this Thesis

[1] *The 2019 surface acoustic waves roadmap*,
Chapter on *Quantum acoustics with surface acoustic waves in semiconductors*
M. J. A. Schuetz, **J. Knörzer**, G. Giedke, J. I. Cirac,
J. Phys. D **52**, 353001 (2019).
See Chapter 1.

[2] *Acoustic Traps and Lattices for Electrons in Semiconductors*
Reprinted with permission from
M. J. A. Schuetz,* **J. Knörzer**,* G. Giedke, L. M. K. Vandersypen, M. D. Lukin, and J. I. Cirac,
Phys. Rev. X **7**, 041019 (2017).

See Chapter 2.

[3] *Solid-state magnetic traps and lattices*
Reprinted with permission from
J. Knörzer,* M. J. A. Schuetz,* G. Giedke, M. Weiler, H. Huebl, M. D. Lukin, and J. I. Cirac,
Phys. Rev. B **97**, 235451 (2018).

See Chapter 3.

[4] *Wigner crystals in two-dimensional transition-metal dichalcogenides: Spin physics and readout*
Reprinted with permission from
J. Knörzer, M. J. A. Schuetz, G. Giedke, D. S. Wild, R. Schmidt, K. de Greeve, M. D. Lukin, and J. I. Cirac,
Phys. Rev. B **101**, 125101 (2020).

See Chapter 4.

Other Publications

[5] *Nonequilibrium Landau-Zener-Stueckelberg spectroscopy in a double quantum dot*
P. Nalbach, **J. Knörzer**, and S. Ludwig
Phys. Rev. B **87**, 165425 (2013)

[6] *Correlated quantum dynamics of a single atom collisionally coupled to an ultracold finite bosonic ensemble*
S. Krönke,* **J. Knörzer**,* and P. Schmelcher
New J. Phys. **17**, 053001 (2015)

[7] *Control of multiple excited image states around segmented carbon nanotubes*
J. Knörzer, C. Fey, H. R. Sadeghpour, and P. Schmelcher
J. Chem. Phys. **143**, 204309 (2015)

[8] *Highly excited electronic image states of metallic nanorings*
C. Fey, H. Jabusch, **J. Knörzer**, and P. Schmelcher
J. Chem. Phys. **146**, 194704 (2017)

[9] *Discrete Interactions between a few Interlayer Excitons Trapped at a* $MoSe_2$-WSe_2 *Heterointerface*
M. Kremser, M. Brotons-Gisbert, **J. Knörzer**, J. Gückelhorn, M. Meyer, M. Barbone, A. V. Stier, B. D. Gerardot, K. Müller, and J. F. Finley
npj 2D Mat. and Appl. **4**, 8 (2020)

(* contributed equally)

Table of Contents

Chapter 1

Introduction

The development of a quantum theory of the physical world is arguably one of the major intellectual achievements in modern science. Quantum mechanics has its historical roots in the beginning of the 20th century, when it was first invoked to explain physical phenomena outside the realm of classical physics, such as black-body radiation [10] or the photoelectric effect [11]. Besides its importance for modern physics and research, quantum physics has also had a great impact on the development of novel technology. Today, there exists a plethora of devices that rely on quantum effects, including semiconductors, transistors and laser systems. The development of quantum mechanics and the successive integration of these devices and functionalities into modern technology is often refered to as *first quantum revolution*.

Similarly, the birth of modern computers had a tremendous impact on society and rapidly fueled scientific, technological and economic progress. Prior to the appearance of first fully automatic digital computers in the 1940s, early results in theoretical computer science laid out a mathematical framework of computation. Notably, it was Alan Turing who formalized the abstract idea of general-purpose machines [12], demonstrating capabilities and limitations of computing devices. In a seminal paper, *Computing Machinery and Intelligence* [13], he also paved the way for what later became known as artificial intelligence. Recent progress with artificial neural networks has renewed interest in this field, fueled by a significantly increased computing power available with modern technology. Until today, we are persistently challenging the question of what is computable, and which processes in the world around us we can model and quantitatively describe and understand.

Initially, quantum physics and computer science seemed rather unrelated, until it was realized that these two major discplines share common ground. Information is intimitely related with its physical manifestation, which led to Rolf Landauer's famous expression, *information is physical* [14]. It was when previously disconnected disciplines from computer science, physics and mathematics came together that quantum science gained a lot of additional momentum, to launch research on quantum information theory. While core principles of computer science and information theory operate on the basis of classical physics, the fundamental concepts of quantum information theory and all novel quantum technologies rely on the laws of quantum mechanics.

1.1 Quantum Science and Technology

Recent advances show that the potential for new discoveries and applications related to quantum science has not been stretched to its limits, and that a new era of quantum technologies has just started. With the advent of physical implementations of quantum information processing (QIP), a variety of novel quantum technologies is on the horizon. This on-going *second quantum revolution* [15] addresses many challenges that can be largely grouped into four categories: (*i*) quantum communication, (*ii*) quantum metrology, (*iii*) quantum computation, and (*iv*) quantum simulation. The tremendous progress in these fields in recent years has led to remarkable scientific discoveries and first technological applications. In fact, significant progress has been made in all of these fields during the relatively short time span between 2016 and 2020, in which the work summarized in this thesis has been carried out. The impressive pace at which new illuminating insights are being obtained is most easily demonstrated by naming several examples from recent years, highlighting both challenges and opportunities associated with novel and upcoming quantum information technologies. Notwithstanding the wealth of research directions within each field, an executive summary of central themes of all four research domains will be provided in the following. Selected research highlights of each category shall serve as a demonstration of the rapid progress, and showcase current developments. While these introductory passages raise no claim of completeness in any regard, they give a taste of current themes in quantum science research.

One common goal of many recent efforts is near-term applicability, with a focus on *quantum advantage*: designing and putting into practice quantum systems that improve specific scientific or technological tools beyond what is possible with devices based on the laws of classical physics. The pursuit of such quantum enhancement rests on properties of quantum systems that are not shared by their classical counterparts. Quantum superpositions and entanglement play a central role in this regard. Entangled quantum states exhibit correlations that have no classical analog. Examples are the four *Bell states*, specific maximally entangled quantum states of two qubits. Suppose Alice and Bob are at distant locations and both hold one qubit each, such that their joint quantum state reads $|\Phi_{12}^{+}\rangle = \frac{1}{\sqrt{2}}(|0\rangle_1 |0\rangle_2 + |1\rangle_1 |1\rangle_2)$. If Alice measures her qubit (subscript 1), the outcome would be perfectly random, either possibility 0 or 1 having 50% probability. But if then Bob (subscript 2) measures his qubit, the outcome would be the same as Alice's. Although their measurement outcomes may seem random, they are in fact perfectly correlated. Albert Einstein famously called this the *spooky action at a distance*, and concluded that the formulation of quantum mechanics must be incomplete [16]. Nowadays, the pecularities of quantum physics, especially quantum entanglement, are at the heart of all promising new quantum technologies.

Quantum communication

Quantum communication is concerned with the transmission of information encoded in quantum states, e.g. in the polarization state of an optical photon [17]. It contrasts classical communication, as it is governed by the laws of quantum mechanics, and allows for intrinsically secure exchange of information. Potential applications are not limited to communication protocols, and include even schemes that can help to significantly extend the baseline of interferometric telescopes [18], and may thus be used to learn more about distant celestial objects, like galaxies. In fact, some quantum communication technologies have already been put into practice and commercialized. Most prominently, quantum key distribution (QKD) provides a recipe for secure communication, as it is decorated with a remarkable property: the presence of any eavesdropper may be detected in a post-processing phase, as any measurement leaves behind its traces in the transmitted quantum state [19]. Despite its commercial availability, QKD and other applications still face a number of challenges. One of these obstacles is related to the fact that all physical communication channels are imperfect and affected by transmission losses. Naturally, noisy channels limit the distance over which information can be transferred. State-of-the-art experiments using ultralow-loss optical fibers achieve transmission distances of several dozens of kilometres [20]. For large-scale quantum networks, e.g. to realize the vision of a quantum internet [21], this is certainly not enough. More than twenty years ago, it has been suggested that this problem may be overcome by employing *quantum repeaters* [22]. Repeaters are widely used in telecommunications to extend transmission of information to longer distances, by receiving and retransmitting a signal. Due to the no-cloning theorem, a profound insight stating that quantum states cannot be replicated, quantum repeaters must conceptually be entirely different from their classical counterparts.

The standard approach to tackle this scalability issue with quantum repeaters requires long-range entanglement, and starts with entanglement generation between adjacent nodes in a network. Subsequent *entanglement swapping* enables to create long-distance entanglement from shorter-distance entanglement. This technique is based upon Bell state measurements (BSM). Suppose, for example, both Alice and Bob, representing two spatially separated nodes of a network, were in possession of a Bell pair each,[1] $|\Phi_{12}^+\rangle = \frac{1}{\sqrt{2}}(|0\rangle_1 |0\rangle_2 + |1\rangle_1 |1\rangle_2)$ and $|\Phi_{34}^+\rangle = \frac{1}{\sqrt{2}}(|0\rangle_3 |0\rangle_4 + |1\rangle_3 |1\rangle_4)$, respectively, such that the full quantum state of the composite system reads $|\Psi\rangle = |\Phi_{12}^+\rangle \otimes |\Phi_{34}^+\rangle$. Charlie, at a third location, receives one of Alice's and one of Bob's particles, and performs a projective measurement on these, in the basis of Bell states $\{|\Phi_{23}^+\rangle, |\Phi_{23}^-\rangle, |\Psi_{23}^+\rangle, |\Psi_{23}^-\rangle\}$. As a result, since $|\Psi\rangle = \frac{1}{2}(|\Phi_{23}^+\rangle |\Phi_{14}^+\rangle + |\Phi_{23}^-\rangle |\Phi_{14}^-\rangle + |\Psi_{23}^+\rangle |\Psi_{14}^+\rangle + |\Psi_{23}^-\rangle |\Psi_{14}^-\rangle)$, the remaining two particles at Alice's and Bob's nodes become entangled. Consecutive application of this entanglement-swapping procedure paves a way for building large-scale repeater-based quantum networks, which enjoy a polynomial scaling of the transmission efficiency with total distance.

Distribution of quantum entanglement between adjacent nodes can be achieved using photons and optical fibres. Photonic BSMs can be implemented directly with linear optics

[1] Alice holds two qubits (subscripts 1 and 2), and Bob holds two qubits (subscripts 3 and 4).

and single-photon detectors, in principle. However, the described scheme then only works when Alice's and Bob's photons arrive at the same time at Charlie's node. To avoid this difficulty and improve the performance of this scheme, a quantum memory at Charlie's location can be used to store information upon arrival of the first photon. In that approach, the state of Alice's photon is stored in Charlie's memory while awaiting receipt of Bob's photon, allowing for asynchronous BSMs.

At the heart of many quantum communication schemes lies therefore the realization of efficient and high-fidelity quantum memories, that can be interfaced with light. In practice, this poses tremendous challenges. However, recent advances present significant steps forward towards practical quantum repeaters and large-scale quantum networks. Various quantum physical setups may help achieving this, including atomic systems, rare-earth doped solids, color centers in solids, and quantum dots.

In order to enhance quantum light-matter interaction, and thus enable high-fidelity light-matter interfaces for building optically addressable memory nodes, two widely used approaches may be distinguished, in general: (i) embedding single quantum emitters in high-finesse optical cavities, and (ii) increasing the number of particles, e.g. with atomic ensembles. In both cases, the light-matter interaction can be increased significantly. To illustrate the most recent progress in this field, two selected research milestones of the past year will be mentioned in the following, that each follow at least one of these two strategies.

Recently, it has been experimentally demonstrated that memory-assisted quantum communication can outperform direct-transmission and repeater-less communication by a large margin in a state-of-the-art laboratory setting [23]. In this experiment, a silicon-vacancy center in diamond served as a quantum memory, embedded in a nanophotonic cavity with a very high cooperativity. Two photons, one from Alice and another from Bob, arriving at different times at the memory node were used to carry out asynchronous BSMs, by photon detection and measuring the spin state of the color center. This experiment demonstrates a scenario in which the memory-assisted BSM success rate exceeds the direct-transmission success rate, due to a sufficiently long coherence time of the quantum memory. As a proof-of-principle result, this shows a form of quantum advantage enabled by memory-based communication nodes which are spatially nearby. It provides a significant step towards realizing functional quantum repeaters and, once implemented in a practical long-distance communication setting, may enable larger-scale repeater-based quantum networks.

The earliest proposal for a physical realization of a repeater-based network is the DLCZ proposal, named after its inventors [24]. It is based on collective interference effects in atomic ensembles and linear optics. In this approach, atomic ensembles realize quantum memories. Recently, entanglement over dozens of kilometeres of optical fibre has been achieved, connecting two memory nodes containing one atomic ensemble each [20]. Quantum frequency conversion techniques allow for a conversion of light from a laser source, used to address the quantum memory, to the telecommunication band. This result presents a significant step forward towards fully functional segments of atomic quantum networks at city-scale distances.

These results highlight the high pace at which progress in quantum communication research is being made. By combining theoretical concepts with modern technology and

further improving state-of-the-art experimental setups, this branch of quantum information research has already led to novel communication technology, and each incremental step is bringing large-scale quantum networks a bit closer. Commercially available QKD systems are offered by several companies now, including ID Quantique, MagiQ Technologies, QuintessenceLabs and SeQureNet, and quantum encryption has already been employed to protect national elections against hacking and data corruption.

Quantum metrology

Measurements lie at the heart of scientific discovery, allow us to define standards and enable technology, trade and commerce. Still today, the boundaries of precision measurements and of what is resolvable are pushed further and further. A few years ago, the Laser Interferometer Gravitational-Wave Observatory (LIGO) detected gravitational waves for the first time, and helped improving our understanding of the universe [25]. This was made possible by extremely precise distance measurements, that enabled to detect changes in distance between two mirrors of the order of 10^{-19} m. Another example are atomic clocks, that have already reached frequency precision of the order of 10^{-19} in recent years [26]. At this level of performance, geophysical processes or even the interplay of quantum mechanics and general relativity may be probed on the millimeter scale. Further impressively accurate metrological achievements include yoctonewton force sensing [27], yoctogram mass sensing [28], and subfemtotesla magnetic field sensing [29]. While the final resolution of all measurements is doomed to be fundamentally limited, it can be improved beyond what is possible with classical measurements by resorting to quantum physics.

Quantum metrology is dedicated to devising highly sensitive measurement schemes that may help to overcome limits posed on classical metrology. Altogether, quantum mechanics has been playing a central role in metrology for decades now. For example, calibrations of electrical resistors are based on the quantum Hall effect. Since 2019, the definition of the standard units of measurement incorporates fixed values of the Planck constant h, and the elementary charge e. It thus circumvents the outdated definition of the kilogram based on a carefully protected prototype and is less prone to errors. On a more fundamental level, quantum-enhanced sensing may be employed to systematically outperform (semi-)classical measurements using entanglement [30].

Precision measurements are often performed by converting a quantity of interest to a phase shift, that can be measured using interferometers. In this procedure, a probe state acts as a sensor, and acquires a phase shift θ during the measurement process, that depends on the desired physical observable. An estimate of this phase shift can be obtained from the measurement outcomes [31]. Precision is always limited by an uncertainty $\Delta\theta$, which can be caused by either technical (classical) or fundamental (quantum) restrictions. The final precision as a function of the resources used, e.g. number of photons N in optical interferometry, number of atoms in atomic spectroscopy, or measurement time, determines the effectiveness of the sensor.

Statistical parameter estimation provides a mathematical framework to bound the uncertainty $\Delta\theta$ from below, a key result that is known as the *Cramer-Rao bound*. The best

classical sensors feature a precision $\Delta\theta_{\mathrm{SQL}} = \mathcal{O}(1/\sqrt{N})$, known as the *standard quantum limit* (SQL). This shot-noise scaling occurs, for example, in photon-counting devices, where the incident photon count follows a Poisson distribution. By contrast, quantum sensors can beat the SQL, and eventually reach $\Delta\theta_{\mathrm{HL}} = \mathcal{O}(1/N)$, known as the *Heisenberg limit* (HL). Overcoming the SQL requires entanglement between particles. As an illustrative example, consider an optical interferometer using coherent and entangled states with average photon number N, respectively. The overlap of two coherent states[2] $|\alpha\rangle$ and $|e^{i\Delta\theta}\alpha\rangle$ is given by $\exp(-|\alpha(1-e^{i\Delta\theta})|^2) \approx \exp(-N\Delta\theta^2)$, for sufficiently small phase displacements $\Delta\theta$. At $\Delta\theta \sim 1/\sqrt{N}$, the two coherent states tend to become orthogonal, which makes them more distinguishable. Repeating this line of reasoning for two entangled states $|\Psi_N\rangle = (|N,0\rangle + |0,N\rangle)/\sqrt{2}$ and $|\Psi_{N,\Delta\theta}\rangle = (|N,0\rangle + e^{iN\Delta\theta}|0,N\rangle)/\sqrt{2}$,[3] one obtains $|\langle\Psi_N|\Psi_{N,\theta}\rangle|^2 = \cos^2(N\Delta\theta/2)$. These states become orthogonal for $\Delta\theta \sim 1/N$, which reproduces the beforementioned Heisenberg scaling.

In quantum systems, noise and decoherence make it very challenging to reach the Heisenberg limit for all practical purposes. It is still an active field of research to determine the maximally achievable accuracy in the presence of different types of noise sources, and how error-correction schemes can be used to enhance sensitivity. Despite these obstacles, quantum-enhanced measurements with multi-particle entangled states beyond the SQL have already been demonstrated in several experiments, e.g. using trapped ions, cold atoms and Bose-Einstein condensates, and in optical interferometry. Recently, measurements on $N = 2$ photonic $NOON$ states have achieved unconditional violation of the shot-noise limit [32]. Furthermore, squeezed states which seek to redistribute the noise between two non-commuting observables while obeying the Heisenberg uncertainty relation, have helped to surpass the SQL in different contexts. For example, squeezed states of light recently enhanced the sensitivity of gravitational wave detection by 3.2 dB [33], and spin squeezing in ensembles with half a million atoms has led to a 11-fold metrological gain in phase sensitivity [34].

A variety of different physical systems are being considered for quantum-enhanced sensing, including trapped ions, quantum dots and nitrogen-vacancy (NV) centers, see Fig. 1.1. Sensors based on single electron spins associated with NV centers in diamond target highly accurate measurements of electromagnetic fields, temperature or strain, with nanoscale resolution. Their recent success partly relies on long spin coherence times, even at room temperature. Furthermore, diamond-based spin sensors can benefit from a close proximity to their target, a wide field of view and extraordinary sensitivity, and have great potential in various contexts, including imaging of living cells under ambient conditions [35], navigation in GPS-denied environments, and dark-matter detection [36]. These exciting prospects underline how mature the field of quantum metrology has become, due to a fruitful convergence of novel technologies and profound theoretical groundwork.

[2] A Coherent state is the closest analog to a classical light field, exhibits a Poisson photon number distribution with an average photon number $N = |\alpha|^2$, and can be written as $|\alpha\rangle = e^{-|\alpha|^2/2}\sum_{n=0}^{\infty}\frac{\alpha^n}{\sqrt{n!}}|n\rangle$ in the number-state basis.

[3] These $NOON$ states correspond to coherent superpositions of N photons in one branch of an optical interferometer, and zero photons in the second branch.

Quantum computation

Quantum computation is a cornerstone of quantum information science and technology, and a universal quantum computer is one of its holy grails. The vision of a useful quantum computer, that outperforms all classical computing devices at specific tasks, has fueled progress in various interconnected disciplines. Even beyond academic research, quantum computation is nowadays of great interest, since world-leading tech companies such as Google, IBM, Microsoft and Intel have joined the race to build a quantum computer.

Four decades ago, the first quantum mechanical model for Turing machines, based on the time evolution of quantum states, was introduced by Paul Benioff [37]. A few years later, David Deutsch described the concept of universal quantum computers, which are capable of efficiently simulating any other quantum computer (just as any universal Turing machine can efficiently simulate any other Turing machine) [38]. As the theoretical description of quantum computing became more developed and mature, the concepts of quantum circuits and quantum gates were established and formalized. It was shown that two-qubit gates are universal for quantum computation [39], and that any operation can be decomposed into controlled-NOT (CNOT) gates between two qubits and a number of single-qubit gates [40].

However, until 25 years ago, no physical system had been demonstrated to realize the required two-qubit interaction to implement a CNOT gate. In 1995, the first physical implementation of a quantum computer was proposed by Ignacio Cirac and Peter Zoller, who showed how a CNOT gate can be realized in a system composed of trapped ions [41]. Soon after, first experimental proof-of-principle demonstration of a CNOT gate was released. At that time, many different physical realizations were being considered for the first time, and explicit proposals for quantum computing platforms were worked out. The Loss-DiVincenzo quantum computer was proposed in 1997, which uses as qubits the spin degree of freedom of electrons confined to electrically defined quantum dots (QDs) [42]. In that proposal, two-qubit gates are realized with the aid of the electrically tunable exchange interaction between two adjacent spin qubits. Silicon-based nuclear-spin quantum computers, that use the nuclear spins of individual phosphorus atoms in silicon as qubits and donor electrons to mediate exchange coupling between them, was proposed by Bruce Kane in 1998 [43].[4] Around the same time, it was shown that superconducting (SC) circuits can be used as qubits, and coherent control of individual SC qubits [45] as well as controlled couplings between them [46] were studied. Global efforts in developing quantum processors based on SC circuits have improved their quality, and a variety of types of SC qubits exists.

In parallel with the exploration of suitable platforms for quantum computation, physicists and information scientists have been conceiving new quantum algorithms, that can be run on future quantum computers and benefit explicitly from their quantum mechanical properties to outperform classical computers at certain tasks. Early milestones in this field include Shor's factoring algorithm [47] and Grover's search algorithm [48]. Perhaps

[4] A main difficulty associated with this approach is the tricky single-qubit addressablity related to focusing magnetic fields down to single qubits. Recently, it was experimentally shown how electric fields may be used to address single qubits in these sytems [44].

the most prominent example of a quantum algorithm, Shor's algorithm outlines a method for determining the prime factors of large integers efficiently, unlike any known classical algorithm. With a sufficient number of qubits and the capability to correct for errors during operation, running Shor's algorithm on a QC could be used to break widely used public-key cryptography schemes. This, in turn, led to the emergence of a new branch of research, post-quantum cryptography, dedicated to designing cryptographic algorithms that are meant to be secure against attacks by quantum computers. On the other hand, Grover's algorithm provides a quadratic speed-up for searching unsorted databases. It also plays a central role in tackling Boolean satisfiability problems, which are known to be very hard to solve. The underlying concepts of these early key results form the basis for many algorithms that have been developed ever since. Quantum phase estimation, for example, a main building block of Shor's algorithm, is equally important for the inner working principle of the HHL algorithm for solving systems of linear equations [49]. Due to the widespread use of linear systems in science and elsewhere, the HHL algorithm has great potential for widespread applicability. Amplitude amplification, on the other hand, the key principle behind Grover's algorithm, is also applied in many other algorithms to obtain quadratic speed-ups.

Since the early 2000's, small-scale versions of these quantum algorithms have successfully been tested on the first quantum processors. In a 2001 experiment, Shor's algorithm was employed to factorize $15 = 3 \cdot 5$ in a proof-of-principle demonstration, using nuclear spins [50]. The current record achieved with Shor's algorithm managed to factor $21 = 3 \cdot 7$ [51], which obviously compares unfavourably with the record for the largest integer factored classically, which is a number with 240 decimal digits at the time of this writing. Similarly, proof-of-principle demonstrations of Grover's algorithm, the HHL algorithm and others have been given in recent years. Despite this progress, improving the performance of quantum processors and turning them into useful computing devices will continue to pose some tremendous challenges for the years to come. These challenges include the protection of qubits from their environment and decoherence to reduce both global and local sources of error, harnessing quantum error-correcting schemes and significantly scaling up system sizes.

While quantum error correction is a main area of current research in quantum information science, and the numbers of qubits in state-of-the-art architectures are steadily growing, a recent paradigm shift towards quantum computing in the NISQ (Noisy Intermediate-Scale Quantum) era [52] puts the focus on noisy quantum devices with about $50 - 100$ qubits, that may already outperform classical computers at certain tasks.

In line with this reasoning, global efforts to demonstrate so-called *quantum supremacy* have recently culminated in an experimental demonstration of a quantum processor that solves a specifically chosen problem much faster than the best currently available classical supercomputers [53]. In particular, this experiment demonstrated efficient sampling from random unitary circuits. In contrast to decision problems, sampling problems output random numbers according to a particular probability distribution. Another well-known example of a sampling problem is Boson sampling, which concerns the probability distribution of photons scattered by an interferometer. It is related to the evaluation of the matrix

permanent, which is known to be a computationally hard problem. Boson sampling has been demonstrated in proof-of-principle experiments [54], and larger-scale implementations are being explored.

While fully fledged, fault-tolerant quantum computers are a driving force and may be the ultimate goal of this research field, current quantum technology offers thrilling possibilities to study hard problems with quantum systems and learn more about quantum physics itself. The current NISQ era may be game-changing, and has most recently brought to us very striking results.

Quantum simulation

The genuine idea of quantum simulation was originally conceived in the early 1980s by Richard Feynman [55] and Yuri Manin [56]. It relies on the observation that well-controlled quantum systems can be used to study properties of other quantum systems, which may be much harder to control or operate with. Importantly, putting this idea into practice is widely believed to offer solutions to very hard and yet unsolved problems, as it enables finding the solution to specific problems without computing their solution directly. In fact, simulation as a tool for scientific discovery is widely used in many branches of science. Its general working principle may be most easily illustrated with the following example. Let us consider a simple mathematical problem, whose solution may be encoded in the outcome of an experiment. Say we wish to determine the square root of a given number $r \in \mathbb{R}^+$. Instead of performing a *computation*, we may as well measure the time t it takes for a mass to hit the ground after free fall from a height r. We realize that $\sqrt{r} = \sqrt{g/2}t$, and thus measuring the elapsed time t in the experiment can be regarded as a simulation of the square-root function. Likewise, quantum simulators may serve as a resource to simulate interacting quantum many-body problems, which may be computationally intractable.

Quantum simulators are promising to unravel complex many-body phenomena in condensed matter and high-energy physics, cosmology or quantum chemistry. They may also encode computationally hard optimization problems, like satisfiability problems. Often digital and analog quantum simulators are distinguished. While the former are based on quantum circuits and may in principle be made fault-tolerant, analog quantum simulators mimic the time evolution of interacting quantum systems in a controlled fashion. Analog quantum simulators have already become available in state-of-the-art experiments.

There is a variety of physical realizations that enable quantum simulation, see Fig. 1.1. Each candidate physical system for quantum simulation should fulfil a number of criteria [57]. Clearly, it should be modeled by a Hamiltonian that describes a problem of interest. Measurements then encode the result to the problem, just like in the square-root example above. Each physical system comes with its own advantages. Cold atomic systems in optical lattices, for example, are rather scalable, while other setups may allow for easier individual control and readout.

In what was possibly the first quantum simulation experiment, a four-level quantum system consisting of two nuclear spins was used to simulate the dynamics of a truncated harmonic oscillator [58]. While the harmonic oscillator is one of theoretical physics' most

widely used toy models that is even analytically solvable, more intricate models and physical effects have since then been studied in experiment, which remain elusive for analytical or numerical treatments. For example, early experiments with atomic BECs have probed phase transitions from superfluid to Mott insulating states [59]: by trapping hundreds of thousands of atoms with only three optical standing waves, a sufficiently complex system can be brought under experimental control, that encodes a Hamiltonian way too complicated for a classical computer to solve exactly. Cold atoms in optical lattices have come a long way, and provide a versatile platform for the study of lattice models, e.g. Hubbard models. Both geometry and dimension are reconfigurable, and tunneling and interaction energies can be set by external parameters. As Hubbard models are suspected to capture the essential physics of high-temperature superconductors, such quantum simulators pave the way for a better understanding of important physical effects which are of immediate relevance, also for industrial applications.

More recently, arrays of $N \sim 50$ Rydberg atoms using optical tweezer technology [60] provided experimental access to a new class of constrained models that may in the future be used to encode solutions to optimization problems that no classical machine can solve. This recent development very nicely demonstrates how Feymman's original idea can be filled with life in a specific context: a physical effect (in this case, the Rydberg blockade) naturally occurs in an atomic Rydberg array and introduces constraints on the excitations in the lattice; calculating the properties of the underlying Hamiltonian can be much harder than performing a measurement on the Rydberg array, once the experimental apparatus is available. This may turn out to be relevant in the context of classical optimization, since the Rydberg-blockade effect gives rise to excitation patterns in the lattice that can be associated with particular combinatorial problems in graph theory [61].

Other experimental approaches use semiconductor technology to trap electrons in arrays of gate-defined quantum dots (see Fig. 1.1). As distant charges interact via long-range Coulomb interactions, in contrast to cold neutral atoms that interact only at short distances, these systems would be more naturally suited for studying models with long-distance couplings. Recent progress with the control of Fermi-Hubbard models in arrays of gate-defined QDs [62] has underlined their great potential for quantum simulations. In another recent work, Nagaoka ferromagnetism, a physical phenomenon predicted in the 1960s, has been observed for the first time, in a system of four electrons in a plaquette of quantum dots [63].

Other current efforts are related to the study of quantum chemistry problems using controlled quantum systems, for example, cold atoms [64] or trapped ions [65]. Like many of the other examples given before, this line of research is also decicated to exploiting the quantum nature of analog and digital quantum simulators to study fundamental processes in nature, that seem to be too complex for a classical supercomputer to handle. While these ideas are all variations on Feynman's original theme, they demonstrate the tremendous potential for obtaining useful quantum advantages enabled by quantum simulators in the years to come.

1.2 Physical Implementations

The realization of each quantum technology demands a physical manifestation. A variety of different systems, that are becoming increasingly relevant for future quantum technologies, is now already a reality. Most platforms can be largely grouped into two categories: (*i*) solid-state systems (e.g., superconducting qubits, quantum dots, color centers) and (*ii*) atomic, molecular and optical (AMO) systems (e.g., cold neutral atoms, trapped ions, photons), see Fig. 1.1. While the former benefit from rapidly evolving nanotechnology and often an intrinsic scalability, the latter constitute a prime example of well-controlled quantum systems which are typically well-isolated from their environment.

It is natural to ask how the advantages of these different paradigms can be brought together either in hybrid quantum systems or by translating fundamental concepts from one to another. These strategies have already been adopted and successfully applied in various cases. Hybrid quantum systems leverage the strengths of their constituents by combining several physical implementations with the aid of an appropriate interface [66]. For example, a mechanical quantum bus may be employed to couple dissimilar qubits, such as trapped ions, SC qubits, and photons. On a more abstract level, the investigation of physical systems with theoretical and experimental tools originally conceived in a different context

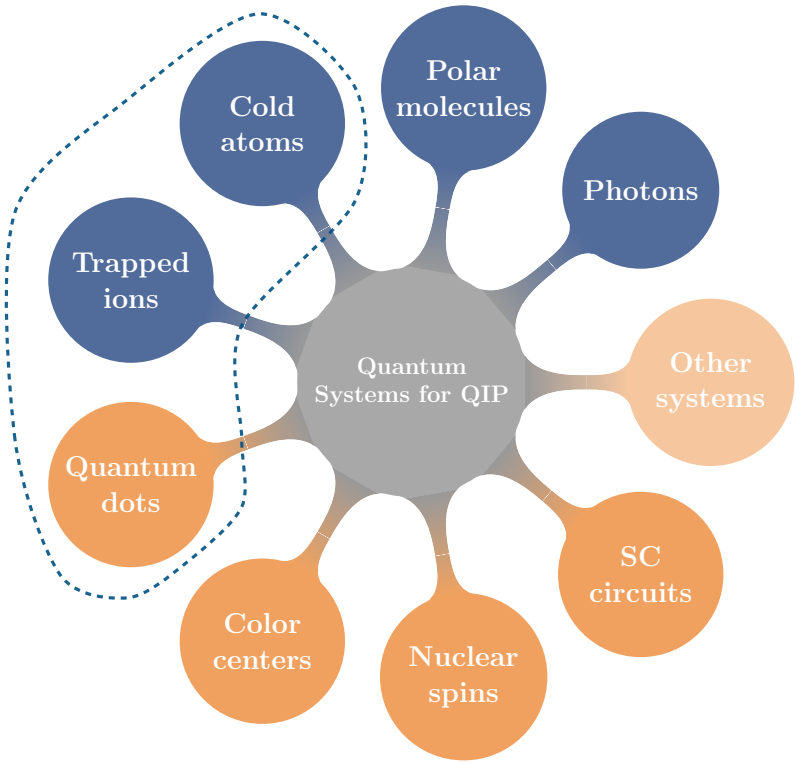

Figure 1.1: Overview of AMO (*blue*) and solid-state (*orange*) implementations for quantum science. The dashed line encircles the physical setups that are related to this thesis.

may put forward fruitful analogies and inspire a fresh take on long-standing problems. In that spirit, we aim at exploring novel solid-state quantum systems from a quantum-optics perspective.

For many QIP-related tasks, it is crucial that well-defined qubits can be held at fixed positions and controlled. The underlying trapping mechanisms vary considerably from system to system. Often they rely on well-controlled electromagnetic fields. For instance, ion traps may be generated from electric potentials on metal electrodes, and neutral atoms can be stored in optical dipole traps and lattices with laser beams. These systems are well-studied, and among the leading contenders for quantum computation and simulations.

In this thesis, we study semiconductor systems that host mobile quasiparticles and charge carriers, which are subject to similarly tailored electromagnetic and strain fields. In particular, we address the usage of controlled sound fields, and the remarkable properties of two-dimensional semiconductors for the realization of traps and lattices for quasiparticles (e.g., electrons) in semiconductors. While being closely related to well-established solid-state implementations based on quantum dots, some of the discussed physical systems bear striking similarities with trapped-ion or cold atomic systems, and bring together several advantages from both the solid-state domain on the one hand, and AMO systems and quantum optics on the other hand.

The following two Sections 1.3 and 1.4 provide a brief theoretical background of sound-matter interaction and two-dimensional semiconductors, respectively. For a better overview, the general structure of this thesis is outlined in Sec. 1.5.

1.3 Quantum Acoustics

Quantum acoustics is a relatively young research field that is concerned with sound-matter interaction in quantum systems. Per se, the underlying physics is not fundamentally different from mechanisms in light-matter interactions. Hence, it is instructive to compare key concepts in this field with their counterparts in quantum optics, see Table 1.1. In quantum acoustical settings, quasiparticles or artificial atoms interact with sound fields in solid-state systems. Sound waves are typically launched by converting electric signals to elastic waves using interdigital transducers (IDTs). Quantum matter can be interfaced with different kinds of sounds modes, e.g. bulk acoustic waves (BAWs) or surface acoustic waves (SAWs). Due to their advantageous properties, which will be summarized in the following, we focus on SAWs in this Thesis.

Surface acoustic waves

In the following, basic properties of surface waves will be summarized. In particular, surface waves in piezoelectric and piezomagnetic solids will be discussed. These concepts are central to the results presented in Chapters 2 and 3.

SAW basics

Elastic waves and their propagation in solids can be described in terms of the displacement vector $\mathbf{u}(\mathbf{x}, t)$. It depends on the spatial coordinate $\mathbf{x}$ and time t, and u_i shall denote the displacement along the ith Cartesian coordinate $\hat{x}_i$ ($\hat{x}_1 \equiv \hat{x}$, $\hat{x}_2 \equiv \hat{y}$, $\hat{x}_3 \equiv \hat{z}$). In a medium with mass density ρ, the displacement field obeys

$$\rho \frac{\partial^2 u_i(\mathbf{x}, t)}{\partial t^2} = \sum_j \frac{\partial T_{ij}}{\partial x_j}, \tag{1.1}$$

where T denotes the stress tensor, and the matrix element T_{ij} is the ith component of force per unit area perpendicular to the $\hat{x}_j$ axis. In the literature, notation concerning summation

Quantum Optics	Quantum Acoustics
Photons (light)	Phonons (sound)
Atoms & ions	Quasiparticles, artificial qubits
Speed of light $c \sim 3 \cdot 10^8$ m/s	Speed of sound $v_\mathrm{s} \sim (1 - 10) \cdot 10^3$ m/s
Laser	Interdigital transducer
Paul ion traps	Acoustic lattices (see Chapter 2)
Optical lattices	Magnetic lattices (see Chapter 3)

Table 1.1: Quantum Optics and Quantum Acoustics: analogies and key ingredients. See also ref. [1].

over repeated indiced is often conveniently shortened using the Einstein convention. In this introductory passage, for clarity, we will explicitly provide all sums, but we will switch to the Einstein convention in the following chapters.

The stress tensor is symmetric, $T_{ij} = T_{ji}, \forall i, j$. Since strain is proportional to stress in the commonly encountered linear regime, T typically obeys a generalized form of Hooke's law,

$$T_{ij} = \sum_{k,l} c_{ijkl} u_{kl}, \tag{1.2}$$

where c is the elasticity tensor (or stiffness tensor), and the strain tensor is defined as

$$u_{kl}(\mathbf{x}, t) = \frac{1}{2}\left(\frac{\partial u_k(\mathbf{x}, t)}{\partial x_l} + \frac{\partial u_l(\mathbf{x}, t)}{\partial x_k}\right). \tag{1.3}$$

Using its symmetry, $u_{kl} = u_{lk}, \forall k, l$, we obtain

$$T_{ij} = \sum_{k,l} c_{ijkl} \frac{\partial u_k}{\partial x_l}. \tag{1.4}$$

Plugging Eq. (1.4) into Eq. (1.1), we obtain the wave equation

$$\rho \frac{\partial^2 u_i(\mathbf{x}, t)}{\partial t^2} = \sum_{j,k,l} c_{ijkl} \frac{\partial^2 u_k}{\partial x_j \partial x_l}. \tag{1.5}$$

Eq. (1.5) gives rise to a variety of solutions, both bulk and surface waves. For quantum acoustics, both kinds of acoustic waves are of interest. Here, we will only address basic properties of surface waves.

For the remainder of this Thesis, we will assume a crystal surface at $z = 0$, spanned by $\hat{x}_1$ and $\hat{x}_2$. In the absence of external forces, the stress-free boundary at $z = 0$ imposed by this surface gives rise to unique acoustic modes whose propagation is confined to the vicinity of the surface. These solutions to Eq. (1.5) are known as surface acoustic waves, and they play an important role in various disciplines, including geophysics and electronics.[5] The boundary conditions ($T_{13} = T_{23} = T_{33} = 0$ at the surface) may be written as

$$T_{i3} = \sum_{k,l} c_{i3kl} \frac{\partial u_k(\mathbf{x} = (x, y, z = 0), t)}{\partial x_l} = 0, \quad (i = 1, 2, 3). \tag{1.6}$$

In general, there exists a variety of different solutions to Eq. (1.1) under the boundary conditions specified in (1.6). Rayleigh waves constitute a particular class of solutions, that are polarized in the sagittal plane, spanned by the wavevector $\mathbf{k}$ (which points in the direction of propagation) and $\hat{x}_3$, the surface normal.[6] In homogeneous and flat elastic solids,

[5] SAWs are being used in electronic components to provide a number of different functionalities, including bandpass filters and delay lines. The wide succcess of SAW devices relies on crystalline host materials in which elastic wave propagation is almost ideal, i.e., with low loss, diffraction and dispersion, and suitable piezoelectric coupling.

[6] Another important kind of surface waves are Love waves, which are polarized in the $(\hat{x}_1, \hat{x}_2)$ plane.

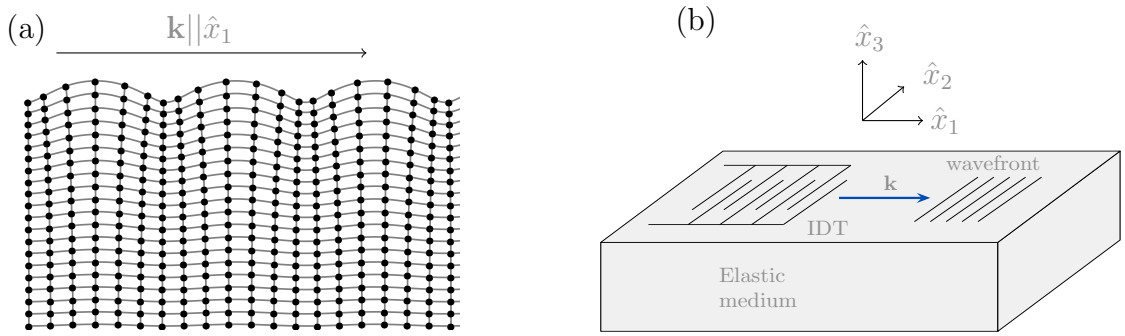

Figure 1.2: Propagation and excitation of Rayleigh waves. (a) Displacements $\mathbf{u}(\mathbf{x}, t_0)$ around crystal lattice sites at fixed time $t = t_0$. (b) Rayleigh wave front excited by interdigital transducer. The polarization of the wave lies in the sagittal plane spanned by $\hat{x}_1$ and $\hat{x}_3$.

Rayleigh waves show no dispersion, i.e., $\omega(k) = v_s k$ is linear. As surface waves, they are bound to the surface and decay exponentially with increasing depth in the solid. Typically, the decay length is of the order of the wavelength λ, see Fig. 1.2(a). Their phase velocity is smaller than that of the slowest bulk wave. Therefore, these surface-wave solutions do not appreciably couple to bulk waves. Note that there also exist surface waves that leak into the bulk. For the purpose of this Thesis, such waves are not considered, but more information can be obtained in Refs. [67, 68].

SAW propagation in piezoelectric materials

In a piezoelectric medium, mechanical stress and strain are coupled to an electric field $\mathbf{E}$ or electric displacement $\mathbf{D}$. As before, we consider only the linear regime where the stress tensor now includes a contribution from the electric field, and reads

$$T_{ij} = \sum_{k,l} c_{ijkl} u_{kl} - \sum_{k} e_{kij} E_k, \tag{1.7}$$

where e denotes the piezoelectric tensor that encodes the piezoelectric coupling strength in a given material. The electric displacement is given by

$$D_i = \sum_{j} \varepsilon_{ij} E_j + \sum_{j,k} e_{ijk} u_{jk}, \tag{1.8}$$

and ε is the permittivity tensor. Eqs. (1.7) and (1.8) are the constitutive equations of a piezoelectric solid, that determine the properties of propagating surface waves. From these relations, a set of coupled equations of motion for the displacement and electric fields $\mathbf{u}(\mathbf{x}, t)$ and $\mathbf{E}(\mathbf{x}, t)$ can be derived.

In a piezoelectric medium with mass density ρ, elastic waves obey Eq. (1.1) with T given by Eq. (1.7). Electromagnetic theory provides another relation, with which a complete set of coupled equations can be obtained that may be solved, given appropriate boundary conditions. While electric material characteristics are governed by Maxwell's equations, the quasi-static approximation of $\nabla \times \mathbf{E} = 0$ can be applied to acoustic wave propagation, since the sound velocity, v_s, is several orders of magnitude smaller than the speed of light, c. Within this approximation, the electric field can be expressed as

$$\mathbf{E}(\mathbf{x}, t) = -\nabla\phi(\mathbf{x}, t), \tag{1.9}$$

where ϕ denotes the electric potential. The electric displacement satisfies $\nabla \cdot \mathbf{D} = q$, and, in a typical piezoelectric solid, the contribution of the charge density q is negligble, i.e., $\nabla \cdot \mathrm{D} \approx 0$.[7] Putting Eqs. (1.1), (1.7)-(1.9) and Gauss's law together, we obtain a set of four coupled equations,

$$\rho\frac{\partial^2 u_i}{\partial t^2} = \sum_{j,k,l} c_{ijkl}\frac{\partial^2 u_k}{\partial x_j \partial x_l} + \sum_{j,k} e_{kij}\frac{\partial^2 \phi}{\partial x_j \partial x_k}, \tag{1.10}$$

$$\sum_{i,j} \varepsilon_{ij}\frac{\partial^2 \phi}{\partial x_i \partial x_j} = \sum_{i,j,k} e_{ijk}\frac{\partial^2 u_j}{\partial x_i \partial x_k}. \tag{1.11}$$

The solutions are mainly characterized by crystal symmetry and, more generally, material properties. For a general piezoelectric medium, upon fixing material parameters and direction of propagation, these equations may be solved numerically. Note that, as a result of the quasi-electrostatic approximation, $\phi(\mathbf{x}, t)$ inherits both the spatial and temporal periodicity from the elastic displacement $\mathbf{u}(\mathbf{x}, t)$. This electric signal, that propagates through the material with a characteristic speed $v_\mathrm{s} \approx (1 - 10)$ km/s, for typical semiconductors, will be important for the ideas presented in Chapter 2.

SAW propagation in piezomagnetic materials

In a piezomagnetic material, similar equations may be derived, based on the constitutive equations

$$T_{ij} = \sum_{k,l} c_{ijkl} u_{kl} - \sum_k h_{kij} H_k, \tag{1.12}$$

$$B_i = \sum_{j,k} h_{ijk} u_{jk} + \sum_j \mu_{ij} H_j. \tag{1.13}$$

Here, $\mathbf{H}$ and $\mathbf{B}$ denote and the magnetic field and induction, respectively, and h is the piezomagnetic tensor. μ is the magnetic permeability. Similar to the piezoelectric case, Eq. (1.1) can be invoked to derive an equation of motion for $\mathbf{u}(\mathbf{x}, t)$. Likewise, Gauss's

[7] In insulating solids, there are no free charges, and $\nabla \cdot \mathrm{D} = 0$ holds exactly.

law for magnetism provides another relation, and the coupled equations can be used as a starting point for further numerical analysis. Note that, more generally, materials which exhibit both piezoelectric and piezomagnetic effects, can be described by [69],

$$T_{ij} = \sum_{k,l} c_{ijkl} u_{kl} - \sum_{k} e_{kij} E_k - \sum_{k} h_{kij} H_k, \tag{1.14}$$

$$D_i = \sum_{j,k} e_{ijk} u_{jk} + \sum_{j} \varepsilon_{ij} E_j + \sum_{j} \alpha_{ij} H_j, \tag{1.15}$$

$$B_i = \sum_{j,k} h_{ijk} u_{jk} + \sum_{j} \mu_{ij} H_j + \sum_{j} \alpha_{ij} E_j. \tag{1.16}$$

Acoustically driven magnetic and electric fields provide the basis for the results discussed in Chapter 3.

Surface waves in semiconductors

Traveling electric potentials $\phi(\mathbf{x}, t)$ that can be generated deterministically hold promise for various applications in semiconductor systems: metrology [70, 71], on-demand single-electron transport [72, 73], implementation of solid-state flying qubits [74], distant spin entanglement [75], and single-photon sources [76, 77], just to name a few. This list is not exhaustive, but it already indicates the great potential of SAW-defined *moving quantum dots* for quantum technologies and information processing.

Arrays of gate-defined quantum dots (QDs) are a key platform for QIP, see Fig. 1.1. While electrons confined to QDs can be used to encode quantum information, efficient manipulation and transfer of quantum states through an array of QDs poses a variety of challenges on experiments. Acoustically defined electron shuttles enable high-fidelity single-electron transport between distant quantum dots. Recent experiments have shown to preserve the electron spin during transport with high fidelity [78], and experiments performing quantum logic operations on flying electron qubits are underway [79, 80]. SAW platforms may also be used to implement a quantum data bus, where the information is encoded in propagating phonon states, to store and transfer quantum information between nodes in a quantum network. Due to the versatility of SAW-based setups, this may enable novel hybrid platforms, where vastly different quantum systems may be coupled [81]. For example, acoustic phonons may be coupled via strain to the internal degrees of freedom of defect centers in solids, e.g. NV or SiV centers in diamond [82, 83, 84]. This strain coupling has been employed for quantum control of internal states and improved spin coherence, and large spin-phonon interaction may be used to realize two-qubit gates between distant defect centers [81, 85].

Yet another direction consists in the design and implementation of SAW-based acoustic traps and lattices for charge carriers in semiconductors. Regular lattices of electrons, for

example, that interact strongly over large distances, present a fresh alternative to more established QIP platforms. This will be discussed in Chapters 2 and 3.

Surface waves and superconducting qubits

A superconducting circuit can serve as a physical realization of a qubit, that may be piezoelectrically coupled to the electric potential ϕ associated with SAW phonons. These systems can realize Hamiltonians that are familiar from quantum optics and circuit quantum electrodynamics (QED), where photons are being replaced by phonons and artificial atoms take over the role of real atoms, see Table 1.1.

The first step in this direction was achieved in 2012 by coupling a single phonon piezoelectrically to a single-electron transistor [86], demonstrating the required sensitivity and feasibility of this approach. Soon after, the coupling of SAW phonons and superconducting transmon qubits was demonstrated [87]. In the meantime, this relatively young research direction has seen various remarkable experimental results, including first cavity quantum acoustodynamics (QAD) experiments in the dispersive regime [88], the demonstration of strong coupling [89, 90], quantum control of SAW phonons [91], and the relaxation dynamics of giant artificial atoms [92].

Due to the fact that some properties of quantum acoustical systems are fundamentally different from their quantum optical counterparts, e.g. the slow propagation of sound (see Table 1.1) or the breakdown of the electric dipole approximation, it can be expected that there will be plenty of opportunities for exploring novel phenomena with quantum acoustics.

Further reading

- D. Morgan, *Surface Acoustic Wave Filters*, Academic Press (2007). See ref. [67].
- P. Delsing, *et al.*, *The 2019 surface acoustic waves roadmap*, J. Phys. D **52**, 353001 (2019). See ref. [1].
- A. F. Kockum, *Quantum optics with giant atoms – the first five years*, preprint available on *arXiv*:1912.13012. See ref. [93].

1.4 Two-Dimensional Semiconductors

Atomically thin materials such as graphene and monolayer transition-metal dichalcogenides (TMDs) have remarkable electronic, optical and mechanical properties due to their reduced dimensionality and crystal structure. Two-dimensional crystals became largely available for studies and applications after graphene was mechanically exfoliated from three-dimensional graphite in pioneering work [94], by pulling single carbon sheets away using adhesive tape. In 2010, following the first demonstration of this higly efficient procedure, the Nobel Prize in Physics was awarded for *groundbreaking experiments regarding the two-dimensional material graphene* [95]. While graphene is certainly the best studied among the two-dimensional materials with great potential for various applications, it lacks a band gap, making it unsuitable for certain optoelectronic tasks. Unlike graphene, a variety of two-dimensional TMDs is semiconducting. While the band structure of bulk TMDs has an indirect band gap, monolayer TMDs have a direct band gap[8] at the K and K' corner points of the Brioullin zone, which was verified experimentally using photoluminescence [96]. This has far-reaching consequences for their optoelectronic properties, and it makes this class of materials precious for numerous applications, including in electronics as transistors, or in optics as emitters, diodes, and solar cells.

Meanwhile, two-dimensional semiconductors emerged as a key platform to explore novel many-body phenomena. Due to their optical band gap and reduced screening in two dimensions, they enable efficient light-matter interfaces. This key insight has triggered various studies of quantum emitters and the optical response of TMDs, and motivates the results discussed in Chapter 4. Other recent developments in this research area include, but are not restricted to strain engineering, valleytronics, and bilayer TMD systems.

Electrostatic interaction

Due to reduced screening in two dimensions, interactions between charge carriers can be significantly enhanced, as compared to settings in bulk semiconductors. A brief summary of the derivation of the electrostatic interaction potential in TMD monolayers is given below.

In three dimensions, macroscopic screening effects are well-described by global properties, and quantified by a dielectric constant ε. In contrast, screening in two dimensions is non-local, and described by a wavevector-dependent dielectric function in momentum space, $\varepsilon(\mathbf{q})$ [97]. We consider a dielectric sheet at $z = 0$, subject to an electric potential $\phi_{\text{ext}}(\mathbf{x})$ due to a point charge Q_1 located at the origin, which is associated with a charge density $n_{\text{ext}} = Q_1\delta(\mathbf{x})$. The total electrostatic potential ϕ and total charge density, $n(\mathbf{x}) = n_{\text{ext}}(\mathbf{x}) + n_{\text{ind}}(\mathbf{x})$, are related by Poisson's equation,

$$\nabla^2\phi(\mathbf{x}) = -4\pi n(\mathbf{x}), \tag{1.17}$$

[8]The crystal momentum of electrons and holes is the same in both the conduction and valence band. The materials MoS_2, $MoSe_2$, WS_2, WSe_2 and $MoTe_2$ all have a direct band gap.

where the induced charge density $n_{\mathrm{ind}}(r, \varphi, z)$ is restricted to the plane at $z = 0$. In the long-wavelength limit, it can be expressed in terms of the polarization $\mathbf{P}_{\mathrm{2D}}$, as $n_{\mathrm{ind}} = -\nabla \cdot \mathbf{P}_{\mathrm{2D}}$. The polarization itself is related to the polarizability α_{2D},

$$\mathbf{P}_{\mathrm{2D}}(r) = -\alpha_{\mathrm{2D}} \nabla_r \phi(r, \varphi, z = 0), \tag{1.18}$$

from which it follows that

$$n_{\mathrm{ind}}(\mathbf{x}) = \delta(z) \alpha_{\mathrm{2D}} \nabla_r^2 \phi(r, \varphi) \tag{1.19}$$

Now, we can write the Poisson equation as

$$\nabla^2 \phi(\mathbf{x}) = -4\pi Q_1 \delta(\mathbf{x}) - 4\pi \alpha_{\mathrm{2D}} \nabla_r^2(r, \varphi) \delta(z). \tag{1.20}$$

This equation can be Fourier transformed and solved in momentum space, such that

$$\phi_{\mathrm{2D}}(\mathbf{q}) = \frac{2\pi Q_1}{|\mathbf{q}|(1 + 2\pi \alpha_{\mathrm{2D}} |\mathbf{q}|)}, \tag{1.21}$$

which defines the two-dimensional electric potential as a function of the in-plane wavevector $\mathbf{q}$. The effective interaction potential between Q_1 and a second test charge Q_2 is given by

$$V(r) = Q_2 \int \mathrm{d}^2\mathbf{q}\ \phi_{\mathrm{2D}}(\mathbf{q}) \mathrm{e}^{i\mathbf{q}\cdot\mathbf{r}}, \tag{1.22}$$

where $\mathbf{r}$ is the location of charge Q_2, and $r = |\mathbf{r}|$ denotes the distance between two charges. The Keldysh interaction potential between Q_1 and Q_2 can now be obtained as

$$V(r) = \frac{Q_1 Q_2}{4\alpha} \left[H_0\left(\frac{r}{2\pi\alpha}\right) - Y_0\left(\frac{r}{2\pi\alpha}\right) \right], \tag{1.23}$$

where H_0 and Y_0 denote Struve and von Neumann functions, respectively. The resulting expression for the electrostatic interaction potential between two charges will be contained in the theoretical model of Chapter 4. Note that the polarizability $\alpha \sim 1/E_{\mathrm{g}}$ can be related to the band gap E_{g} [98]. Plugging in typical TMD parameters, one obtains $\alpha \approx 7$ Å for MoS_2, and similar values for other monolayer TMDs. At distances $r \gg 2\pi\alpha$, Eq. (1.23) is well described by a Coulomb-like interaction, $V(r) \sim 1/r$ (see Fig. 1.3).

Excitons, trions and optical properties

In semiconductors, the absorption of a photon with suitable energy may cause an electron to be promoted from the valence to the conduction band, leaving behind a hole in the valence band. Electrons and holes can form bound states, referred to as excitons, by means of attractive Coulomb interation, see Fig. 1.3. TMD monolayers host excitons with relatively large binding energies of the order of ~ 0.5 eV, which is due to strong electrostatic interactions. For this reason, their fundamental optical properties are largely determined

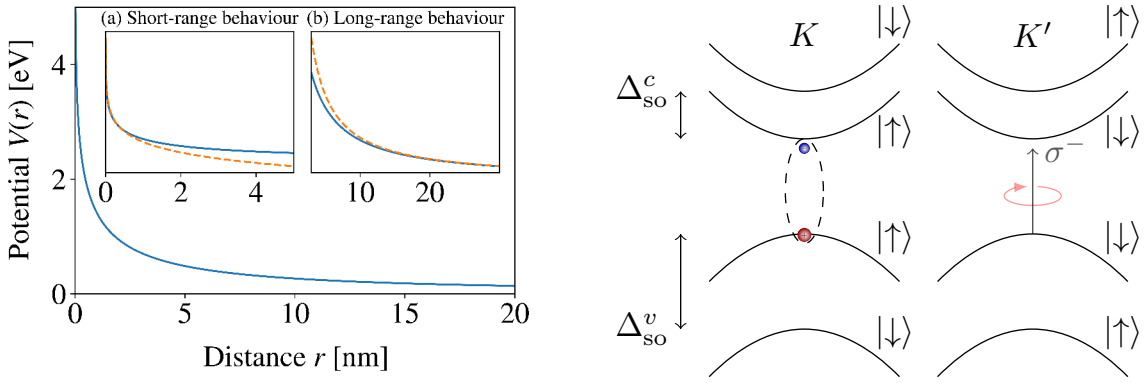

Figure 1.3: (*Left*): Keldysh potential for typical TMD parameters. Insets: Orange dotted lines show logarithmic 2D ($1/r$-like 3D) Coulomb potential that approximates the short-range (long-range) behaviour of the Keldysh potential. (*Right*): Band structure of MoX_2 monolayers at the K and K' valleys, with spin-orbit splittings between spin states in the conduction and valence bands.

by strong excitonic resonances, both at cryogenic and room temperature. These exciton transitions exhibit large oscillator strengths, resulting in large radiative linewidths. In addition, the excitonic response may be controlled and tuned electrically. Optical absorption and photoluminescence spectroscopy of monolayer TMDs, as a function of charge-carrier density, has revealed the presence of strongly bound, electrically charged trions [150], and further multi-particle excitonic states have been theoretically predicted and detected in experiment.

Spin and valley optical selection rules further enrich the low-dimensional physics of monolayer TMDs. Importantly, TMD monolayer crystals have no inversion symmetry center, which allows access to the *valley* degree of freedom of charge carriers. The direct band gaps of monolayer TMDs are located at two inequivalent points in momentum space, K and K', at the corners of the hexagonal Brioullin zone. Interband transitions near these points couple exclusively to right or left circularly polarized light, respectively. This enables polarization-dependent addressing of specific valley states, see Fig. 1.3. In addition, strong spin-orbit coupling in TMD monolayers leads to large spin-orbit splittings, Δ^v_{SO} and Δ^c_{SO}, of the order of hundreds of meV (a few meV) in the valence (conduction) band. This results in spin-valley coupling and optical spin selection rules. Taken together, these properties enable stable valley polarization and, more general, pave the way to control the internal quantum degrees of freedom of charge carriers in TMDs.

Further reading

- G. Wang, *et al.*, *Colloquium: Excitons in atomically thin transition metal dichalcogenides*, Rev. Mod. Phys. **90**, 021001 (2018). See ref. [99].
- T. Mueller, and Ermin Malic, *Exciton physics and device applications of two-dimensional transition metal dichalcogenide semiconductors*, npj 2D Mat. and Appl. **2**, 29 (2018). See ref. [100].
- S. Manzeli, *et al.*, *2D transition metal dichalcogenides*, Nat. Rev. Mater. **2**, 17033 (2017). See ref. [101].

1.5 Outline of this Thesis

Various approaches towards QIP are being explored, and many physical implementations thereof are being considered (see Fig. 1.1), each with its own unique advantages. In this thesis we address how several ideas taken from quantum optics inspire novel setups and implementations of QIP in solid-state settings.

To this end, we develop strategies to enable the realization of well-defined lattices for electrons and other quasiparticles in semiconductors. We distinguish two key strategies: (i) quantum acoustical implementations in semiconductors, **inspired** by quantum optical systems, and (ii) solid-state systems **interfaced** with quantum optical readout tools and methodology. As summarized in Fig. 1.4, the structure of this thesis follows this concept. In the first part of this thesis, we investigate how SAWs may be used to create well-defined potentials for mobile electrons. In the second part of this thesis, we focus on realization and detection of self-assembled electron lattices in TMDs.

In Chapter 2, we propose and analyze a solid-state platform based on surface acoustic waves for trapping, cooling, and controlling (charged) particles, as well as the simulation of quantum many-body systems. We develop a general theoretical framework demonstrating the emergence of effective time-independent acoustic trapping potentials for particles in two- or one-dimensional structures. As our main example, we discuss in detail the generation and applications of a stationary, but movable, acoustic pseudolattice with lattice parameters that are reconfigurable in situ. We identify the relevant figures of merit, discuss potential experimental platforms for a faithful implementation of such an acoustic

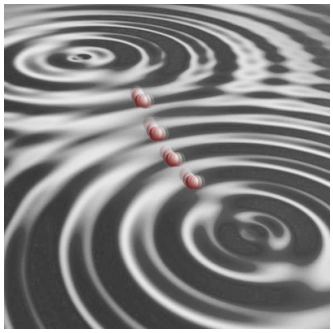

Acoustically Defined Lattices

- *Inspired:* quantum acoustical systems inspired by quantum optical systems.
- Introductory remarks in Sec. 1.3.
- Results discussed in Chapters 2 and 3.

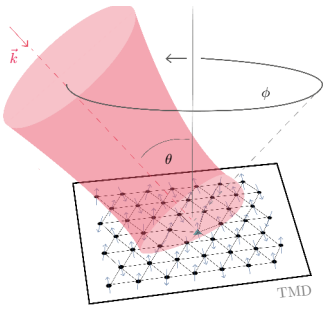

Self-Assembled Lattices

- *Interfaced:* exploration of semiconductor systems with quantum optics tools.
- Introductory remarks in Sec. 1.4.
- Results discussed in Chapter 4.

Figure 1.4: Structure and building blocks of this thesis. Lower figure adapted from Ref. [4].

lattice, and provide estimates for typical system parameters. With a projected lattice spacing on the scale of 100nm, this approach allows for relatively large energy scales in the realization of fermionic Hubbard models, with the ultimate prospect of entering the low-temperature, strong interaction regime. Experimental imperfections as well as readout schemes are discussed. The results presented in this chapter are based on Ref. [2].

In Chapter 3, we propose and analyze magnetic traps and lattices for electrons in semiconductors. We provide a general theoretical framework and show that thermally stable traps can be generated by magnetically driving the particle's internal spin transition, akin to optical dipole traps for ultracold atoms. Next we discuss in detail periodic arrays of magnetic traps, i.e., magnetic lattices, as a platform for quantum simulation of exotic Hubbard models, with lattice parameters that can be tuned in real time. Our scheme can be readily implemented in state-of-the-art experiments, as we particularize for two specific setups, one based on a superconducting circuit and another one based on surface acoustic waves. The results presented in this chapter are based on Ref. [3].

In Chapter 4, we discuss and analyze self-assembled Wigner crystals in two-dimensional semiconductors. Wigner crystals are prime candidates for the realization of regular electron lattices under minimal requirements on external control and electronics. However, several technical challenges have prevented their detailed experimental investigation and applications to date. We propose an implementation of two-dimensional electron lattices for quantum simulation of Ising spin systems based on self-assembled Wigner crystals in transition-metal dichalcogenides. We show that these semiconductors allow for minimally invasive all-optical detection schemes of charge ordering and total spin. For incident light with optimally chosen beam parameters and polarization, we predict a strong dependence of the transmitted and reflected signals on the underlying lattice periodicity, thus revealing the charge order inherent in Wigner crystals. At the same time, the selection rules in transition-metal dichalcogenides provide direct access to the spin degree of freedom via Faraday rotation measurements. The results presented in this chapter are based on Ref. [4].

In Chapter 5, we discuss possible future research directions that go beyond the scope of this work, but are closely related. While this thesis is of theoretical nature, it is quite closely connected with experimental considerations, that may enable the realization of the proposed ideas in the near future.

Chapter 2

Acoustic Traps and Lattices

2.1 Motivation

The ability to trap and control particles with the help of well-controlled electromagnetic fields has led to revolutionary advances in the fields of biology, condensed-matter physics, high-precision spectroscopy and quantum information, enabling unprecedented control both in the study of isolated single particles as well as few- and many-body systems subject to controlled and tunable interactions. Prominent examples range from using optical tweezers for probing the mechanical properties of DNA [102, 103], to the realizations of Bose-Einstein condensates [104, 105, 106] and numerous breakthrough investigations of strongly-correlated quantum many-body systems with both trapped ions [107] and ultracold atoms in optical lattices [108, 109]. At the same time, the ever improving control of materials and fabrication of semiconductor nanostructures has led to a proliferation of quasi-particles in such systems and a quest to trap and isolate them in order to gain deeper insights into their properties and interactions. While quantum dots have been developed into excellent traps for charged and neutral quasiparticles and have contributed to a wealth of exciting insights [110], scaling them to the many-body regime remains either a fabrication or operational challenge. This motivates our search for trapping mechanisms that bring the generality and flexibility of optical lattices to the solid-state setting.

While an optical approach may be feasible [111], surface-acoustic waves (SAWs) have recently been used in a range of exciting experiments to trap electrons [72, 73, 112, 113, 114] or excitons [115] in *moving* potentials. When following this approach, however, particles are typically lost on a relatively fast timescale of $\sim$ 10ns, as a consequence of finite sample sizes and propagation speeds set by the speed of sound to $\sim 3 \times 10^3$m/s. Inspired by these experiments, here we propose and analyze engineered stationary and quasi-stationary (movable) *acoustic* trapping potentials and acoustic lattices (ALs) as a generic strategy for trapping, cooling and controlling quasi-particles as well as a potential on-chip, solid-state platform for the simulation of quantum many-body systems. While in this work we use the generation of an effective standing-wave lattice for electrons as the main example of our technique, our theoretical approach generalizes immediately to other trap configurations.

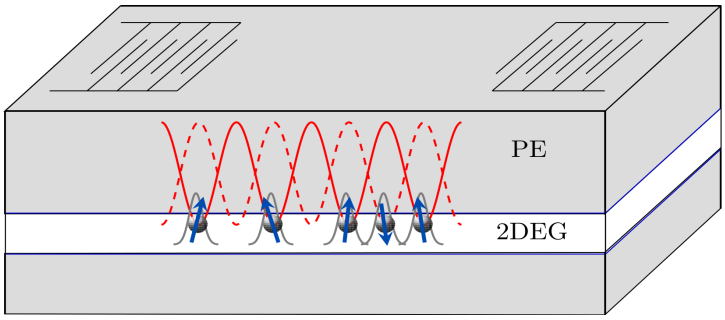

Figure 2.1: (color online). Schematic illustration of the setup. In a piezo-electric solid (PE) counter-propagating SAWs (as induced by standard IDTs deposited on the surface [67, 68]) generate a *time-dependent*, periodic electric potential for electrons confined in a conventional two-dimensional electron gas (2DEG). If the SAW frequency $\omega/2\pi = v_s/\lambda$ is sufficiently high (as specified in the main text), the electron's potential landscape can effectively be described by a *time-independent* pseudo-lattice with a lattice spacing $a = \lambda/2$. The potential depth (lattice spacing) can be controlled conveniently via the power (frequency) applied to the IDTs; while an additional screening layer (not shown) allows for tuning the strength of the Coulomb interaction between the particles [120]. In more complex structures, the setup can consist of multiple layers on top of some substrate.

In particular, focused SAWs [116] might allow for the generation of quasi zero-dimensional traps for electrons akin to optical tweezers, thereby entering a new parameter regime in the context of *acoustic tweezers*; so far, the latter have been used only in a high-temperature, classical regime to trap and manipulate microparticles immersed in fluids above the SAW-carrying solid [117].

2.2 Executive Summary

Our basic scheme involves counter-propagating SAWs that are launched in opposite directions from two (or more) standard interdigital transducers (IDTs) [67, 68] patterned either directly onto a piezoelectric substrate such as GaAs or on some piezoelectric island as demonstrated for example in Ref. [118]; for a schematic illustration compare Fig.3.1. Because of the intrinsic piezoelectric property of the material, the SAWs are accompanied by a (time-dependent) periodic electric potential and strain field, generating a well-controlled potential landscape (of the same spatial and temporal periodicity) for electrons confined in conventional quantum wells or purely two-dimensional crystals such as transition metal dichalcogenides (TMDs), with a periodicity on the order of $\sim$ 100nm for SAW frequencies of $\sim$ 20GHz [119]. Based on a perturbative Floquet approach, we show that the electron's potential landscape can effectively be described by a *time-independent* pseudo-lattice with a lattice spacing $\sim a = \lambda/2$, provided that certain conditions are fulfilled (as specified below). Intuitively, the occurrence of such an effective time-independent potential can be understood from the fact that sufficiently heavy electrons cannot adiabatically follow a

rapidly oscillating force as created by the SAW-induced electric potential; therefore, the electron will effectively be trapped close to the potential minimum if its wavefunction spreads slowly enough such that it is still close to its original position after one oscillation period of the SAW field. We identify the relevant figures of merit for this novel setup [cf. Eq.(2.2)] and show how the system parameters can be engineered and dynamically tuned. As a guideline for an experimental realization of the proposed setup, we derive a set of self-consistency requirements which allows us to make clear predictions about the material properties needed for a faithful implementation. Consequently, we identify strategies to meet these requirements with state-of-the-art experimental techniques and suitable material choices. Concerning the latter, we analyze the viability of different heterostructures with high effective electron masses which support high-velocity sound waves, e.g. AlN/diamond or, alternatively, TMDs such as MoS_2 or WSe_2. While we discuss the relevant decoherence mechanisms as well as other relevant experimental imperfections for specific systems, the very basic principles of our approach should be of broad applicability to various physical solid-state platforms. In particular, thanks to the generic nature of our analysis and the variety of fields (strain, electric, magnetic) that potentially accompany SAWs, our framework is readily applicable to a broad class of (quasi-)particles, including for example electrons, holes, trions and excitons. While our theoretical treatment is (to some extent) reminiscent of trapped ions, allowing us to capitalize on ideas and results from this well-developed field of research, we show that the emergent effective dynamics can be captured by the Fermi-Hubbard model, very much like for fermionic ultra-cold atoms in optical lattices, albeit in unprecedented parameter regimes, because of ultra-high charge-to-mass ratios and naturally long-ranged Coulomb interactions. Our approach provides an alternative to standard (gate-defined) quantum dots, providing a highly regular periodicity simply set by the SAW wavelength, with minimal fabrication requirements (without any further gate patterning), and the potential to deterministically move around the acoustically-defined quantum dots by simply changing the phase of the excitation applied to the IDTs. Also, our trapped-ion-inspired pseudo-potential approach makes our proposal significantly different from previous theoretical [120] and experimental investigations [115, 118], where particles trapped inside a dynamic, *moving* AL (rather than a quasi-stationary, *standing* AL, as considered here) are inevitably lost within a rather short timescale $\sim$ 10ns.

2.3 Theoretical Framework

In this section we first develop a general theoretical framework describing particles in low-dimensional semiconductor structures in the presence of (SAW-induced) high-frequency standing waves. We employ both classical and quantum-mechanical tools in order to identify the relevant figures of merit and specify the conditions for the validity of our theoretical framework. The experimental feasibility of our scheme will be discussed for specific setups thereafter in Section 2.4.

Surface acoustic waves.—SAWs are phonon excitations which propagate elastically on

the surface of a solid within a depth of roughly one wavelength λ [67, 68]. In the case of a piezoelectric material, SAWs can be generated electrically based on standard interdigital transducers (IDTs) deposited on the surface, with a SAW amplitude proportional to the amplitude (square root of the power) applied to the IDTs [67, 68, 72]. Typically, such an IDT consists of two thin-film electrodes on a piezoelectric material, each formed by interdigitated fingers. Whenever a radio frequency (RF) signal is applied to such an IDT, a SAW is generated if the resonance condition $p = v_{s,\alpha}/f$ is met; here, p, $v_{s,\alpha}$ and $f = \omega/2\pi$ refer to the IDT period, the sound velocity of a particular SAW mode α and the applied frequency, respectively [67, 68, 121]. As evidenced by numerous experimental studies [122, 123, 124, 125], SAWs can interact with a two-dimensional electron gas (2DEG) via the electric (and/or strain) field accompanying this elastic wave.

Classical analysis.—To illustrate our approach, let us first consider the classical dynamics of a single, charged particle of mass m (also referred to as *electron* in the following) exposed to a SAW-induced monochromatic piezo-electric standing wave of the form $\phi(x,t) = \phi_0 \cos(kx)\cos(\omega t)$. Here, $\omega = v_s k$ refers to the dispersion relation of a specific SAW mode and the time-dependent potential experienced by the electron is $V(x,t) = e\phi(x,t)$ with an amplitude $V_{\mathrm{SAW}} = e\phi_0$ (where e denotes the electron's charge). In the absence of a piezoelectric potential, a similar periodic potential derives from the (strain-induced) deformation potential associated with a SAW [115]; our theoretical analysis applies to both scenarios, as it is independent of the microscopic origin of the SAW-induced potential $V(x,t) = V_{\mathrm{SAW}} \cos(kx)\cos(\omega t)$. While the motion in the z-direction is frozen out for experimentally relevant temperatures, a potential pattern of the same periodic form could be produced in the y-direction using appropriately aligned pairs of IDT's launching counter-propagating SAWs [120]. In this scenario the electron's motional degrees of freedom are separable into two one-dimensional problems of the same structure. Alternatively, using for example etching techniques or gate-defined structures as described in Refs.[72, 73], effectively one-dimensional wires with strong transverse confinement in the y-direction may be considered. Therefore, in any case only the motion in the x-direction will be discussed in the following. Then, in dimensionless units, where $\tilde{x} = kx$ and $\tau = \omega t/2$, Newton's equation of motion for the electron's position $x(t)$ reads

$$\frac{d^2\tilde{x}}{d\tau^2} + 2q\sin(\tilde{x})\cos(2\tau) = 0, \tag{2.1}$$

where we have introduced the (dimensionless) stability parameter $q = V_{\mathrm{SAW}}/E_S$, with the emerging energy scale

$$E_S = mv_s^2/2, \tag{2.2}$$

that is, the classical kinetic energy of a particle with mass m and velocity equal to the speed of sound v_s of the driven SAW-mode; as will be shown below, the energy scale E_S turns out to be a key figure of merit in our setup. In the Lamb-Dicke limit $\tilde{x} \ll 1$, Eq. (2.1) reduces to the so-called Mathieu equation [cf. Eq.(2.9)], which is known to govern the dynamics of ions in Paul traps [126, 127]. We assess the stability of the electron's motion against thermal noise by numerically solving Eq. (2.1), for initial conditions set as

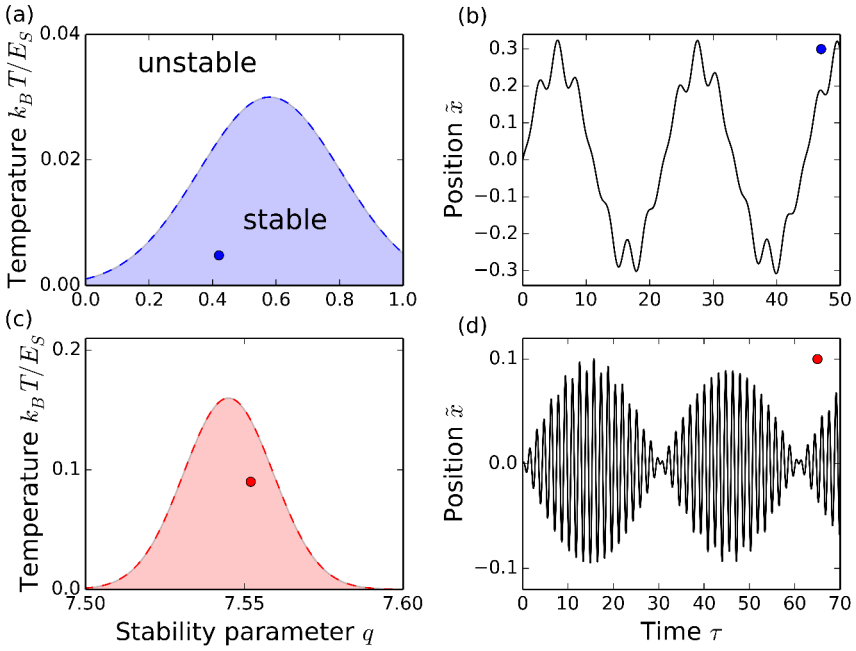

Figure 2.2: (color online). Approximate stability diagrams of the classical equation of motion in the low-q (upper plot) and high-q (lower plot) regimes, respectively. The dots denote trajectories corresponding to some exemplarily chosen parameter sets (q, k_BT/E_S).

$\tilde{x}_0 = 0$, $\tilde{v}_0 := [d\tilde{x}/d\tau]_{\tau=0} = \sqrt{2k_BT/E_S}$; here, according to $mv_0^2/2 = k_BT/2$, the initial velocity v_0 is identified with the temperature T by simple equipartition. Solutions to this problem are deemed *stable* if the maximal excursion $x_{\max}$ is smaller than one half of the lattice spacing ($\tilde{x}_{\max} < \pi$), even for very long timescales, and *unstable* otherwise. The results of this classification procedure are shown in Fig.2.2: Stable (bounded) solutions can only be found for sufficiently low temperatures (with $k_BT \ll E_S$) and certain values of the stability parameter q. In particular, in the regime $q^2 \ll 1$, $k_BT \ll E_S$ stable trajectories $\tilde{x}(\tau)$ consist of slow harmonic oscillations at the secular frequency $\omega_0/\omega \approx q/\sqrt{8}$, superimposed with fast, small-amplitude oscillations at the driving frequency ω (also referred to as micromotion [127]); compare Fig.2.2(b). When neglecting the micromotion within the so-called pseudo-potential approximation (as routinely done in the field of trapped ions [127]), the electron's (secular) dynamics is effectively described by that of a time-independent harmonic oscillator with (slow) frequency $\omega_0 \ll \omega$; for further analytical and numerical details we refer to Appendix 2.A.

Quantum-mechanical Floquet analysis.—The results described above can be corroborated within a fully quantum-mechanical model. Here, the electron's dynamics are governed by the *time-dependent* Hamiltonian

$$H_S(t) = \frac{\hat{p}^2}{2m} + V_{\mathrm{SAW}} \cos(\omega t) \cos(k\hat{x}), \tag{2.3}$$

where $\hat{x}$ and $\hat{p}$ refer to the particle's position and momentum operators, respectively. The

Hamiltonian $H_S(t)$ satisfies $H_S(t+T) = H_S(t)$ due to the time-periodic nature of the external driving, with $T = 2\pi/\omega$. In a high-frequency field, where the period of the force T is small compared to all other relevant timescales, the particle's dynamics can be approximately described by a *time-independent* Hamiltonian H_{eff}. As detailed in Appendix 2.B, H_{eff} can be calculated in a systematic expansion in the inverse of the driving frequency ω [128, 129]. Then, up to second order in $\sim \omega^{-1}$, we obtain

$$H_{\text{eff}} = \frac{\hat{p}^2}{2m} + V_0 \sin^2(k\hat{x}), \tag{2.4}$$

where $V_0 = \varepsilon^2 E_S$, with the small parameter $\varepsilon = q/\sqrt{8}$. The second term $V_{\text{eff}}(\hat{x}) = V_0 \sin^2(k\hat{x})$ demonstrates the formation of an effectively *time-independent*, spatially periodic acoustic lattice, with a lattice spacing $a = \lambda/2 = \pi/k$ and potential depth $V_0 = \varepsilon^2 E_S$. Similar to the case for trapped ions, lattice sites are found at the nodes of the time-dependent force $\mathbf{F}(x,t) \sim \sin(kx)\cos(\omega t)\mathbf{x}$ associated with the potential $V(x,t)$. This force changes its sign on a timescale $\sim \omega^{-1}$; if this is fast compared to the particle's dynamics $\sim \omega_0^{-1}$, the particle will be dynamically trapped, because it does not have sufficient time to react to the periodic force before this force changes its sign again. Within the usual harmonic approximation, where $V_{\text{eff}}(\hat{x}) \approx (m/2)\omega_0^2 \hat{x}^2$, the effective trapping frequency ω_0 can be estimated as $\omega_0/\omega \approx q/\sqrt{8}$, which coincides exactly with the (classical) result for the slow secular frequency ω_0 in the pseudopotential regime (with $q^2 \ll 1$). Accordingly, the AL can be rewritten as $V_{\text{eff}}(\hat{x}) = (\omega_0/\omega)^2 E_S \sin^2(k\hat{x})$, with the first (perturbative) factor accounting for the inherent separation of timescales between the fast driving frequency ω and the slow secular frequency ω_0. Written in this form, the effective acoustic potential $V_{\text{eff}}(\hat{x})$ is reminiscent of standard dipole traps for ultra-cold atoms. Here, the effective optical potential for a two-level system driven by a Rabi-frequency Ω with detuning Δ in a electromagnetic standing wave takes on the form $V_{\text{opt}}(\hat{x}) = (\Omega^2/4\Delta^2)\Delta \sin^2(k\hat{x})$, with the self-consistent requirement $\Delta \gg \Omega$. Therefore, with the pre-factor $\sim \Omega^2/4\Delta^2$ being small for self-consistency, we can associate the role E_S plays in the acoustical case with the role the detuning Δ plays in the optical setting. Along these lines, for robust trapping it is favourable to increase the material-specific quantity E_S, thereby achieving a larger trap depth V_0 while keeping both the stability parameter $q = V_{\text{SAW}}/E_S$ and thus also the perturbative parameter ε constant. This can be well understood intuitively, since trapping due to a rapidly oscillating (SAW) field only becomes possible if the particle is too inert to adiabatically follow the periodically applied force: an electron does not significantly move away from a potential minimum if during one oscillation period of the SAW field its wavefunction spreads slowly enough such that it is still close to its original position when the minimum reforms. This simplified (pseudo-potential) picture is valid for relatively heavy electrons with high mass m and sufficiently high driving frequency (that is, high speed of sound v_s), as captured by an elevated sound energy $E_S = (m/2)v_s^2$.

Cooling in the presence of micromotion.—While our previous discussion has exclusively focused on the time-dependent system's dynamics, in the following we extend our studies and introduce a dissipative model, which describes the electron's motional coupling to the (thermal) phonon reservoir. For details of the derivation, we refer to Ap-

pendix 2.C. Within one unified Born-Markov and Floquet framework, we derive an effective quantum-master equation (QME) for the electronic motion in the vicinity of one lattice site, fully taking into account the explicit time-dependence of the system Hamiltonian (2.3). Since the quantum-state evolution due to this QME is Gaussian, one can readily derive a closed set of equations for the first- and second-order moments of the position and momentum observables; formally, it takes on the form $\dot{\mathbf{v}} = \mathcal{M}(t)\,\mathbf{v} + \mathbf{C}(t)$ with $\mathbf{v} = (\langle\hat{x}\rangle_t, \langle\hat{p}\rangle_t, \langle\hat{x}^2\rangle_t, \langle\hat{p}^2\rangle_t, \langle\hat{x}\hat{p}+\hat{p}\hat{x}\rangle_t)^\top$. This equation of motion can be readily solved by numerical integration; a prototypical result of this procedure is displayed in Fig.2.3. In the regime $q^2 \ll 1$, our numerical findings show that (i) the electronic motion can be described very well by a simple damped harmonic oscillator with secular frequency ω_0, (ii) the electronic motion is cooled by the phonon reservoir and (iii) the Lamb-Dicke approximation is well-satisfied. Let us elaborate on these statements in some more detail: (i) As evidenced by the dashed red line in Fig.2.3, we find that the effective, time-independent

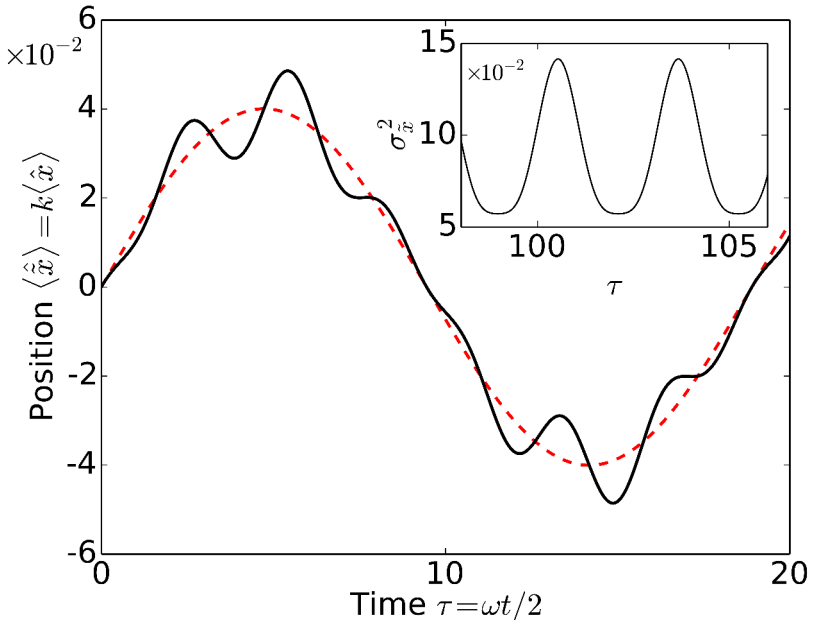

Figure 2.3: (color online). Exact numerical simulation [based on Eqs.(2.70) and (2.5)] for the electron's trajectory $\langle\hat{x}\rangle_t$ (solid black line), showing a slow secular motion with frequency ω_0 that is superimposed by fast, small-amplitude micromotion oscillations. When disregarding micromotion, the dynamics can approximately be described by a simple damped harmonic oscillator with secular frequency ω_0 (dashed red line). The initial state has been set as a coherent state with $\langle\hat{\tilde{x}}\rangle = 0, \langle\hat{\tilde{p}}\rangle = 0.01$. Other numerical parameters: $q = 0.47$, $\gamma/\omega_0 = 10^{-3}$, $k_B T/\hbar\omega_0 = 10^{-1}$, $\omega_0/\omega \approx 0.17$. Inset: Position variance $\sigma^2_{\tilde{x}} = \langle\hat{\tilde{x}}^2\rangle - \langle\hat{\tilde{x}}\rangle^2$ at times when transient effects have decayed.

master equation

$$\dot{\rho} = -i\omega_0 \left[a^\dagger a, \rho\right] + \gamma \left(\bar{n}_{\rm th}\left(\omega_0\right) + 1\right) \mathscr{D}\left[a\right]\rho + \gamma \bar{n}_{\rm th}\left(\omega_0\right) \mathscr{D}\left[a^\dagger\right]\rho, \tag{2.5}$$

captures very well the most pertinent features of the electronic dynamics (for $q^2 \ll 1$). Here, γ is the effective, incoherent damping rate due to coupling to the thermal phonon reservoir, $\bar{n}_{\rm th}\left(\omega_0\right) = 1/\left(\exp[\hbar\omega_0/k_B T] - 1\right)$ gives the thermal occupation number of the phonon bath at frequency ω_0, $\mathscr{D}\left[a\right]\rho = a\rho a^\dagger - (1/2)\left\{a^\dagger a, \rho\right\}$ denotes the standard dissipator of Lindblad form, and $a^{(\dagger)}$ refers to the usual annihilation (creation) operators for the canonical harmonic oscillator. As a consequence of the presence of the dissipator, the first-order moments $\langle\hat{x}\rangle_t$, $\langle\hat{p}\rangle_t$ decay towards zero in the asymptotic limit $t \to \infty$. However, the second-order moments retain the periodicity of the external driving for arbitarily long times (with a periodicity $\bar{T} = \omega T/2 = \pi$), which is the signature of an emerging quasi-stationary state [cf. Appendix 2.C for details] and the persisting micromotion which manifests itself in the fast oscillating dynamics of the position and momentum variances, as depicted in the inset of Fig.2.3. (ii) As suggested by our analytical results [cf. Appendix 2.C for details], the phonon reservoir provides an efficient cooling mechanism for the electron provided that the host temperature is sufficiently low, that is $k_B T \ll \hbar\omega_0$. The influence of the electronic micromotion on this cooling mechanism can be condensed in the following statement: in the pseudopotential regime (for which $q^2 \ll 1$), the expectation value for the averaged quantum kinetic energy (over one micromotion period) features a surplus of energy, in addition to the zero-point kinetic energy in the ground state of $\hbar\omega_0/4$. This excess energy $\Delta_{\rm heat} \gtrsim \hbar\omega_0/4$ may be viewed as micromotion-induced heating and amounts to merely a factor of two increase only in the particle's time-averaged kinetic energy [130]. These results are explicated in greater detail in Appendix 2.C. (iii) We have numerically verified that both the expectation value for the electron's motion as well as the corresponding fluctuations are small compared to the SAW wavelength $\lambda = 2\pi/k$, i.e., $k\left\langle\hat{x}\right\rangle_t \ll 1$ and $k\sigma_x \ll 1$ with $\sigma_x^2 = \left\langle\hat{x}^2\right\rangle_t - \left\langle\hat{x}\right\rangle_t^2$, thereby justifying our Lamb-Dicke approximation (with $\cos\left(k\hat{x}\right) \approx \mathbf{1} - (k^2/2)\,\hat{x}^2$) self-consistently.

Self-consistency requirements.—Our theoretical framework is valid provided that the following conditions are satisfied: (i) First, the Markov approximation holds given that autocorrelations of the bath (which typically decay on a timescale $\sim \hbar/k_B T$) decay quasi instantaneously on the timescale of system correlations $\sim \gamma^{-1}$ [131]. In principle, the damping rate γ should be replaced by the thermally enhanced rate $\gamma_{\rm eff} = \gamma\left(\bar{n}_{\rm th}\left(\omega_0\right) + 1\right)$; however, we will be interested mostly in the low-temperature, pseudopotential regime where $\gamma_{\rm eff} \approx \gamma$. Thus, the Markov approximation yields the condition $\hbar\gamma \ll k_B T$. (ii) Second, the (weak-coupling) Born approximation holds provided that the dissipative damping rate γ is small compared to the relevant system's transition frequencies, yielding the requirement $\gamma \ll \omega_0$. In the low-q limit, taking conditions (i) and (ii), together with the prerequisite for efficient ground-state cooling, $k_B T \ll \hbar\omega_0$, yields the chain of inequalities $\hbar\gamma \ll k_B T \ll \hbar\omega_0$. In this regime, the weak-coupling Born approximation ($\gamma \ll \omega_0$) is satisfied very well. (iii) Third, the characteristic separation of timescales between the (slow) secular motion and the (fast) micromotion, with $\omega_0 = \varepsilon\omega$ and $\varepsilon = q/2\sqrt{2} \ll 1$, gives the requirement

$\omega_0 \ll \omega$. (iv) Fourth, the energy scale $\hbar\omega$ has to be much smaller than E_S in order to ensure the existence of at least one bound state per lattice site; the latter can be estimated as $n_b = V_0/\hbar\omega_0 = \varepsilon E_S/\hbar\omega = (\varepsilon/2)mv_s/\hbar k$, leading to $\hbar\omega \ll E_S$ in the regime $\varepsilon \ll 1$, $n_b \gtrsim 1$. Note that the existence of at least one bound state per lattice site ($n_b \gtrsim 1$) may always be fulfilled by choosing the lattice spacing $a = \pi/k$ sufficiently large, at the expense of more severe temperature requirements for ground state cooling and smaller energy scales in the emerging Hubbard model (see below). Finally, the parameter regime of interest can be condensed into one line of inequalities as ($\hbar = 1$)

$$\gamma \ll k_B T \ll \omega_0 \ll \omega \ll E_S. \tag{2.6}$$

Let us discuss the implications of Eq. (2.6) in some more detail: (i) In the parameter regime described by Eq. (2.6) the acoustic trap is stable against thermal fluctuations, because $k_B T \ll V_0$ with $V_0 = \varepsilon^2 E_S$; in other words, $V_0 = n_b\omega_0 \gg k_B T$, if $\omega_0 \gg k_B T$ and $n_b \gtrsim 1$, as desired. The condition $k_B T \ll \omega_0$, however, may be relaxed if ground-state cooling is not necessarily required, akin to the physics of optical tweezers. In this case, the less stringent condition $V_0 \gg k_B T$ still ensures a thermally stable trap. (ii) The self-consistency requirement $\gamma \ll k_B T$ derives from the Markov assumption of having a short correlation time of the phonon bath $\gamma\tau_c \ll 1$, with $\tau_c \sim 1/k_B T$. However, in the low-temperature regime, the correlation time τ_c may as well be set by the bandwidth of the bath Δ_B (that is, the frequency range over which the bath at hand couples to the system), rather than just temperature. In that case, one may drop the condition $\gamma \ll k_B T$, leading to a slightly refined regime of interest with $\gamma, k_B T \ll \omega_0 \ll \omega \ll E_S$, provided that the Markov assumption $\gamma\tau_c \ll 1$ is still satisfied with $\tau_c \sim \Delta_B^{-1}$. (iii) As a direct consequence of the presence of Mathieu-type instabilities, the proposed setup operates at relatively low SAW-induced amplitudes set by the energy scale E_S, with the potential amplitude due to a single IDT given as $V_{\mathrm{IDT}} = V_{\mathrm{SAW}}/2 = (q/2)E_S < E_S$.

Again, Eq. (2.6) underlines a remarkably close connection to the established field of trapped ions, where (as a direct consequence of Mathieu's equation, just as in our setting) the inherent separation of timescales ($\omega_0 \ll \omega$) between (slow) secular motion and (fast) micromotion is well-known, albeit at very different energy scales with typical driving frequencies $\omega/2\pi \sim 100\mathrm{kHz} - 100\mathrm{MHz}$ [127]. Beyond this close analogy, our work identifies the importance of the energy scale $E_S = (m/2)v_s^2$ in the proposed solid-state, SAW-based setting, as displayed by Eq. (2.6). Moreover, the first two inequalities in Eq. (2.6) derive directly from the intrinsic solid-state cooling mechanism provided by the phonon bath, whereas ions are typically cooled down to the motional ground state using laser-cooling techniques that (as opposed to our solid-state approach) explicitly involve the ion's internal level structure [127].

In the following we will address the experimental implications of the requirements listed in Eq. (2.6) for realistic setups and show how some of the conditions may in fact be relaxed.

2.4 Implementation: How to Meet the Requirements

Our previous conceptual analysis has revealed a specific set of requirements [as summarized in Eq. (2.6)] which should be fulfilled in order to ensure a faithful implementation of the proposed AL setup in an actual experiment. In the following we discuss several practical strategies in order to meet these conditions. Thereafter, we address several practical considerations which might be relevant under realistic experimental conditions.

Requirements.—First, rough (potentially optimistic; see below) estimates for the spontaneous emission rate of acoustic phonons $\sim \gamma$ may be inferred from low-temperature experiments on charge qubits in (GaAs) double quantum dots which indicate rates as low as $\gamma/2\pi \gtrsim 20\text{MHz}$ ($\hbar\gamma \gtrsim 0.1\mu\text{eV}$) [132, 133, 134, 135]. We consider this estimate for the relaxation rate $\sim \gamma$ to be an optimistic, but still adequate ballpark value for our SAW-induced acoustic traps, because the typical (i) temperatures ($T \sim (20-100)\,\text{mK}$), (ii) length-scales ($\sim$ 300nm for the dot-to-dot distance), (iii) transition frequencies ($\sim$ GHz in Ref.[134]), and (iv) host materials (GaAs) studied in Refs.[132, 133, 134, 135] are all compatible with our setup. Furthermore, in Ref.[134] a ohmic spectral density has been assumed (just like in our theoretical model discussed above) in order to fit the experimental data with the (thermally enhanced) decoherence rate $\gamma_{\text{eff}} = \gamma\,(2\bar{n}_{\text{th}}(\omega_0)+1)$, yielding $\gamma = \zeta\omega_0$ with the fit parameter $\zeta = (\pi/4)\times 0.03 \sim 2.35\times 10^{-2}$. Second, we consider typical dilution-fridge temperatures in the range of $T \sim (10-100)\,\text{mK}$ (corresponding to $k_B T \sim (1-10)\,\mu\text{eV}$) [136]. For $\gamma/2\pi \approx 20\text{MHz}$ the first inequality in Eq.(2.6) is then safely satisfied even for the lowest temperatures under consideration ($k_B \cdot 10\text{mK}/2\pi \sim 200\text{MHz}$). Still, since γ varies significantly with both energy and length scales, phonon relaxation rates of $\gamma/2\pi \approx 20\text{MHz}$ for GaAs-based systems may be overly optimistic. In this case, operation at higher temperatures [in order to satisfy Eq.(2.6)] may still be avoided by employing (for example) phonon band gaps as discussed in Ref.[132] or different materials such as silicon [121, 137] where the corresponding phonon-induced relaxation rates are much smaller [138], as a consequence of a much smaller electron-phonon coupling strength. All other things being equal, the SAW-induced potential depth V_{SAW} will be reduced as well in a silicon-based setup, which, however, can be compensated by simply applying a larger RF power to the IDTs. Lastly, recall that the spontaneous emission rate γ may be as large as $\gamma \approx k_B T$ and still be fully compatible with the desired regime of interest, if the correlation time of the phonon bath is set by (for example) the bandwidth Δ_B rather than temperature. Third, for high SAW frequencies $\omega/2\pi \approx 25\text{GHz}$ [119], the energy $\hbar\omega \approx 100\mu\text{eV}$ yields a trapping frequency $\hbar\omega_0 \lesssim 20\mu\text{eV}$ ($q^2 \ll 1$). Altogether, we thus conclude that Eq.(2.6) can be satisfied with state-of-the art experimental setups, provided that the material-specific energy scale E_S is much larger than $\hbar\omega \approx 100\mu\text{eV}$. For electrons in standard GaAs and the *lowest* Rayleigh mode, however, we find $E_S \approx 2\mu\text{eV}$. In the following, we identify three potential, complementary strategies to solve this problem.

(1) Material engineering.—Our first approach involves sophisticated material engineering, with the aim to crank up the energy scale E_S. Here, we can identify three general,

setup	m/m_0	v_s[km/s]	$E_S[\mu\text{eV}]$
electrons in GaAs*	0.067	~ 3	~ 1.7
heavy holes in GaAs**	0.45	$\sim (12-18)$	$\sim 184-415$
electrons in Si**	0.2	$\sim (12-18)$	$\sim 82-184$
holes in GaN**	1.1	$\sim (12-18)$	$\sim 450-1010$
electrons in MoS_2**	0.67	$\sim (12-18)$	$\sim 274-617$
trions in MoS_2**	1.9	$\sim (12-18)$	$\sim 794-1787$

Table 2.1: Estimates for the energy scale E_S for different physical setups. Examples marked with * refer to the lowest SAW mode in GaAs whereas those marked with ** refer to relatively fast (diamond-boosted) values of v_s in diamond-based heterostructures featuring high-frequency SAW and PSAW modes as investigated in [142, 143]. Further details are given in the text.

complementary strategies to increase the sound energy [cf. Eq. (2.2)]. (i) First, the effective mass m crucially depends on both (a) the type of particle and (b) the host material: (a) heavy holes or composite quasi-particles such as trions (also known as charged excitons) typically feature much higher effective masses than electrons in GaAs. (b) Compared to standard GaAs, where the effective electron mass is $m \approx 0.067m_0$ (m_0 refers to the free electron mass), in Si/SiGe structures $m \approx 0.2m_0$, while for electrons (heavy holes) in AlN $m \approx 0.33m_0$ ($m_{hh} = 3.89m_0$). (ii) Second, following common practice in the quest for SAW devices operating at ultra-high frequencies [139, 140, 141], v_s can be effectively increased by employing a specialized heterostructure involving for example diamond (which features the highest speed of sound). (iii) Third, the speed of sound $v_{s,\alpha} = \omega_\alpha/k$ can be enhanced even further by exciting higher-order Rayleigh modes ($\alpha > 1$) in the sample at the same wavelength [67]. In particular, layered half-space structures (such as AlN/diamond, with h denoting the thickness of the piezoelectric AlN layer) support so-called pseudo-surface acoustic waves (PSAWs) propagating with exponential attenuation due to wave energy leakage into the bulk, in contrast to regular (undamped) SAWs [67, 142, 143]. As shown both theoretically and experimentally [142, 143], this leakage loss can, however, become vanishingly small for certain *magic* film-thickness-to-wavelength ratios h/λ, such that for all practical purposes this PSAW mode can be seen as a true SAW mode which propagates with negligible attenuation. While SAWs by definition may not exceed the shear wave velocity c_s ($c_s \approx 12.32$km/s for diamond) in the lower half-space, PSAW velocities can be significantly larger than c_s and reach values of up to $v_s \approx 18$km/s [142, 143], that is about 40% higher than those of regular SAWs [143] and about a factor of ~ 3.2 higher as compared to the lowest Rayleigh mode for a homogeneous AlN half-space where $v_s \approx 5.6$km/s [142]. Lastly, even higher velocities may be achieved if leakage losses into the bulk are suppressed when using freely suspended two-dimensional electron gases [144] rather than a (quasi) semi-infinite half-space.

We have verified these considerations using numerical finite-element calculations, performed with the software package *COMSOL* [145] for GaAs/diamond (AlN/diamond) het-

erostructures; our simulations indeed show that the effective speed of sound can be significantly scaled up in comparison with the standard values in GaAs (AlN) [146]. In Fig. 2.4, the behaviour of v_s as a function of the width h of the GaAs (AlN) layer is displayed. The results show both the second Rayleigh SAW modes in GaAs/diamond and AlN/diamond, respectively, as well as one particular PSAW mode (as identified previously in Ref.[142]). For large h, the second Rayleigh SAW modes coincide with the corresponding second modes in the raw materials GaAs and AlN (without a diamond layer), as expected. On the other hand, in the limit of comparatively small $h \approx (50-200)$ nm, the SAW velocities are significantly larger compared to the first and second Rayleigh modes in pure GaAs (AlN), while for the PSAW mode $v_s \approx 18$km/s at $h/\lambda \approx 0.57$. Moreover, in the case of piezoelectric coupling, the electric potential which accompanies the SAW has to be non-zero at the

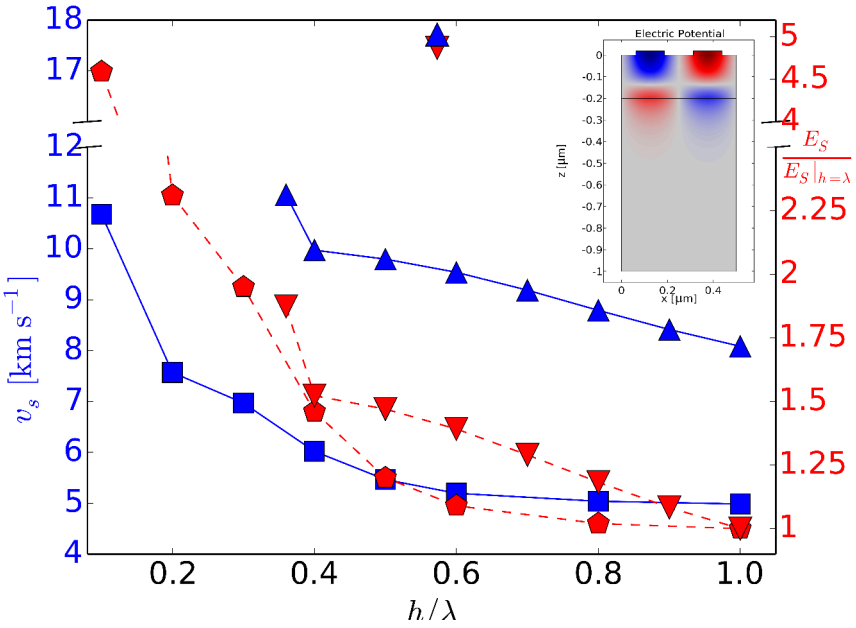

Figure 2.4: (color online). Speed of sound v_s (left axis) and kinetic sound energy E_S normalized to its value at $h = \lambda$ (right axis) in layered heterostructures made of gallium arsenide (aluminium nitride) and diamond. All results are given as a function of h, which denotes the thickness of the GaAs (AlN) layer. Results for the second SAW modes and heavy holes are shown. Squares and pentagons (triangles) denote the numerical results for a GaAs/diamond (AlN/diamond) heterostructure. $E_S(h = \lambda) \approx 32\mu$eV for GaAs/diamond ($\approx 205\mu$eV for AlN/diamond). The data points are connected by lines to guide the eye. The isolated data points at $h \approx 0.57\lambda$ denote a ultra-high velocity PSAW mode in AlN/diamond (cf. Ref.[142]). Inset: Distribution of the piezoelectric potential at $f = 12.2$ GHz of a second SAW mode for a layer thickness of $h = 0.2\mu$m in a GaAs/diamond heterostructure. The IDT finger spacing, hence the SAW wavelength, is set to be $\lambda = 500$ nm. The results were obtained with the software package *COMSOL*.

2DEG which is located somewhere in the center of the top GaAs (AlN) layer. As shown in Fig. 2.4, such configurations do exist in GaAs/diamond (AlN/diamond) heterostructures, while reaching the parameter regime $k_BT = 1\mu\text{eV} \lesssim (10^{-3} - 10^{-2})E_S$. Hence, when suitably combining strategies (i)-(iii), we predict the feasibility of reaching $E_S \gtrsim 1$ meV, which is sufficiently large to safely satisfy condition (2.6), as desired. Consider for example a two-dimensional hole gas at a AlN/GaN interface on top of diamond; here, the effective heavy-hole mass of GaN amounts to $m \approx 1.1m_0$. When driving the PSAW mode identified in Fig. 2.4, we find $E_S \approx 1.0$meV. Alternatively, we may consider TMDs such as MoS_2 or WSe_2, on top of some high-speed material such as diamond. While all TMDs are piezoelectric due to the lack of inversion symmetry [147], some of them show relatively large effective masses; for example, the effective electron and hole mass in MoS_2 amount to approximately $m \approx 0.67m_0$ and $m \approx 0.6m_0$, respectively [148, 149]. Then, for electrons (charged trions) in MoS_2 with effective mass $m \approx 0.67m_0$ ($m \approx 1.9m_0$) [149], as experimentally investigated for example in Refs.[150, 151], and a diamond-boosted speed-of-sound $v_s \approx 18$km/s, we estimate E_S to be as large as $E_S \approx 617\mu$eV ($E_S \approx 1.78$meV). Further estimates of this type for different physical setups are summarized in Tab.2.1. Here, we have covered the most relevant material properties for the implementation of the proposed AL setups only, whereas the interplay of different material-design strategies (i)-(iii), leads to an intricate problem involving various parameters (such as piezoelectric properties and the electron mobility), which we cannot cover in its full depth within the scope of this work.

While this material-engineering based approach is fully compatible with our general theoretical framework, as described in Section 2.3, in the following we present two additional schemes that allow for thermally stable trapping, at potentially higher temperatures than what we have found so far, but at the expense of a more involved theoretical description [which, however, is not necessarily restricted to the parameter regime given in Eq.(2.6)]; here, similar to Section 2.3, we first present a classical analysis of the dynamics, whereas a detailed, quantum-mechanical analysis thereof goes beyond the scope of this work and will be subject to future research.

(2) Exotic stability regions.—In the context of ion traps where stability is governed by the Mathieu equation [cf. Eq.(2.9)], ion motion is stable in the primary stability region ($a_{\text{dc}} = 0,\ 0 < q < 0.908$) and then becomes unstable as q is increased [127]. Stable motion, however, reoccurs at higher q values which we refer to as exotic stability regions in the following; these exotic stability regions were studied to some extent in the context of ion traps [152, 153]. Here, we propose, as a second strategy to meet the self-consistency requirements, to extend the previously established classical stability analysis to the next higher-lying ($a_{\text{dc}} = 0,\ 7.5 \lesssim q \lesssim 7.6$) stability region of the Mathieu equation. As evidenced in Fig.2.2(d), in this high-q regime, a separation between secular and fast (micro-)motion is no longer possible. However, while the theoretical description of the dynamics becomes more involved, still the particles are found to be dynamically *trapped*, already at temperatures much higher than what we found in the low-q regime. While $k_BT \lesssim 0.03E_S$ for small q, in the high-q regime (with $7.5 < q < 7.6$) thermal stability sets in already at $k_BT \lesssim 0.15E_S$, thus alleviating temperature requirements by about an order of magnitude,

cf. Fig.2.2(c).

(3) Optimized driving schemes.—As a third strategy, we suggest to utilize polychromatic driving schemes, rather than the simple monochromatic driving considered so far. Recently, it has been experimentally demonstrated that such polychromatic drivings can eventuate arbitrary SAW wavefronts [154], thus allowing us to consider more general equations of motion of the form $\ddot{x}+f(\tau)x=0$, with some particular time dependence $f(\tau)$. For example, instead of the Mathieu equation for which $f(\tau)=2q\cos(2\tau)$ (no dc contribution), a simple two-tone driving scheme can be used to expand the stability regions as previously suggested in Ref.[155]. Our numerical studies suggest that the superposition of higher harmonics in the form of $f(\tau)=2q[c_1\cos(2\tau)+c_2\cos(4\tau)+...]$ may already enhance the robustness of the stability region in Fig. 2.2(a) against temperature by a factor of two, as compared to the standard Mathieu equation.

Technical considerations.—We now address several technical considerations which might be relevant for a faithful experimental realization of our proposal: (i) Since the potential amplitude due to a single IDT is limited by Mathieu-type stability arguments as $V_{\rm IDT}=V_{\rm SAW}/2=(q/2)E_S\lesssim 0.5$meV [156], the proposed setup operates at SAW-induced amplitudes that are about two orders of magnitude smaller than what is common for SAW-induced electron transport experiments (where typically $V_{\rm IDT}\approx 40$meV [72, 157]). Note that this comparatively low driving amplitude amounts to a fraction of typical quantum dot charging energies. Today, quantum dots are routinely pulsed with similarly high amplitudes, and yet excellent charge and spin coherence is seen in experiments [158, 159, 160]. (ii) In a similar vein, as a direct consequence of the low-amplitude external drive, potential microwave-induced heating effects of the sample should be small. Furthermore, undesired heating may be suppressed efficiently by placing the IDTs very far away from the center of the trap, without losing acoustic power, thereby avoiding local heat dissipation near the center of the trap due to the applied RF power; for further details we refer to Appendix 3.5. (iii) Minimization of crosstalk-related effects can be accomplished based on various techniques [161]: these can involve, for example, very careful choice of metal-packaging structure and dimensions, the judicious placement of ground connections to avoid ground loop effects, and the placement of thin metal-film ground strips between the IDTs. Moreover, because of the vast difference between the speed of light ($c\approx 10^8$m/s) and the speed of sound ($v_s\approx 10^4$m/s), for a given frequency the wavelength associated with the EM crosstalk is about four orders of magnitude larger than the SAW wavelength (even when accounting for the refractive index of the specific material), and therefore practically flat on the relevant lengthscale of a few lattice sites; for $\omega/2\pi\approx 30$GHz, the wavelength is in the millimeter range, i.e., much larger than the acoustic lattice spacing $a=v_s/(\omega/\pi)\approx 170$nm.

2.5 Applications

The possibility to acoustically trap charged particles in a semiconductor environment should open up many experimental possibilities, well beyond the scope of this work. Here, we briefly describe just two potential exemplary applications; see also our discussion in the

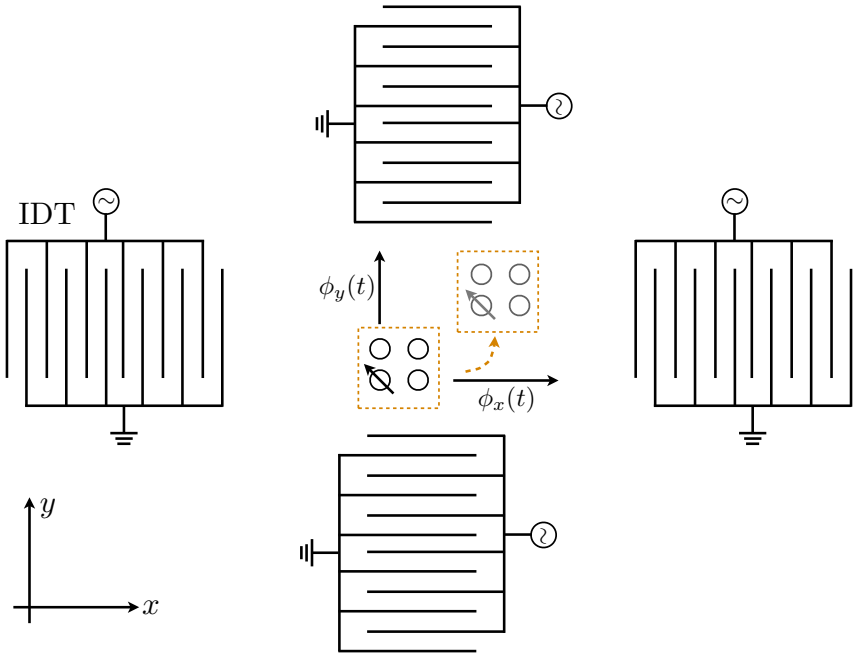

Figure 2.5: (color online). Schematic illustration (top view; not to scale) for a quasi-stationary two-dimensional AL which can be controllably displaced in both x- and y-direction by adiabatically tuning the phases applied to the IDTs. The dashed (orange) box highlights a small sub-lattice consisting of just four lattice sites, before and after the adiabatic ramp.

final section of this chapter.

Mobile Acoustic Quantum Dots

By adiabatically tuning the phases applied to the IDTs one may displace the AL in both the x- and y-direction, thereby creating *mobile* acoustic quantum dots, with the possibility to transfer in this way quantum information stored in the spin degree of freedom of the particle; for a schematic illustration compare Fig. 2.5. Here, in contrast to standard SAW-based mobile quantum dots [72, 73], the speed $v_{\rm eff}$ at which the trapped particles can be moved around between different locations in the 2DEG would not simply be set by the SAW's speed of sound v_s, but could rather be controlled *in situ* by the time derivative of the phases applied to the IDTs, with an upper bound roughly given by the adiabaticity condition ($\varepsilon_{\rm ad} \ll 1$) as $v_{\rm eff} = \varepsilon_{\rm ad} a(\omega_0/2\pi) \lesssim 100$m/s. Apart from thermal fluctuations, the trapping lifetime in such a mobile quantum dot will be limited by tunnel-coupling to neighbouring mobile quantum dots inside the AL (while the spin lifetime remains unaffected for spin-coherent tunneling); as shown in more detail below, this coupling can be suppressed controllably by going to a larger SAW wavelength λ, at the expense of more stringent ground-state cooling requirements as the level spacing ω_0 decreases. For a mobile AL with near unit filling, however, tunnelling is largely suppressed due to Coulomb

blockade effects and the (spin) dynamics is governed by the next lower energy scale (the exchange coupling), as discussed and quantified next.

Towards Many-Body Physics

While our previous discussion has exclusively focused on dynamically trapping and cooling *single* particles in SAW-induced potentials, in our second example we provide a simple characterization of our setup for the potential investigation of quantum *many-body* systems. We show that (at dilution fridge temperatures) our system can be naturally described by an extended Anderson-Hubbard model, with the ultimate prospect of entering the low temperature, strong interaction regime where $k_B T \ll t < U$; here t and U refer to the standard hopping and interaction parameters of the Hubbard model, as specified below. We provide estimates for these quantities in terms of the relevant parameters characterizing the AL, and show how they can be engineered and (dynamically) tuned. For this analysis, again we restrict ourselves to the pseudopotential regime ($\omega_0 \ll \omega$) where the effects of the fast, small-amplitude micromotion on the Hubbard parameters t, U can be neglected. Thereafter, we discuss several approaches that may be used in order to detect and accurately probe the resulting quantum phases of matter.

Estimates for Hubbard parameters.—Consider an ensemble of fermionic charged particles inside a periodic one or two-dimensional AL, with roughly one particle per site (corresponding to electron densities $\sim 10^{10}\mathrm{cm}^{-2}$ for a two-dimensional AL with $a \sim 100$nm). If all energy scales involved in the system dynamics are small compared to the excitation energy to the second band $\sim \hbar\omega_0$ (for example $k_B T \ll \hbar\omega_0$, as required for ground state cooling), the electrons will be confined to the lowest Bloch band of the AL, and the system can effectively be described by the extended Anderson-Hubbard Hamiltonian [120, 163, 164, 162]

$$H_{\mathrm{AFH}} = -t \sum_{\langle i,j\rangle,\sigma} \left(c^{\dagger}_{i,\sigma} c_{j,\sigma} + \mathrm{h.c.} \right) + \sum_{i,\sigma} \mu_i n_i + \sum_{\sigma,\sigma'} \sum_{ijkl} U_{ijkl} c^{\dagger}_{i,\sigma'} c^{\dagger}_{j,\sigma} c_{k,\sigma} c_{l,\sigma'}, \tag{2.7}$$

where the fermionic operator $c_{i,\sigma}(c^{\dagger}_{i,\sigma})$ annihilates (creates) an electron with spin $\sigma = \uparrow, \downarrow$ at site i; $n_{i,\sigma} = c^{\dagger}_{i,\sigma} c_{i,\sigma}$ and $n_i = n_{i,\uparrow} + n_{i,\downarrow}$ refer to the spin-resolved and total occupation number operators, respectively. In Eq.(2.7) we have retained the nearest neighbour hopping term only, as specified by a tunneling amplitude t, but accounted for the full effect of the repulsive (long-range) Coulomb interactions $\sim U_{ijkl}$. The remaining (second) term, with a variable on-site energy μ_i, acts like a spatially varying chemical potential and describes potential disorder effects (as discussed in more detail below). In the limit of homogeneous on-site energies with $\mu_i = \mathrm{const.}$, Eq.(2.7) reduces to the minimal Hubbard model, if all but the largest on-site interaction terms are neglected (with $U_{iiii} = U$ in standard notation). In the limit $V_0 \gg E_R$ (where $E_R = \hbar^2 k^2/2m$ is the recoil energy), the tunneling rate t is given by $t/E_R \approx (4/\sqrt{\pi})\,(V_0/E_R)^{3/4} \exp\left[-2\sqrt{V_0/E_R}\right]$ [108], setting the upper limit $t < E_R$. In terms of the relevant AL parameters, this relation can be rewritten as

$$t/E_S \approx \left(2\sqrt{2\pi n_b}\right)^{-1} q^2 \exp\left[-4n_b\right], \tag{2.8}$$

showing that the tunneling rate $t \sim q^2$ can be tuned via the stability parameter q, reaching at maximum $t/E_S \lesssim 3 \times 10^{-3}$ within the lowest stability region for (fixed) $n_b \gtrsim 1$; here, the existence of at least one bound state ($n_b \gtrsim 1$) ensures both $V_0/E_R = 4n_b^2 \gtrsim 4$ and $t \ll \hbar\omega_0$, as required. Therefore, with $E_R/E_S = \varepsilon^2/(4n_b^2)$, we find $t < E_R \ll E_S$ such that realistically $E_S \gg 300\mu$eV is required in order to access the coherent many-body regime where $t \gg k_B T$, at dilution fridge temperatures. Making use of the strategies outlined in the previous section, this regime seems to lie within reach of state-of-the-art experimental capabilities. The order of magnitude for the Coulomb integral U_{ijkl} can be roughly estimated as $U_{ijkl} \sim e^2/4\pi\epsilon a$ (where ϵ denotes the effective dielectric constant of the material). Since $t \sim E_R \sim a^{-2}$ and $U_{ijkl} \sim 1/a$, the relative importance of the hopping term $\sim t$ as compared to the Coulomb interactions can be conveniently controlled via the SAW frequency $\omega = \pi v_s/a$ [120]. Taking (for example) $a \sim 300$nm, this rough estimate yields $U_{ijkl} \sim 380\mu$eV (for GaAs, where $\epsilon \approx 12.5\epsilon_0$), which exceeds any realistic hopping amplitude t by far, but also violates the assumptions underlying the model Hamiltonian (2.7). To enter a parameter regime where the simplified toy model (2.7) becomes applicable, special heterostructures with a metallic screening layer close to the 2DEG may be employed, while in a similar vein the thickness of the spacer layer (separating the 2DEG from the δ-doping layer) may also be reduced in favour of increased screening effects [120, 136]. In this scenario, a simple image-charge based estimate shows that the Coulomb interaction is reduced by a factor $f_{\rm scr} \approx 1 - [1 + 4\,(d/a)^2]^{-1/2}$ (where d refers to the distance between the 2DEG and the metallic screening plate), while retaining its $\sim 1/r$ scaling [120]. Accordingly, the estimate quoted above reduces from $\sim 380\mu$eV for $d \to \infty$ down to $\sim 50\mu$eV for $d \sim 0.3a \sim 90$nm. As discussed in more detail below, this approach does not only allow for tuning the strength of the Coulomb interaction (albeit not *in situ*), but at the same time reduces the detrimental effects due to background impurities [136]. In a regime where the latter is negligible, the next lower energy scale is set by the exchange coupling $J = 4t^2/U$, which describes effective spin-spin interactions via virtual hopping processes in the regime $U \gg t$. With the Coulomb interaction reduced to $U \approx 10t$, the regime $t \gg k_B T$ (and therefore $J \approx t/2 \gg k_B T$) should then give access to experimental studies of quantum magnetism [108]. For a comprehensive overview of the key quantities of our analysis and self-consistent estimates thereof we refer to Appendix 2.D. In this Appendix we also discuss relevant electron spin decoherence effects which may compete with the observation of coherent spin physics.

Detection schemes.—In order to measure the resulting collective many body state in an actual experiment, several approaches may be available: (i) First, the electron excitation spectrum could be probed using inelastic light scattering, as has been done experimentally in a closely related setup (based on electrons confined in etched pillars in a high-quality GaAs quantum well with mobility $\mu \sim 3 \times 10^6 {\rm cm}^2/{\rm Vs}$) in Ref.[165]. (ii) Second, transport measurements, in which a small dc voltage $V_{\rm dc}$ is applied across the AL, should carry signatures of the phase of the Hubbard model in the resulting dc current; compare for example Refs.[120, 166, 167]. The corresponding dc current $I_{\rm dc}$ will be blocked in the Mott-insulator regime, whereas Ohm's law $I_{\rm dc} \propto V_{\rm dc}$ should hold in a metallic phase [120, 62]. (iii) Third, charge-imaging methods could also be used to demonstrate regular carrier

localization in the acoustic lattice, somewhat similar to the detection of single electrons trapped by impurity centres [168, 169]. (iv) Fourth, capacitance spectroscopy techniques (as demonstrated for example in Ref.[170]) could be used in order to measure the density of states by detecting the ability to tunnel in from a back-plane. (v) Fifth, optical readout of the charge- and spin-state could be achieved with methods developed for self-assembled quantum dots [171], in particular in TMD-based setups [147, 150, 151, 172]. Similar to self-assembled quantum dots, our SAW-defined quantum dots and lattices trap both electrons and holes at the same location and could thus support quantum-dot excitons and trions. The charge- and spin-dependent interaction with quasi-resonant light fields can be used for read-out via resonance fluorescence [173] or the Kerr effect [174, 175]. Moreover, it is conceivable that related optical techniques for state preparation and spin rotation can be adapted as well. Note that due to the expected homogeneity of our SAW-generated lattice sites, we also expect largely identical optical spectra across the lattice which may facilitate global readout and collective optical effects. (vi) Lastly, apart from these well-established measurement techniques, we propose to perform local site-resolved detection by adiabatically changing the phases at the IDTs $\phi(t)$ and then loading one lattice site after the other (very much like in a CCD camera) into nearby gate-defined quantum dots, where both the charge as well as the spin degree of freedom could be measured via well-established spin-to-charge conversion techniques [176].

2.6 Effects of Disorder

Disorder in the AL will affect the (Anderson) Hubbard model, as described by the second term in Eq.(2.7), where (in the presence of disorder) μ_i is essentially a randomly fluctuating variable. In a semiconductor the dominant source of disorder is due to charged impurities, which includes both (i) desired contributions (such as the dopants used for forming the 2DEG) as well as (ii) undesired ones due to bulk or surface impurities [136]. While the dominant source of disorder (i) due to remote donor scattering can be largely removed in structures with a relatively large spacer thickness ~ 85nm [136, 177], the second one (ii) has been identified as the main mechanism limiting the mobility μ in ultra-clean 2DEGs [178, 179]. Still, as experimentally demonstrated in Ref.[179], mobilities exceeding $\sim 10^7 \mathrm{cm}^2/\mathrm{Vs}$ can be realized for dilution-fridge temperatures $T \sim 100$mK, resulting in a mean-free-path $l_{\mathrm{mfp}} = \mu v_{\mathrm{F}} m/e$ of up to $l_{\mathrm{mfp}} \sim 120\mu$m (here, v_{F} refers to the Fermi velocity [120]). In the low-density regime of interest with $n_{\mathrm{el}} \sim 10^{10}\mathrm{cm}^{-2}$ (corresponding to half-filling for a lattice spacing of $a \sim 100$nm) the mean-free-path is expected to drop to $l_{\mathrm{mfp}} \sim 15\mu$m [179], which is still much larger than the lattice spacing $a \sim 100$nm. To further compensate for residual disorder originating from background impurities (ii) one may resort to special heterostructures with a conducting backplane, as suggested in Ref.[136]. Also, in periodic arrays of quantum dots signatures of Hofstadter's butterfly [180] have been observed at high magnetic fields [167, 166], as a result of the interplay between the periodic potential and quantized Hall orbitals, suggesting that disorder from the substrate can in fact be sufficiently small to investigate coherent lattice physics. This discussion certainly provides

the basis for some optimism, but a dedicated research program (rather than just a literature survey) may be required to fully understand and characterize the role of disorder in this system; compare Ref.[62] for recent efforts in this direction based on gate-defined lattices in GaAs. While the effect of disorder on the single-particle level is well understood [181], the intricate interplay between interactions and disorder in the Hubbard model (as studied in Refs.[182, 183, 184, 185]) yields a non-trivial regime in its own right which may be explored systematically in the proposed setup by deliberately controlling the amount of disorder.

2.7 Conclusions and Outlook

In summary, we have proposed and analyzed the formation of an all-solid-state acoustic lattice with a highly regular periodicity set by the SAW wavelength (without any further gate patterning). We have developed a theoretical framework reminiscent of trapped-ion physics thus connecting two previously unrelated fields of research. With this framework at our disposal, we have identified the relevant figures of merit for this system and discussed potential experimental platforms for a faithful implementation of such acoustic lattices, with the ultimate potential to study yet unexplored parameter regimes, thanks to specific system properties such as ultra-light particle masses, intrinsic electron-phonon cooling and strong inter-particle interactions. Here, let us emphasize again the flexibility (and generic nature) of the proposed scheme: SAWs exist in many materials (semiconductor heterostructures, TMDs), can be endowed with a variety of accommpanying fields (depending on the material used: strain, electric, magnetic) and superposed to different standing wave patterns. Therefore the proposed scheme should be applicable to a variety of different (quasi-) particles and allow to study different lattice geometries.

Finally, we highlight possible directions of research going beyond our present work: (i) While we have focused on a simple square-lattice geometry, more sophisticated lattice geometries might be explored, given the design flexibilities associated with SAW devices [67]. (ii) For simplicity, in this work we have disregarded the potential presence of magnetic fields and/or spin-orbit effects, which stem from the underlying material properties. Therefore, without any further sophisticated engineering, these additional ingredients could be readily implemented, giving rise to rich phase diagrams and, for example, the formation of topological quantum spin Hall states [186]. Finally, we may envisage several setups that are complementary to the system studied in this work: (iii) *Acoustic lattices for dipoles*: Our ideas can be generalized towards an acoustic lattice for solid-state dipoles (rather than charged particles), e.g., for indirect excitons which consist of electrons and holes from two different parallel quantum well (QW) layers, thereby complementing previous experimental studies on SAW-induced lattices for exciton-polaritons both in moving [118] and standing-wave [187] configurations in the regime of many particles per lattice site. As evidenced by several experiments (where the repulsive character of the interaction shows up as a positive and monotonic line shift with increasing density [188]), indirect excitons behave as effective dipoles perpendicular to the plane [189, 190]. Because of the spatial separation between the electron and hole layers in this coupled QW structure, the intrinsic radiative lifetimes

of optically active indirect excitons exceeds that of their direct counterparts by orders of magnitude and can be in the range of several microseconds [190]. In TMD-based setups our approach may be used to *dynamically* trap and to spatially and spectrally isolate single excitons, thereby complementing experiments based on *static* strain-engineering [191]. (iv) *Acoustic lattices for ions*: The electric potential (created and controlled at the surface) due to standard IDTs extends into the material, but also into the vacuum above the surface [81]. In principle, this should allow for the integration of our SAW-based setup with ions above the surface that are exposed to this acoustically induced electric potential, leading to new hybrid setups and complementing other approaches towards regular, disorder-free surface traps for ions in which the lattice spacing is simply set by the SAW wavelength. With comparatively large parameter values for E_S ($\approx$ 420meV for Be ions on top of GaAs), preliminary estimates show that a pseudopotential trap depth of several $\sim$ meV should be possible within the lowest stability region (where $q^2 \ll 1$), provided that the ion can be stabilized in the direction normal to the surface within the SAW wavelength. (v) *Magnetic lattices*: While the acoustic lattice described above is based on coupling to the particle's *external* motional degree of freedom (as is the case with Paul traps for ions), in closer analogy to optical lattices for ultra-cold atoms, SAWs in piezo-magnetic materials such as Terfenol-D [192, 193, 194] may be used in order to couple to the particle's *internal* spin degree of freedom, thereby inducing a spatially inhomogeneous Stark shift on the electron's spin resonance which will act as an external potential for the electron's motion [3]. In this setup, for a fixed detuning of the ESR driving frequency from the Zeeman splitting, the effective trap depth can (in principle) be made arbitrarily large, provided that sufficient SAW power is available.

In conclusion, this discussion indicates that by combining the control and flexibility of SAWs with the rich variety of material properties of heterostructures, the emerging field of quantum acoustics opens a large number of further research directions with the ultimate goal of understanding the behavior of correlated electrons in technologically relevant materials and molecules and building a universal quantum simulator.

Appendices

2.A Classical Stability Analysis

Mathieu equation
Performing a Taylor expansion for the electric field close to the origin, $\sin(\tilde{x}) \approx \tilde{x}$, Eq. (2.1) can be mapped onto the well-known *Mathieu* differential equation by identifying the parameters appearing in the standard *Mathieu* differential equation,

$$\frac{d^2\tilde{x}}{d\tau^2} + [a_{\mathrm{dc}} + 2q\cos(2\tau)]\,\tilde{x} = 0, \tag{2.9}$$

as $a_{\mathrm{dc}} = 0$ (no dc voltage) and $q = V_{\mathrm{SAW}}/E_S$.

In the case of vanishing dc contribution, according to Ref.[126], there is a stability zone for $0 < q < q_{\max}$, with $q_{\max} \approx 0.92$, resulting in the maximum potential depth of $V_{\mathrm{SAW}} = q_{\max}E_S$. The lowest-order approximation to the ion trajectory $x(t)$ in the case $q^2 \ll 1$ is found to be

$$x(t) \approx 2AC_0 \underbrace{\cos\left(\beta\frac{\omega}{2}t\right)}_{\text{secular}} \underbrace{\left[1 - \frac{q}{2}\cos(\omega t)\right]}_{\text{micromotion}}, \tag{2.10}$$

where $\beta \approx q/\sqrt{2}$. If the fast low-amplitude oscillations contained in in the second factor are neglected, the secular motion can be approximated by that of a harmonic oscillator with frequency $\omega_0 = \beta\omega/2 \ll \omega$. The condition for the lowest-order approximation $q^2 \ll 1$ is equivalent to a separation of timescales between secular and micromotion, that is $\omega_0 \ll \omega$. In this regime, the dynamics can be described by an effective pseudopotential.

Classical pseudopotential
The classical dynamics in a high frequency field can be described by an effective *time-independent* Hamiltonian. Following Refs.[128, 129], it can be calculated in a systematic expansion in the inverse of the frequency ω. If the period of the force is small compared to the other time scales of the problem, it is possible to separate the motion of the particle into slow and fast parts. This simplification is due to the fact that the particle does not have sufficient time to react to the periodic force before this force changes its sign. Based on this separation of time scales, the motion for the slow part is computed explicitly up to the order ω^{-4}. Note that the effective time-independent Hamiltonian depends on a

coordinate $X(t)$ which describes the slow part of the motion; this coordinate is not the location of the particle, even though they are almost identical at high frequencies ω. As outlined in Refs.[128, 129], the decomposition of $x(t)$ into slow and fast components can be written as

$$x(t) = X(t) + \xi\left(X, \dot{X}, \omega t\right), \tag{2.11}$$

where the fast part of the motion ξ fulfills

$$\bar{\xi} = \frac{1}{2\pi}\int_0^{2\pi} d\tau \xi\left(X, \dot{X}, \tau\right) = 0. \tag{2.12}$$

By expanding ξ in powers of $1/\omega$,

$$\xi = \sum_{i=1}^{\infty} \frac{1}{\omega_i}\xi_i, \tag{2.13}$$

such that Eq.(2.9) leads to an equation for X that is time-independent and following Refs.[128, 129], we find the following (classical) effective Hamiltonian describing the slow dynamics $X(t)$

$$H_{\text{eff}} = \frac{P^2}{2m}\left[1 + \frac{3}{8}q^2\cos^2(kX)\right] + \frac{q}{8}V_{\text{SAW}}\sin^2(kX) + \mathcal{O}\left(\omega^{-5}\right). \tag{2.14}$$

Here, P is the momentum conjugate to X. Given a solution $X(t)$, the solution of the original problem can be obtained to appropriate order of $1/\omega$ since ξ is known explicitly in terms of X [128, 129]. The pseudo-potential for the average motion of the electron, $V_{\text{eff}} = V_0\sin^2(kX)$, with an amplitude given by

$$V_0 = \frac{q}{8}V_{\text{SAW}} = \frac{q^2}{8}E_S, \tag{2.15}$$

is also referred to as ponderomotive potential [127]. Note that the correction to the kinetic term in Eq. (2.14) is a fourth-order term, while the pseudo-potential V_{eff} is a second-order contribution in $1/\omega$. Close to the origin $x = 0$, the effective potential V_{eff} can be approximated by a harmonic potential $V_{\text{eff}}(x) = (m/2)\omega_0^2 x^2$ with an oscillation frequency $\omega_0 = \frac{q}{\sqrt{8}}\omega$, which is equivalent to result obtained above from the Mathieu equation. Using this definition of the trapping frequency, the ponderomotive potential becomes

$$V_{\text{eff}} = \left(\frac{\omega_0}{\omega}\right)^2 E_S\sin^2(kX) \tag{2.16}$$

We can then estimate the number of bound states n_{b} as

$$n_{\text{b}} \approx \frac{V_0}{\hbar\omega_0} = \frac{1}{2}\sqrt{\frac{V_0}{E_R}}, \tag{2.17}$$

with the recoil energy $E_R = \hbar k^2/2m$.

Stability diagrams

Here, we provide further details on our classical stability analysis. First, we would like to note that the stability diagrams shown in Sec.2.3 are of approximate character as they were obtained by interpolating our numerical results. This is due to the deliberate choice of defining a stable trajectory in terms of the maximal excursion during a sufficiently long propagation time: two trajectories with almost equal parameters q and k_BT/E_S can be judged as stable and unstable by this definition, respectively, because only one of their amplitudes exceeds the cut-off value set to one half of the lattice constant ($a/2$). Second, the notion of (thermal) stability may be defined via the mean-free path as well, by taking l_{mfp} as our cut-off value, in contrast to the trapping condition $\tilde{x}_{\max} < \pi$. In that case, the regions of thermal stability increase as compared to the ones shown in the main text, provided that $l_{\mathrm{mfp}} > a/2$. The last inequality is likely to be fulfilled in high-mobility 2DEGs where $l_{\mathrm{mfp}} \sim 10\mu$m. Third, the stability analysis underlying Fig. 2.2 neglects damping in the classical equation of motion; incorporating an additional friction term may alter the notion of stability, since particles which escape one lattice site can then be dynamically trapped at a different lattice site. Lastly, the state initialization via equipartition of thermal and kinetic energies describes an average condition; in practice, only a fraction of the electrons will fulfill this condition, where the details depend on the statistical distribution of the initial conditions. In order to estimate the statistical fraction of electrons whose (initial) velocity v is smaller than $v_0 = \sqrt{k_BT/m}$, given by equipartition of thermal and kinetic energies of the particle, we assume a Maxwell-Boltzmann distribution of velocities,

$$p(v)\mathrm{d}v = 2\sqrt{\frac{m}{2\pi k_BT}}\exp\left(-\frac{mv^2}{2k_BT}\right)\mathrm{d}v, \tag{2.18}$$

which yields $\int_0^{v_0} p(v)\mathrm{d}v \approx 0.68$; i.e., given a thermal ensemble of particles we find that a significant fraction of the electrons is found to be trapped.

2.B Quantum-Mechanical Floquet Analysis

Preliminaries.—We consider a quantum system with a Hamiltonian that is periodic in time, $H(t+T) = H(t)$. Floquet theory provides a natural framework to treat such a system [128, 129]. The Bloch-Floquet theorem states that the eigenstates of the Schrödinger equation

$$i\frac{\partial}{\partial t}|\Psi\rangle = H|\Psi\rangle, \tag{2.19}$$

obey the form

$$|\Psi_\lambda\rangle = e^{-i\lambda t}|u_\lambda(\omega t)\rangle, \tag{2.20}$$

where u_λ are periodic with respect to ωt with period 2π, that is $u_\lambda(x, \omega(t+T)) = u_\lambda(x, \omega t)$ with $\omega = 2\pi/T$. The states u_λ are called Floquet states and λ is the so-called quasienergy. They have a natural separation into a slow part $e^{-i\lambda t}$ (with the natural choice $0 \leq \lambda < \omega$) and a fast part $u_\lambda(x, \omega t)$. Now, the goal is to find an effective description for the slow part

of the dynamics as was done above for the classical dynamics. Formally, this is done by introducing a gauge transformation

$$|\phi\rangle = e^{iF(t)} |\Psi\rangle , \tag{2.21}$$

where $F(t)$ is a Hermitian operator which is a periodic function of time t, with the same period as $H(t)$, such that the effective Hamiltonian H_{eff} in the Schrödinger equation

$$i\frac{\partial}{\partial t}|\phi\rangle = H_{\text{eff}}|\phi\rangle , \tag{2.22}$$

$$H_{\text{eff}} = e^{iF}He^{-iF} + i\left(\frac{\partial}{\partial t}e^{iF}\right)e^{-iF}, \tag{2.23}$$

is *time-independent*. In particular, H_{eff} can then be used to predict trapping due to oscillating potentials [128].

Typically, F and H_{eff} cannot be computed exactly. Following Refs.[128, 129], we expand H_{eff} and F in powers of $1/\omega$ and choose F such that H_{eff} is time-independent to any given order. In the following, we compute the effective Hamiltonian,

$$H_{\text{eff}} = \sum_n \frac{1}{\omega^n} H_{\text{eff}}^{(n)}, \tag{2.24}$$

explicitly up to fourth order in $1/\omega$.

Second order

Given the temporal periodicity of the driving only, it has been shown [128, 129] that the odd terms $H_{\text{eff}}^{(1)}$, $H_{\text{eff}}^{(3)}$ from the perturbative expansion (2.24) vanish. Hence, the leading-order term (besides the purely kinetic contribution $p^2/2m$) of the effective Hamiltonian is of second order in $1/\omega$.

For the single-particle Hamiltonian under consideration,

$$H(t) = \frac{\hat{p}^2}{2m} + V_{\text{SAW}} \cos(\omega t) \cos(k\hat{x}) , \tag{2.25}$$

up to second order in $1/\omega$ we find

$$H_{\text{eff}} = \frac{\hat{p}^2}{2m} + \frac{q}{8} V_{\text{SAW}} \sin^2(k\hat{x}) , \tag{2.26}$$

which is the second-order result given in Eq. (2.4). Hence, similar to the classical treatment, also within the quantum mechanical Floquet framework, the effective potential, which is of second order in the dimensionless coefficient ω_0/ω, can be written as

$$V_{\text{eff}}(\hat{x}) = \left(\frac{\omega_0}{\omega}\right)^2 E_S \sin^2(k\hat{x}) . \tag{2.27}$$

Leading-order corrections to this result are of the order $\mathcal{O}(\omega^{-4})$.

Fourth order
Computing (2.24) explicitly up to $\mathcal{O}(\omega^{-4})$ yields

$$\begin{aligned} H_{\text{eff}} &= \frac{\hat{p}^2}{2m} + \frac{q}{8} V_{\text{SAW}} \sin^2(k\hat{x}) \\ &\quad + \frac{1}{2m}\left[\hat{p}^2 g(\hat{x}) + 2\hat{p} g(\hat{x})\,\hat{p} + g(\hat{x})\,\hat{p}^2\right] \\ &\quad + \frac{q^2}{32} E_R \sin^2(k\hat{x}) + \mathcal{O}\left(\omega^{-5}\right), \end{aligned} \tag{2.28}$$

where

$$g(\hat{x}) = \frac{3}{32} q^2 \cos^2(k\hat{x}). \tag{2.29}$$

In the classical limit (where $\hat{x}$ and $\hat{p}$ commute), Eq.(2.29) correctly reproduces the kinetic correction term given in Eq.(2.14). Compared to the classical result in Eq.(2.14), Eq.(2.28) also contains a fourth-order quantum-correction term which provides a contribution to the pseudo-potential and which scales as $\sim q^2 E_{\text{R}}$. The eigenvalues of H_{eff} yield the Floquet quasienergies. If the eigenstates of H_{eff} are known, then the Floquet states can be computed up to order ω^{-4} using the explicit expressions for F derived in Refs.[128, 129]. Similarly to the classical analysis above, we find an effective potential up to fourth order in $1/\omega$ which reads

$$V_{\text{eff}}(\hat{x}) = \left[\frac{q}{8} V_{\text{SAW}} + \frac{q^2}{32} E_R\right] \sin^2(k\hat{x}), \tag{2.30}$$

$$= \varepsilon^2 E_S \sin^2(k\hat{x}), \tag{2.31}$$

where we have introduced the factor

$$\varepsilon^2 = \frac{q^2}{8}\left[1 + \tilde{q}\right], \qquad \tilde{q} = \frac{E_R}{4E_S} = \left(\frac{\hbar k}{2p_s}\right)^2, \tag{2.32}$$

where the momentum p_s is given by $p_s = m v_s$. Within the usual HO approximation, we obtain the corresponding trapping frequency as

$$\frac{\omega_0}{\omega} = \varepsilon = \frac{q}{2\sqrt{2}}\sqrt{1 + \tilde{q}^2}. \tag{2.33}$$

2.C Phonon-Induced Cooling in the Presence of Micromotion

In this Appendix we discuss in detail the phonon-induced cooling-heating dynamics and the resulting effective temperature of acoustically trapped charge carriers, with full consideration of the time-dependence of the SAW-induced trapping potential. Here, we focus

on the relevant decoherence processes due to coupling of the particle's motion to the (thermal) phonon reservoir. Our analysis is built upon the master equation formalism, a tool widely used in quantum optics for studying the irreversible dynamics of a quantum system coupled to a macroscopic environment. We detail the assumptions of our approach and discuss in detail the relevant approximations.

Time-Dependent System Dynamics

The system dynamics describing the motion of an electron (of mass m) exposed to a SAW-induced standing wave is described by the Hamiltonian given in Eq.(2.3). In the following, we restrict ourselves to the so-called Lamb-Dicke regime in which the electron's motion is confined to a region much smaller than the SAW wavelength $\lambda = 2\pi/k$. The corresponding approximation $\cos(k\hat{x}) \approx \mathbf{1} - (k^2/2)\,\hat{x}^2$ will be justified self-consistently below. Dropping the first term $\sim \mathbf{1}$ (which results in an irrelevant, global phase only), the Hamiltonian $H_S(t)$ may be written as

$$H_S(t) \approx \frac{\hat{p}^2}{2m} + \frac{m}{2} W(t)\,\hat{x}^2, \tag{2.34}$$

where $W(t) = -(\omega^2/2)\,q\cos(\omega t)$ can be identified as a time-varying spring constant, with the stability parameter $q = V_{\mathrm{SAW}}/E_S$. In this form, the Hamiltonian $H_S(t)$ and the corresponding dynamics have been studied extensively in the literature (primarily in the context of trapped ions), from both a classical and a quantum-mechanical point of view; see for example Refs.[127, 130, 195]. Still, in order to set up the relevant notation for the subsequent analysis, here we provide a self-contained discussion, closely following Refs.[127, 130, 195].

Starting out from Eq.(2.34), the Heisenberg equations of motion for the electron's position $\hat{x}$ and momentum operators $\hat{p}$ read

$$\dot{\hat{x}}(t) = \frac{1}{i\hbar}\left[\hat{x}(t), H_S(t)\right] = \hat{p}(t)/m, \tag{2.35}$$

$$\dot{\hat{p}}(t) = \frac{1}{i\hbar}\left[\hat{p}(t), H_S(t)\right] = -mW(t)\,\hat{x}(t), \tag{2.36}$$

which, when taken together, yield the well-known quantum Mathieu equation

$$\ddot{\hat{x}}(t) + W(t)\,\hat{x}(t) = 0. \tag{2.37}$$

This equation is equivalent to its classical counterpart if one replaces the operator $\hat{x}(t)$ with a function $u(t)$ which satisfies the classical Mathieu equation [127, 130, 195]. As well known in the context of trapped ions, stable solutions exist only for certain values of the parameter q, which are usually defined in terms of a stability chart; as compared to the standard analysis, here we consider the simplified scenario without any dc voltage [130]. According to Floquet's theorem, such a stable solution $u(t)$ takes on the form

$$u(t) = \sum_{n=-\infty}^{\infty} c_{2n} e^{i(\omega_0 + n\omega)t} = e^{i\omega_0 t}\Phi(t), \tag{2.38}$$

where $\Phi(t)$ is a periodic function with period $T = 2\pi/\omega$, i.e. $\Phi(t+T) = \Phi(t)$. Following Ref.[127], we consider solutions of the Mathieu equation subject to the boundary conditions

$$u(0) = 1, \quad \dot{u}(0) = i\omega_0. \tag{2.39}$$

As will be seen later, this choice of boundary conditions is convenient for the appropriate definition of commutation relations. The (secular) frequency ω_0/ω is a function of q and the coefficients can be expressed in terms of a continued fraction; see e.g. Refs.[127, 130]. In the limit $q^2 \ll 1$ it can be shown that $c_0 \gg |c_{\pm 2}|$, such that the solution $u(t)$ is dominated by the so-called secular frequency $\omega_0/\omega \approx q/\left(2\sqrt{2}\right)$, which is much smaller than the driving frequency ω. In the corresponding pseudo-potential regime, a small-amplitude modulation with micromotion frequency ω is superimposed on the slow (secular) macro-motion. To lowest order in $\sim q$, the solution $u(t)$ simplifies to $u(t) = \exp[i\omega_0 t]$, without accounting for the micromotion.

Since the solution $u(t)$ and its complex conjugate $u^*(t)$ form linearly independent solutions (which are related to each other by the time-inversion symmetry inherent to the Mathieu equation) [127, 131], they obey the Wronskian identity

$$\begin{aligned} \mathcal{W}(t) &= u^*(t)\,\dot{u}(t) - u(t)\,\dot{u}^*(t), & (2.40)\\ &= u^*(0)\,\dot{u}(0) - u(0)\,\dot{u}^*(0), & (2.41)\\ &= 2i\omega_0. & (2.42) \end{aligned}$$

The second equality simply follows from the fact that $\mathcal{W}(t)$ is a constant of motion. With this normalization, we obtain the sum rule

$$\sum_n c_n^2 \left(\frac{\omega_0 + n\omega}{\omega_0}\right) = 1. \tag{2.43}$$

Since $\hat{x}(t)$ and $u(t)$ by definition satisfy the same differential equation, one can construct an operator $\hat{C}(t)$ which consists of an explicitly time-dependent linear combination of the position and momentum operators as

$$\hat{C}(t) = i\sqrt{\frac{m}{2\hbar\omega_0}}\left[u(t)\,\dot{\hat{x}}(t) - \dot{u}(t)\,\hat{x}(t)\right], \tag{2.44}$$

but which (being proportional to the Wronskian $\mathcal{W}$) turns out to be a constant of motion [127, 130, 195]. Then, since

$$\hat{C}(t) = \hat{C}(0) = \frac{1}{\sqrt{2m\hbar\omega_0}}\left[m\omega_0\hat{x}(0) + i\hat{p}(0)\right], \tag{2.45}$$

one can readily identify $\hat{C}(t)$ with the well-known annihilation operator associated with a *static* harmonic oscillator of mass m and frequency ω_0 as

$$\hat{C}(t) = \hat{C}(0) = A, \tag{2.46}$$

with the usual standard commutation relation

$$\left[A, A^{\dagger}\right] = 1. \tag{2.47}$$

This static potential harmonic oscillator is usually referred to as *reference oscillator* [127]. Since the operator A is time-independent, the same is true for

$$N = A^{\dagger}A, \tag{2.48}$$

whose eigenstates are simply the familiar Fock states of the (static potential) reference oscillator, with the standard ladder algebra

$$A\left|n\right\rangle_{\omega_0} = \sqrt{n}\left|n-1\right\rangle_{\omega_0}, \tag{2.49}$$

$$A^{\dagger}\left|n\right\rangle_{\omega_0} = \sqrt{n+1}\left|n+1\right\rangle_{\omega_0}, \tag{2.50}$$

yielding directly $N\left|n\right\rangle = n\left|n\right\rangle_{\omega_0}$.

The Heisenberg operators $\hat{x}\left(t\right)$ and $\hat{p}\left(t\right)$ can then be expressed in terms of the classical Mathieu solutions $u\left(t\right)$ as well as the (time-independent) creation and annihilation operators of the reference oscillator as

$$\hat{x}\left(t\right) = \sqrt{\frac{\hbar}{2m\omega_0}}\left[u^{*}\left(t\right)A + u\left(t\right)A^{\dagger}\right], \tag{2.51}$$

$$\hat{p}\left(t\right) = \sqrt{\frac{\hbar m}{2\omega_0}}\left[\dot{u}^{*}\left(t\right)A + \dot{u}\left(t\right)A^{\dagger}\right]. \tag{2.52}$$

Accordingly, the time dependence of the Heisenberg operators $\hat{x}\left(t\right)$ and $\hat{p}\left(t\right)$ is captured entirely by the classical Mathieu equation $u\left(t\right)$ and its complex conjugate. Note that $\left[\hat{x}\left(t\right), \hat{p}\left(t\right)\right] = \frac{\hbar}{2\omega_0}\mathcal{W}\left(t\right) = i\hbar$, as desired. For later reference, here we also define the Heisenberg operator for the kinetic energy as

$$\frac{\hat{p}^2\left(t\right)}{2m} = \frac{\hbar}{4\omega_0}\left[\left|\dot{u}\left(t\right)\right|^2\left(A^{\dagger}A + AA^{\dagger}\right) + \left(\dot{u}^{*}\left(t\right)\right)^2A^2 + \left(\dot{u}\left(t\right)\right)^2\left(A^{\dagger}\right)^2\right]. \tag{2.53}$$

Since the annihilation (creation) operators $A\left(A^{\dagger}\right)$ associated with the reference oscillator satisfy the usual algebra, in complete analogy to the standard oscillator one may define a set of basis states (in the Schrödinger picture) labeled as $\left|n;t\right\rangle$ with $n = 0, 1, 2, \ldots$, which form the *dynamic* counterpart of the harmonic oscillator Fock states. The states $\left|n;t\right\rangle$ are not stationary states, but do depend explicitly on time, as indicated by the argument t in the ket vector [195]. The ground state of the reference oscillator $\left|n=0\right\rangle_{\omega_0}$ obeys the condition

$$A\left|n=0\right\rangle_{\omega_0} = \hat{C}\left(t\right)\left|n=0\right\rangle_{\omega_0} = 0. \tag{2.54}$$

We can relate the Heisenberg operator $\hat{C}\left(t\right)$ to its counterpart in the Schrödinger picture $\hat{C}_S\left(t\right)$ as $\hat{C}_S\left(t\right) = U\left(t\right)\hat{C}\left(t\right)U^{\dagger}\left(t\right)$, with the unitary operator $U\left(t\right)$ which fulfills

$$\dot{U}\left(t\right) = -iH_S\left(t\right)U\left(t\right). \tag{2.55}$$

Explicitly, we find

$$\hat{C}_S(t) = \frac{1}{2i}\left[\dot{u}(t)\sqrt{\frac{2m}{\hbar\omega_0}}\hat{x} - u(t)\sqrt{\frac{2}{m\hbar\omega_0}}\hat{p}\right]. \tag{2.56}$$

Then, Eq.(2.54) can be rewritten as

$$\hat{C}_S(t)\,U(t)\,|n=0\rangle_{\omega_0} = \hat{C}_S(t)\,|n=0;t\rangle = 0, \tag{2.57}$$

where we have introduced the state $|n=0;t\rangle$ in the Schrödinger picture which evolves unitarily starting from the ground state of the reference oscillator as $|n=0;t\rangle = U(t)\,|n=0\rangle_{\omega_0}$. The ladder-operator relations stated in Eqs.(2.49) and (2.50) for the reference oscillator can easily be transferred to the Schrödinger picture, yielding

$$\begin{aligned}\hat{C}_S(t)\,|n;t\rangle &= \sqrt{n}\,|n-1;t\rangle\,,\\ \hat{C}_S^{\dagger}(t)\,|n;t\rangle &= \sqrt{n+1}\,|n+1;t\rangle\,,\end{aligned} \tag{2.58}$$

implying $N_S(t)\,|n;t\rangle = n\,|n;t\rangle$, with $N_S(t) = \hat{C}_S^{\dagger}(t)\,\hat{C}_S(t)$. Since the Schrödinger operators $\hat{C}_S(t)$, $\hat{C}_S^{\dagger}(t)$ act as shift operators for the Floquet states $|n;t\rangle$, they will be referred to as Floquet shift operators [131]. Therefore, all other states forming the complete orthonormal basis $\{|n;t\rangle\}$ can be constructed by repeated operation on the ground state with the Schrödinger creation operator $\hat{C}_S(t)$ (with the proper normalization) as

$$|n;t\rangle = \frac{[\hat{C}_S(t)]^n}{\sqrt{n!}}\,|n=0;t\rangle\,. \tag{2.59}$$

When expressing this equation in coordinate space, the micromotion appears in the wavefunctions as a pulsation with the period $T = 2\pi/\omega$ [127]. Although the states $|n;t\rangle$ are not energy eigenstates (since they periodically exchange energy with the driving field), they are typically referred to as *quasi-stationary states*, because for stroboscopic times (that are integer multiples of the driving period T) the full evolution $U(t)$ boils down to multiplying the wavefunction by a simple phase factor (as is the case for standard stationary states for all times). Because of the periodicity of the micromotion, the quantum number n (labeling the quasi-energy states) can thus be tied to the electron's energy averaged over a period $T = 2\pi/\omega$ of the drive frequency. This connection will be explored in greater detail below.

The System-Bath Model

While our previous discussion has exclusively focused on the time-dependent system's dynamics [as described by the Hamiltonian $H_S(t)$ given in Eq.(2.34)], in the following we will develop a microscopic dissipative model, which describes the electron's motional coupling to the (thermal) phonon reservoir.

The global Hamiltonian, describing both the electronic motion as well as the phonon reservoir, can be formally decomposed as

$$H(t) = H_S(t) + H_B + H_I. \tag{2.60}$$

Here, the time-dependent system Hamiltonian $H_S(t)$ is given in Eq.(2.34). The Hamiltonian for the phonon bath H_B is of the usual form

$$H_B = \sum_{\mathbf{q},s} \omega_{\mathbf{q},s} a^\dagger_{\mathbf{q},s} a_{\mathbf{q},s}, \tag{2.61}$$

where $a^\dagger_{\mathbf{q},s}$ ($a_{\mathbf{q},s}$) creates (annihilates) an acoustic phonon with wave vector $\mathbf{q} = \left(\mathbf{q}_{||}, q_z\right)$, polarization s and dispersion $\omega_{\mathbf{q},s}$. Optical phonons can be disregarded at sufficiently low energies as considered here [196]. Following Ref.[137], generically the electron-phonon interaction takes on the form

$$H_I = \sum_{\mathbf{q},s} W_{\mathbf{q},s} a_{\mathbf{q},s} e^{i\mathbf{q}\cdot\hat{\mathbf{r}}} + \text{h.c.}, \tag{2.62}$$

with $\hat{\mathbf{r}} = (\hat{x}, \hat{y}, \hat{z})$ denoting the electron's three-dimensional position operator. The coupling constant $W_{\mathbf{q},s}$ comprises both the deformation potential as well as the piezoelectric coupling mechanism [137, 196]; it strongly depends on specific material properties, but can be left unspecified for the sake of our discussion. For low-dimensional quasi-2D systems as considered here, the Hamiltonian H_I may be simplified by projecting the electronic motional degrees of freedom onto the lowest electronic orbital $\psi_0(z)$, leading to

$$H_I \approx \sum_{\mathbf{q},s} \mathcal{F}(q_z) W_{\mathbf{q},s} a_{\mathbf{q},s} e^{i\mathbf{q}_{||}\cdot\hat{\mathbf{r}}_{||}} + \text{h.c.}, \tag{2.63}$$

with the in-plane position operator $\hat{\mathbf{r}}_{||} = (\hat{x}, \hat{y})$. The form factor $\mathcal{F}(q_z) = \int dz e^{iq_z z} |\psi_0(z)|^2$ introduces a momentum cut-off, with $\mathcal{F}(q_z)$ approaching unity in the limit $|q_z| \ll d^{-1}$ and vanishing for $|q_z| \gg d^{-1}$; here, $d \sim 10$nm denotes the size of the quantum well along the z-axis [196]. For the sake of clarity, here we will consider a quasi-one-dimensional structure (a quantum wire) where the electron's motion is restricted to the x-direction; compare our previous discussion in Sec.2.C. In this case, the electron-phonon interaction reduces to

$$H_I \approx \sum_{\mathbf{q},s} \tilde{W}_{\mathbf{q},s} a_{\mathbf{q},s} e^{iq\hat{x}} + \text{h.c.}, \tag{2.64}$$

where the coupling $\tilde{W}_{\mathbf{q},s}$ accounts for transversal confinement in both the y- and z-direction; moreover, we have set $q = q_x$. Along the lines of Sec.2.C, again we restrict ourselves to the Lamb-Dicke regime in which the electron's motion is confined to a region much smaller than the wavelength of the relevant, resonant phonon modes. Then, taking $e^{iq\hat{x}} \approx \mathbf{1} + iq\hat{x}$, and introducing displaced bosonic bath modes as

$$b_{\mathbf{q},s} = -i\left(a_{\mathbf{q},s} + \tilde{W}^*_{\mathbf{q},s}/\omega_{\mathbf{q},s}\right), \tag{2.65}$$

$$b^\dagger_{\mathbf{q},s} = i\left(a^\dagger_{\mathbf{q},s} + \tilde{W}_{\mathbf{q},s}/\omega_{\mathbf{q},s}\right), \tag{2.66}$$

we finally arrive at the following microscopic system-bath model with bilinear coupling between the system [as described by Eq.2.34] and a bath of noninteracting harmonic oscillators (i.e., the phonon reservoir),

$$H_B = \sum_\nu \omega_\nu b_\nu^\dagger b_\nu, \tag{2.67}$$

$$H_I = \hat{x}\sum_\nu g_\nu \hat{x}_\nu + \hat{x}^2 \sum_\nu \frac{g_\nu^2}{2m_\nu \omega_\nu^2}. \tag{2.68}$$

where, to simplify the notation, we have introduced the multi-index $\nu = (\mathbf{q}, s)$ and g_ν specifies the coupling strength between the system and each bath oscillator mode ν. Following the standard procedure in the literature, in Eq.(2.68) we have also included a correction term which acts in the Hilbert space of the particle only and compensates for a renormalization of the potential $V(\hat{x}, t) = \frac{m}{2} W(t)\, \hat{x}^2$ stemming from the system-reservoir coupling [131, 197]. In this model, the reservoir spectral density, defined as

$$J(\omega) = \pi \sum_\nu \frac{g_\nu^2}{2m_\nu \omega_\nu} \delta(\omega - \omega_\nu), \tag{2.69}$$

encodes all features of the environment relevant for the reduced system description [131].

Quantum Master Equation, Quasi-Stationary State and Effective Temperature The time-dependent, dissipative quantum system described by Eqs.(2.60), (2.34), (2.67) and (2.68), commonly referred to as parametrically driven, dissipative harmonic quantum oscillator, has been studied in great detail previously in Ref.[131]. Within one unified Born-Markov and Floquet framework, the authors of Ref.[131] have derived a quantum Master equation for the electronic motion, fully taking into account the explicit time-dependence of the system Hamiltonian $H_S(t)$.

Master equation.—By tracing out the unobserved degrees of freedom of the phonon reservoir Kohler *et al.* derive an effective equation of motion for the reduced, electronic density matrix ρ, which is irreversibly coupled to a thermal phonon reservoir [131]. In addition to the standard assumptions of a weak system-reservoir coupling (Born approximation), and a short reservoir correlation time (Markov approximation), the analysis has been restricted to an ohmic spectral density where $J(\omega) \sim \omega$ (which, however, may be generalized to a more general setting straight-forwardly). Under these conditions, the central master equation can be written as

$$\dot{\rho} = -\frac{i}{\hbar}\left[\hat{H}_S(t), \rho\right] + \mathcal{L}_\gamma \rho, \tag{2.70}$$

with

$$\mathcal{L}_\gamma \rho = \gamma(N+1)\,\mathscr{D}\left[\hat{C}_S(t)\right]\rho + \gamma N \mathscr{D}\left[\hat{C}_S^\dagger(t)\right]\rho. \tag{2.71}$$

Here, $\mathscr{D}[c]\,\rho = c\rho c^\dagger - \frac{1}{2}\left\{c^\dagger c, \rho\right\}$ is a dissipator of Lindblad form, γ denotes the effective, incoherent damping rate due to coupling to the thermal phonon reservoir, and

$$N = \sum_n c_{2n}^2 \frac{\omega_0 + n\omega}{\omega_0} \bar{n}_{\rm th}\left(\omega_0 + n\omega\right), \tag{2.72}$$

with $\bar{n}_{\rm th}(\omega) = \left(\exp\left[\hbar\omega/k_B T\right] - 1\right)^{-1}$, refers to a generalized effective thermal-bath occupation number. Note that Eq.(2.70) retains the periodicity of the driving and exhibits Lindblad form. Moreover, the dissipative part of Eq.(2.70) is of the same form as for the well-known undriven dissipative harmonic oscillator, with the Floquet shift operators defined in Eqs.(2.56) and (2.58) replacing the usual creation and annihilation operators. Note that in the pseudopotential limit (where c_0 is much larger than all other Floquet coefficients) the effective thermal occupation reduces to $N = \bar{n}_{\rm th}(\omega_0)$, that is the standard bosonic thermal occupation at the secular frequency ω_0.

The Master equation given in Eq.(2.70) is valid provided that the following conditions are satisfied [131]: (i) First, the Markov approximation is satisfied provided that autocorrelations of the bath (which typically decay on a timescale $\sim \hbar/k_B T$) decay quasi instantaneously on the timescale of system correlations $\sim \gamma^{-1}$. In principle, the damping rate γ should be replaced by the thermally enhanced rate $\gamma_{\rm eff} = \gamma(N+1)$; however, we will be interested mostly in the low-temperature, pseudopotential regime where $\gamma_{\rm eff} \approx \gamma$. Thus, the Markov approximation yields the condition $\hbar\gamma \ll k_B T$. (ii) Second, the (weak-coupling) Born approximation holds provided that the dissipative damping rate γ is small compared to the relevant system's transition frequencies, yielding the requirement $\gamma \ll \omega_0$. Taking together conditions (i) and (ii) (and setting $\hbar = 1$ for the moment) gives the requirement

$$\gamma \ll \omega_0, k_B T, \tag{2.73}$$

which (as shown below) comprises the regime for ground-state cooling where $\gamma \ll k_B T \ll \omega_0$. (iii) Finally, when deriving Eq.(2.70), the reservoir spectral density $J(\omega)$ has been assumed to be ohmic (i.e., $J(\omega) \sim \omega$).

Quasi-stationary state.—Using Eq.(2.58), the (asymptotic) quasi-stationary solution $\rho_{\rm ss}(t)$ associated with the Master equation (2.70) is readily found to be

$$\rho_{\rm ss}(t) = \frac{1}{N+1} \sum_{n=0}^{\infty} \left(\frac{N}{N+1}\right)^n |n;t\rangle\langle n;t|, \tag{2.74}$$

where $|n;t\rangle$ refer to the generalized (time-dependent) Fock states as discussed above [131]. The quasi-stationary solution $\rho_{\rm ss}(t)$ is dark with respect to the phonon-induced dissipation, that is $\mathcal{L}_\gamma \rho_{\rm ss}(t) = 0$ for all times, and, being a mixture of the Floquet solutions $|n;t\rangle$, evolves periodically with the period of the driving field, i.e., $\rho_{\rm ss}(t+T) = \rho_{\rm ss}(t)$.

While the notion of temperature becomes ambiguous for an explicitly time-dependent problem as considered here, in the following we will adopt the reasoning presented in Ref.[130] and take the mean kinetic energy (defined as the quantum kinetic energy $\overline{\langle \hat{p}^2(t)\rangle}/2m$, time-averaged over one period $T = 2\pi/\omega$ of the fast micromotion) as our figure of merit

for assessing the cooling-heating dynamics in more detail. To do so, let us first transform our analysis into a frame that is moving with the electron. Formally, this transformation is defined as $\varrho = U^{\dagger}(t)\,\rho U(t)$, with the unitary operator that satisfies

$$\dot{U}(t) = -iH_S(t)\,U(t)\,. \tag{2.75}$$

Then, in the corresponding interaction picture (which coincides with the Heisenberg picture defined in Sec.2.C) the dynamics described by Eq.(2.70) reduces to a purely dissipative master equation, $\dot{\varrho} = \mathcal{L}\varrho$,

$$\dot{\varrho} = \gamma(N+1)\,\mathscr{D}[A]\,\varrho + \gamma N \mathscr{D}\left[A^{\dagger}\right]\varrho, \tag{2.76}$$

where A $\left(A^{\dagger}\right)$ refers to the time-independent annihilation (creation) operator associated with the reference oscillator discussed in Sec.2.C. Since the Liouvillian $\mathcal{L}$ is time-independent, one can easily explain the phonon-induced cooling dynamics via the eigenstates of $A^{\dagger}A$, as defined in Sec.2.C. For simplicity, let us focus on the pseudopotential regime where $N \approx \bar{n}_{\rm th}(\omega_0)$ as discussed above; then, for sufficiently low temperatures ($k_BT \ll \hbar\omega_0$) the cooling dynamics dominate over the heating processes such that, at the end of the cooling process, we have $\left\langle A^{\dagger}A\right\rangle = \langle A^2\rangle = \left\langle A^{\dagger}A^{\dagger}\right\rangle = 0$. In this regime the expectation value for the quantum kinetic energy reduces to

$$\frac{\langle\hat{p}^2(t)\rangle}{2m} \overset{\text{cooling}}{\longrightarrow} \frac{\hbar}{4\omega_0}\left|\dot{u}(t)\right|^2, \tag{2.77}$$

as one can readily deduce from Eq.(2.53). Averaging this expression (which still fully accounts for the time dependence of the potential) over one micromotion period, we obtain

$$\overline{\frac{\langle\hat{p}^2(t)\rangle}{2m}} = \frac{\hbar}{4\omega_0}\sum_n |c_{2n}|^2\,(\omega_0+n\omega)^2\,, \tag{2.78}$$

$$= \frac{\hbar\omega_0}{4} + \Delta_{\rm heat}, \tag{2.79}$$

where we have separated the residual kinetic zero-point motion in the ground state of the secular reference oscillator $\sim \hbar\omega_0/4$ from the non-zero heating term

$$\Delta_{\rm heat} = \frac{\hbar}{4\omega_0}\sum_{n\neq 0} |c_{2n}|^2\,(\omega_0+n\omega)^2\,, \tag{2.80}$$

which may be viewed as micromotion-induced heating. While the full expression given in Eq.(2.78) can be evaluated numerically using the well-known solutions of the Mathieu equation (compare for example Ref.[130]), a simple estimate (for $q^2 \ll 1$) shows $\Delta_{\rm heat} \gtrsim \hbar\omega_0/4$. Therefore, in agreement with the results presented in Ref.[130] for trapped ions, we then find $\overline{\langle\hat{p}^2(t)\rangle}/2m \gtrsim \hbar\omega_0/2$ for the time-averaged kinetic energy in the pseudo-potential regime, which coincides with twice the residual kinetic zero-point motion in the ground state of the reference oscillator.

In conclusion, our analysis shows that micromotion does lead to some heating as compared to the naive estimate based on the slow secular motion only, but (in the pseudopotential regime of interest, where $q^2 \ll 1$) this apparent heating mechanism is strongly suppressed and amounts to merely a factor of 2 increase only in the particle's time-averaged kinetic energy.

Exact Numerical Simulations and Discussion

Since the electronic dynamics described by Eq.(2.70) are purely Gaussian, an exact solution is feasible. Therefore, in the following we will complement our analytical findings with numerically exact simulations for the electron's dynamics. Based on Eq.(2.70), one can readily derive a closed dynamical equation

$$\frac{d}{dt}\mathbf{v} = \mathcal{M}(t)\,\mathbf{v} + \mathbf{C}(t)\,, \tag{2.81}$$

where $\mathbf{v}$ is a five-component vector comprising the first- and second-order moments, that is $\mathbf{v} = (\langle\hat{x}\rangle_t, \langle\hat{p}\rangle_t, \langle\hat{x}^2\rangle_t, \langle\hat{p}^2\rangle_t, \langle\hat{x}\hat{p}+\hat{p}\hat{x}\rangle_t)^\top$. Since the first- and second-order moments are decoupled, the dynamical matrix $\mathcal{M}$ is of block-diagonal form.

Numerical results.—As illustrated in Fig.2.3, in the regime $q^2 \ll 1$ we numerically find that (i) the electronic motion can be described very well by a simple damped harmonic oscillator with secular frequency ω_0, (ii) the electronic motion is cooled by the phonon reservoir and (iii) the Lamb-Dicke approximation is well satisfied. Let us elaborate on these statements in some more detail: (i) When disregarding micromotion, the dynamics can approximately be described by a simple damped harmonic oscillator with secular frequency ω_0. As shown in Fig.2.3, the effective, time-independent master equation

$$\dot{\rho} = -i\omega_0\left[a^\dagger a, \rho\right] + \gamma\left(\bar{n}_{\rm th}(\omega_0)+1\right)\mathscr{D}[a]\,\rho + \gamma\bar{n}_{\rm th}(\omega_0)\,\mathscr{D}\left[a^\dagger\right]\rho, \tag{2.82}$$

with a $\left(a^\dagger\right)$ denoting the usual annihilation (creation) operators for the canonical harmonic oscillator, captures well the most pertinent features of the electronic dynamics, provided that $q^2 \ll 1$; compare the dashed orange line in Fig.2.3. (ii) As suggested by our analytical analysis, the phonon reservoir provides an efficient cooling mechanism for the electron provided that the host temperature is sufficiently low, that is $k_B T \ll \omega_0$. (iii) Regarding the last statement (iii) we have numerically verified that both the expectation value for the electron's motion as well as the corresponding fluctuations are small compared to the SAW wavelength $\lambda = 2\pi/k$, i.e., $k\langle\hat{x}\rangle_t \ll 1$ and $k\sigma_x \ll 1$ with $\sigma_x^2 = \langle\hat{x}^2\rangle_t - \langle\hat{x}\rangle_t^2$. Furthermore, the Lamb-Dicke approximation underlying the bilinear system-bath interaction Hamiltonian [compare Eq.(2.68)] can be justified as follows: Since the effective transition frequency ω_0 is much smaller than the SAW driving frequency ($\omega_0 = \varepsilon\omega$, with $\varepsilon \ll 1$), the same is true for the relevant phonon wavenumber k_0. Using the relation $\omega_0 = v_s^{(b)}k_0$ (where $v_s^{(b)}$ refers to the speed of sound associated with some relevant bulk phonon mode), the latter can be expressed as $k_0 = \varepsilon(v_s/v_s^{(b)})k$ (with v_s denoting the speed of sound of the SAW mode driven by the IDTs, as usual). Therefore, even for higher Rayleigh SAW-modes whose speed of sound v_s may exceed the lowest value of $v_s^{(b)}$, our approximate treatment of

$\hbar\omega[\mu\text{eV}]$	$q = V_{\text{SAW}}/E_S$	$\hbar\omega_0[\mu\text{eV}]$	$V_0[\mu\text{eV}]$	$n_b = V_0/\hbar\omega_0$	$a = \lambda/2[\text{nm}]$	$d[\text{nm}]$
207	0.5 - 0.7	37-51	31-61	0.85-1.2	180	10-100

$t\ [\mu\text{eV}]$	$U[\mu\text{eV}]$	$k_BT[\mu\text{eV}]$
0.7-1.8	5-270	1-10

Table 2.2: Important (energy) scales for an exemplary setup with $E_S = 1\text{meV}$ and $f = 50\text{GHz}$. d denotes the distance between the screening layer and the 2DEG.

the system-bath Hamiltonian is well justified, provided that $v_s \lesssim v_s^{(b)}/\varepsilon$ holds. Note that material-engineering strategies as discussed in the main text would increase v_s in the same way as $v_s^{(b)}$, providing a very good justification for our linearized Hamiltonian (2.68) since $k_0 \lesssim \varepsilon k$.

Finally, the parameter regime of interest is summarized and discussed extensively in Section 2.3 of the main text, while the experimental feasibility thereof is discussed in Section 2.4.

2.D Case Study & Practical Considerations

In this Appendix we provide further details regarding several practical considerations that are relevant for a faithful experimental realization of our proposal. First, we provide comprehensive overview of the key quantities of our analysis and self-consistent estimates thereof. Next, we address microwave-induced heating effects. Lastly, we discuss electron spin decoherence effects due to (nuclear) spin noise.

Case study.—Typical parameter regimes for the key quantities of our analysis are given in Table 2.2. The parameters are chosen self-consistently with respect to the requirements derived in the main text, see Eq. 2.6. Note that the high-SAW frequencies lead to large energy scales in the effective (harmonic-oscillator) problem. For comparison, ions are typically confined in traps with harmonic-oscillator energy $\hbar\omega_0 \sim 10\text{MHz}$ [127]. For the SAW velocity v_s, we assume an ultra-fast PSAW mode in AlN/diamond ($v_s \approx 18\text{km/s}$) as described in the main text and a corresponding effective hole mass $m = 1.1m_0$ in the host material GaN where the 2DEG is located.

Heating.—In order to avoid excessive heating of the effective electron temperature above the dilution fridge temperature in the presence of RF driving, we (i) either need the heat dissipation W_{heat} to be balanced by the applied cooling power P_{cool} (for which, in an actual experiment, the way the sample is heat sunk is very important) and/or (ii) the heat dissipation to be too slow to change the electron's temperature on relevant experimental timescales after the IDT induced driving has been turned on. In the following we argue why the requirements (i) and (ii) can both be fulfilled under realistic conditions: (i) First, recall that our proposal is based on low power SAWs (as a direct consequence of the limitations imposed by Mathieu's equation) [156]. Since the potential amplitude due to a single IDT is limited by Mathieu-like stability arguments as $V_{\text{IDT}} = V_{\text{SAW}}/2 = (q/2)E_S \lesssim 0.5\text{meV}$, the proposed setup operates at SAW-induced amplitudes that are about two orders of

magnitude smaller than what is common for SAW-induced electron transport experiments (where typically $V_{\mathrm{IDT}} \approx 40\mathrm{meV}$ [72, 157]). Based on experimental results presented in Refs.[72, 198, 199], we find that SAW amplitudes $V_{\mathrm{IDT}} \approx 1\mathrm{meV}$ can be reached with an applied RF power $P \approx -10\mathrm{dBm}(0.1\mathrm{mW})$, in the desired SAW frequency range $\omega/2\pi \approx 30\mathrm{GHz}$ (as needed to enter the pseudo-potential regime), whereas high-amplitude electron transport measurements operate at $P > +10\mathrm{dBm}(10\mathrm{mW})$ [72]. This estimate is based on experiments with relatively wide IDTs in GaAs; therefore, the power budget P could be further reduced (if needed) by reducing the width W of the IDTs (which is typically several hundreds of μm long [200], i.e., much longer than necessarily required for an acoustic trap or lattice) and/or using strongly piezoelectric materials [67, 68, 201] where the electromechanical coupling efficiency is much larger than for the weakly piezoelectric material GaAs. Heating effects as a function of the applied RF power P have been investigated experimentally in detail in Refs.[198, 199]: Here, at a comparatively large microwave power $P = +5\mathrm{dBm}$ the SAW-induced heating has been measured to be $W_{\mathrm{heat}}^{\mathrm{SAW}} \approx 0.1\mathrm{mW}$. We may estimate this source of heating as $W_{\mathrm{heat}}^{\mathrm{SAW}} \approx \hbar\omega \times (V_{\mathrm{SAW}}/V_0)^2 \kappa$, where $\hbar\omega$ is the energy of a single phonon and the second factor gives the total phonon loss rate in terms of the phonon number $N_{\mathrm{ph}} \approx (V_{\mathrm{SAW}}/V_0)^2$ and the decay rate $\kappa = \omega/Q$; here, V_0 refers to the amplitude associated with a single phonon [81] and Q is the quality factor associated with the driven SAW mode. However, it has been shown in Ref.[199] that $W_{\mathrm{heat}}^{\mathrm{SAW}}$ accounts for $\sim 10\%$ of the overall heating only, due to the limited efficiency of the IDTs. While this ratio may be improved with more sophisticated IDT designs [67, 68, 202], an overall heating of $W_{\mathrm{heat}} \approx 10 W_{\mathrm{heat}}^{\mathrm{SAW}} \approx 1\mathrm{mW}$ is still compatible with the cooling power of state-of-the-art dilution refrigerators, which can reach $P_{\mathrm{cool}} = 1\mathrm{mW}$ at $T \approx 100\mathrm{mK}$ [203]; here, to maximize the cooling efficiency in an actual experiment, attention should be paid to the the specific way the sample is heat sunk. Since the proposed AL setup operates at much lower RF power levels [$P \lesssim -10\mathrm{dBm}(0.1\mathrm{mW})$ as compared to $P = +5\mathrm{dBm}(3\mathrm{mW})$], the overall heat dissipation W_{heat} can be balanced by the applied cooling power P_{cool} for the specific parameters under consideration. This finding is further supported by the experiments presented in Refs.[198, 199], where for low-power SAWs no significant heating above the base temperature has been observed. (ii) Second, the IDTs generating the SAWs can be placed very far away from the center of the trap, without losing acoustic power, thereby reducing local heat dissipation near the center of the trap due to the applied RF power. For example, in Ref.[72] (and many similar setups) the SAW transducer has been placed approximately 2mm away from the center of the sample. In this way, the dominant local heating at the IDT may be suppressed efficiently, at least on timescales that are short compared to the one set by the material-specific thermal diffusivity (which specifies the rate of transfer of heat from the IDT to the cold center of the trap). While this timescale is strongly material-dependent, a rough estimate for GaAs shows that it can lie in the millisecond range (for IDTs placed $\sim 1\mathrm{mm}$ away from the center of the trap), which is much longer than any relevant experimental timescale. This reasoning is also in line with experimental results showing that the effective temperature increase could be further reduced when using pulsed schemes rather than CW [198]; note that this approach is fully compatible with our discussion on optimized driving schemes. In summary, we conclude

that for realistic cooling powers and/or IDTs placed sufficiently far away from the center of the trap microwave induced heating effects should not lead to a significant increase of the effective particle temperature (as compared to the base temperature) since the AL setup is based on low amplitude SAWs with $V_{\rm IDT} \lesssim 0.5$meV, as a direct consequence of the Mathieu-type stability arguments.

Nuclear spin noise.—The observation of coherent spin physics as outlined in Sec.2.5 may be impeded by electron spin decoherence. For GaAs-based systems, the electron spin coherence timescale will be largely limited by the relatively strong hyperfine interaction between the electronic spin and the nuclei in the host environment [204], resulting in a random, slowly evolving magnetic (Overhauser) field for the electronic spin, and eventually leading to a loss of spin coherence on a timescale $\sim T_2^\star$. The latter depends on the number of nuclear spins the electron effectively interacts with. Since the electron's spatial extension $\Delta x/a \approx 1/\left(\pi\sqrt{2n_b}\right)$ is comparable to the typical size of gate-defined quantum dots for realistic parameter values, we estimate $T_2^\star \sim 15$ns [204]. Then, in the first approximation, the detrimental effects due to Overhauser noise may be neglected provided that the condition $J \gg 1/T_2^\star$ is fulfilled, i.e., if coherent spin exchange $\sim 1/J$ is much faster than electron spin dephasing. According to our estimates provided above this regime is within reach even for GaAs-based systems, where electron spin dephasing is known to be relatively fast [204]. In this respect, even more promising estimates apply to nuclear spin free systems such as ^{28}Si/SiGe where the influence of nuclear spins on the electron spins is largely eliminated [205]. While such a silicon-based setup will require a more sophisticated heterostructure including some piezoelectric layer on top (as has been studied experimentally in Ref.[121]), it should profit from significantly prolonged dephasing times $T_2^\star > 100\mu$s [206]. Finally, as argued for example in Ref.[73], Overhauser-field induced spin dephasing can be suppressed based on motional-narrowing techniques, when moving around the acoustic dots (lattice sites) such that the electron effectively samples many different Overhauser fields.

Chapter 3

Magnetic Traps and Lattices

3.1 Motivation

The advent of cold atoms trapped in optically defined potential landscapes has enabled experimental breakthroughs in various discplines ranging from condensed-matter physics to quantum information processing [208, 109]. Especially, thanks to largely tunable system parameters and the possibility to mimic and gain understanding of complex solid-state systems, ultra-cold atomic gases have become a rich playground and valuable tool to explore novel quantum many-body physics [108]. On a complementary route towards controllabe quantum matter and a fully fledged quantum simulator, solid-state platforms allow to pursue the same goals in a very different physical context, both bearing challenges such as to overcome impurity-induced disorder in semiconductor systems [136], but also offering the potential to benefit from long-range inter-particle interactions, access to a wide variety of quasiparticles and, in principle, means to build scalable on-chip architectures for quantum information processing. To this end, different kinds of quasiparticle traps in semiconductor nanostructures have been proposed and realized [110, 111, 114, 209, 210, 211, 212]. Likewise, in the realm of atomic [213, 214] and molecular [215, 216] systems, mesoscopic on-chip platforms have been tailored to miniaturize experiments with ultracold quantum matter. Apart from more established solid-state platforms like, e.g., quantum-dot based architectures [62], it has recently been proposed [2] to employ surface acoustic waves (SAWs) to trap and control semiconductor quasiparticles such as electrons in intrinsically scalable and tunable *acoustic lattices* (see Chapter 2). The latter operate at elevated energy scales with typical lattice spacings $a \gtrsim 100$ nm and recoil energies $E_{\mathrm{R}}/k_{\mathrm{B}} \sim (0.1 - 1)\ K$ (where $E_{\mathrm{R}} = h^2/(8ma^2)$ with an effective particle mass m which is typically of the order of the electron rest mass) as compared with optical lattices where typically $E_{\mathrm{R}}/k_{\mathrm{B}} \sim 10^{-7} K$ [217]. Inspired by these results and recent advances in the rapidly evolving field of nanomagnetism [218, 219], i.e., the generation and control of (high-frequency) magnetic fields on the nanoscale, the present work aims to bring the favourable scaling properties and flexibility of optical lattices to the solid-state domain.

3.2 Executive Summary

In contrast to electrically defined confinement potentials for charged particles in quantum wells, the spin degree of freedom (DOF) can be addressed with magnetic field gradients in order to trap and control particles in semiconductor nanostructures; note that this is in close analogy to the working principle of optical dipole traps where the induced AC Stark shift of the atomic levels gives rise to a dipole potential for the atom [220]. In previous theoretical proposals [221, 222] and experimental demonstrations [223, 224], magnetic traps for charge carriers in low-dimensional quantum wells were induced by a spatially inhomogeneous *giant Zeeman splitting* in dilute magnetic semiconductors (DMS) [225], which feature extremely large g-factors $\sim 10^2$. In particular, microscale magnets [226] and current loops [227] as well as superconducting (SC) vortex lattices [222] have been considered in this context. So far, however, none of these previous results have yet been tailored to scalable architectures and, moreover, only static traps with limited tunability of system parameters have been taken into account. In this work, we take a significant next step towards tunable and scalable magnetic lattices and develop a general theoretical framework fit to describe the latter. We show that a non-standard form of the Hubbard model with two independently tunable hopping parameters can readily be implemented. Ultimately, two alternative implementations of the developed model will be discussed in detail, one based on SAWs and the other based on magnetic field gradients generated by SC nanowires, both operated in yet unexplored parameter regimes and with highly favourable tunability and scalability properties.

The basic scheme is depicted in Fig. 3.1. We consider electrons with two internal (spin) states $|\uparrow\rangle$ and $|\downarrow\rangle$ which are confined to a conventional low-dimensional quantum well or a purely two-dimensional material, e.g., from the group of transition-metal dichalcogenides (TMDs), and subject to a spatially inhomogeneous magnetic driving field. Due to the thereby induced AC Stark shift acting on the internal energy levels, the electrons feel an effective state-dependent potential which is periodic along one axis (in the one-dimensional setup we consider here), as illustrated in Fig. 3.1. As a result, the electrons are attracted to a regular lattice of antiferromagnetic character, since the two internal states are found to be trapped at nodes or antinodes of the magnetic field distribution, respectively, cf. Fig. 3.1(b). For simplicity, we consider only one-dimensional systems, but all results can readily be generalized to two dimensions.

This chapter is organized as follows. In Sec. 3.3, we first introduce the theoretical framework to describe magnetic trapping potentials for electrons confined to a two-dimensional electron gas (2DEG). All requirements for the validity of the theoretical treatment and relevant approximations are discussed, followed by an investigation of hopping and interactions in magnetic lattices and a detailed description of possible implementations in Sec. 3.4. Finally, we will provide case studies for both implementations with realistic parameters in Sec. 3.5.

3.3 Theoretical Framework

Single-particle physics in magnetic traps

We consider an electron confined to a 2DEG with effective mass m and the two internal states $|\uparrow\rangle$ and $|\downarrow\rangle$ exposed to an external magnetic field, $\mathbf{B}(\mathbf{r},t) = \mathbf{B}_\perp(\mathbf{r},\omega t) + \mathbf{B}_{||}$. The spatially homogeneous, static (in-plane) part of the field, $\mathbf{B}_{||} = B_0\hat{\mathbf{z}}$, gives rise to a Zeeman splitting, $\hbar\omega_0 = g_\mathrm{s}\mu_\mathrm{B}B_0$, and the inhomogeneous (*time-dependent* or *time-independent*) (out-of-plane) field component, $\mathbf{B}_\perp(\mathbf{r},\omega t) = B_1\Lambda(\mathbf{r})\cos(\omega t)\hat{\mathbf{x}}$, drives spin transitions with frequency ω. The corresponding Hamiltonian can be written as (here and in the following, we adopt the convention that $\hbar = 1$)

$$H = \frac{\hat{p}^2}{2m} + h(\hat{z}) = \frac{\hat{p}^2}{2m} + \frac{\omega_0}{2}\sigma^z + \frac{\Omega(\hat{z})}{2}\cos(\omega t)\sigma^x, \tag{3.1}$$

where $\hat{z}$, $\hat{p}$, $\sigma^x = |\uparrow\rangle\langle\downarrow| + |\downarrow\rangle\langle\uparrow|$, $\sigma^z = |\uparrow\rangle\langle\uparrow| - |\downarrow\rangle\langle\downarrow|$ denote the particle's position, momentum and Pauli spin operators, respectively. The inhomogeneous Rabi frequency is denoted by $\Omega(\hat{z}) = \Omega_0\Lambda(\hat{z})$ with $\Omega_0 = \gamma B_1$, where $\gamma = g_\mathrm{s}\mu_\mathrm{B}$ is the gyromagnetic ratio of the electron. We assume $\Lambda(\hat{z}) = \cos(k\hat{z})$ in the following, where k denotes the wavevector, but more general periodic functions can be considered. While the universality of this model will become more apparent later, especially when we consider different implementations in Sec. 3.4, we may already distinguish between two physically dissimilar cases both captured by Eq. (3.1): (*i*) *static* traps ($\omega = 0$) are time-independent and (*ii*) *dynamic* traps ($\omega > 0$) are explicitly time-dependent realizations of the model. Due to their intrinsic flexibility and *in-situ* tunability of system parameters, we put the main focus on *dynamic* magnetic traps, i.e., $\omega > 0$.

Within a co-rotating frame and rotating-wave approximation (RWA) for $|\Delta| = |\omega_0 - \omega| \ll \omega_0 + \omega$ and $\Omega_0 \ll \omega$, the time-independent internal model $h_\mathrm{RWA}(\hat{z}) = [\Delta/2]\sigma^z + [\Omega(\hat{z})/2]\sigma^x$ can be diagonalized exactly which yields the local eigenenergies $\pm\varepsilon(\hat{z})$ with $\varepsilon(\hat{z}) = \frac{1}{2}\sqrt{\Omega^2(\hat{z}) + \Delta^2}$ and position-dependent eigenstates,

$$|+\rangle_{\theta(\hat{z})} = \cos\frac{\theta(\hat{z})}{2}|\uparrow\rangle + \sin\frac{\theta(\hat{z})}{2}|\downarrow\rangle,$$
$$|-\rangle_{\theta(\hat{z})} = -\sin\frac{\theta(\hat{z})}{2}|\uparrow\rangle + \cos\frac{\theta(\hat{z})}{2}|\downarrow\rangle,$$

where $\theta(\hat{z}) = \arcsin[\frac{\Omega(\hat{z})}{\sqrt{\Omega^2(\hat{z})+\Delta^2}}]$. The trap depth of the effective potentials $\pm\varepsilon(\hat{z})$, which is given by the difference $|\max_z \varepsilon(\hat{z}) - \min_z \varepsilon(\hat{z})|$, depends only on Ω_0 and Δ and will be denoted by V_0 in the following [see Fig. 3.1]. In the limit $\Omega_0 \ll |\Delta|$, the standard result from second-order perturbation theory, $\varepsilon(\hat{z}) \approx |\Delta|/2 + \Omega_0^2\Lambda^2(\hat{z})/(4|\Delta|)$, can be recovered. Note that the periodic modulation of the internal energy levels $|\pm\rangle_{\theta(\hat{z})}$ amounts to a state-dependent potential for the motional DOF such that the states are trapped at nodes and antinodes of the driving field, respectively. As a consequence, magnetic trapping potentials for the two spin components are shifted with respect to one another, as illustrated in Fig. 3.1(b). In fact, this result is reminiscent of state-dependent optical lattices which can be enriched

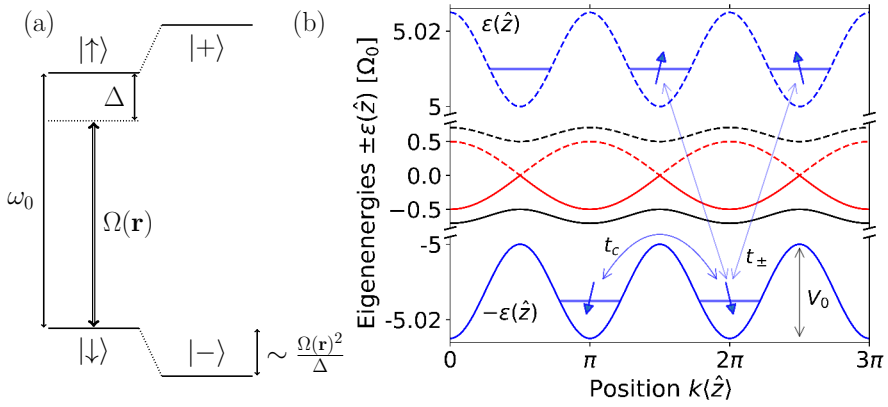

Figure 3.1: (color online). Schematic illustration of the trapping scheme and magnetic lattice. (a) At each point, the two-level spin systems experience an AC Stark shift which defines an effective (state-dependent) potential landscape for the electrons. (b) The local eigenenergies $\pm\varepsilon(\hat{z})$ of the two spin components $|+\rangle_{\theta(\hat{z})}$ and $|-\rangle_{\theta(\hat{z})}$ are shifted with respect to each other. The energies $+\varepsilon(\hat{z})$ (dashed) and $-\varepsilon(\hat{z})$ (solid) are shown for $\Delta/\Omega_0 = 10$ (blue), $\Delta/\Omega_0 = 1$ (black) and $\Delta/\Omega_0 = 0$ (red) in units of Ω_0. The hopping matrix elements t_c and $t_\pm$ denote next-nearest neighbour spin-conserved and nearest-neighbour spin-flip assisted tunneling, respectively. V_0 denotes the trap depth.

by laser-assisted tunneling between internal atomic states [162, 228], whereby gauge fields for ultracold atoms can be generated [229, 230, 231, 232].

Note that, in the realm of the RWA introduced before, the Rabi frequency Ω_0 is limited to relatively small values, as compared to other relevant energy scales. This limitation can be overcome, to some extent, by deriving an effective Floquet Hamiltonian without RWA, see Appendix 3.A for details.

Until now, we have not explicitly taken into account the presence of the kinetic term, $\hat{p}^2/(2m)$, in Eq. (3.1). Its presence induces a coupling between the local spin eigenstates $|\pm\rangle_{\theta(\hat{z})}$ and, as a consequence, undesired spin flips may result in particle loss from the trap [233]. In order to quantify this effect, it is instructive to introduce a unitary transformation $U(\hat{z})$ which diagonalizes $h_{\mathrm{RWA}}(\hat{z})$ at each point, such that $|+\rangle_{\theta(\hat{z})} = U(\hat{z})\,|\uparrow\rangle$ ($|-\rangle_{\theta(\hat{z})} = U(\hat{z})\,|\downarrow\rangle$). The thereby transformed Hamiltonian, $\tilde{H} = U^\dagger[\frac{p^2}{2m} + h_{\mathrm{RWA}}(\hat{z})]U = \hat{p}^2/2m + \tilde{h}(\hat{z}) + \Delta T$, contains the kinetic term from Eq. (3.1), the diagonal (in the local eigenbasis spanned by $|+\rangle_{\theta(\hat{z})}$ and $|-\rangle_{\theta(\hat{z})}$) spin Hamiltonian $\tilde{h} = U^\dagger h_{\mathrm{RWA}} U$ and an additional term ΔT, which stems from the transformation of the kinetic term, see Appendix 3.B for details. If the latter contributes only a small correction to the system's characteristic energy scale set by the motional quantum ω_{HO}, the internal spin DOF follows adiabatically the local direction of the magnetic field and the contribution from ΔT can be safely neglected. For this *adiabatic approximation* (also refered to as Born-Oppenheimer approximation) to hold, the local eigenstates of the two-level system spanned by $|+\rangle_{\theta(\hat{z})}$ and $|-\rangle_{\theta(\hat{z})}$ must be sufficiently separated in energy. If this energy gap by far exceeds ω_{HO}, i.e. $\chi := \omega_{\mathrm{HO}}/|\Delta| \ll 1$, spin-flip

processes are typically negligible [233].

Requirements.—Following the line of arguments outlined above, we have implicitly made a few assumptions about the system parameters which we are going to summarize in the following: (*i*) We have assumed idealized two-level spin systems with well-resolved energy levels and thus a relatively small intrinsic linewidth $\Gamma \ll |\Delta|$. (*ii*) We require a weak electron-phonon coupling, i.e., the spontaneous phonon emission rate γ which quantifies motional damping of the electron must be small compared to all other characteristic system's time scales; explicitly, we demand that it should be smaller than the motional transition frequencies, i.e., $\gamma \ll \omega_{\mathrm{HO}}$. (*iii*) In order to obtain thermally robust traps and minimize particle loss from the trap, we need thermal energies $k_{\mathrm{B}}T \ll V_0$ (where k_{B} denotes the Boltzmann constant). Typically, in case ground-state cooling is desired, this requirement is replaced by the stronger condition $k_{\mathrm{B}}T \ll \omega_{\mathrm{HO}}$. (With at least one bound state, $n_b = V_0/\omega_{\mathrm{HO}} \geq 1$, supported by the trap, the latter condition is more restrictive.) (*iv*) The magnetic trap depth V_0 is either much smaller than Ω_0, i.e. $V_0 = \Omega_0^2/(4|\Delta|)$ in the perturbative regime $\Omega_0 \ll |\Delta|$, or approaches $V_0 \to \Omega_0/2$ in the opposite limit $|\Delta|/\Omega_0 \to 0$; however, in both cases V_0 is limited from above by $\Omega_0/2$. In terms of other relevant physical parameters contained in $\Omega_0 = \gamma B_1$, this means that strong magnetic radio-frequency (RF) fields $\sim B_1$ and large g-factors are favourable. (*v*) The Rabi frequency Ω_0, in turn, is typically much smaller than the driving frequency within the RWA, $\Omega_0 \ll \omega$, but this condition can be relaxed as mentioned earlier. However, for too large Ω_0, even the high-frequency expansion of the Floquet Hamiltonian fails to converge. For our purposes, we therefore demand $\Omega_0 < \omega$. (*vi*) Finally, introducing the small number $\varepsilon_{\mathrm{ad}} = V_0/\omega \lesssim 0.5$, the adiabaticity condition $\chi \ll 1$ can be rewritten as $\omega \ll n_b|\Delta|/\varepsilon_{\mathrm{ad}}$. However, this condition may be relaxed at the cost of higher loss rates. The Majorana loss rate Γ_{loss}, compared to the natural frequency scale ω_{HO} of the trap, can be estimated as $\eta := \Gamma_{\mathrm{loss}}/\omega_{\mathrm{HO}} \approx 2\pi \exp(-4/\chi)$ [233] (compare also Ref. [234] for a related description of non-adiabatic spin-flips in radio-frequency dressed magnetic traps for cold atoms); deep in the adiabatic regime with $\chi = 0.1$, spin-flip losses are negligible as $\eta \sim 10^{-17}$, but even for moderate values $\chi = 0.5$ ($\chi = 1$), the loss rates are relatively small with $\eta \approx 2 \cdot 10^{-3}$ ($\eta \approx 1.2 \cdot 10^{-1}$). Hence, the adiabaticity condition may be relaxed in order to obtain well-performing traps. Putting these findings together results in a concise list of necessary requirements and, in general, without resorting to the RWA or the perturbative regime where $\Omega_0 \ll |\Delta|$, we find:

$$\gamma, k_{\mathrm{B}}T \ll \omega_{\mathrm{HO}} \lesssim V_0 \lesssim \Omega_0/2 \lesssim \omega/2. \tag{3.2}$$

In order to obtain reliable magnetic traps, both implementations discussed in Sec. 3.4 need to be operated in a parameter regime where Eq. (3.2) is fulfilled and η is sufficiently small.

Engineering of Hubbard models

Based on the theoretical framework fit to describe single traps as worked out above, the following paragraphs are dedicated to the study of Fermi-Hubbard physics in magnetic lattices, i.e., periodic arrays of magnetic traps. Explicitly, we show that spin-dependent

forms of the Hubbard model with independently tunable hopping parameters t_c and $t_\pm$ can be realized with the aid of additional driving fields [see Appendix 3.C for more details] in the fashion of zigzag optical lattices for cold atoms [235, 236]. Here and in the following, t_c denotes spin-conserved next-nearest neighbour coherent tunneling processes and $t_\pm$ describes spin flip-assisted tunneling between adjacent lattice sites, cf. Fig. 3.1(b). Another genuine prospect is the operation in a low-temperature, strong-interaction regime (at dilution-fridge temperatures $T \approx (10-100)$ mK) where the thermal energy is much smaller than the hopping parameters $t_c,\ t_\pm$ which, in turn, are small compared to the on-site interaction strength U, i.e., $k_\mathrm{B}T \ll t_c, t_\pm < U$.

As a starting point, we consider the single-particle Hamiltonian $\tilde{H}$ within the adiabatic approximation which can be written as

$$\tilde{H} \approx \frac{\hat{p}^2}{2m} + \tilde{h}(\hat{z}) = \frac{\hat{p}^2}{2m} + \varepsilon(\hat{z})\tilde{\sigma}^z, \tag{3.3}$$

with $\tilde{\sigma}^z = |+\rangle\langle+| - |-\rangle\langle-|$. In a next step, we now consider an ensemble of electrons in a magnetic lattice. At sufficiently low temperatures ($k_\mathrm{B}T \ll \omega_\mathrm{HO}$) such that the electrons are confined to the lowest Bloch band, we find that the system is characterized by a Fermi-Hubbard model of the form [120]

$$\begin{aligned} H_\mathrm{FH} &= -t_c \sum_{\langle\langle i,j\rangle\rangle,s} (c_{is}^\dagger c_{js} + \mathrm{h.c.}) - \varepsilon \sum_{is} (-1)^i n_{is} \\ &\quad + \sum_i \mu_i n_i + \sum_{s,s'} \sum_{ijkl} U_{ijkl} c_{is'}^\dagger c_{js}^\dagger c_{ls} c_{ks'}, \end{aligned} \tag{3.4}$$

where the fermionic operator $c_{is}^{(\dagger)}$ annihilates (creates) an electron with spin $s = +, -$ at lattice site i, $n_{is} = c_{is}^\dagger c_{is}$ and $n_i = n_{i+} + n_{i-}$ are the spin-resolved and total occupation numbers, respectively. The summation over $\langle\langle\cdot,\cdot\rangle\rangle$ is performed for next-nearest neighbours (accordingly, $\langle\cdot,\cdot\rangle$ in Eq. (3.5) denotes a summation over neighbouring sites). $U_{ijkl} = \int \mathrm{d}z\mathrm{d}z' w_i^*(z') w_j^*(z) U_\mathrm{C}(z,z') w_k(z) w_l(z')$ quantifies the inter-particle interaction strength ($U = U_{iiii}$ denotes the on-site interaction strength), where w_i is a Wannier basis function which is typically strongly localized around the respective lattice i. Typically, it is inversely proportional to the lattice constant a, depends on the dielectric constant ϵ of the substrate and can be reduced with the aid of an additional metallic screening layer positioned at a distance d_scr from the 2DEG. The screened Coulomb interaction can be written as $U_\mathrm{C} = e^2 f_s(z,z')/(4\pi\epsilon|z-z'|)$, where $f_s = 1 - |z-z'|/\sqrt{(z-z')^2 + 4d_\mathrm{scr}^2}$ incorporates screening [120, 237]. In Eq. (3.4) the spin-dependent energy offset $\sim \varepsilon$ [see Fig. 3.1] incorporates the remnant of the Zeeman splitting (in the rotating frame) and the AC Stark shifts. Moreover, the site-dependent chemical potential μ_i can take disorder effects into account [2]. In the tight-binding limit where the potential is sufficiently deep, i.e., $E_\mathrm{R} \ll V_0$ (with the recoil energy $E_\mathrm{R} = k^2/2m$), the hopping parameter is approximately given by $t_c/E_R \approx (4/\sqrt{\pi})(V_0/E_R)^{3/4} \exp[-2\sqrt{V_0/E_\mathrm{R}}]$ [108]. Realistic parameter values [see below for details] suggest that the low-temperature, strong-interaction regime

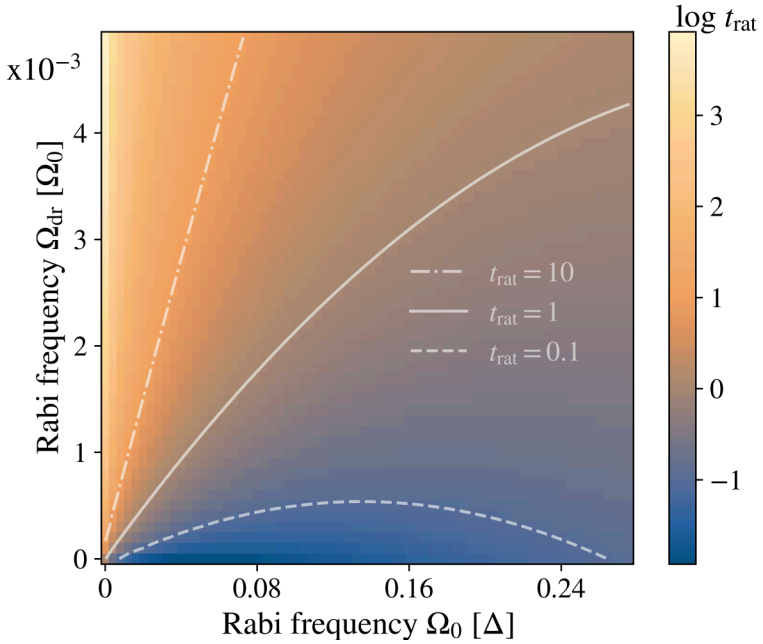

Figure 3.2: (color online). Overview of $\log t_{\mathrm{rat}}$ as a function of $\Omega_{\mathrm{dr}}/\Omega_0$ and Ω_0/Δ. The contour lines depict parameter constellations of equal t_{rat}: $t_{\mathrm{rat}} = 10$ (dash-dotted), $t_{\mathrm{rat}} = 1$ (solid), $t_{\mathrm{rat}} = 0.1$ (dashed). Other parameters: $n_b = 1$.

$U \approx 10t_c \gg t_c \gg k_B T \approx 1\mu$eV lies within reach with state-of-the-art experimental techniques.

As illustrated in Fig. 3.1(b), the standing-wave field distribution, as described by Eq. (3.1), gives rise to spatially separated traps for the different spin components. Hence, adjacent potential minima host two different spin states $|+\rangle_{\theta(\hat{z})}$ and $|-\rangle_{\theta(\hat{z})}$, respectively. As a consequence, spin-flip assisted tunneling $\sim t_\pm$ between neighbouring lattice sites is strongly suppressed, whereas next-nearest neighbours, occupying the same internal state, are coupled much more strongly via direct tunneling $\sim t_c$, as captured by Eq. (3.4). In order to control these hopping matrix elements independently, we consider the application of an additional magnetic driving field at frequency $\omega_2 \neq \omega$ which effectively couples different spin states (at adjacent lattice sites), thus increasing the hopping parameter $t_\pm$ and at the same time also the ratio $t_{\mathrm{rat}} := t_\pm/t_c$. As outlined in Appendix 3.C, this introduces a second hopping term to the Fermi-Hubbard model in Eq. (3.4) and the resulting Hamiltonian can be written in a suitable co-rotating frame as

$$\begin{aligned} H_{\mathrm{FH2}} \;=\; & -t_c \sum_{\langle\langle i,j\rangle\rangle,s} (c_{is}^\dagger c_{js} + \mathrm{h.c.}) - t_\pm \sum_{\langle i,j\rangle,s} (c_{is}^\dagger c_{j\bar{s}} + \mathrm{h.c.}) \\ & + \sum_i \mu_i n_i + \sum_{s,s'} \sum_{ijkl} U_{ijkl} c_{is'}^\dagger c_{js}^\dagger c_{ls} c_{ks'}, \end{aligned} \tag{3.5}$$

where s and $\bar{s}$ denote opposite spins (i.e., $s = +$, $\bar{s} = -$ or vice versa).

The additional transverse driving field of strength $\sim \Omega_{\rm dr}$ has to be sufficiently small in order to be considered a perturbation to the magnetic-lattice Hamiltonian in Eq. (3.3); more precisely, we demand $\Omega_{\rm dr} \ll \Omega_0$. In general, the time-dependence and exact form of this spatially homogeneous field can be derived and reverse-engineered from the desired Hamiltonian in the adiabatic frame, see Appendix 3.C for further details. Since, in the tight-binding regime, next-nearest neighbour hopping is exponentially suppressed, weak driving fields $\Omega_{\rm dr}/\Omega_0 \ll 1$ are sufficient to reach situations where $t_\pm \gtrsim t_c$ and, typically, for moderate driving strengths direct tunneling processes $\sim t_c$ can be safely neglected [162]. In Fig. 3.2, it is shown how the ratio $t_{\rm rat}$ is affected by sweeping $\Omega_{\rm dr}/\Omega_0$ and Ω_0/Δ, while keeping the number of bound states $n_b \approx \sqrt{V_0/(4E_R)}$ at a constant value. Evidently, smaller driving fields $\Omega_{\rm dr}$ lead to smaller $t_\pm$. Moreover, at small $\Omega_0/\Delta \ll 1$ (i.e. deep in the perturbative regime), $t_{\rm rat}$ tends to decrease with increasing Ω_0/Δ. By choosing adequate driving fields, the tunneling matrix elements t_c and $t_\pm$ can thereby be independently tuned over a relatively wide range.

Spin-orbit interaction.—In the presence of strong spin-orbit interaction (SOI), transitions between different spin states at adjacent lattices sites can be induced (eventually, for strong enough SOI, without any external driving field) such that the Hubbard model in Eq. (3.4) may contain additional SOI-induced hopping terms. Specifically, SOI-induced hopping parameters can be estimated as $t_\pm^\lambda/E_{\rm R} \approx \lambda\sqrt{V_0 E_{\rm R}}\pi^2/a \exp\left(-\pi^2/16\sqrt{V_0/E_{\rm R}}\right)$, where $\lambda = \alpha_{\rm R}, \beta_{\rm D}$ denotes the Rashba and Dresselhaus coupling strengths, respectively. For realistic parameter values, this may give rise to $t_\pm^\lambda/t_c \gtrsim 1$ such that nearest and next-nearest neighbour hopping terms become comparable, see Sec. 3.5 for further details. Both the Rashba and Dresselhaus SOI strengths depend on the orientation of the lattice in the host material and can thereby induce anisotropic hopping. This gives access to a wider class of Hubbard models than those captured by Eq. (3.5).

3.4 Implementation: How to Meet the Requirements

In the following, we propose two experimental setups for the realization of our model. First, we consider magnetic field gradients provided by a classical current source as an example for a setup which can be operated both in a static ($\omega = 0$; compare Eq. (3.1)) or dynamic ($\omega > 0$) mode. Subsequently, we will discuss a purely dynamic (i.e., always $\omega > 0$) setup based on surface acoustic waves.

Superconducting circuit

As a first example for a realization of our model as described by Eq. (3.1), we consider SC circuits operating at GHz frequencies. The electrons are confined in a 2DEG at a distance d from a current-carrying wire, which is located above the surface. For our purposes, SC circuits and circuit resonators are attractive because of their capability to generate AC magnetic fields by carrying relatively large currents and the possibility to integrate them

in semiconductor nanostructures [239, 240]. In a simple toy model, we describe the circuit by a meandering wire carrying an AC current $\sim I_0 \cos(\omega t)$ through parallel sections of the wire separated by a lattice constant a, see Fig. 3.3(a) for an illustration of the setup. Note that, in principle, this setup can also be operated in the static regime ($\omega = 0$) when DC currents and, thus, time-*independent* fields are considered. The classical electric current density $\mathbf{J}$ induces a magnetic field which is calculated using the Biot-Savart law, see Fig. 3.3(b) for an exemplary field distribution as induced by a current source at fixed positions $\mathbf{r} = (0 < x < a, y = 0, 23.5 < z/a < 26.5)$ [242].

Here, we consider only one-dimensional trapping potentials in which the electrons are confined to a one-dimensional channel such that the y motional DOF is frozen out. Furthermore, we assume that the spatial extension of the meandering wire exceeds the size of the trapping region within the 2DEG, such that finite-size effects of the induced magnetic field can be neglected. This simplifies the mathematical description and we obtain the AC magnetic field distribution $\mathbf{B}_{\mathrm{AC}}(\mathbf{r}, t) = \Omega(\mathbf{r}) \cos(\omega t)\hat{\mathbf{x}}$ for a given wire geometry by summing up the induced fields of all parallel wire segments, see Fig. 3.3 [for details, cf. Appendix 3.D]. In the presence of an additional static homogeneous field $\mathbf{B}_{\mathrm{ext}} = B_{\mathrm{ext}}\hat{\mathbf{z}}$, the resulting Hamiltonian, $H(t) = \hat{p}^2/(2m) + \gamma(\mathbf{B}_{\mathrm{AC}}(\hat{\mathbf{r}}, t) + \mathbf{B}_{\mathrm{ext}}) \cdot \boldsymbol{\sigma}$, approximately coincides with our model in Eq. (3.1), where we can identify $\omega_0 = \gamma B_{\mathrm{ext}}$ and the amplitude Ω_0 of the Rabi frequency is given by

$$\Omega_0 = \gamma \frac{\mu_0 I_0 d}{\pi a^2} \sum_{n \in \mathbb{N}_0} \frac{(-1)^n}{(n + \frac{1}{2})^2 + \left(\frac{d}{a}\right)^2}. \tag{3.6}$$

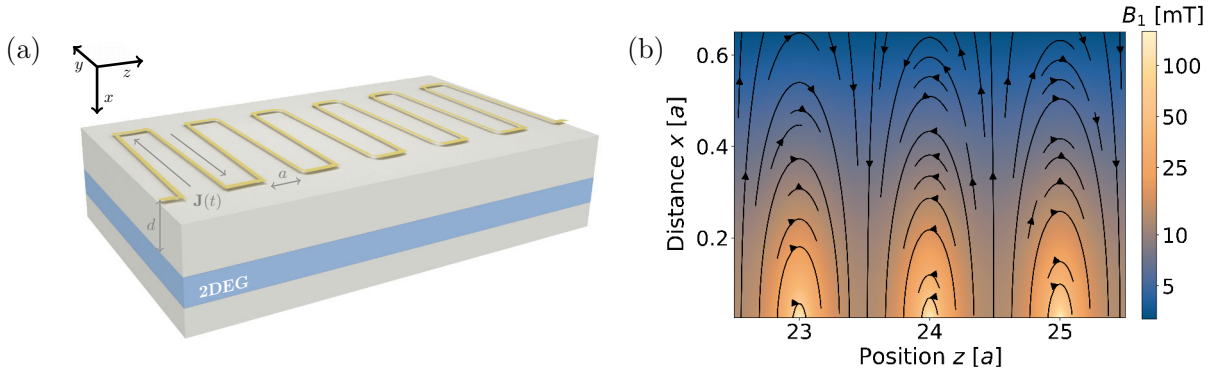

Figure 3.3: (color online). (a) Sketch of the meandering-wire setup. A current provides a magnetic field as described by the Biot-Savart law. At a distance $x = d$ from the surface, the two-dimensional electron gas is located (see text). (b) Magnetic field distribution for an example of a meandering nanowire that consists of $N = 50$ parallel wires which are separated by the lattice constant $a = 1$ μm. The vector field $\mathbf{B}_{\mathrm{AC}}(\mathbf{r}, t = 0)$ is shown and its scalar field $|\mathbf{B}_{\mathrm{AC}}|$ is plotted on a logarithmic scale. Magnetic field strenghts of the order of $B_1 \sim (10 - 50)$ mT are obtained in the proximity ($x \lesssim 0.6a = 600$ nm) of the wire. Other numerical parameters: $I_0 = 70$ mA at a current density $J_c = 30$ MA/cm^2 [241] and wire dimensions of 480 nm x 480 nm.

Eq. (3.6) becomes exact in the limit of an infinitely long wire and it converges to the numerically exact result in the limit of a long wire and in the center region below the wire [see App. 3.D for further details]; for all practical purposes, it yields sufficiently exact results for typical resonator geometries. The exact spatial pattern of the Rabi frequency $\Omega(\hat{z})$ depends on both the geometry of the resonator and the ratio d/a. Neglecting finite-size effects and for a perfectly periodic resonator geometry, the Rabi frequency can be approximately written as $\Omega(\hat{z}) = \Omega_0 \cos(\pi\hat{z}/a + \phi)$, see Appendix 3.D for further details.

Let us conclude the description of the proposed setup with a few general remarks. Firstly, we note that the calculation of the Hamiltonian results in an additional time-dependent term $\propto \sigma^z$ which we have neglected here and which is typically very small compared to the time-independent contribution from B_{ext}, see Appendix 3.D for more information. Secondly, the calculated RF field strength $B_1 \approx (10 - 50)$ mT [see Fig. 3.3(b)] at a given distance $d \lesssim 0.6a$ and given current intensity $I_0 = 70$ mA from the surface ranges from realistic to very optimistic values. The highest given values can only be obtained in close proximity to the surface. Moreover, the critical current density $J_{\text{c}} = 30$ MA/cm^2 [241] used in our calculations is optimistic because high ($\sim$ GHz) frequencies and strong ($\sim$ T) in-plane magnetic fields might reduce this value. However, especially the frequency dependence of J_{c} is still a current topic of research and, as noted earlier, the proposed setup may also be operated at $\omega = 0$, i.e., with DC currents. For g-factors ~ 15 (e.g., in InAs-based quantum wells), the given range of field strengths amounts to trap depths $V_0 \lesssim (4 - 22)\ \mu\text{eV} = k_{\text{B}} \cdot (46 - 255)$ mK. An explicit case study for specific material parameters follows in Sec. 3.5, where we check when the requirements set by Eq. (3.2) can be fulfilled. Finally, we stress that the relevant system parameters from Eq. (3.2) do not depend on the material choice (except for the g-factor of the quantum well) and due to its simplicity, the setup can, in principle, readily be implemented in an experiment. While the trap depth V_0 is tunable, the geometry is predefined in this setup, and therefore the lattice constant a (thus also the ratio d/a) is fixed. In the following, we will discuss an implementation which overcomes this limitation by construction, allowing for more widely tunable system parameters and lattice geometries.

Surface acoustic waves

As a second implementation, we discuss time-dependent ($\omega > 0$) magnetic field gradients induced by SAWs. In piezomagnetic materials which exhibit a significant (inverse) magnetostrictive effect, mechanical and magnetic DOFs are coupled which can be captured by the constitutive relations for magnetostriction, cf. Appendix 3.E. Specifically, the magnization $\mathbf{m}$ of a sample with non-zero magnetoelastic coupling changes due to mechanical stress applied to the material, which is described by a stress tensor $\underline{\underline{T}}$.

We consider a ferromagnetic film of thickness δ deposited on top of a SAW-carrying substrate, where the surface waves generate RF strain fields which, in turn, can induce magnetization dynamics in the ferromagnet and may thus provide strong time-dependent magnetic stray fields; for related experimental works, see Refs. [219, 243]. This setup is schematically shown in Fig. 3.4(a). Two counter-propagating SAWs, which can be launched from interdigital transducers (IDTs) patterned on top of the material, generate a standing-

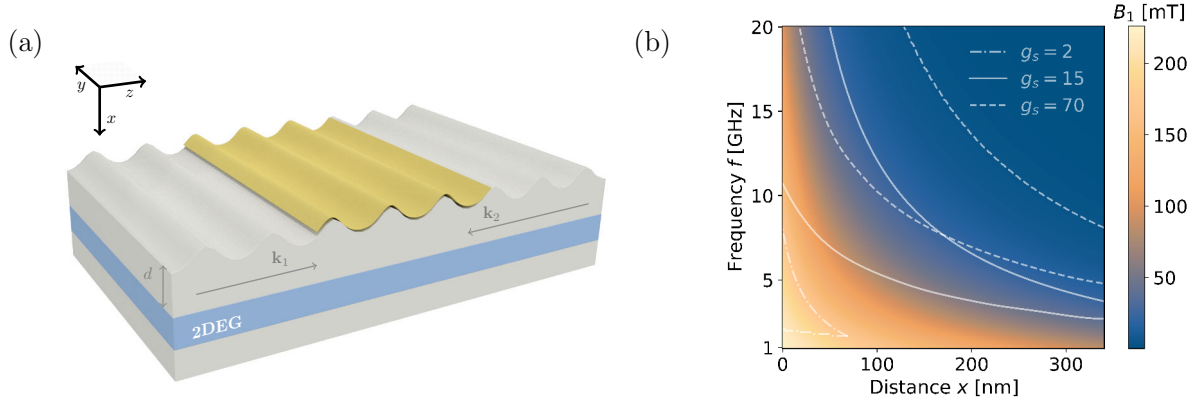

Figure 3.4: (a) Sketch of the SAW-based setup with a ferromagnetic film above the surface. Two counter-propagating SAWs generate standing-wave mechanical and magnetic field distributions. (b) Magnetic field strength B_1 as a function of distance x from the ferromagnetic film and SAW frequency f. The contour lines indicate the regions where $k_\mathrm{B}T = 1\mu\mathrm{eV} \ll \gamma B_1/2 \ll 2\pi f$ [see Eq. (3.2)] can be fulfilled for different g-factors: $g_\mathrm{s} = 2$ (dash-dotted lines), $g_\mathrm{s} = 15$ (solid lines), $g_\mathrm{s} = 70$ (dashed lines). Other numerical parameters: Speed of sound $v_\mathrm{s} = 3500$ m/s, film thickness $\delta = 25$ nm, saturation magnetization $\mu_0|\mathbf{m}_\mathrm{s}| = 1.8\,T$, strain amplitude $\varepsilon_{xx} = 2{\cdot}10^{-4}$, damping constant $\alpha = 0.01$, magnetoelastic constant $h = 10\,T$, g-factor of the ferromagnetic film $g_{\mathrm{s,FM}} = 2.1$.

wave pattern of both the mechanical field and induced spin wave, introducing a periodicity which defines the lattice constant $a = \lambda/2$ where λ is the SAW wavelength; the dispersion relation of the SAW, $\omega = 2\pi f = kv_s$, yields $\lambda = v_s/f$, where v_s denotes the speed of sound in the host material. This results in a spatially and time-periodic magnetic field as needed for the realization of Eq. (3.1). The coupled equations of motion for the (i) mechanical and (ii) magnetic field distributions can be described by (i) $\rho\ddot{u}_i = \partial T_{ij}/\partial z_j$, where ρ and $\mathbf{u}(\mathbf{x}, t)$ denote the mass density and the mechanical displacement vector, respectively, with the displacement u_i along the coordinate $\hat{z}_i$ $(= \hat{x}, \hat{y}, \hat{z})$ and (ii) the Landau-Lifshitz-Gilbert (LLG) equation, respectively. The latter describes the motion of the unitless magnetization direction $\mathbf{m}$ due to an effective magnetic field $\mathbf{H}_\mathrm{eff}$ and reads [244, 245]

$$\frac{\partial \mathbf{m}}{\partial t} = -\gamma \mathbf{m} \times \mu_0 \mathbf{H}_\mathrm{eff} + \alpha \mathbf{m} \times \frac{\partial \mathbf{m}}{\partial t}, \tag{3.7}$$

where μ_0 and α denote the magnetic constant and phenomenological Gilbert damping parameter, respectively, and $\mathbf{H}_\mathrm{eff}$ accounts for the SAW-induced magnetic field.

Given the effective magnetic field $\mathbf{H}_\mathrm{eff}$ at the ferromagnetic film $(x = 0)$ which is calculated from Eq. (3.7), we estimate the stray field at the 2DEG, see Appendix 3.E for details. The accessible range of field strenghts B_1 strongly depends on the specific material-dependent parameters, i.e., the saturation magnetization $\mathbf{m}_\mathrm{s}$, the damping parameter α, the g-factor $g_{\mathrm{s,FM}}$ and magnetoelastic constant h of the film and, moreover, the amplitude of the SAW-induced strain field. The latter is technically limited due to undesired heating

effects at too large amplitudes. Fig. 3.4(b) shows the RF field strength B_1 as a function of distance x from the ferromagnetic film and SAW frequency f. The numerical parameters are chosen such that they can be implemented in state-of-the-art experiments [see caption of Fig. 3.4]; note that even much higher strain amplitudes [246], magnetoelastic constants [243] and lower damping constants [247] have been realized in experiment, which renders our chosen set of parameters very realistic. As a result, we obtain strong driving fields $B_1 \approx (10-100)$ mT at given distance $x = (0.1-0.5)a$ from the film which amounts to trap depths $V_0 \lesssim (4-43)\,\mu$eV at $g_\mathrm{s} \sim 15$. However, for increasing frequencies $f \sim (10-50)$ GHz, the field strength decreases at fixed distance x. Hence, the lattice constant cannot be made arbitrarily small. In Sec. 3.5, we provide an overview of realistic parameter regimes (specifically, with a focus on Eq. (3.2)) based on the derived driving fields.

Strain-induced acoustic traps.—So far, we have neglected strain-induced deformation potentials and electric-field components generated in a piezoelectric host material. In principle, these electric fields couple to the motional DOF of a charged particle and thereby induced time-dependent electric potentials can either constitute stable traps or, if the driving amplitude of the electric field becomes too large, destabilize the motion of the electron [2]. In order to take both the electric and magnetic field-induced couplings to the external *and* internal DOFs into account, we extend our previous analysis to the more general model

$$\begin{aligned} H_\mathrm{hyb} &= \frac{\hat{p}^2}{2m} + V_\mathrm{SAW}\cos(k\hat{z})\cos(\omega t) \\ &\quad + \frac{\omega_0}{2}\sigma^z + \frac{\Omega_0}{2}\cos(k\hat{z})\cos(\omega t)\sigma^x, \end{aligned} \tag{3.8}$$

which contains a kinetic term, a time-dependent strain-induced potential of amplitude V_SAW and the remaining terms from the Hamiltonian in Eq. (3.1). Following the procedure outlined in Refs. [128, 129], we derive an effective time-independent Hamiltonian for the hybrid (strain-induced and magnetic) lattice by performing a high-frequency expansion of Eq. (3.8) in $1/\omega$. Starting from Eq. (3.8), we obtain an effective model of the form

$$H_\mathrm{hyb}^\mathrm{eff} = \frac{\hat{p}^2}{2m} + \frac{|\Delta|}{2}\tilde{\sigma}^z + \left[\frac{V_\mathrm{SAW}^2}{8E_\mathrm{S}} - \frac{\Omega_0^2}{4|\Delta|}\tilde{\sigma}^z\right]\sin^2(k\hat{z}), \tag{3.9}$$

with $E_\mathrm{S} = mv_s^2/2$. This result can be self-consistently verified in the limit $\Omega_0/|\Delta|, V_\mathrm{SAW}^2/(8E_\mathrm{S}^2) \ll 1$. The second term in Eq. (3.9) describes a spin-dependent energy offset [compare Fig. 3.1] and the third term is a spin-dependent effective potential.

From Eq. (3.9), by projecting onto the adiabatic eigenstates $|+\rangle_{\theta(\hat{z})}$ and $|-\rangle_{\theta(\hat{z})}$, respectively, we obtain the spin-dependent potential amplitudes, i.e., $V_0^- = \Omega_0^2/(4|\Delta|) + V_\mathrm{SAW}^2/(8E_\mathrm{S})$ and $V_0^+ = |\Omega_0^2/(4|\Delta|) - V_\mathrm{SAW}^2/(8E_\mathrm{S})|$. We can deduce that strain-induced and magnetic potentials add up constructively (destructively) for the $|-\rangle_{\theta(\hat{z})}$ ($|+\rangle_{\theta(\hat{z})}$) adiabatic potential. In Fig. 3.5 the effective trap depths for both spin components are shown as a function of Ω_0 and V_SAW. Since the strain-induced deformation potential is typically very weak [81, 110, 248], we consider the strain-induced potential $\sim V_\mathrm{SAW}$ to become important

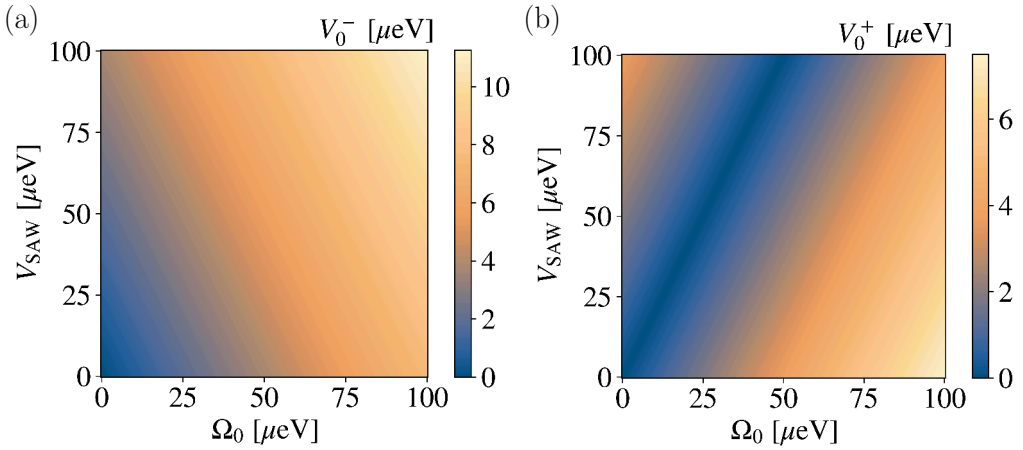

Figure 3.5: Spin-dependent trap depth of effective potential as given by Eq. (3.9) plotted as a function of Rabi frequency Ω_0 and strain-induced potential amplitude V_{SAW} for fixed $\Omega_0/|\Delta| = 0.3$ and $V_{\mathrm{SAW}}/E_{\mathrm{S}} = 0.3$. (a) Effective trap depth of hybrid trap for the $s = -$ spin component. The magnetic and strain-induced potentials add up and the effective potential becomes deeper if either the magnetic or strain contribution is increased. (b) Effective trap depth of hybrid trap for the $s = +$ spin component. The magnetic and strain-induced potentials have different signs. At $V_{\mathrm{SAW}} = 2\Omega_0$, the two potentials cancel each other.

only in piezoelectric materials. However, since the magnetic traps operate at relatively high strain amplitudes, in piezoelectric materials this contribution will typically not be negligible and also depends on the orientation of the magnetic lattice with respect to the crystalline structure of the piezoelectric host medium. More details on the derivation of Eq. (3.9) and a stability analysis of the time-dependent model Hamiltonian given in Eq. (3.8) can be found in Appendix 3.E.

3.5 Case Studies

Faithful implementation of magnetic traps.—As outlined above, a faithful implementation of magnetic traps is only possible if Eq. (3.2) can be fulfilled. This can be achieved in state-of-the-art experiments, e.g., in the setups discussed in Sec. 3.4, as we outline in the following: (*i*) The spontaneous phonon emission rate can be as low as $\gamma \sim 0.3$ μeV in InAs-based setups [249] and similar values are expected for InSb-based setups [250]. Even for much higher emission rates, the regime $\gamma \ll \omega_{\mathrm{HO}}$ can still be reached and, typically, $k_{\mathrm{B}}T \approx (1-10)$ μeV $\ll \omega_{\mathrm{HO}}$ imposes a stronger constraint on the minmum energy ω_{HO}. (*ii*) Based on the results shown in Figs. 3.3 and 3.4, Table 3.1 gives an overview of realistic Rabi frequencies Ω_0 in both described setups for different host materials [251]. Since the trap depth $V_0 \lesssim \Omega_0/2$ is limited from above by half of the Rabi frequency Ω_0, it is evident that relatively low-g_{s} materials, like, e.g., GaAs, do not prove to be promising

host material	$\lvert g_\mathrm{s}\rvert$	$\Omega_0^\mathrm{wire}[\mu\mathrm{eV}]$	$\Omega_0^\mathrm{SAW}[\mu\mathrm{eV}]$
GaAs	0.44	$\sim(0.3-1.3)$	$\sim(1.3-2.5)$
InAs	14.9	$\sim(8.6-43)$	$\sim(43-86)$
InSb	~ 70	$\sim(41-200)$	$\sim(200-410)$
DMS	$\sim(10^2-10^3)$	$\sim(58-2900)$	$\sim(290-5800)$
MoS_2	2.21	$\sim(1.3-6.4)$	$\sim(6.4-13)$
WS_2	2.84	$\sim(1.6-8.2)$	$\sim(8.2-16)$

Table 3.1: Estimates for achievable Rabi frequencies in both the nanowire and SAW setups. The table shows Rabi frequencies based on both state-of-the-art ($B_1^\mathrm{wire}=10\mathrm{mT}$, $B_1^\mathrm{SAW}=50\mathrm{mT}$) and more optimistic ($B_1^\mathrm{wire}=50\mathrm{mT}$, $B_1^\mathrm{SAW}=100\mathrm{mT}$) maximum driving field strengths [compare Figs. 3.3 and 3.4].

candidates for magnetic trapping as described in Sec. 3.3 since, in particular, the condition $k_\mathrm{B}T \ll V_0 \lesssim \Omega_0/2$ from Eq. (3.2) cannot be fulfilled easily. Assuming thermal energies $k_\mathrm{B}T \approx (1-10)\ \mu$eV, a comparison with the data shown in Table 3.1 suggests that a faithful implementation of magnetic traps should be feasible with state-of-the-art experiments using materials with moderate (e.g., TMDs like MoS_2 or WS_2) to relatively high g-factors $\lvert g_\mathrm{s}\rvert \gtrsim 15$ (as can be found, e.g., in III-V semiconductors like InAs or InSb). Only then, thermal stability as required by Eq. (3.2) can be guaranteed. (*iii*) Given that trap depths of the order of $V_0 \sim 100\ \mu$eV may be reached in SAW-based setups at $\lvert g_\mathrm{s}\rvert \gtrsim 15$, the requirements $k_\mathrm{B}T \ll \omega_\mathrm{HO} \lesssim V_0 < \omega/2$ can be fulfilled at oscillator frequencies $\omega_\mathrm{HO} \gtrsim 5\ \mu$eV ($\gtrsim 7.5$ GHz). In this parameter regime, accordingly, the trap can support a couple of bound states $n_b \approx 1-5$. (*iv*) Moreover, as discussed in detail in Sec. 3.3, high driving frequencies $f = \omega/(2\pi) \gtrsim 10$ GHz are another important bottleneck towards the experimental realization of reliable magnetic traps; these can be provided by both the proposed nanowire and SAW-based setups, as has been experimentally demonstrated, reaching ultra-high frequencies $f \approx 25$ GHz ($\omega \approx 103\ \mu$eV) [119]. Using existing technology, as indicated, e.g., by the solid lines in Fig. 3.4, experiments could therefore be operated in a regime where $\Omega_0 \lesssim \omega$ (and even the more demanding requirement (within RWA) $\Omega_0 \ll \omega$) is clearly fulfilled. (*v*) 2DEGs in InAs-based quantum wells can have a long mean-free path of the order of a few μm [252, 253] which is much larger than a lattice spacing of a few hundred nm. This provides optimism that disorder may not become too large in some of the high g-factor materials considered here, cf. also Ref. [2] for a more detailed discussion on the role of disorder in related systems.

Parameter regimes for Fermi-Hubbard physics in magnetic lattices.—Typical tunneling rates t_c in magnetic lattices (as described in Sec. 3.3) can reach values of a couple of μeV as discussed below. By sufficiently screening the Coulomb interaction, e.g., with the aid of a metallic screening layer [120], we may enter a parameter regime where both $t_c \gg k_\mathrm{B}T$ and $U \approx 10t_c$ can be reached simultaneously which itself is interesting for studying phenomena of quantum magnetism [108]. Furthermore, we introduced in Sec. 3.3 the possibility to enrich the standard Fermi-Hubbard model, typically including only tunneling

processes between adjacent lattice sites, by the application of additional driving fields [see also Appendix 3.C], thus allowing for independent tuneability of the hopping parameters t_c and $t_\pm$. Weak driving fields $\Omega_{\rm dr} \ll \Omega_0$ already give access to all the different regimes $t_\pm \ll t_c$, $t_\pm \approx t_c$ and $t_\pm \gg t_c$.

For SOI-induced hopping process $\sim t_\pm^\lambda$, we estimate that $t_\pm^\lambda \sim 50$ μeV can be reached at lattice spacings of a few 100 nm in InAlAs/InGaAs quantum wells where the Dresselhaus SOI is mostly negligible [254] and the Rashba parameter is given by $\alpha_{\rm R} \approx 10^4$ m/s [255]. Note that this value depends very strongly on the host material and, naturally, in some materials both the Rashba and Dresselhaus couplings become important which can induce significant anisotropies [110]. Most notably, this shows that the parameter regime $t_\pm^\lambda \gtrsim t_c$ is accessible and the next-nearest neighbour tunneling processes may become important even without the application of any additional driving fields.

Within our tight-binding model where we consider the limit $V_0 \gg E_{\rm R}$, $\omega_{\rm HO}$ is typically of the order of a few recoil energies [108]. Considering, e.g., InAs or InSb as host materials, the effective electron mass becomes relatively small, i.e., $m_{\rm InAs} = 0.023 m_0$ and $m_{\rm InSb} = 0.014 m_0$, both expressed in terms of the electron's rest mass m_0 [256]. Then, only relatively large lattice spacings $a \gtrsim 1$ μm give rise to small recoil energies $E_{\rm R} \ll V_0$. In turn, much smaller lattice spacings $a \gtrsim 300$ nm can be self-consistently achieved in TMD-based setups, where, e.g., $m_{\rm MoSe2} = 0.67 m_0$.

Spin relaxation and dephasing.—The specific value for the spin relaxation time T_1 is material-dependent. Generically, however, T_1 can be very long ($T_1 \sim 10$ ms), as is well known from spin relaxation measurements in quantum dots [257, 258]. Therefore, on the relevant timescales considered here, spin relaxation can be largely neglected, allowing for the faithful realization of spinful (two-species) magnetic lattices. Only in the presence of very strong magnetic fields, care must be taken to avoid too fast spin relaxation, since $1/T_1 \sim B_0^5$ [259]. Conversely, spin dephasing times $\sim T_2^\star$ tend to be much shorter than T_1. In InAs [260] and InSb [261], e.g., values of $T_2^\star \sim 10$ ns have been reported. While spin dephasing should not affect our ability to magnetically *trap* single electrons, the observation of coherent (many-body) spin physics may be severely limited by electron spin decoherence, since the many-body wavefunction of N electrons will dephase on a timescale set by $\sim T_2^\star/N$.

Specific examples: InAs and InSb.—Finally, we discuss the full set of relevant system parameters for two specific material choices, i.e., InAs-based and InSb-based setups. In the following, we assume dilution-fridge temperatures $T = 10$ mK, i.e., $k_{\rm B}T \approx 1$ μeV. Hence, the spontaneous phonon emission rate given above fulfills $\gamma \sim 0.3$ μeV $< k_{\rm B}T$, underlining that a low γ is expected to set the smallest energy scale in Eq. (3.2) if thermal stability ($k_{\rm B}T \ll \omega_{\rm HO}, V_0$) is ensured. First, we consider electrons in InAs with an effective mass $m = 0.023 m_0$. For $\Omega_0 = 86$ μeV [compare Table 3.1] and small detunings $|\Delta| \ll \Omega_0$, we can reach trap depths $V_0 \approx 43$ μeV which ensures thermal robustness of the trap at considered temperatures. Operating at a high frequency $f = 22$ GHz, the highest energy scale in Eq. (3.2) is set by $\omega \approx 92$ μeV at a lattice spacing $a = 900$ nm. For self-consistency, we check that the recoil energy is given by $E_{\rm R} \approx 20$ μeV which means that we are not deep in the tight-binding limit ($E_{\rm R} \ll V_0$). Still, the tunneling parameter can be estimated as

$t_c \approx 5.2$ μeV [108]. Note that, in this setting ($|\Delta| \ll \Omega_0$), the harmonic approximation around a local potential minimum is typically not well justified. Secondly, we consider heavy holes in InAs with an effective mass $m = 0.836 m_0$. For an ambitious Rabi frequency $\Omega_0 = 100$ μeV and a large detuning $\Delta = 380$ GHz $= 250$ μeV, we obtain a trap depth $V_0 = |\max_z \varepsilon(\hat{z}) - \min_z \varepsilon(\hat{z})| \approx \Omega_0/10 = 10$ μeV. Operating at a high SAW frequency $f = 25$ GHz, we obtain $\omega \approx 103$ μeV at a lattice spacing $a = 500$ nm and $v_s = 25$ km/s. Hence, the recoil energy is given by $E_\mathrm{R} \approx 1.8$ μeV which ensures the validity of the tight-binding approximation. Since the harmonic approximation, $\varepsilon(\hat{z}) \propto \Omega^2(\hat{z}) \propto \hat{z}^2$, is well justified in this case, we estimate $m\omega_\mathrm{HO}^2 \hat{z}^2/2 \approx \Omega(\hat{z})^2/(4|\Delta|)$, i.e.,

$$\omega_\mathrm{HO} = 118 \text{ MHz} \times \sqrt{\frac{\left(g_s[g_0]\right)^2}{m[m_0]}} \times \frac{B_1\,[\mathrm{mT}]}{a\,[\mu\mathrm{m}]\,\sqrt{|\Delta[\mathrm{GHz}]|}},$$

where $g_0 = 2$ denotes the g-factor of the free electron. Accordingly, we obtain $\omega_\mathrm{HO} = 5.4$ μeV for heavy holes in InAs, as considered here. Hence, all conditions imposed by Eq. (3.2) are fulfilled. In this scenario, the tunneling parameter amounts to only $t_c \approx 0.2$ μeV. However, the second hopping parameter introduced in Sec. 3.3, $t_\pm$, can be significantly enhanced such that $t_\pm \gg t_c$ with the aid of additional driving fields, as discussed in more detail in Appendix 3.C. Thirdly, we consider heavy holes in InSb with an effective mass $m = 0.627 m_0$. For a Rabi frequency $\Omega_0 = 200$ μeV [compare Table 3.1] and a relatively small detuning $\Delta = 38$ GHz $= 25$ μeV, we obtain a trap depth $V_0 \approx 90$ μeV. Assuming a very high (SAW) frequency $f = 50$ GHz, we obtain $\omega \approx 207$ μeV at $a = 100$ nm and (in the SAW implementation) $v_s = 10$ km/s. The recoil energy is then given by $E_\mathrm{R} \approx 60$ μeV. The tunneling parameter can be estimated as $t_c \approx 18$ μeV.

Altogether, these considerations clearly suggest that thermally stable and well-performing magnetic traps may be implemented with current technology; more specifically, fulfilling Eq. (3.2) should be possible in host materials possessing high enough g-factors. Furthermore, note that the values presented in Table 3.1 might be further enhanced; in the SAW setup, the values calculated in Sec. 3.4 have been derived assuming a magnetoelastic constant $h = 10$ T and strain amplitudes $\varepsilon_{xx} = 2 \cdot 10^{-4}$, which both may be elevated further in experiment, yielding even higher Rabi frequencies than the ones given in Table 3.1.

3.6 Conclusions and Outlook

To summarize, we have proposed magnetic traps and scalable lattices for electrons in semiconductors. Firstly, we have derived a general theoretical framework fit to characterize the traps and parameter regimes in which they can be operated under realistic experimental conditions and at dilution-fridge temperatures. Secondly, we have described two possible platforms suitable for an experimental demonstration of thermally stable magnetic traps and, eventually, coherent lattice physics in scalable arrays of magnetic traps. The developed model which is based on a periodically modulated AC Stark shift induced by magnetic RF fields is reminiscent of the working principle of optical lattices; moreover, very much

in analogy to experiments performed with ultracold atoms in optical lattices, the SAW setup offers similarly attractive features such as *in-situ* tunable system parameters and favourable scaling properties. Furthermore, the applicability of the derived results is not limited to electron traps but is more general; in principle, all generalizations to quasiparticles with an internal level structure that can be used to realize the model from Eq. (3.1) are candidates for a realization of the proposed magnetic traps. Quantitatively, the projected trap depths should allow for the implementation of thermally robust and low-loss magnetic traps with state-of-the-art technology and high g-factor materials such as InAs, InSb or dilute magnetic semiconductors. With the possibility to reach yet unexplored parameter values, especially in the low-temperature and strong-interaction regime of the Fermi-Hubbard model, solid-state magnetic lattices may constitute a novel platform for studying superfluidity, quantum magnetism and strongly correlated electrons in periodic systems.

Finally, we discuss possible future research directions. (*i*) By contrast with effectively one-dimensional systems discussed in this work, two-dimensional lattices with vastly different geometries might be studied. Due to the flexibility of SAW-based setups, these lattice geometries could be altered during an experiment. By dynamically modulating the lattice, this may allow for the investigation of intricate band structures or resonant coupling between different Bloch bands, akin to experiments with shaken optical lattices [262, 263, 264, 265]. (*ii*) Instead of considering electrons with two Zeeman-split internal spin states, quasiparticles with a richer internal energy-level structure might be examined (e.g., spin-3/2 holes). Here, one interesting prospect could be the realization of tunable subwavelength potential barriers for quasiparticles on the nanoscale, in close analogy to dark-state optical lattices with subwavelength spatial structure [266, 267]. (*iii*) Apart from the two possible implementations studied in this work, other implementations may be considered, either as stand-alone alternatives or in combination with, e.g., SAWs. Specifically, nanoengineered vortex arrays have been considered in the past both for magnetic atom traps [217] and strong magnetic modulations of Bloch electrons in 2DEGs [268]. (*iv*) Since we have only considered one-dimensional lattices, anisotropies of system parameters were negligible so far. In contrast, in two-dimensional systems, anisotropic effective electron masses or g-factors can lead to strongly non-uniform potential landscapes and anisotropic tunneling matrix elements. Besides that, SOI can itself be a strongly anisotropic interaction, thus modulating the SOI-induced hopping amplitude $t_{\pm}^{\lambda}$ ($\lambda = \alpha_{\mathrm{R}}, \beta_{\mathrm{D}}$ in the presence of Rashba or Dresselhaus SOI, respectively) in a way that it becomes anisotropic. In this way, the effect of anisotropic hopping on the phase diagram of a (spin-dependent) Fermi-Hubbard model might be studied, inheriting its rich physics from a number of versatile material properties.

Appendices

3.A Beyond the Rotating-Wave Approximation

A fundamental limitation in the above discussion stems from the condition $\Omega_0 \ll \omega$ necessary for the RWA to be justified. Due to this restriction, Rabi frequencies, and hence ultimately the trap depths, are limited to values much smaller than the driving frequency ω. One way to lift this built-in restriction is to drop the RWA, keeping counter-rotating terms $\propto \Omega(\hat{z})\sigma^{\pm}e^{\pm 2i\omega t}$ in the Hamiltonian Eq. (3.1) which can be written in a rotating frame as

$$H = \Delta\sigma^z + \frac{\Omega(\hat{z})}{2}\sigma^x + \frac{\Omega(\hat{z})}{2}\left(\sigma^+ e^{2i\omega t} + \sigma^- e^{-2i\omega t}\right). \tag{3.10}$$

If we now consider the corresponding time-evolution operator evaluated at stroboscopic times $t_n = t_0 + nT/2$ with $T = 2\pi/\omega$,

$$U(t_n) = \mathcal{T}_{\leftarrow} \exp\left(i\int_{t_0}^{t_n} \mathrm{d}\tau H(\tau)\right), \tag{3.11}$$

a Magnus expansion [269] up to second order in $1/\omega$ yields

$$U(t_n, t_0) = \exp\left(-iH_F[t_0]nT/2\right), \tag{3.12}$$

with the stroboscopic Floquet Hamiltonian H_F given by

$$H_F = H_F^{(0)} + H_F^{(1)} + H_F^{(2)} + ..., \tag{3.13}$$

with the three lowest-order contributions

$$H_F^{(0)} = \frac{\Delta}{2}\sigma^z + \frac{\Omega(\hat{z})}{2}\sigma^x, \tag{3.14}$$

$$H_F^{(1)} = \frac{\Omega(\hat{z})}{16\omega}\left(2\Delta\sigma^x - \Omega(\hat{z})\sigma^z\right), \tag{3.15}$$

$$H_F^{(2)} = -\frac{\Omega(\hat{z})}{64\omega^2}\left(4\Delta^2 + \Omega^2(\hat{z})\right)\sigma^x. \tag{3.16}$$

Numerical results of the dynamics generated by the zeroth- and second-order results are compared with the dynamics generated by the full time-dependent Hamiltonian [the internal Hamiltonian h in Eq. (3.1), without RWA] in Fig. 3.6. From the numerical results we conclude that the (stroboscopic) characterization of the system dynamics by H_F works well only if $\Omega_0 \lesssim \omega$. In this regime, even at higher orders we still obtain a time-independent periodic Hamiltonian which allows for the implementation of magnetic (super-)lattices.

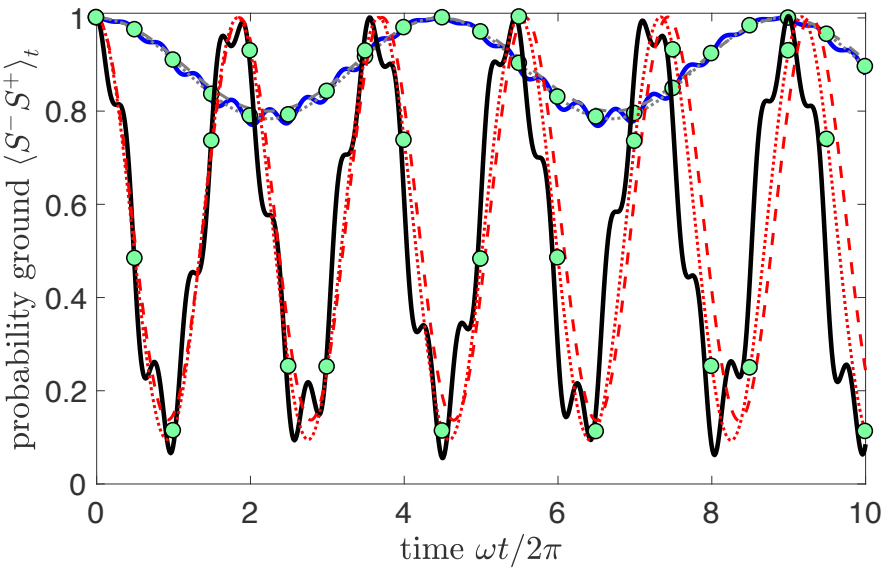

Figure 3.6: (color online). Numerical simulation of the dynamics generated by the time-dependent (i.e., without any RWA) Hamiltonian (3.1) for $\Omega(\hat{z}) = \Omega_0 = 0.1\omega$ (blue solid line) and $\Omega_0 = 0.5\omega$ (black solid line), respectively. The corresponding dashed (dotted) lines refer to the dynamics generated by the time-independent zeroth-order (second-order) Floquet Hamiltonian H_F, with dots highlighting the results according to the second-order Floquet Hamiltonian H_F at stroboscopic times $t_n = nT/2$. The initial state has been set as $|\Psi\rangle_0 = |\downarrow\rangle$. Other numerical parameters: $\Delta/\omega = 0.2$.

3.B Spin-Flip Transitions in Magnetic Traps and Lattices

Based on Ref. [233], we investigate undesired spin-flip losses from a magnetic trap. We consider the model

$$H = \frac{\hat{p}^2}{2m} + \omega_0 \sigma^z + \Omega(\hat{z}) \cos(\omega t) \sigma^x, \tag{3.17}$$

which, in a rotating frame and within a rotating-wave approximation, can be written as

$$H = \frac{\hat{p}^2}{2m} + \Delta \sigma^z + \frac{\Omega(\hat{z})}{2} \sigma^x = \hat{T} + h(\hat{z}), \tag{3.18}$$

where $\hat{T} = \hat{p}^2/(2m)$ and

$$h(\hat{z}) = \frac{1}{2} \begin{pmatrix} \Delta & \Omega(\hat{z}) \\ \Omega(\hat{z}) & -\Delta \end{pmatrix}. \tag{3.19}$$

We introduce a unitary operator $U(\hat{z}) = \exp(-i\frac{\theta(\hat{z})}{2}\sigma^y)$ acting on the internal states such that

$$\begin{aligned} |+\rangle_\theta &= U(\hat{z})|\uparrow\rangle, \\ |-\rangle_\theta &= U(\hat{z})|\downarrow\rangle. \end{aligned} \tag{3.20}$$

Note that $U^\dagger(\hat{z})$ rotates the effective magnetic field to be parallel to the z axis. The transformed Hamiltonian $\tilde{H}$ takes the form

$$\begin{aligned}\tilde{H} &= U^\dagger(\hat{z})HU(\hat{z}) \\ &= \hat{T} + \left[U^\dagger(\hat{z})\hat{T}U(\hat{z}) - \hat{T}\right] + U^\dagger(\hat{z})\left[h(\hat{z})\right]U(\hat{z}) \\ &= \hat{T} + \Delta T + \varepsilon(\hat{z})\tilde{\sigma}^z,\end{aligned} \tag{3.21}$$

where $\Delta T = \left[U^\dagger(x)\hat{T}U(x) - \hat{T}\right]$, $\varepsilon(\hat{z}) = \frac{1}{2}\sqrt{\Delta^2 + \Omega^2(\hat{z})}$ and $\tilde{\sigma}^z = |+\rangle\langle+| - |-\rangle\langle-|$. The adiabatic approximation amounts to neglecting the contribution which stems from ΔT [233]. This is justified provided that $\chi = \omega_{\rm HO}/|\Delta| \ll 1$, i.e., that the potentials defined by ε and $-\varepsilon$ are sufficiently separated in energy.

3.C Spin-Flip Assisted Tunneling Processes in Magnetic Lattices

In Eq. (3.5) in the main text, we present an extended Hubbard model which includes both next-nearest (spin-conserving) neighbour hopping ($\sim t_c$, compare with Eq. (3.4)) and nearest neighbour (spin-flip assisted) hopping ($\sim t_\pm$) processes. In the following, we show how this Hamiltonian and, more specifically, the additional hopping term $\sim t_\pm$ can be constructed with the aid of additional RF driving fields.

Starting from Eq. (3.1), we consider two auxiliary time-dependent fields in addition to the field $\mathbf{B}(\mathbf{r}, \omega t)$: (i) The driving field $\mathbf{B}_{\rm dr}(t) = B_{\rm dr}\cos(\omega_2 t)\hat{\mathbf{x}}$, a second rapidly oscillating transverse field, is weaker than the RF field $\mathbf{B}_\perp(\mathbf{r}, \omega t)$ which provides the lattice and detuned from it so as to be resonant with the energy difference between the two local spin directions. (ii) The third time-dependent field $\mathbf{B}_3 = B_3\cos(\omega_3 t)\hat{\mathbf{z}}$ is slowly varying and parallel to the constant field $\mathbf{B}_{||}$ which provides the Zeeman splitting; its purpose is to (partially) compensate the longitudinal components that $\mathbf{B}_{\rm dr}$ acquires in the adiabatic frame.

In the presence of these additional fields, two new terms appear in the model of Eq. (3.1),

$$H_{\rm dr} = \frac{\hat{p}^2}{2m} + \omega_0\sigma^z + \Omega(\hat{z})\cos(\omega t)\sigma^x + \Omega_{\rm dr}\cos(\omega_2 t)\sigma^x + \Omega_3\cos(\omega_3 t)\sigma^z, \tag{3.22}$$

where $\Omega_{\rm dr} = \gamma B_{\rm dr}$ and $\Omega_3 = \gamma B_3$. In the following, we require $\omega, \omega_2 \gg |\omega - \omega_2| \equiv \delta \approx \omega_3$ as well as $|\Omega_0| \gg |\Omega_{\rm dr}|, |\Omega_3|$.

Defining a rotating frame by $|\psi_t^{\rm rot}\rangle = U_t\,|\psi_t\rangle$ (where $|\psi_t\rangle$ denotes a solution of the Schrödinger equation in the lab frame) with $U_t = \exp(it\omega\sigma^z)$, we obtain the Hamiltonian

in the rotating frame as

$$H_{\rm dr}^{\rm rot} = \frac{\hat{p}^2}{2m} + \Delta\sigma^z + \frac{\Omega(\hat{z})}{2}\sigma^x + \frac{\Omega(\hat{z})}{2}\left[|\uparrow\rangle\langle\downarrow| e^{i2\omega t} + \text{h.c.}\right] + \frac{\Omega_{dr}}{2}\left[|\uparrow\rangle\langle\downarrow| (e^{i\delta t} + e^{i(\omega+\omega_2)t}) + \text{h.c.}\right] + \Omega_3\cos(\omega_3 t)\sigma^z. \tag{3.23}$$

Within a RWA, where we keep only the constant and slowly oscillating terms, we obtain

$$H_{\rm dr}^{\rm rot} = \frac{\hat{p}^2}{2m} + \Delta\sigma^z + \frac{\Omega(\hat{z})}{2}\sigma^x + \frac{\Omega_{dr}}{2}\left[e^{i\delta t}|\uparrow\rangle\langle\downarrow| + \text{h.c.}\right] + \Omega_3\cos(\omega_3 t)\sigma^z. \tag{3.24}$$

Now, by employing the unitary transformation $U(\hat{z})$ introduced in the main text, we can (locally) diagonalize the constant contribution stemming from $\hat{p}^2/(2m) + h_{\rm RWA}(\hat{z})$ [see Sec. 3.3]. Then, neglecting the non-adiabatic correction due to ΔT and simplifying the resulting expressions yields

$$\begin{aligned}\tilde{H} = &\frac{\hat{p}^2}{2m} + \varepsilon(\hat{z})\tilde{\sigma}^z \\ &+ \left[\frac{\Omega_{\rm dr}}{2}\cos^2\vartheta\cos(\delta t) - 2\Omega_3\sin\vartheta\cos\vartheta\cos(\omega_3 t)\right]\tilde{\sigma}^x \\ &+ \left[2\Omega_{\rm dr}\sin\vartheta\cos\vartheta\cos(\delta t) + \Omega_3(\cos^2\vartheta - \sin^2\vartheta)\cos(\omega_3 t)\right]\tilde{\sigma}^z,\end{aligned} \tag{3.25}$$

where $\vartheta := \theta(\hat{z})/2 = \arcsin[\frac{\Omega(\hat{z})}{\sqrt{\Omega^2(\hat{z})+\Delta^2}}]/2$ and $\tilde{\sigma}^z = |+\rangle\langle+| - |-\rangle\langle-|$, $\tilde{\sigma}^x = |+\rangle\langle-| + |-\rangle\langle+|$. Clearly, in comparison with Eq. (3.3), we get additional contributions due to the additional time-dependent fields.

We now use the fact that the newly introduced driving fields are relatively weak compared to the fields considered in the main text and treat these terms as a perturbation to the tight-binding model in Eq. (3.4). Furthermore, from Eq. (3.25), it becomes clear that the third driving field $\mathbf{B}_3$ can be used to compensate for undesired (time-dependent) on-site terms due to $\mathbf{B}_{\rm dr}$. At the resonance $\omega_3 = \delta$ and within a rotating frame $U_t^{\rm rot2} = \exp(it\delta\tilde{\sigma}^z)$, the Hamiltonian (3.25) can be further simplified and a RWA with respect to 2δ can be performed, given that the off-resonant spin-flip terms oscillate much faster than their strength. Eventually, we obtain the extended Fermi-Hubbard model

$$\begin{aligned}H_{\rm FH3} &= -t_c\sum_{\langle\langle i,j\rangle\rangle,s}(c_{is}^\dagger c_{js} + \text{h.c.}) - t_\pm\sum_{\langle i,j\rangle,s}(c_{is}^\dagger c_{j\bar{s}} + \text{h.c.}) \\ &\quad + \sum_{i,s}\mu_{is}n_{is} + \sum_{s,s'}\sum_{ijkl}U_{ijkl}c_{is'}^\dagger c_{js}^\dagger c_{ls}c_{ks'},\end{aligned} \tag{3.26}$$

which reduces to Eq. (3.5) at the resonance $\delta = \Delta$. Here, the nearest-neighbour tunneling is characterized by $t_\pm = \langle w_j|\frac{\Omega_{\rm dr}}{2}\cos^2\vartheta - 2\Omega_3\sin\vartheta\cos\vartheta|w_{j+1}\rangle$ with the Wannier function w_j located at lattice site j.

3.D Implementation I: Superconducting Circuit

In the following, we describe the magnetic field due to an electric current density $\mathbf{J}$ by the Biot-Savart law. Since we are dealing with AC fields, this description can only be approximately valid. A more precise picture follows from the Jefimenkov equations [270]:

$$\mathbf{B}_{\mathrm{AC}}(\mathbf{r},t) = \frac{\mu_0}{4\pi}\int_V \mathrm{d}^3\mathbf{r}' \left(\mathbf{J}(\mathbf{r}',t_{\mathrm{ret}}) \times \frac{\mathbf{r}-\mathbf{r}'}{|\mathbf{r}-\mathbf{r}'|^3} + \frac{1}{c}\frac{\partial \mathbf{J}(\mathbf{r}',t_{\mathrm{ret}})}{\partial t} \times \frac{\mathbf{r}-\mathbf{r}'}{|\mathbf{r}-\mathbf{r}'|^2}\right). \tag{3.27}$$

where the right-hand side of the equation is evaluated at the retarded time $t_{\mathrm{ret}} = t - |\mathbf{r} - \mathbf{r}'|/c$ and c denotes the speed of light in the dielectric medium. However, since the time-dependence of the current density $\mathbf{J}(\mathbf{r}',t) \sim \exp(i\omega t)$, the correction term in Eq. (3.27) is expected to be of the order of $|\mathbf{r}-\mathbf{r}'|\omega/c \sim d\omega/c$ with the distance d between meandering wire and 2DEG. The wires are located above the surface at $x = 0$. For typical distances $d \sim (0.1 - 1)$ μm and frequencies $\omega \sim (1 - 100)$GHz, the correction term in Eq. (3.27) may be neglected and the Biot-Savart law is recovered which then accurately describes the induced magnetic field due the electric current density $\mathbf{J}$,

$$\mathbf{B}_{\mathrm{AC}}(\mathbf{r},t) = \frac{\mu_0}{4\pi}\int_V \mathrm{d}^3\mathbf{r}'\ \mathbf{J}(\mathbf{r}',t) \times \frac{\mathbf{r}-\mathbf{r}'}{|\mathbf{r}-\mathbf{r}'|^3}. \tag{3.28}$$

In the following, we assume the spatial extension of the meandering wire to exceed the relevant size of the 2DEG, i.e., the trapping region. This assumption guarantees the absence of finite-size effects at the turning points of the meandering wire, i.e., we model each parallel line in the meandering wire as an infinite wire which induces a magnetic field on its own. Also, we neglect boundary effects from the border of the 2DEG. In the case of an infinitely long wire which runs parallel to the y axis (cf. Fig. 3.3), the Biot-Savart law simplifies to [270]

$$\mathbf{B}_{\mathrm{AC}}(\mathbf{r} = (\rho,\phi,y),t) = \frac{\mu_0 I(t)}{2\pi\rho}\mathbf{e}_\phi, \tag{3.29}$$

where $I(t)$ denotes the current in a single wire. In the presence of many parallel wires (whose current flow alternates between the $+y$ and $-y$ directions), which is the situation that accurately describes the setup sketched in Fig. 3.3, the magnetic field at point $\mathbf{r}$ is given by

$$\begin{aligned} \mathbf{B}_{\mathrm{AC}}(\mathbf{r} &= (x,y,z)) = -\sum_n^N \frac{\mu_0 \mathbf{I}_n(t)}{2\pi} \times \frac{\mathbf{r}_n}{\mathbf{r}_n^2} \\ &= \frac{\mu_0 I_0 \cos(\omega t)}{2\pi} \sum_n^N \frac{(-1)^n}{(z-na)^2 + x^2} \begin{pmatrix} x \\ 0 \\ z - na \end{pmatrix}, \end{aligned} \tag{3.30}$$

with the center of the wires positioned at $x = 0$ and given a time-dependent current amplitude $I(t) = I_0 \cos(\omega t)$ in each wire and the position vectors $\mathbf{r}_n$ which denote the position at which the field is evaluated relative to the nth wire. An exemplary field distribution

$\mathbf{B}_{\mathrm{AC}}(\mathbf{r}, t = 0)$ is shown in Fig. 3.3(b). Due to the translational symmetry along the axis parallel to the wires, Eq. (3.30) enables us to write the spin Hamiltonian, in the presence of an additional external magnetic field, as

$$\begin{aligned} H &= \gamma \mathbf{B}_{\mathrm{AC}}(\hat{\mathbf{r}}, t) \cdot \sigma + \gamma B_{\mathrm{ext}} \sigma^z \\ &= \frac{\gamma \mu_0 I_0}{2\pi} \sum_{n=1}^{N} \frac{(-1)^n x}{\hat{z}^2 - 2na\hat{z} + n^2a^2 + x^2} \sigma^x \cos(\omega t) \\ &\quad + \frac{\gamma \mu_0 I_0}{2\pi} \sum_{m=1}^{N} \frac{(-1)^m (\hat{z} - ma)}{\hat{z}^2 - 2ma\hat{z} + m^2a^2 + x^2} \sigma^z \cos(\omega t) \\ &\quad + \gamma B_{\mathrm{ext}} \sigma^z. \end{aligned} \tag{3.31}$$

The induced electric field due to a time-dependent magnetic field is described by Faraday's law, $\nabla \times \mathbf{E} = -\partial \mathbf{B}/\partial t$. By (anti-)symmetries of the straight long wire and its magnetic field — translations along the y axis, rotations about y axis, and the reflection $y \to -y$ —the induced electric field points in a direction parallel to the wire, i.e., along y. Hence, the induced electric field should not affect the magnetic lattice along z. The motional DOF along y could experimentally be frozen out, e.g., via the implementation of an etched channel.

We define $\omega_0 = g_{\mathrm{s}} \mu_{\mathrm{B}} B_{\mathrm{ext}}$ and rewrite (3.31) as

$$H = \left[\omega_0 + \Omega_0^z(\hat{z}) \cos(\omega t)\right] \sigma^z + \Omega_0^x(\hat{z}) \cos(\omega t) \sigma^x \tag{3.32}$$

Next, we take a closer look at the spatial profiles of the Rabi frequencies $\Omega_0^z(\hat{z})$ and $\Omega_0^x(\hat{z})$ in Eq. (3.32). The time-dependent field amplitudes in Eq. (3.32) can be exactly expressed via the Digamma function $\digamma$ (logarithmic derivative of the Γ function; [271, 272]). Denoting the two sums appearing there as b_x and b_z, respectively, setting $a = 1$ and using $\xi = -z + ix$, it holds that

$$\begin{aligned} b_z + i b_x &= -\frac{1}{2} \digamma\left(\xi/2 + \lfloor (N-1)/2 \rfloor + 1\right) + \frac{1}{2} \digamma(\xi/2) \\ &\quad + \frac{1}{2} \digamma\left([\xi + 1]/2 + \lfloor N/2 \rfloor\right) - \frac{1}{2} \digamma([\xi + 1]/2) \\ &\overset{N \to \infty}{=} \frac{1}{2} \left(\digamma(\xi/2) - \digamma([\xi + 1]/2)\right). \end{aligned} \tag{3.33}$$

For $N \gg z \gg 1$ the real and imaginary parts of this function are (approximately) periodic with period 1 and have zeros at integer (half-integer) values of z, respectively. For an odd number of wires, the z (x) field components are antisymmetric (symmetric) with respect to the axis $z = z_s \equiv (N-1)/2$; (for even N, B_z is symmetric and B_x antisymmetric). The fields are well approximated by $b_z + i b_x \propto \exp(-i\pi z)$, with errors less than 0.1% but not approaching zero as $N \gg z \to \infty$. Using properties of the Digamma function, we can write

$$b_z + i b_x = \frac{1}{2} \sum_{l=0}^{\lfloor N/2 \rfloor - 1} \frac{1}{l + (\xi + 1)/2} - \frac{1}{2} \sum_{l=0}^{\lfloor (N-1)/2 \rfloor} \frac{1}{l + \xi/2}. \tag{3.34}$$

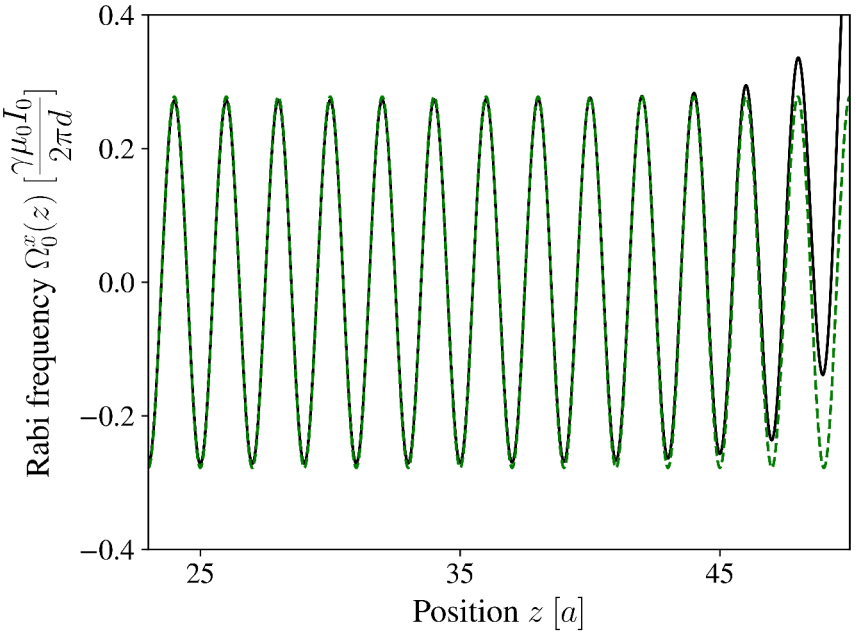

Figure 3.7: (color online). Spatial pattern of Rabi frequency (at given time), compare $\Lambda(\mathbf{x})$ in Sec. 3.3. *Black (solid):* calculated from Eq. (3.31), *green (dashed):* sin-fit. At the ends of the meandering wire, i.e. at the edges of the lattice, finite-size effects become apparent, but in the center of the lattice $\Lambda(\hat{z})$ is well-described by the sinusoidal fitting curve. Parameters: $d = a$ and $N = 50$ wires.

As shown in Fig. 3.7, the spatial dependence of $\Omega_0^x(\hat{z})$ and $\Omega_0^z(x)$ (not shown) can (depending on the choice of parameters) be well-described by a *sine* function. Hence, we can approximately write

$$H = \left[\omega_0 + \Omega_0^z \sin(\frac{\pi}{a}\hat{z} + \varphi)\cos(\omega t)\right]\sigma^z + \Omega_0^x \ \sin(\frac{\pi}{a}\hat{z})\cos(\omega t)\sigma^x, \tag{3.35}$$

where φ denotes a phase shift between $\Omega_0^x(\hat{z})$ and $\Omega_0^z(\hat{z})$.

In the center region, where finite-size effects are negligible, the Rabi frequencies Ω_0^x and Ω_0^z are approximately given by

$$\Omega_0^z = \gamma\frac{\mu_0 I_0}{\pi a}\sum_{n=0,1,..}\frac{(-1)^n\,(n+1/2)}{(n+1/2)^2+(d/a)^2}, \tag{3.36}$$

$$\Omega_0^x = \gamma\frac{d}{a}\frac{\mu_0 I_0}{\pi a}\sum_{n=0,1,..}\frac{(-1)^n}{(n+1/2)^2+(d/a)^2}. \tag{3.37}$$

The expressions (3.36) and (3.37) become exact in the limit of infinitely many wires, $N \to \infty$. For all practical purposes considered in this work, Ω_0^z is very small such that $\Omega_0^z \ll \omega_0$ and it may be safely neglected.

3.E Implementation II: Surface Acoustic Waves

Magnetization dynamics and effective magnetic field

The governing constitutive relations for magnetostriction [273] read (see also Chapter 1.3)

$$T_{ij} = c_{ijkl}u_{kl} - h_{kij}H_k, \tag{3.38}$$

$$B_{\mathrm{dr},i} = h_{ijk}u_{ik} + \mu_{ij}H_j, \tag{3.39}$$

where $\underline{\underline{T}}$, $\mathbf{B}_{\mathrm{dr}}$, $\mathbf{H}$ and $\underline{\underline{h}}$ denote the stress tensor, the magnetic induction, the magnetic field (intensity vector) generated by a magnetoelastic wave and the effective piezomagnetic tensor, respectively. μ is the magnetic permeability and the strain field is defined as $u_{kl}(\mathbf{x}) = (\partial u_k/\partial x_l + \partial u_l/\partial x_k)/2$.

Given Eq. (3.39), we provide an estimate for the effective driving field in the ferromagnet,

$$B_{\mathrm{dr},1} \approx hkU = 2\pi h\frac{U}{\lambda}, \tag{3.40}$$

where h denotes the magnetoelastic constant, k is the wavevector and U denotes the amplitude of the displacement field. For small strain-field amplitudes $kU \approx 10^{-6}$ and a magnetoelastic constant $h = 10$ T, this magnitude can be estimated as $B_{\mathrm{dr},1} \approx 25\ \mu$T [243].

At ferromagnetic resonance, the effective magnetic field can be significantly enhanced. The response of a ferromagnet to small time-varying magnetic fields can be described with the aid of Eq. (3.7). The resulting dynamical component of the magnetization $\mathbf{m}$ is given by

$$\mu_0|\mathbf{m}_{\mathrm{s}}|\mathbf{m} = \bar{\chi}\mathbf{B}_{\mathrm{dr}}, \tag{3.41}$$

where $\bar{\chi}$ denotes the Polder susceptibility which describes the magnetic response of a ferromagnet to small time-varying magnetic fields perpendicular to the magnetization equilibrium direction [243]. In practical terms this means that the resulting effective magentic field can be enhanced by about two orders of magnitude.

In a next step, the field at the 2DEG is then calculated from the field distribution at the ferromagnetic thin film by discretizing the field distribution at the film and summing up the dipole fields of these volume elements. At high strain amplitudes $kU \sim 10^{-4} - 10^{-3}$ and a magnetoelastic constant $h = (10 - 25)$ T, the relevant magnitude of the field at the 2DEG can be numerically estimated as $B_1 \sim (10 - 100)$ mT. In our numerical calculations, the amplitude of the displacement field, the magnetoelastic coupling constant and the wavevector are input parameters which determine the microwave field strength at the ferromagnetic layer.

Strain-induced potentials

Starting from Eq. (3.8) and in a suitable rotating frame, we obtain

$$\begin{aligned} H_{\mathrm{hyb}}^{\mathrm{rot}} &= \frac{\hat{p}^2}{2m} + V_{\mathrm{SAW}}\cos(k\hat{z})\cos(\omega t) \\ &\quad + \frac{\omega_0}{2}\sigma^z + \frac{\Omega(\hat{z})}{2}\left(\sigma^x + e^{2i\omega t}\sigma^+ + e^{-2i\omega t}\sigma^-\right), \end{aligned} \tag{3.42}$$

with $\sigma^+ = |\uparrow\rangle\langle\downarrow|$ and $\sigma^- = |\downarrow\rangle\langle\uparrow|$. Following the procedure outlined in Refs. [128, 129] and using results from [2], we derive an effective time-independent Hamiltonian up to second order in $1/\omega$ which reads

$$H_{\rm hyb}^{\rm eff} = \frac{\hat{p}^2}{2m} + \tilde{\varepsilon}(\hat{z})\tilde{\sigma}^z + \left(\frac{q^2}{8}E_{\rm S} + \frac{r}{4}|\Delta|\right)\sin^2(k\hat{z}), \tag{3.43}$$

with $\tilde{\varepsilon}(\hat{z}) = \frac{1}{2}\sqrt{\Omega^2(\hat{z}) + \tilde{\Delta}^2}$, $\tilde{\Delta} = |\Delta| + \Omega_0^2/(8E_{\rm S})$, $q = V_{\rm SAW}/E_{\rm S}$ and $r = \Omega_0^2/(4E_{\rm S}\Delta)$. For typical parameter values $r \ll 1$, $q^2/8 \ll 1$ and $\Omega_0 \ll |\Delta|$, we obtain the simplified form

$$H_{\rm hyb}^{\rm eff} \approx \frac{\hat{p}^2}{2m} + \frac{|\Delta|}{2}\tilde{\sigma}^z + \left[\frac{V_{\rm SAW}^2}{8E_{\rm S}} - \frac{\Omega_0^2}{4|\Delta|}\tilde{\sigma}^z\right]\sin^2(k\hat{z}), \tag{3.44}$$

which coincides with the result given in Eq. (3.9). Writing Eq. (3.44) in the form $H_{\rm hyb}^{\rm eff} = \hat{p}^2/2m + |\Delta|/2\tilde{\sigma}^z + V_{\rm hyb}\sin^2(k\hat{z})$, we find that the spin-dependent potential amplitudes read

$$\begin{aligned}
\langle +|V_{\rm hyb}|+\rangle &\approx \frac{\Omega_0^2}{4|\Delta|} - \frac{q^2}{8}E_{\rm S}, \\
\langle -|V_{\rm hyb}|-\rangle &\approx -\frac{\Omega_0^2}{4|\Delta|} - \frac{q^2}{8}E_{\rm S}.
\end{aligned} \tag{3.45}$$

The resulting trap depths are depicted in Fig. 3.5.

Stability analysis of hybrid magnetic and strain-induced traps

The discussion in this section completes the discussion of hybrid magnetic and strain-induced traps and is devoted to the stability analysis of such traps, meaning whether or not electrons can be trapped in time-dependent trapping potentials of the kind of those featured in Eq. (3.8).

Starting from Eq. (3.8), we would like to predict whether a given set of parameters $\{m,\ \omega,\ \omega_0,\ V_{\rm SAW},\ \Omega_0\}$ gives rise to a stable (hybrid strain-induced and magnetic) trap or not. To this end, we first derive the coupled Heisenberg equations of motion for the set of observables $\{\langle z\rangle, \langle p\rangle, \langle\sigma^x\rangle, \langle\sigma^y\rangle, \langle\sigma^z\rangle\}$ within a RWA.

Equations of motion.—In order to determine the EOMs of interest, we consider the time evolution ($\tau = \omega t/2$) of the operators $\tilde{z} := k\hat{z}, \tilde{p} := {\rm d}\tilde{z}/{\rm d}\tau, \sigma^x, \sigma^y, \sigma^z$ which is given by the Heisenberg EOMs,

$$\begin{aligned}
\langle\dot{\tilde{z}}\rangle &= \langle\tilde{p}\rangle, \\
\langle\dot{\tilde{p}}\rangle &= \frac{2\Omega_0}{E_S}\langle\sin(\tilde{z})\rangle\cos(2\tau) + \frac{V_{\rm SAW}}{2E_S}\langle\sin(\tilde{z})\rangle\langle\sigma^x\rangle, \\
\langle\dot{\sigma}^x\rangle &= -2\frac{\Delta}{\omega}\langle\sigma^y\rangle, \\
\langle\dot{\sigma}^y\rangle &= 2\frac{\Delta}{\omega}\langle\sigma^x\rangle - \frac{V_{\rm SAW}}{\omega}\langle\cos(\tilde{z})\rangle\langle\sigma^z\rangle, \\
\langle\dot{\sigma}^z\rangle &= \frac{V_{\rm SAW}}{\omega}\langle\cos(\tilde{z})\rangle\langle\sigma^y\rangle,
\end{aligned}$$

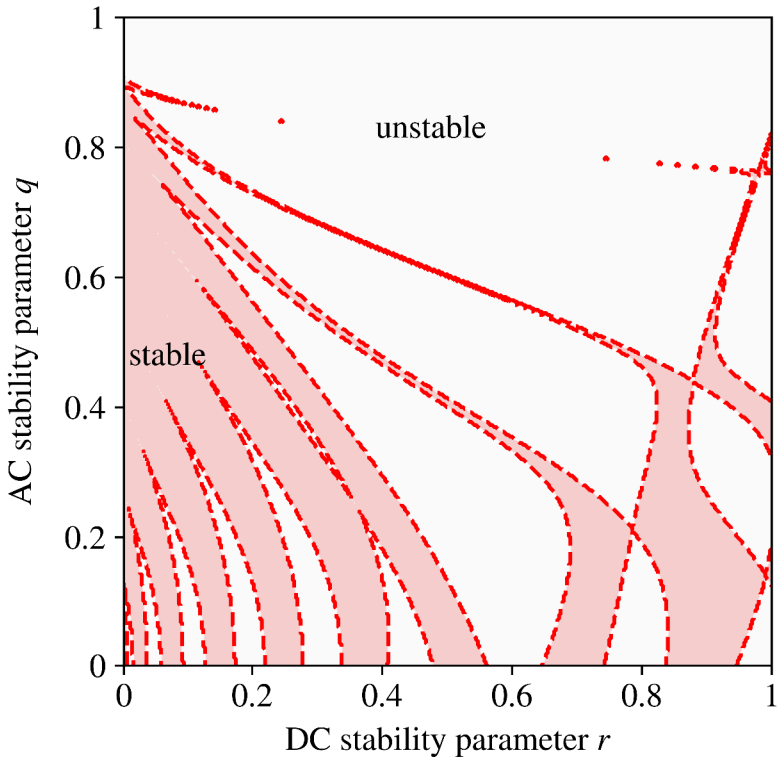

Figure 3.8: Stability diagram of Eq. (3.46) with stability paramters $q = V_{\mathrm{SAW}}/E_{\mathrm{S}}$ and $r = \Omega_0^2/(4E_{\mathrm{S}}\Delta)$. Red areas denote regions of stable trapping, i.e. stable solutions of Eq. (3.46), and white areas, in turn, denote unstable areas. On the $r = 0$ axis, the standard Mathieu equation is recovered which, for a purely time-dependent drive, yields stable trajectories in the region $0 \leq q \lesssim 0.908$. Other numerical parameters: $\eta = 0.1$.

with $E_{\mathrm{S}} = m(\omega/k)^2/2$ and assuming that there exists no significant correlation between external and internal DOFs, i.e., decorrelated expressions such as, e.g., $\langle \sin(\tilde{z} + \varphi)\sigma^i \rangle \approx \langle \sin(\tilde{z} + \varphi) \rangle \langle \sigma^i \rangle$.

Two limiting cases.—We consider the two limiting cases (i) $\Omega_0 = 0$ and (ii) $V_{\mathrm{SAW}} = 0$: (i) At $\Omega_0 = 0$, we recover a Hamiltonian which is discussed in great detail in Ref. [2]; in the limit $\tilde{z} \ll 1$, the Heisenberg EOMs yield a Mathieu equation [127] whose stability diagram in terms of V_{SAW} and $E_{\mathrm{S}} = mv_s^2/2$ is well-known, where v_{s} denotes the speed of sound. (ii) For $V_{\mathrm{SAW}} = 0$ and in the large-detuning regime $\Omega_0 \ll |\Delta|$, an EOM can be derived which corresponds for a given spin state to a Hamiltonian of the form $H = \hat{p}^2/(2m) + \Omega_0^2/(4|\Delta|) \sin^2(k\hat{z})$. Intuitively, these results agree very well with our expectation, since the case (i) coincides with a result known from the physics of trapped ions; this is not surprising since only the electric field contributes. On the other hand, case (ii) reproduces an effective Hamiltonian which is very familiar from optical lattices for cold (neutral) atoms [208]; this finding, in turn, underlines the close relation between the proposed magnetic traps and optical dipole traps which are both based on the AC Stark effect. In general,

i.e., $V_{\mathrm{SAW}}, \Omega_0 \neq 0$, the EOM leads to more involved dynamics. By adiabatic elimination of the internal DOFs, we obtain [corresponding to the constructive case in Eq. (3.45)] an EOM of the form

$$\ddot{\tilde{z}} + [r + 2q\cos(2\tau) - r\cos(2\eta\tau)]\tilde{z} = 0, \tag{3.46}$$

with stability parameters $r = \Omega_0^2/(4E_{\mathrm{S}}|\Delta|)$ and $q = V_{\mathrm{SAW}}/E_{\mathrm{S}}$ and dimensionless quantities $\tilde{x} = kx$ and $\tau = \omega t/2$. The ratio $\eta = |\Delta|/\omega$ is typically small in the RWA regime. Based on Eq. (3.46), we extract stability diagrams (to predict the stability of solutions to Eq. (3.46)) in terms of q, r and η. These diagrams can have an intricate structure, see also Ref. [274, 275]. Here, we are mainly interested in the prediction of parameter constellations that give rise to stable solutions of Eq. (3.46). A prototypical stability diagram is shown in Fig. 3.8 for $\eta = 0.1$. It can be seen that a $r = 0$ cut in Fig. 3.8 reproduces the well-known result that stable behaviour of solutions to the Mathieu equation occurs at $0 < q \lesssim 0.908$ for $r = 0$. At $r > 0$, the stability properties can be rather sensitive to slight changes in q. An operation in the stable regime therefore requires a balanced choice of these parameters. However, Fig. 3.8 shows that several values $r > 0$ support a range of stable values q which indicates that operation in a stable regime is possible for a significant range of parameters. Moreover, the numerical parameters used in Fig. 3.4 give rise to $q \ll 1$ which allows for stable trajectories for many different r. We conclude that, even in the presence of induced electric fields, stable magnetic traps can be operated.

Chapter 4

Quantum Wigner Crystals in Two-Dimensional Semiconductors

4.1 Motivation

Ever since its theoretical inception 85 years ago [276], Wigner crystallization has stimulated both theoretical and experimental research to find unambiguous evidence for this elusive state of matter. Since the earliest indication for quantum Wigner crystals (WCs) obtained from high-magnetic-field transport measurements [277, 278], it has proven to be a very demanding task to study WCs, especially in a minimally invasive manner without destroying the crystalline order. Recent experimental work demonstrated non-destructive read-out of the charge distribution of one-dimensional WCs in carbon nanotubes [279]. However, it remains an open challenge to find approaches for the non-invasive detection of WCs in two-dimensional and a broader range of one-dimensional quantum systems.

Apart from a fundamental interest in the physics of Wigner crystallization, self-assembled crystals promise a route towards highly ordered and scalable many-body systems under minimal external control. Thus, they meet some of the key requirements posed by quantum computers [280] and simulators [57]. It has therefore been proposed that Wigner crystals hosted in semiconductor nanostructures [281, 282], trapped above the surface of liquid helium [283, 284] or composed of trapped ions [285, 286] can be utilized for quantum information processing and simulation. In particular, electrons confined to low-dimensional semiconductors [287] may be brought into the low-temperature regime $k_{\mathrm{B}}T \ll \varepsilon_{\mathrm{F}}$ (Fermi energy ε_{F}) where quantum phenomena occur and spin-exchange interactions can play an important role. Since solid-state systems also offer a genuine prospect for miniaturization and on-chip integration, the quest for a faithful implementation of solid-state quantum WCs at zero magnetic field remains tantalizing.

4.2 Executive Summary

As recently pointed out, monolayer transition-metal dichalcogenides (TMDs) [288] and TMD-based moiré superlattices [289, 290, 291] are unique platforms for realizing strongly correlated systems and the study of WCs in particular owing to the combination of reduced screening in two dimensions and a relatively high effective electron mass. Their optical bandgap offers exciting possibilities to probe quasiparticle excitations, e.g., excitons or trions [150, 267, 292, 293] optically [294, 295, 296].

In this chapter, we demonstrate the potential of scalable quantum simulators based on two-dimensional WCs in TMDs and propose an all-optical detection scheme for charge ordering and partial spin information in these systems (see Fig. 4.1). In particular, the scheme possesses three key properties: (i) It provides clear evidence for Wigner crystallization in monolayer TMDs. (ii) Under conditions specified below, the detection scheme is non-invasive and leaves charge and spin order intact. (iii) Optical selection rules provide spin-selective addressability which is a crucial requirement for quantum simulation.

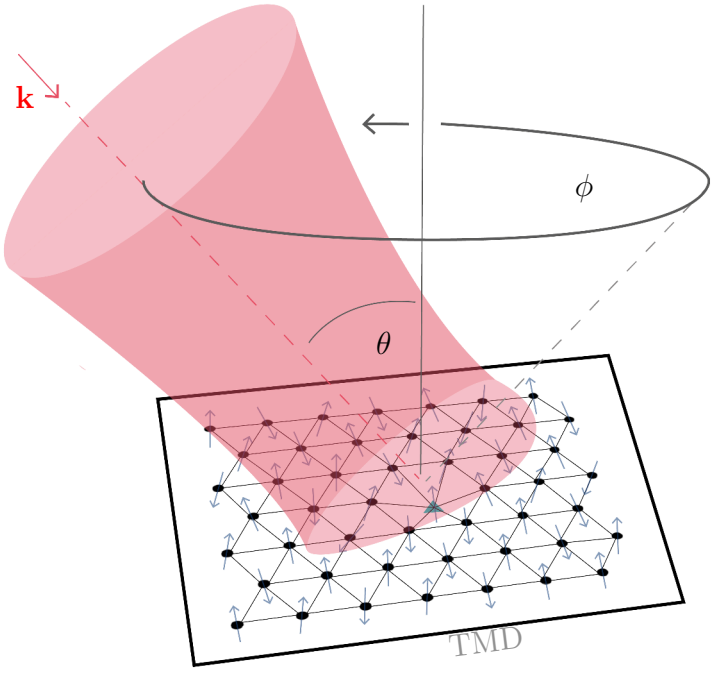

Figure 4.1: (color online). Schematic illustration of proposed setup and optical detection scheme. Charge ordering of electrons in a lattice (black dots) competes with random disorder-induced dislocations of lattice sites in the presence of impurities and defects (green triangle). The angle-dependent (ϕ) reflection of a tilted (θ) focused laser beam with wavevector $\mathbf{k}$ from a WC probes its lattice geometry. Light polarization provides further information about the spin via optical selection rules of TMDs.

4.3 Theoretical Framework

Wigner crystals.—At electron densities n below a critical density n_{cr} and in the presence of an external confinement potential, interacting charge carriers (refered to as electrons in the following) arrange themselves in a lattice [1], leading to a periodic modulation of charge density $n(\mathbf{r})$. In this low-density regime, electrostatic interactions dominate over the kinetic energy of electrons. In two dimensions, this regime is characterized by a sufficiently large interaction parameter $r_{\mathrm{s}} = 1/(\sqrt{\pi n} a_{\mathrm{B}})$, with the Bohr radius $a_{\mathrm{B}} = 4\pi\varepsilon\hbar^2/(e^2 m)$, effective electron mass m and permittivity ε. Monolayer TMDs feature an extraordinarily small Bohr radius $a_{\mathrm{B}} \gtrsim 0.5$ nm and thus render the large-r_{s} regime accessible at experimentally achievable [297, 298] densities $n \lesssim n_{\mathrm{cr}}$. For our calculations, we choose $n_{\mathrm{cr}} = 10^{11}$ cm^{-2} [288] and $m = 0.5 m_0$ (representative of MoX_2 monolayers where X = S, Se [299]), where m_0 denotes the bare electron mass. In a square (triangular) lattice, this maximum electron density corresponds to a minimum lattice spacing of $a \gtrsim 32$ nm ($a \gtrsim 34$ nm).

Model.—We consider N electrons trapped at $z = 0$ in a global harmonic potential such that the total potential reads

$$V(\mathbf{r}_1, ..., \mathbf{r}_N) = \frac{m\omega^2}{2} \sum_{i=1}^{N} \left(x_i^2 + y_i^2\right) + \sum_{i \neq j} V_{\mathrm{int}}\left(\mathbf{r}_i, \mathbf{r}_j\right), \tag{4.1}$$

where $\mathbf{r}_i = (x_i,\ y_i,\ 0)$ denotes the position of the ith electron. The confinement is characterized by the trapping frequency ω and V_{int} denotes the two-body interaction potential. In TMDs, the former may be induced by strain [300, 301] or defined via local gates [302] and the latter is usually modeled by the Keldysh potential [303],

$$V_{\mathrm{int}}(\mathbf{r}_i, \mathbf{r}_j) = \frac{\pi e^2}{2 r_0} \left[H_0\left(\frac{|\mathbf{r}_i - \mathbf{r}_j|}{r_0}\right) - Y_0\left(\frac{|\mathbf{r}_i - \mathbf{r}_j|}{r_0}\right)\right], \tag{4.2}$$

with a material-specific length scale $r_0 \approx 5$ nm. H_0 and Y_0 are Struve and Bessel functions, respectively. At electron concentrations $n < n_{\mathrm{cr}}$, the inter-particle distance $|\mathbf{r}_i - \mathbf{r}_j| \gg r_0$ and hence $V_{\mathrm{int}}(\mathbf{r}_i, \mathbf{r}_j) \sim 1/|\mathbf{r}_i - \mathbf{r}_j|$ behaves like a Coulomb potential.

In a WC, the electrons are localized around lattice sites at $\mathbf{r}_i^0$ $(i = 1, ..., N)$ which can be determined from the equilibrium conditions $\nabla_i V|_{\mathbf{r}_i = \mathbf{r}_i^0} = 0$. Numerical calculations show that harmonic confinement potentials, as described in Eq. (4.1), give rise to triangular lattice geometries while other potentials can give rise to, e.g., square lattices; see Appendix 4.A for details. For any ω, the maximum number of WC electrons can be calculated given a critical density, and vice versa. Small systems containing $N \sim (10 - 100)$ electrons require $\hbar\omega \sim (1 - 3)$ meV at $n \sim n_{\mathrm{cr}}$ (see Fig. 4.2).

The strong interactions in Eq. (4.2) enable the description of charge excitations in terms of phonons in the WC. These can be expressed as small displacements $\mathbf{q}_i = \mathbf{r}_i - \mathbf{r}_i^0$ $(i = 1, ..., N)$ from the lattice sites such that $V = (m/2) \sum \mathcal{K}_{ij}^{\alpha\beta} q_i^{\alpha} q_j^{\beta}$ $(\alpha, \beta \in \{x, y\})$

[1] For simplicity, we refer to this lattice as a WC, despite the absence of long-range order. In the literature, these systems are also referred to as Wigner molecules.

with an elasticity matrix $\mathcal{K}$. All $2N$ normal modes of the system with eigenfrequencies Ω_n ($n = 1, ..., 2N$) are readily obtained by diagonalization of $\mathcal{K}$ and for the non-zero eigenfrequencies one finds that $\Omega_n \gtrsim \omega$ (cf. Appendix 4.A). Given the relation between ω and N at $n \sim n_{\mathrm{cr}}$, this indicates that large WCs have low-energy phonon modes. Using anharmonic potentials, there is no limit placed on N by the phonon modes or n_{cr}.

Requirements.—Wigner crystallization requires low disorder. Disorder-induced potential fluctuations are incorporated based on Eq. (4.1) by adding further randomly distributed local confinement terms to analyze the impact of impurities (e.g., atomic defects or charges) on the electron lattice. In order to obtain a regular lattice structure with an approximately equidistant spacing between adjacent electrons (see schematic Fig. 4.1), the impurity density n_{imp} should be significantly smaller than the electron density, i.e. $n_{\mathrm{imp}} \lesssim 0.1n$; see Appendix 4.B for details. To date, atomic and charge defects in TMDs still prevent the realization of systems with sufficiently low disorder [304]. However, both sample quality and deterministic control over defects [305] have been improving rapidly in recent years and defect densities around n_{cr} can already be achieved. Moreover, WCs require sufficiently low temperature. Cooling into the motional ground state requires low temperatures $T \sim 1$ K for $\hbar\omega \lesssim$ meV, as the thermal occupation $\bar{n}_{\mathrm{th}} = 1/[\exp(\hbar\Omega_n/(k_{\mathrm{B}}T)) - 1]$ of the modes increases as ω is decreased (cf. Appendix 4.C).

There are many interesting aspects about the dynamics of strongly correlated electrons that can be studied in the system we describe, including the entanglement properties of the ground state, the nature and dynamics of excitations and the transitions to neighboring phases. In the following, we focus on the spin physics.

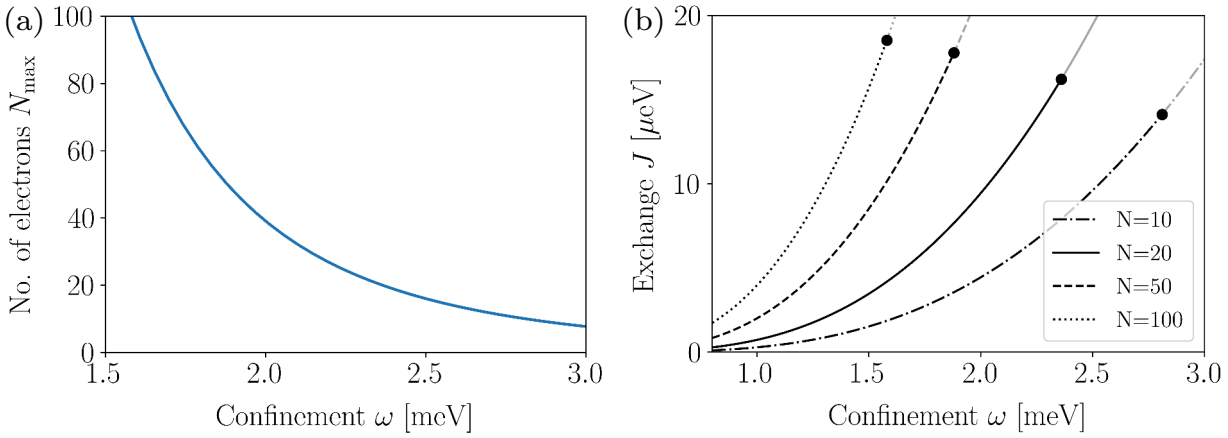

Figure 4.2: Spin coupling and system size. (a) Maximum number of electrons as a function of ω such that $n < n_{\mathrm{cr}}$. (b) Coupling constant J as a function of the confinement ω for different particle numbers $N = 10$ (*dash-dotted*), $N = 20$ (*solid*), $N = 50$ (*dashed*), $N = 100$ (*dotted*). Black dots: maximum frequency ω for given N such that $n < n_{\mathrm{cr}}$.

4.4 Spin Physics

TMD monolayers exhibit strong spin-orbit coupling and an intricate interplay between spin and valley degrees of freedom. Here we focus on the case where, by energetic isolation of the lower spin states of the conduction band, spin and valley become locked [306]. For this reason, we require that the electron density be sufficiently low such that the Coulomb interaction energy $E_{\mathrm{int}} \sim r_{\mathrm{s}} \cdot \varepsilon_{\mathrm{F}} = r_{\mathrm{s}} \pi \hbar^2 n/m$ is small compared to the spin-orbit splitting in the conduction band, Δ_{SO}^{c}. At $n \lesssim n_{\mathrm{cr}}$, one typically finds $E_{\mathrm{int}} \lesssim 10$ meV, such that the above condition is readily satisfied in $MoSe_2$ ($\Delta_{\mathrm{SO}}^{c} \approx 23$ meV), though not necessarily in MoS_2 ($\Delta_{\mathrm{SO}}^{c} \approx 3$ meV) [307]. Nevertheless, the requirement can be met in all TMDs by considering holes instead of electrons, since the spin-orbit splitting in the valence band Δ_{SO}^{v} is on the order of a hundred meV [267].

At low temperature and small displacements $\mathbf{q}_i$, we assume that the electron spins are localized around the lattice sites at $\mathbf{r}_i^0$. Adjacent spins are coupled via exchange interactions that can be either ferromagnetic or antiferromagnetic, depending on the density n [308, 309]. Here, we provide an estimate for the magnitude of the spin-spin coupling, demonstrating the potential of TMD-based electron lattices as a platform for quantum simulation of prototypical spin systems. As exchange couplings decay exponentially with a^2, where a denotes the inter-particle distance, the low-density regime necessary for WCs stands in contrast with the strong couplings of interest for spin physics. However, at intermediate densities $n \lesssim n_{\mathrm{cr}}$ we still find significant exchange couplings which exceed predicted spin relaxation rates [310, 311].

Due to the spin polarization in each of the K and K' valleys, we find that the effective spin model in the spin-valley locked, low-temperature regime reduces to an Ising Hamiltonian (cf. Appendix 4.D for details) of the form

$$H_\sigma = \sum_{i,j} J_{ij} \sigma_i^z \sigma_j^z. \tag{4.3}$$

Here σ_i^z is a Pauli operator and J_{ij} denotes the coupling strength between spins at sites i and j. In a tight-binding approximation, we calculate J_{ij} ($1 \leq i < j \leq N$) using Gaussian ansatz wavefunctions centered around the sites $\mathbf{r}_i^0$. The width of these wave functions is expressed in terms of the normal mode frequencies Ω_n and, upon inserting typical material parameters, we find for the magnitude J of the spin-spin interaction between nearest neighbours typical values in the range $J \sim (5 - 30)$ μeV for $n \lesssim n_{\mathrm{cr}}$. Due to the exponential decay of J_{ij} with distance, nearest-neighbour interactions are dominant and typically roughly one order of magnitude larger than next-nearest-neighbour interactions. In Fig. 4.2(b), we show the resulting spin-coupling constant J as a function of ω for different particle numbers $10 \leq N \leq 100$. At the intermediate densities $n \lesssim n_{\mathrm{cr}}$ considered here, we find antiferromagnetic exchange couplings which can result in geometrical frustration [312] depending on the lattice structure.

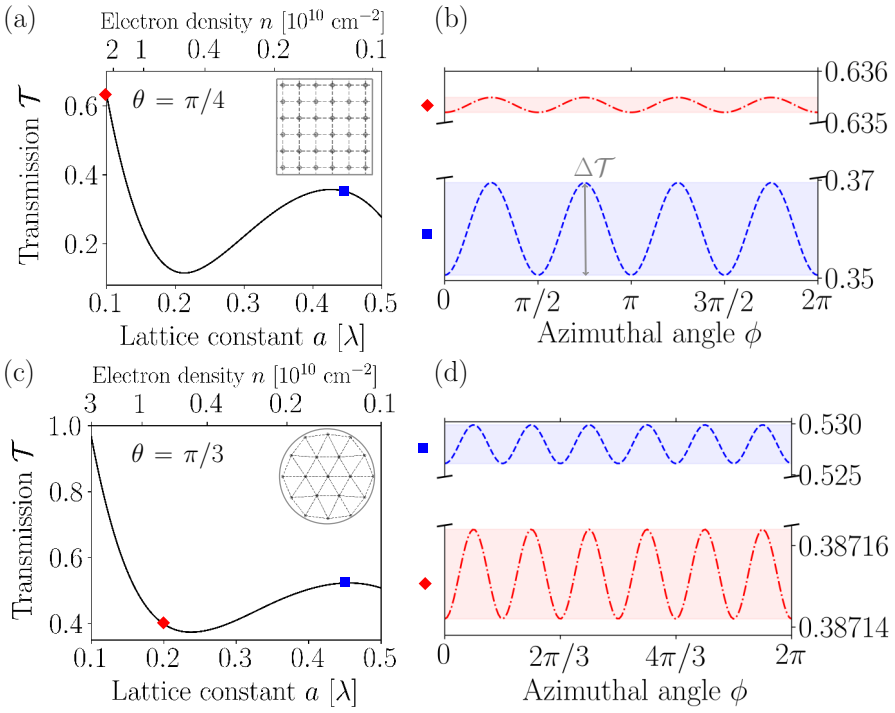

Figure 4.3: Density and angle-dependent transmission of elliptically polarized (see Eq. (4.25)) incoming light beam at incident angle θ and in-plane rotation angle ϕ (see Fig. 4.1). (a) Transmission $\mathcal{T}$ at a tilt angle $\theta = \pi/4$ for a square lattice configuration as a function of lattice constant a and density n. (b) $\mathcal{T}(\phi)$ at chosen values for $a/\lambda = 0.1$ (*red, dash-dotted line*), $a/\lambda = 0.45$ (*blue, dashed line*) and same parameters as in (a). Contrast $\Delta\mathcal{T}$ is depicted by oscillation amplitude of $\mathcal{T}(\phi)$. (c) Same as (a) but for a triangular lattice configuration. Angle of incidence $\theta = \pi/3$. (d) $\mathcal{T}(\phi)$ at chosen values for $a/\lambda = 0.2$ (*red, dash-dotted line*), $a/\lambda = 0.45$ (*blue, dashed line*) and same parameters as in (c). *Numerical parameters:* Gaussian beam waist $w_0 = 1.0\lambda$, $N = 40 \times 40$, detuning $\Delta_0 = 0$.

4.5 Optical Readout

We now address the optical detection of charge ordering in TMD-based WCs and consider an incoming ($z < 0$) Gaussian laser beam $\mathbf{E}_{\text{in}}(\mathbf{r})$ with wavelength λ focused to a spot on the electron lattice ($z = 0$) at a tilt angle θ (see Fig. 4.1). Our approach is similar in nature to the one taken in Refs. [313, 314], where the reflection and transmission of arrays of discrete atomic emitters in a lattice configuration was analyzed. Such an approach is valid for highly localized charges [315], in contrast to the study of mobile polarons [316]. Due to optical transition selection rules in monolayer TMDs, specific electron spin states can be addressed using circularly polarized σ^+ and σ^- light. For example, σ^- (σ^+) light may couple a WC electron in a $|\uparrow_{\text{K}}\rangle$ ($|\downarrow_{\text{K}'}\rangle$) spin state to a trionic state $|\uparrow_{\text{K}}, \downarrow_{\text{K}'}\Downarrow_{\text{K}'}\rangle$ ($|\downarrow_{\text{K}'}, \uparrow_{\text{K}}\Uparrow_{\text{K}}\rangle$) with a hole spin $\Uparrow$ ($\Downarrow$) in the K' (K) valley. For our calculations, we assume a low-amplitude light beam with sufficiently small detuning $\hbar\Delta_0 \ll E_b, E_g$ from the trion resonance such that

other quasiparticle excitations and transitions can be neglected. Prototypical values for the trion binding energy $E_b \sim 20$ meV and quasiparticle band gap $E_g \sim 500$ meV are given in Ref. [267]. When the incoming beam is sufficiently close to resonance with a dipole transition at lattice points $\mathbf{r}_n^0$, the scattered light field $\mathbf{E}(\mathbf{r})$ at position $\mathbf{r}$ is obtained by solving a set of coupled linear equations,

$$\mathbf{E}(\mathbf{r}) = \mathbf{E}_{\text{in}}(\mathbf{r}) + \frac{4\pi^2}{\varepsilon_0 \lambda^2} \sum_{n=1}^{N} G(k, \mathbf{r}, \mathbf{r}_n^0) \alpha_n(\Delta_0) \mathbf{E}(\mathbf{r}_n^0), \tag{4.4}$$

with the detuning from resonance Δ_0, the dyadic Green's function G evaluated at $k = 2\pi/\lambda$ and the polarizability tensor α_n. The magnitude of the polarizability tensor is given by the scalar polarizability $\alpha(\Delta_0)$, while the orientation depends on the electron spin at site n; see Appendix 4.E for more details.

In order to probe charge ordering, it is advantageous to address all WC electrons equally. To this end, we assume for the following discussion that the WC is fully spin polarized, which could be achieved by applying a large magnetic field or via optical pumping [317]. Alternatively, one could consider a TMD heterobilayer system where an electron-hole pair excited in one layer forms a trion state with a WC electron in the other layer, such that both valleys can be addressed independent of the spin of the resident electron [267].

The total power P transmitted by the WC to $z > 0$ is obtained by integrating the transmitted signal ($\mu_0 = 1$),

$$P = \frac{1}{2} \int_{\mathcal{S}} \text{Re}\,[\mathbf{E} \times \mathbf{B}^*] \cdot \hat{\mathbf{z}}\ \text{dA}, \tag{4.5}$$

with the electric and magnetic fields $\mathbf{E}$ and $\mathbf{B}$, respectively, and $\mathbf{B}^*$ denotes the complex conjugate of $\mathbf{B}$. The transmission $\mathcal{T} = P_{\text{wc}}/P_0$ is calculated as a function of density n, incidence angle θ, and rotation angle ϕ (see Fig. 4.1) by comparing the transmitted power P_{wc} in the presence of a WC with a reference signal P_0 obtained in the absence of localized dipoles [313], e.g. in a system with no doping at $n = 0$.

In Fig. 4.3, $\mathcal{T}$ is shown as a function of the electron density $n \sim 1/a^2$ for square [Fig. 4.3(a)] and triangular [Fig. 4.3(c)] lattices with a lattice constant a. Here we consider $\Delta_0 = 0$, which corresponds to a wavelength $\lambda \sim (700 - 800)$ nm in state-of-the-art TMD setups [318, 319]. We choose θ such that the cross section of the Gaussian beam is small enough and does not exceed the size of the WC. Varying the twist angle ϕ of the laser beam leads to smooth variations in $\mathcal{T}(\phi)$. The periodic modulation of $\mathcal{T}(\phi)$ reflects the rotational symmetry of the WC. Figs. 4.3(b) and (d) display the $2\pi/4$ and $2\pi/6$ rotational symmetry of a square and triangular lattice, respectively. The amplitude of this periodic signal shows that the contrast $\Delta\mathcal{T} = \max_{0 \le \phi < 2\pi} \mathcal{T}(\phi) - \min_{0 \le \phi < 2\pi} \mathcal{T}(\phi)$ can be of the order of a few percent. This modulation provides an unambiguous experimental signature of Wigner crystallization. The beam parameters and polarization of the incident light can be optimized to maximize the transmission contrast (cf. Appendix 4.E). Momentum transfer onto the WC can be safely neglected since the recoil energy $E_{\text{R}} = \hbar^2 k^2/(2m) \sim (5 - 10)\mu$eV is much smaller

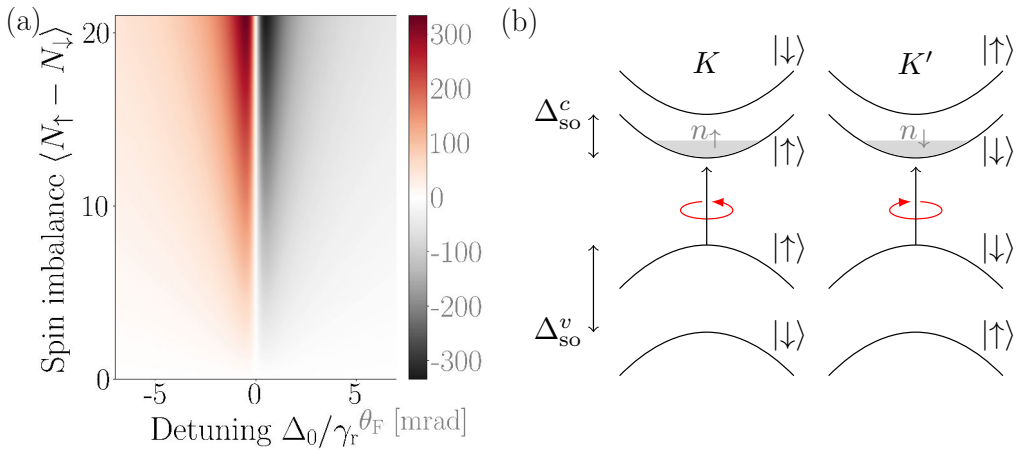

Figure 4.4: Faraday rotation and optical selection rules. (a) θ_F from Eq. (4.6) as a function of detuning Δ_0 from the bare resonance and spin imbalance $N_\uparrow - N_\downarrow$. Results for a total number of $N = N_\uparrow + N_\downarrow = 25$ electrons in a square lattice at $a/\lambda = 0.4$. (b) Energy level diagrams for conduction and valence bands at the K and K' valleys of MoX_2 monolayers with spin-orbit splittings between $|\downarrow\rangle$ and $|\uparrow\rangle$ in the conduction (Δ^c_{SO}) and valence (Δ^v_{SO}) bands. Carrier densities $n_\uparrow$ and $n_\downarrow$ in the $|\uparrow_K\rangle$ and $|\downarrow_{K'}\rangle$ conduction bands, respectively. Right-circularly (left-circularly) polarized light couples only to spin-up (spin-down) electron states in the K (K') valley. *Numerical parameters:* nonradiative linewidth $\hbar\gamma_{nr} = 0$, tilt angle $\theta = 0$ (normal incidence) and beam waist $w_0 = 1.0\lambda$.

than interaction energy and trapping potential. This approach already incorporates spin information, as it can be used to detect ferromagnetic ground states and may pick up signatures of the lattice constant $2a$ prevailing in an antiferromagnetic ground state.

Faraday rotation.—While we have focused on the detection of charge ordering in a spin-polarized WC before, we now further examine the spin degree of freedom by analyzing the polarization of the scattered field. With the probe beam $\mathbf{E}_{in}$ detuned far enough from the trionic resonance, the presence of the optical transition merely imprints a state-dependent phase shift on the incoming field. According to selection rules of monolayer TMDs [320, 321], σ^+ (σ^-) polarized light couples to the resident electron density $n_\uparrow$ ($n_\downarrow$) in the K (K') valley (see Fig. 4.4(b)). In optical Faraday (Kerr) rotation using linearly polarized light, the polarization of the transmitted (reflected) part of the light is rotated by an angle θ_F which depends on the spin imbalance $n_\uparrow$ - $n_\downarrow$ [175, 317]. Here we inspect the Faraday rotation of an incident s or p-polarized beam, which is given by [322]

$$\theta_F = \frac{1}{2}\arctan\frac{2\mathrm{Re}\chi_F}{1-|\chi_F|^2}, \tag{4.6}$$

where $\chi_F = t_{ps}/t_{ss}$ for s-polarized light ($\chi_F = -t_{sp}/t_{pp}$ for p-polarized light) depends on the Jones matrix elements t_{ss}, t_{ps} (t_{pp}, t_{sp}) encoding the polarization state of the scattered light [323]. We consider $N_\uparrow$ ($N_\downarrow$) electrons in the $|\uparrow_K\rangle$ ($|\downarrow_{K'}\rangle$) conduction band and numerically calculate θ_F as a function of spin imbalance $N_\uparrow - N_\downarrow$ and detuning Δ_0. Here we assume that

the electron sites $\mathbf{r}_i^0$ are distributed in a square-lattice configuration in the spot of the beam with $N_\uparrow$ ($N_\downarrow$) randomly assigned $|\uparrow\rangle$ ($|\downarrow\rangle$) states. We average over many such configurations. In Fig. 4.4(a) the resulting Faraday rotation is depicted for a p-polarized input field, yielding the strongest signal at $|\Delta_0| = \gamma_\mathrm{r}/2$ with the radiative linewidth γ_r. For the strongly localized quantum emitters considered here, we estimate $\hbar\gamma_\mathrm{r} \sim 10^{-2}$ μeV. Nonradiative decay processes can also be taken into account in our framework, yielding weaker Faraday signals for larger nonradiative decay rates γ_nr (cf. Appendix 4.E). Since the Faraday rotation is proportional to $N_\uparrow - N_\downarrow$, it provides a measure for the spin imbalance in the system. With this tool, one may distinguish between ferromagnetic and antiferromagnetic configurations or even locally probe domain walls in the spin system, where the spatial resolution would be limited by the spot size $\sim \lambda^2$.

4.6 Conclusions and Outlook

In conclusion, we have proposed an all-optical detection scheme for TMD-based Wigner crystals, highlighting their potential as a platform for the quantum simulation of geometrically frustrated magnetism with adjustable and self-assembled lattice structures. Beyond the Ising model considered here, richer spin physics with multi-spin exchange interactions has been predicted for these systems, potentially offering a platform to study three- and four-body interactions [324, 325]. Moreover, recent results show that multi-electron quantum dots hold promise as exchange-based mediators of quantum information [326]. In this context, intermediate-scale Wigner crystals in 2D semiconductors could be interesting for achieving long-range spin coupling with minimal external control requirements [282]. Control over the spin degree of freedom may be provided via magnetic fields or optical pumping into a specific valley, e.g. in parts of the system to study the formation of domain walls. Inversion symmetric TMD bilayers, whose bands are spin degenerate, may further give rise to a wider range of spin Hamiltonians and allow for coherent optical control of the electron spin as no momentum is required to flip the spin. High-quality samples of monolayer TMDs should provide access to first proof-of-principle experiments with small system sizes. Local spin probes may be enabled by illuminating only parts of the WC. Besides the optical techniques we propose, which we believe can be readily implemented given sufficiently clean samples, we envisage that it might become possible in the future to extend existing and developing work on high-resolution electron beam imaging with (close-to) single site resolution [327, 328] to the point that a single electron charge can be directly spatially probed. Furthermore, other detection schemes could be considered like magnetic noise spectroscopy [329], microwave spectroscopy [330], or using surface acoustic waves in piezoelectric TMD monolayers [331].

Appendices

4.A Calculation of Lattice Structure and Normal Modes

We consider a general potential of the form

$$V_p = \sum_{i=1}^{N} \mu_p \left(x_i^p + y_i^p\right) + \sum_{i \neq j} V_{\text{int}}(\mathbf{r}_i, \mathbf{r}_j), \tag{4.7}$$

where μ_p is the strength of the potential and the interaction potential V_{int} is modeled by the Keldysh interaction potential given in Eq. (2). The results presented in the main text are derived for the special case $p = 2$ and $\mu_2 = m\omega^2/2$.

Lattice structure

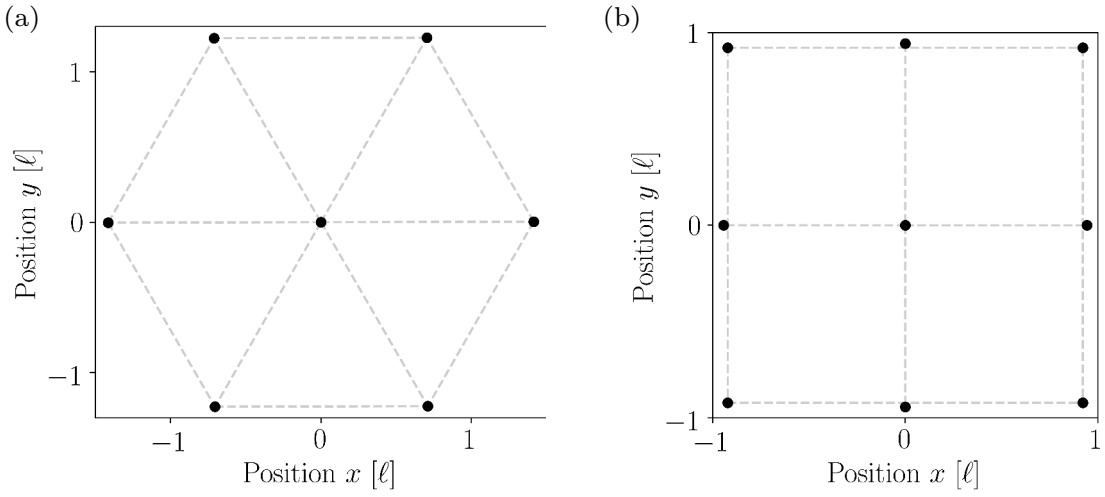

Figure 4.5: Lattice configurations $\{\mathbf{r}_i^0\}_{1 \leq i \leq N}$ (*black dots*) for small systems of (a) $N = 7$ electrons in a harmonic potential with $p = 2$ and (b) $N = 9$ electrons in an anharmonic potential with $p = 8$.

The lattice sites $\mathbf{r}_i^0$ are calculated by solving the equations

$$\left.\frac{\partial V_p}{\partial x_i}\right|_{\mathbf{r}_i=\mathbf{r}_i^0} = \left.\frac{\partial V_p}{\partial y_i}\right|_{\mathbf{r}_i=\mathbf{r}_i^0} = 0 \tag{4.8}$$

for each electron $i \in \{1, ..., N\}$. This leads to a set of $2N$ coupled equations which are of the form

$$\mu_p p \alpha_i^{p-1} + \xi \sum_{j\neq i} (\alpha_j - \alpha_i)\, h\left(|\mathbf{r}_j - \mathbf{r}_i|/r_0\right) = 0, \tag{4.9}$$

with $\alpha \in \{x, y\}$, $\xi = \pi e^2/(2r_0^3)$ and the function

$$h(x) = H_{-1}(x) - H_1(x) + Y_1(x) - Y_{-1}(x) + \frac{1}{\sqrt{\pi}\Gamma(\frac{3}{2})}, \tag{4.10}$$

which is obtained by making use of recurrence relations for the *Struve* and *Bessel functions of the second kind* H_ν and Y_ν ($\nu \in \mathbb{N}$), respectively. In order to solve Eqs. (4.9), it is instructive to introduce dimensionless variables scaled by a length scale $\ell = [e^2/(4\pi\varepsilon p\mu_p)]^{1/(p+1)}$. For $r_0 \ll \ell$, we find that the obtained lattice configurations agree very well with the corresponding results obtained with a Coulomb interaction potential, $V_{\rm int}(\mathbf{r}_i, \mathbf{r}_j) \sim 1/|\mathbf{r}_i - \mathbf{r}_j|$. Since $\ell \approx 30$ nm at $\hbar\omega = 1$ meV, this condition is typically well satisfied in the situations considered in the main text. The resulting lattice structure $\{\mathbf{r}_1^0, ..., \mathbf{r}_N^0\}$ depends on the details of the confinement potential. Two exemplary charge configurations are shown in Fig. 4.5.

Normal modes

A two-dimensional lattice with N electrons has $2N$ elementary excitations, the so-called *normal modes* of the crystal. The normal-mode excitation spectrum of WCs can be calculated from the the system's *elasticity matrix* $\mathcal{K}$.

Starting with Eq. (4.7), the elasticity matrix is obtained from the second-order derivatives of V_p with respect to the spatial coordinates. In the general case of arbitrary $p \geq 2$ and the interaction potential in Eq. (2), we find that

$$\frac{\partial^2 V_p}{\partial\alpha_m\partial\alpha_n} = \begin{cases} \mu_p(p-1)p\alpha_m^{p-2} + \xi\left[\sum_{i\neq m}\frac{(\alpha_i-\alpha_m)^2}{r_0^2} g(|\mathbf{r}_i-\mathbf{r}_m|/r_0) - h(|\mathbf{r}_i-\mathbf{r}_m|/r_0)\right], \\ \text{if } m = n, \\ -\xi\left[\frac{(\alpha_n-\alpha_m)^2}{r_0^2} g(|\mathbf{r}_m-\mathbf{r}_n|/r_0) - h(|\mathbf{r}_m-\mathbf{r}_n|/r_0)\right], \\ \text{if } m \neq n, \end{cases} \tag{4.11}$$

and

$$\frac{\partial^2 V_p}{\partial\alpha_m\partial\beta_n} = \begin{cases} \xi\sum_{i\neq m}\frac{(\alpha_i-\alpha_m)(\beta_i-\beta_m)}{r_0^2} g(|\mathbf{r}_i-\mathbf{r}_m|/r_0), & \text{if } m = n, \\ -\xi\frac{(\alpha_n-\alpha_m)(\beta_n-\beta_m)}{r_0^2} g(|\mathbf{r}_n-\mathbf{r}_m|/r_0), & \text{if } m \neq n, \end{cases} \tag{4.12}$$

where $\alpha, \beta \in \{x, y\}$, $\alpha \neq \beta$ and the function g is given by

$$g(x) = H_2(x) + H_{-2}(x) - 2H_0(x) - Y_2(x) - Y_{-2}(x) + 2Y_0(x) + \frac{2}{\sqrt{\pi}\Gamma(\frac{3}{2})x} - \frac{x}{2\sqrt{\pi}\Gamma(\frac{5}{2})}. \quad (4.13)$$

The eigenmodes of the system are then calculated from the eigenvalues of the elasticity matrix $\mathcal{K}^{\alpha\beta}_{mn} = \partial^2 V_p/(\partial\alpha_m \partial\beta_n)$.

4.B Impurity-Induced Positional Disorder: Equidistance Measure

Random dislocations of single electrons from their lattice sites $\mathbf{r}_i^0$ may not only affect the lattice structure of a Wigner crystal, but also the detection scheme and spin couplings discussed in the main text. For a simple estimate of how severe the impact of impurities on the lattice is, we consider N_{imp} randomly distributed Gaussian confinement potentials in addition to the potential in Eq. (4.7), and draw both size and depth of these local confinement potentials from normal distributions. For our calculations, we assume that they are localized on a nanometer length scale and have a depth of the order of $\sim$ meV. In a monolayer TMD, such defects could be, e.g., atomistic defects [332]. Starting from Eq. (1), we take these into account by adding a disorder term,

$$\begin{aligned} V(\mathbf{r}_1, ..., \mathbf{r}_N; \{\mathbf{s}_i\}_{1\leq i\leq N_{\text{imp}}}) &= \frac{m\omega^2}{2}\sum_{i=1}^{N}\left(x_i^2 + y_i^2\right) \\ &+ \sum_{i\neq j} V_{\text{int}}\left(\mathbf{r}_i, \mathbf{r}_j\right) + V_{\text{rand}}(\mathbf{r}_1, ..., \mathbf{r}_N; \{\mathbf{s}_i\}_{1\leq i\leq N_{\text{imp}}}), \end{aligned} \quad (4.14)$$

with

$$V_{\text{rand}}(\mathbf{r}_1, ..., \mathbf{r}_N; \{\mathbf{s}_i\}_{1\leq i\leq N_{\text{imp}}}) = -\sum_{i=1}^{N}\sum_{j=1}^{N_{\text{imp}}} \frac{D_{\text{j}}}{\sqrt{2\pi\sigma_j^2}} \exp\left[-\frac{(\mathbf{r}_i - \mathbf{s}_j)^T(\mathbf{r}_i - \mathbf{s}_j)}{2\sigma_j^2}\right], \quad (4.15)$$

with random variables $D_j \sim$ meV and $\sigma_j \sim$ nm (where both means and standard deviations are of these orders), where $\{\mathbf{s}_j\}_{1\leq j\leq N}$ denote the positions of the impurities. To illustrate how this impurity model affects the lattice site distribution $\mathbf{r}_i^0$ $(i = 1, ..., N)$ of a small system, an exemplary numerical result obtained with $N = 8$ is shown in Fig. 4.6(a). The same result, but obtained in the presence of two randomly located (in the lattice) local harmonic potentials, is shown in Fig. 4.6(b). Averaging over many such instances and calculating the density-density correlations in the WC yields a measure of how much the crystal structure is affected by the presence of disorder. Similarly, here we look at another measure, χ, which quantifies how *equidistantly* the lattice sites $\mathbf{r}_i^0$ are distributed in the

x-y-plane by summing up the distances between nearest neighbours,

$$\chi = \frac{2n}{N} \sum_i \min_{j \neq i} \left| \mathbf{r}_i^0 - \mathbf{r}_j^0 \right| . \tag{4.16}$$

Below we show that $\chi = 2\sqrt{2/\sqrt{3}}$ ($\chi = 1$) for an equidistantly (completely randomly distributed) set of points $\mathbf{r}_i^0$ ($i = 1, ..., N$). By increasing the number of impurities for a given system size, i.e., increasing the impurity density n_{imp} as compared to the electron density n, χ drops from its maximum value very fast, see Fig. 4.6. As would be intuitively expected, this underlines that $n_{\mathrm{imp}} \ll n$ should be fulfilled in any experiment in order to maximize the chances to observe charge ordering in *regular* electron lattices.

We briefly show that χ is upper-bounded by $\chi_{\max} = r_{\mathrm{m}}/r_\infty = 2\sqrt{2}/3^{1/4} \approx 2.15$ [333]. This can be achieved by (i) calculating an upper bound for $r_{\mathrm{m}} = \sum_i \min_{j \neq i} |\mathbf{r}_i - \mathbf{r}_j|/N$ and (ii) estimating $r_\infty = 1/(2\sqrt{n})$ as a function of the average electron density n: (i) In a close-packed lattice with an average nearest-neighbour distance r_{m}, the unit cell occupies an area in $A_{\mathrm{uc}} = \sqrt{3} r_{\mathrm{m}}^2/2$. The electron density is then given by $n = 2/(\sqrt{3} r_{\mathrm{m}}^2)$. (ii) The mean number of lattice sites in a sector of area $A_k = \pi r^2/k$ is $m = nA_k$. The probability of finding N sites in A_k is given by a Poisson distribution $P(N \text{ sites in } A_k) = m^N e^{-m}/N!$. Hence, we obtain the probability that two lattice sites are separated by a distance $|\mathbf{r}_i^0 - \mathbf{r}_j^0|$ smaller than a given r, $P_<(r) := P(|\mathbf{r}_i^0 - \mathbf{r}_j^0| < r) = 1 - \exp(-n\pi r^2/k)$. Therefore, we obtain for the mean of the distance distribution ($k = 1$),

$$r_\infty = \int_0^\infty \frac{\mathrm{d}P_<(r)}{\mathrm{d}r} r \mathrm{d}r = \frac{1}{2\sqrt{n}}. \tag{4.17}$$

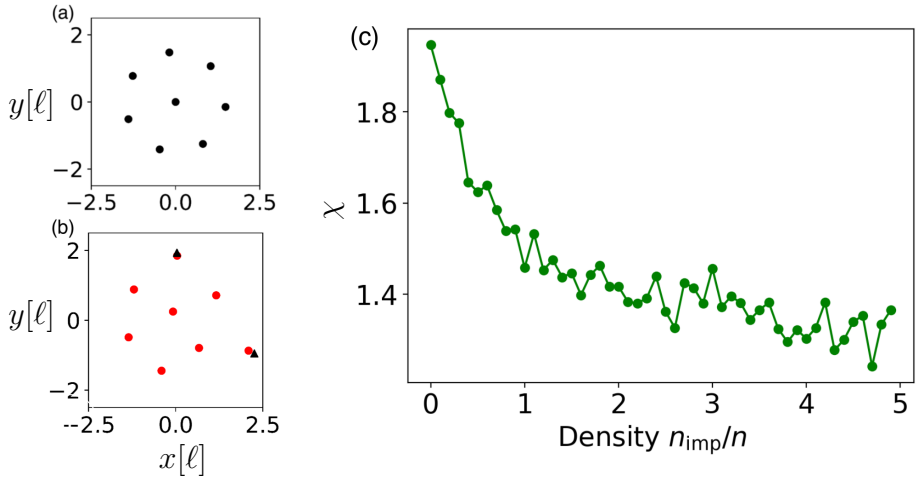

Figure 4.6: Impact of disorder-induced potential fluctuations on the lattice structure of a small WC with $N = 8$ resident electrons in a harmonic confinement potential. (a) Electron configuration without disorder. (b) Exemplary electron configuration (*red dots*) in the presence of two randomly positioned local confinement potentials (*black triangles*). (c) Equidistance measure χ is shown as a function of impurity density n_{imp}/n for $N = 10$ electrons.

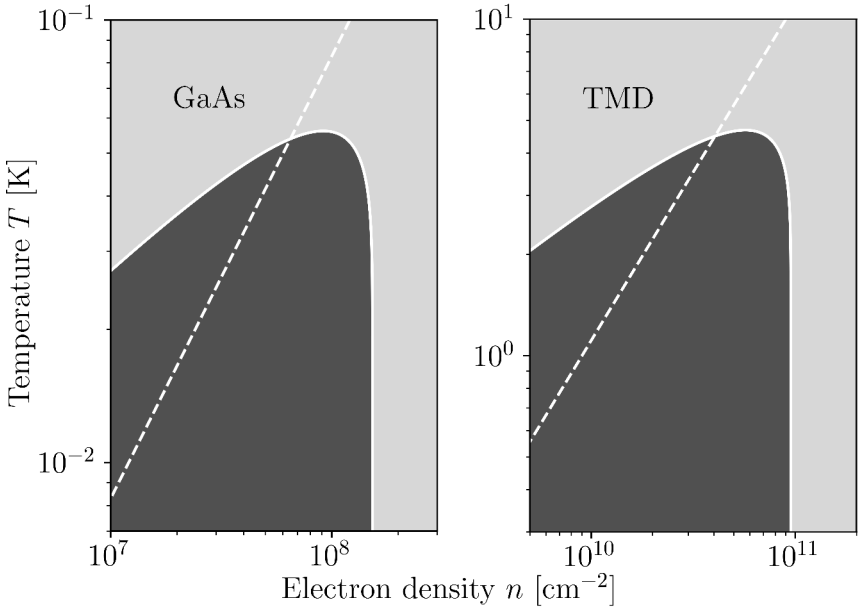

Figure 4.7: Melting curves of *(left)* GaAs and *(right)* monolayer TMD systems according to the Lindemann criterion. The dark areas indicate the onset of WC electron lattices, obtained for $N = 20$ electrons. The dashed line indicates $k_\mathrm{B}T = \varepsilon_\mathrm{F}$.

Combining the findings from (i) and (ii), we obtain an upper bound for χ, $\chi_\mathrm{max} = 2\sqrt{2}/3^{1/4} \approx 2.15$. Similarly, it can be shown that $\chi = 1$ for a random distribution of lattice sites.

In our numerical calculations, we have seen that the detection scheme is only weakly affected by disorder if the impurity density $n_\mathrm{imp}/n \lesssim 0.1$. The influence of disorder on cooperative resonances such as the ones discussed in the main text has also been investigated in Ref. [314].

4.C Finite Temperature Effects

We first provide a simple estimate of the melting temperature T_m of a WC by employing the *Lindemann criterion*, which has been used extensively in the literature [334, 335]. It states that, in a lattice with charge-carrier density n, melting occurs if the root-mean square (RMS) displacement of a charge carrier from its lattice site $\mathbf{r}_i^0$ exceeds a certain fraction of the inter-particle distance a. The RMS displacement can be obtained from the thermally occupied vibrational (normal) modes of the system at thermal equilibrium. Accordingly, the melting temperature T_m and electron density n can be related. Although it is only a phenomenological criterion, it provides an efficient tool for estimating the melting temperature of a lattice. The thereby numerically calculated melting curves, obtained using typical material parameters of GaAs and monolayer TMD systems, respectively, are shown

in Fig. 4.7. For the latter, we estimate melting temperatures of the order of $T_\mathrm{m} \sim 5$ K, which is in agreement with previous estimates [288].

Cooling the system into its motional ground state puts more demanding constraints on temperature than considering melting only. We compare the thermal energy set by $k_\mathrm{B}T$ to the mode frequencies Ω_n and calculate the thermal mode occupation $\bar{n}_\mathrm{th} = [\exp(\hbar\Omega_n/(k_\mathrm{B}T)-1]^{-1}$. Fig. 4.8 shows that for the center-of-mass (COM) mode it is $\bar{n}_\mathrm{th} \ll 1$ at $T \lesssim (1-5)$ K and $\hbar\omega \gtrsim 0.5$ meV.

4.D Spin-Spin Interactions: Derivation of Coupling Constant

We estimate the spin-coupling strength J as given by Eq. (4) in the main text. For this, we model the interaction potential $V_\mathrm{int}(\mathbf{r}_i, \mathbf{r}_j)$ between two electrons at $\mathbf{r}_i$ and $\mathbf{r}_j$ with a Coulomb potential $\sim 1/|\mathbf{r}_i - \mathbf{r}_j|$. In the parameter regime considered here, this (i) simplifies the calculation and (ii) yields the same results as obtained with the Keldysh interaction potential from Eq. (2) to a very good approximation, as confirmed by our numerical calculations.

Estimate of spin-coupling constant

We calculate the spin-exchange interaction between two electrons from the energy difference between the spin-singlet and spin-triplet energies [336],

$$J = \frac{J_{ab} - S^2 C}{1 - S^4}, \tag{4.18}$$

where J_{ab}, C and S denote the exchange, Coulomb and overlap integrals, respectively, which are given by (in atomic units)

$$\begin{aligned} J_{ab} &= \int \mathrm{d}^2\mathbf{r}_1 \int \mathrm{d}^2\mathbf{r}_2 \Psi_\mathrm{a}(\mathbf{r}_1)^* \Psi_\mathrm{b}(\mathbf{r}_2)^* \frac{1}{|\mathbf{r}_1 - \mathbf{r}_2|} \Psi_\mathrm{b}(\mathbf{r}_1)\Psi_\mathrm{a}(\mathbf{r}_2), \\ S &= \int \mathrm{d}^2\mathbf{r} \Psi_\mathrm{b}(\mathbf{r})\Psi_\mathrm{a}(\mathbf{r}), \\ C &= \int \mathrm{d}^2\mathbf{r}_1 \int \mathrm{d}^2\mathbf{r}_2 |\Psi_\mathrm{a}(\mathbf{r}_1)|^2 \frac{1}{|\mathbf{r}_1 - \mathbf{r}_2|} |\Psi_\mathrm{b}(\mathbf{r}_2)|^2, \end{aligned} \tag{4.19}$$

where $\Psi_{a/b}(\mathbf{r}) = \phi_{a/b}(\mathbf{r}) \cdot \chi_{a/b}(\mathbf{r})$ denotes the electronic wave function and the labels a and b refer to the two electrons located at around $\mathbf{r}^0_{a/b} = (x^0_{a/b}, y^0_{a/b})$. We model the wave functions with a Gaussian wave packet of width $\mathrm{w}r_\mathrm{ZPF}$ (see Sec. S4.2),

$$\phi_i(\mathbf{r}) = \left(\frac{1}{2\pi \mathrm{w}^2 r^2_\mathrm{ZPF}}\right)^{1/2} \exp\left(-\frac{(x - x^0_i)^2 + (y - y^0_i)^2}{4\mathrm{w}^2 r^2_\mathrm{ZPF}}\right),$$

where $i \in \{a, b\}$, and take into account spin-valley locking by setting the Bloch wave $\chi_i(\mathbf{r}) = \exp(iKx)$ ($\chi_i(\mathbf{r}) = \exp(iK'x)$) if the i electron, $i \in \{a, b\}$, is in a spin-$|\uparrow\rangle$ (spin-$|\downarrow\rangle$) state.

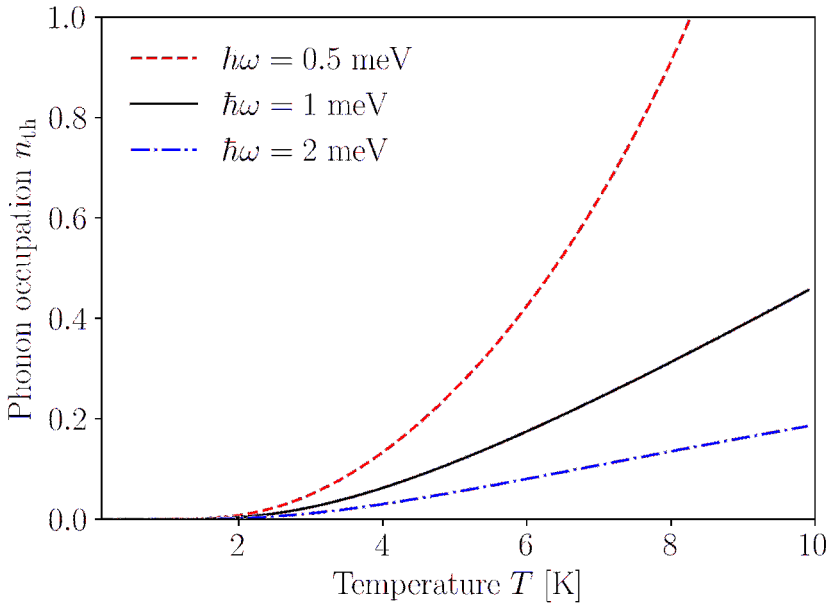

Figure 4.8: Bose-Einstein distribution $\bar{n}_{\rm th}(\Omega_1)$ at COM frequency $\Omega_1 = \omega$ and temperature T.

Next, we evaluate the exchange integral in the spin basis spanned by $|\uparrow\uparrow\rangle, |\uparrow\downarrow\rangle, |\downarrow\uparrow\rangle, |\downarrow\downarrow\rangle$. With the electrons in different valleys (i.e., opposite spins), by performing some of the integrations analytically, we find for J_{ab} in Eq. (4.19) that

$$J_{ab}^{\rm KK'} = \frac{e^{-\frac{a^2}{4{\rm w}^2 r_{\rm ZPF}^2}}}{\pi {\rm w}^2 r_{\rm ZPF}^2} \times \int_{-\infty}^{\infty} {\rm d}x e^{-\frac{x^2}{8{\rm w}^2 r_{\rm ZPF}^2}} \cos\left(\frac{8\pi}{3}\frac{x}{a_{\rm TMD}}\right) K_0\left(\frac{x^2}{8{\rm w}^2 r_{\rm ZPF}^2}\right),$$

where $a^2 = (x_a^0 - x_b^0)^2 + (y_a^0 - y_b^0)^2$, with a TMD lattice constant $a_{\rm TMD} \approx 0.3$ nm for MoX_2 (X = S, Se) [337] and $|\mathbf{K} - \mathbf{K}'| = 8\pi/(3a_{\rm TMD})$. K_0 denotes the *modified Bessel function of the second kind*. Inserting our numerical results for w, and in particular with ${\rm w}r_{\rm ZPF} \gg a_{\rm TMD}$, we find numerically that $J_{ab}^{\rm KK'}$ evaluates to negligibly small values as compared with $J_{ab}^{\rm KK}$, with which we denote the case where the two electrons are in the same valley. We find that $J_{ab}^{\rm KK'}/J_{ab}^{\rm KK} \sim a_{\rm TMD}/({\rm w}r_{\rm ZPF})$ and that typically $J_{ab}^{\rm KK'}$ is several orders of magnitude smaller than $J_{ab}^{\rm KK}$.

For $J_{ab}^{\rm KK}$, we find an analytical expression and insert TMD parameters such that

$$J_{ab}^{\rm KK} \approx 35.5{\rm meV}\ \frac{\sqrt{\hbar\omega\,[{\rm meV}]}}{\rm w}\ e^{-37.9\times\frac{\hbar\omega[{\rm meV}]}{n[10^{10}{\rm cm}^{-2}]{\rm w}^2}}, \tag{4.20}$$

where we have expressed the electron density as $n = 2/(\sqrt{3}a^2)$ for a triangular lattice.

Similarly, we find for the overlap integral S in Eq. (4.19) that

$$S \approx \exp\left(-37.9 \times \frac{\hbar\omega\,[{\rm meV}]}{n\,[10^{10}{\rm cm}^{-2}]}\right). \tag{4.21}$$

In the low-density regime considered here, we find $S \ll 1$ such that $J \approx J_{ab}$ in Eq. (4.18) to a very good approximation.

Also the Coulomb integral C in Eq. (4.19) can be calculated analytically by employing the convolution and Parseval's theorems. Defining $f_{a/b}(\mathbf{r}) := |\phi_{a/b}(\mathbf{r})|^2$ and $g(\mathbf{x}) = 1/|\mathbf{x}|$, we insert TMD parameters and find that

$$\begin{aligned} C &= \int \mathrm{d}^2\mathbf{r}_1 f_\mathrm{A}(\mathbf{r}_1)\,(f_\mathrm{B} * g)\,(\mathbf{r}_1) = 2\pi \int \mathrm{d}^2\mathbf{q} \frac{\widetilde{f_\mathrm{A}}(\mathbf{q})\widetilde{f_\mathrm{B}}(-\mathbf{q})}{|\mathbf{q}|} \\ &\approx 35.5\mathrm{meV}\ \frac{\sqrt{\hbar\omega\,[\mathrm{meV}]}}{\mathrm{w}}\ e^{-18.9\times\frac{\hbar\omega[\mathrm{meV}]}{n[10^{10}\mathrm{cm}^{-2}]\mathrm{w}^2}} \times I_0\left(18.9\frac{\hbar\omega\,[\mathrm{meV}]}{n\,[10^{10}\mathrm{cm}^{-2}]\,\mathrm{w}^2}\right), \end{aligned} \tag{4.22}$$

where I_0 is the *modified Bessel function of the first kind*.

Putting our results together, we find that $J^{\mathrm{KK}'}$ is several orders of magnitude smaller than J^{KK} for realistic parameters. Evaluating the Coulomb interaction Hamiltonian in the spin basis, with these results we obtain the spin model from Eq. (3) in the main text. Finally, putting the results from Eqs. (4.20)-(4.22) and Eq. (4.18) together, we obtain coupling strengths in the range $\sim (5-30)\ \mu$eV at densities $n \lesssim n_\mathrm{cr}$, as presented in Fig. 2(a) of the main text.

Width of ansatz wavefunction

We have considered two approaches to calculate w, for which we have found good agreement. (*i*) *Mean-field approximation*: First, we (iteratively, until the result is found to be converged) calculate the effective potential seen by a single electron due to the neighbouring electrons by summing up the Coulomb interaction terms. From this potential, we calculate the wave function with a Gaussian ansatz, which yields the width of the wave function $\sim$ w. (*ii*) *Harmonic model*: Secondly, we consider an expansion of the individual electron displacements in the set of collective displacement modes. In this way, we relate w to the normal modes which we have calculated before,

$$\mathrm{w}^2 = \frac{1}{N}\sum_{n=1}^{2N}\frac{1}{\Omega_n}, \quad r_\mathrm{ZPF} = \sqrt{\frac{\hbar}{2m\omega}}, \tag{4.23}$$

where the mode frequencies Ω_n are expressed in units of the external confinement ω. For a confinement $\hbar\omega = 3$ meV, we obtain $r_\mathrm{ZPF} \approx 5$ nm.

4.E Optical Readout: Numerical and Analytical Treatment

Here we first briefly summarize how we solve the scattering problem of light incident on a finite Wigner crystal, and then continue with an analytical treatment of the scattering problem for an infinite lattice. The latter provides us with more physical insight into the

problem and is useful for optimizing the beam parameters in order to maximize the transmission or reflection contrast of the readout scheme.

Finite arrays

The principle behind the optical readout scheme discussed in the main text is based on a cooperative resonance effect as described in detail in Refs. [314, 313]. As depicted in Fig. 1, we consider a Gaussian beam $\mathbf{E}_{\text{in}}(x', y', z')$ incident on the xy plane with a tilt angle θ and azimuthal angle ϕ, where

$$\mathbf{E}_{\text{in}}(x, y, z) = E_0 \mathbf{e}_{\text{pol}} \frac{w_0}{w(z)} \exp\left(-\frac{x^2+y^2}{w(z)^2}\right) \times \exp\left(-i\left[kz + k\frac{x^2+y^2}{R(z)} - \varphi(z)\right]\right),$$

that is scattered from a lattice of dipoles. Here we have introduced the coordinates

$$\begin{pmatrix} x' \\ y' \\ z' \end{pmatrix} = \begin{pmatrix} x\cos\theta\cos\phi - y\cos\theta\sin\phi - z\sin\theta \\ x\sin\phi + y\cos\phi \\ x\sin\theta\cos\phi - y\sin\theta\sin\phi + z\cos\theta \end{pmatrix}. \tag{4.24}$$

In Eq. (4.24), E_0 denotes the the beam amplitude, w_0 and $w(z) = w_0\sqrt{1+(z/z_{\text{R}})^2}$ are beam waist and radius at z, respectively, $z_{\text{R}} = \pi w_0^2/\lambda$ is the *Rayleigh length* and $\varphi = \arctan z/z_{\text{R}}$ refers to the *Gouy phase* of the laser beam [338]. $\mathbf{e}_{\text{pol}}$ encodes the polarization of the beam. For the results presented in Fig. 3 in the main text we consider elliptically polarized light with

$$\mathbf{e}_{\text{pol}}(\theta, \phi) = -\frac{1}{\sqrt{1+\cos^2\theta}} \begin{pmatrix} \cos^2\theta\cos\phi + i\sin\phi \\ \cos^2\theta\sin\phi - i\cos\phi \\ \sin\theta\cos\theta \end{pmatrix}. \tag{4.25}$$

At small detunings Δ_0 from the transition frequency ω_0, $|\Delta_0| \ll \omega_0$, each lattice site is modeled as a dipole with polarizability

$$\alpha(\Delta_0) = -\frac{3}{8\pi^2}\varepsilon_0\lambda^3 \frac{\gamma_{\text{r}}}{\Delta_0 + i(\gamma_{\text{r}}+\gamma_{\text{nr}})/2}, \tag{4.26}$$

with the radiative (nonradiative) linewidth γ_{r} (γ_{nr}). In general, the radiative linewidth γ_{r} can be enhanced by the presence of a medium [339], especially for high refractive-index materials like TMDs [340]. At low temperatures as considered here, hexagonal boron nitride (hBN) encapsulated TMD monolayers feature optical transitions with a radiative linewidth $\hbar\gamma_0 \sim$ meV [341]. In our calculations, we assume that the excitons are localized on a length scale much smaller than the wavelength, i.e. $a_{\text{B}} \ll \lambda$. Those spatially localized quantum emitters show much narrower linewidths ~ 100 μeV [172, 342, 343, 344]. Using Fermi's golden rule, the increased radiative lifetime of such localized excitons can be calculated, yielding a significantly enhanced emission time as compared to free excitons [345]. We estimate the radiative linewidth of a localized exciton to be of the order of $\hbar\gamma_{\text{r}} \approx 4\pi/3(a_{\text{B}}/\lambda)^2\gamma_0 \approx 10^{-5}\ \gamma_0 \approx 10^{-2}$ μeV. In the results presented in the main text, we have considered $\gamma_{\text{nr}} = 0$.

Given the Gaussian input field from Eq. (4.24), we solve the Lippmann-Schwinger equation (4), with the Green's function [346]

$$G_{\alpha\beta}(k,\mathbf{r},\mathbf{r}_n^0) = \frac{\exp\left(ik\left|\mathbf{r}-\mathbf{r}_n^0\right|\right)}{4\pi\left|\mathbf{r}-\mathbf{r}_n^0\right|} \times \left[\left(1+\frac{ik\left|\mathbf{r}-\mathbf{r}_n^0\right|}{k^2\left|\mathbf{r}-\mathbf{r}_n^0\right|^2}\right)\delta_{\alpha\beta} + \left(\frac{3-3ik\left|\mathbf{r}-\mathbf{r}_n^0\right|}{k^2\left|\mathbf{r}-\mathbf{r}_n^0\right|^2}-1\right)\frac{\left(\mathbf{r}-\mathbf{r}_n^0\right)_\alpha\left(\mathbf{r}-\mathbf{r}_n^0\right)_\beta}{\left|\mathbf{r}-\mathbf{r}_n^0\right|^2}\right], \tag{4.27}$$

with $\alpha,\beta \in \{x,y,z\}$. We solve Eq. (4) self-consistently for various angles of incidence θ and ϕ, beam profiles, detunings, and electron lattices. At normal incidence, i.e. $\theta = 0$, the resulting transmission and reflection signals depend on the lattice constant [see Fig. 4.9] but clearly not on ϕ. For $0 < \theta < \pi/2$, the transmission and reflection contrasts can be of the order of a few percent. An analytical derivation of the maximum contrast for an infinite lattice, depending on the angle of incidence θ and detuning Δ_0, is presented below.

Faraday rotation

In the main text we investigate the Faraday rotation angle according to Eq. (6). For the

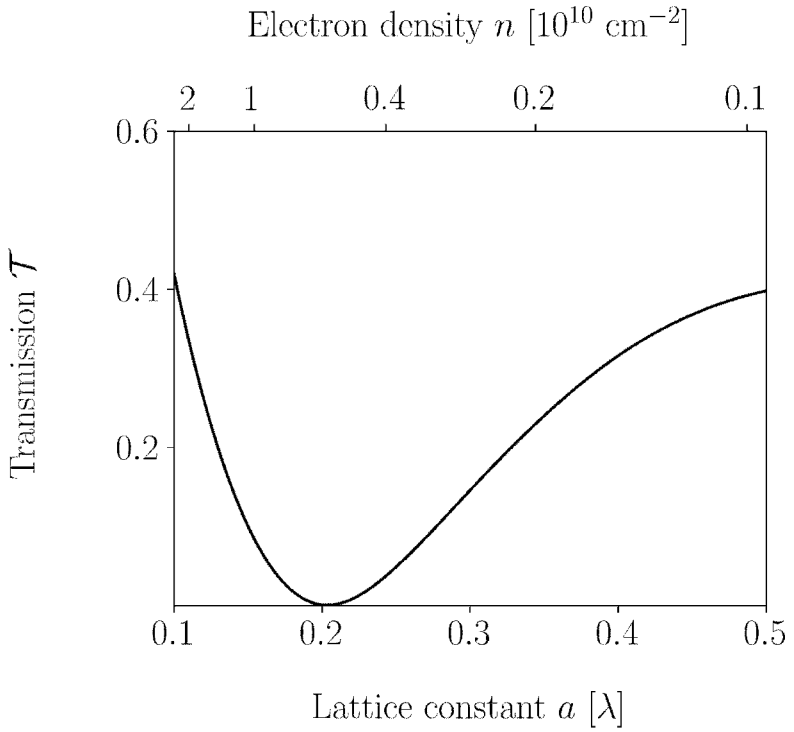

Figure 4.9: Transmission at normal incidence ($\theta = 0$) for a square lattice. Other numerical parameters as in Fig. 3 in the main text.

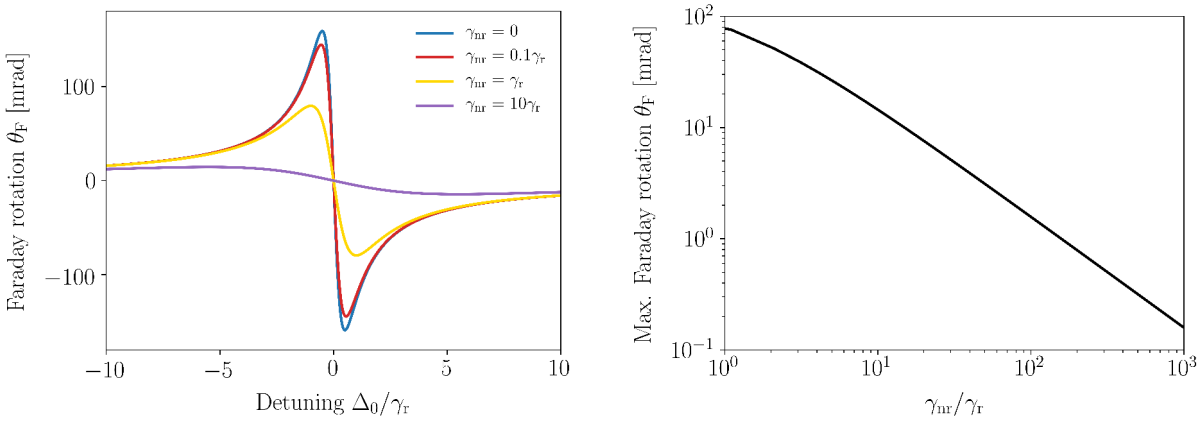

Figure 4.10: Faraday rotation for different $\gamma_{\rm nr}$ and the same numerical parameters as in Fig. 3 at $N_\uparrow = 15$, $N_\downarrow = 5$. Also shown is the maximum Faraday signal as a function of $\gamma_{\rm nr}/\gamma_{\rm r}$.

results in Fig. 4, we consider an incoming beam at normal incidence ($\theta = 0$) with

$$\mathbf{e}_{\rm pol} = \begin{pmatrix} 1 \\ 0 \\ 0 \end{pmatrix}. \tag{4.28}$$

We consider $N \equiv N_\uparrow + N_\downarrow$ dipoles which are located at lattice sites $\mathbf{r}_i^0$ with the spins assigned randomly to these lattice lattices for fixed $N_\uparrow$ and $N_\downarrow$. Next we average over sufficiently many ($\sim 10^4$) instances of such configurations to calculate the Faraday rotation.

In Fig. 4 we show results for $\gamma_{\rm nr} = 0$. For $\gamma_{\rm nr} > 0$, the maximum Faraday rotation decreases and shifts towards more highly detuned frequencies, cf. Fig. 4.10.

Infinite arrays

Here we consider light scattering off an (infinite) two-dimensional lattice of dipoles. If the transition dipole is parallel to the unit vector $\hat{\mathbf{e}}$, the electric field at position $\mathbf{r}$ satisfies the equation

$$\mathbf{E}(\mathbf{r}) = \mathbf{E}_{\rm in}(\mathbf{r}) + \alpha(\Delta_0)\frac{k_0^2}{\varepsilon_0}\sum_n G(\mathbf{r}, \mathbf{r}_n)\hat{\mathbf{e}}\hat{\mathbf{e}}^\dagger \mathbf{E}(\mathbf{r}_n), \tag{4.29}$$

where k_0 denotes the wavenumber of the transition. This equation can be readily solved using a Fourier transform, assuming that the medium surrounding the lattice is translationally invariant in the plane of the lattice. One obtains

$$\begin{aligned} \mathbf{E}(\mathbf{k}, z) = \quad & \mathbf{E}_{\rm in}(\mathbf{k}, z) + \alpha(\Delta_0)\tfrac{k_0^2}{\varepsilon_0 A} G(\mathbf{k}, z)\hat{\mathbf{e}}\hat{\mathbf{e}}^\dagger \times \\ & \left[\mathbb{I} - \alpha(\Delta_0)\tfrac{k_0^2}{\varepsilon_0 A}\tilde{G}(\mathbf{k})\hat{\mathbf{e}}\hat{\mathbf{e}}^\dagger\right]^{-1} \textstyle\sum_{\mathbf{B}} \mathbf{E}_{\rm in}(\mathbf{k} + \mathbf{B}, 0) \end{aligned} \tag{4.30}$$

where A is the area of the unit cell and

$$\tilde{G}(\mathbf{k}) = \sum_{\mathbf{B}} G(\mathbf{k}+\mathbf{B}, 0), \tag{4.31}$$

where the sum runs over all reciprocal lattice vectors, denoted by $\mathbf{B}$.

For an incident plane wave with momentum $\mathbf{k}$, only a single term contributes to the sum in Eq. (4.30). The plane wave will be Bragg scattered to momenta $\mathbf{k}+\mathbf{B}$. However, for sufficiently small lattice constants, $|\mathbf{k}+\mathbf{B}| > k_0$ for any $\mathbf{B} \neq 0$, such that all nonzero scattering orders are evanescent. In this case, the far field is completely described by

$$\mathbf{E}(\mathbf{k}, z) = \mathbf{E}_{\text{in}}(\mathbf{k}, z) - \frac{3\pi\gamma_{\text{r}}/k_0 A}{\Delta_0 + i\gamma_{\text{nr}}/2 + 3\pi\gamma_{\text{r}}\hat{\mathbf{e}}^\dagger \tilde{G}(\mathbf{k})\hat{\mathbf{e}}/k_0 A} G(\mathbf{k}, z)\hat{\mathbf{e}}\hat{\mathbf{e}}^\dagger \mathbf{E}_{\text{in}}(\mathbf{k}, 0). \tag{4.32}$$

We were able to turn the matrix inversion into a simple division by using the fact that $\hat{\mathbf{e}}\hat{\mathbf{e}}^\dagger$ is a projector. It is straightforward to show that the condition $|\mathbf{k}+\mathbf{B}| > k_0$ is equivalent to $|\mathbf{B}| > 4\pi/\lambda$. For a square lattice, one obtains $a < \lambda/2$, while for a triangular lattice $a < \lambda/\sqrt{3}$.

To simplify Eq. (4.32) further, we consider the special case that the array is placed in free space. The free space Green's function is given by

$$G(\mathbf{k}, z) = \frac{i}{2k_z} e^{ik_z|z|} P_{\pm}(\mathbf{k}), \tag{4.33}$$

where

$$k_z = \sqrt{k_0^2 - |\mathbf{k}|^2} \tag{4.34}$$

and $P_{\pm}(\mathbf{k})$ denotes the projector onto transverse polarizations for waves propagating up ($+$, $z > 0$) or down ($-$, $z < 0$). Explicitly, the $P_{\pm}(\mathbf{k})$ projects onto the two-dimensional space spanned by

$$\hat{\mathbf{s}}(\phi) = \begin{pmatrix} -\sin\phi \\ \cos\phi \\ 0 \end{pmatrix}, \qquad \hat{\mathbf{p}}_{\pm}(\theta, \phi) = \begin{pmatrix} \pm\cos\theta\cos\phi \\ \pm\cos\theta\sin\phi \\ -\sin\theta \end{pmatrix}, \tag{4.35}$$

where we defined the angles θ and ϕ according to

$$k_x = k_0 \sin\theta\cos\phi, \quad k_y = k_0 \sin\theta\sin\phi, \quad k_z = k_0\cos\theta. \tag{4.36}$$

We note that k_z is always taken to have a positive real ($|\mathbf{k}| < k_0$) or imaginary ($|\mathbf{k}| > k_0$) part. When $|\mathbf{k}| < k_0$, all angles are real, and the vector $(k_x, k_y, -k_z)$ is simply the wavevector of the incident wave. We also point out that the Green's function is discontinuous at $z = 0$. Right at $z = 0$, one should take [2]

$$G(\mathbf{k}, 0) = \frac{i}{4k_z} e^{ik_z|z|} \left[P_+(\mathbf{k}) + P_-(\mathbf{k})\right]. \tag{4.37}$$

[2] We further neglect an unimportant δ-function contribution.

We focus on a circularly polarized transition, that is,

$$\hat{\mathbf{e}} = \frac{1}{\sqrt{2}} \begin{pmatrix} 1 \\ i \\ 0 \end{pmatrix}. \tag{4.38}$$

When there is no Bragg scattering, it is easy to see that $\operatorname{Im} \tilde{G}(\mathbf{k}) = \operatorname{Im} G(\mathbf{k}, 0)$ such that

$$\hat{\mathbf{e}}^\dagger \operatorname{Im} \tilde{G}(\mathbf{k}) \hat{\mathbf{e}} = \frac{i}{4k_0} \frac{1 + \cos^2\theta}{\cos\theta}. \tag{4.39}$$

A straightforward calculation further yields

$$P_+(\mathbf{k}) \hat{\mathbf{e}} \hat{\mathbf{e}}^\dagger P_-(\mathbf{k}) = \frac{1}{2}(1 + \cos^2\theta) \hat{\mathbf{v}}_+(\theta, \phi) \hat{\mathbf{v}}_-(\theta, \phi)^\dagger, \tag{4.40}$$

where

$$\hat{\mathbf{v}}_\pm(\theta, \phi) = \frac{1}{\sqrt{1 + \cos^2\theta}} \left[i\hat{\mathbf{s}}(\phi) \pm \cos\theta \hat{\mathbf{p}}_\pm(\theta, \phi) \right]. \tag{4.41}$$

Since $\mathbf{E}_{\text{in}}(\mathbf{k}) = P_-(\mathbf{k}) \mathbf{E}_{\text{in}}(\mathbf{k})$, we thus obtain

$$\mathbf{E}(\mathbf{k}, z) = \left[e^{-ik_z z} - e^{ik_z |z|} \frac{i\Gamma(\theta)/2}{\Delta_0 + \tilde{\Delta}(\theta, \phi) + i\gamma_{\text{nr}}/2 + i\Gamma(\theta)/2} \hat{\mathbf{v}}_\pm(\theta, \phi) \hat{\mathbf{v}}_-(\theta, \phi)^\dagger \right] \mathbf{E}_{\text{in}}(\mathbf{k}, 0), \tag{4.42}$$

where

$$\Gamma(\theta) = \frac{3\pi\gamma_{\text{r}}}{2k_0^2 A} \frac{1 + \cos^2\theta}{\cos\theta} \tag{4.43}$$

and

$$\tilde{\Delta}(\theta, \phi) = \frac{3\pi\gamma_{\text{r}}}{k_0 A} \hat{\mathbf{e}}^\dagger \operatorname{Re} \tilde{G}(\mathbf{k}) \hat{\mathbf{e}}. \tag{4.44}$$

Eq. (4.42) has a simple physical interpretation. The light probes a collective resonance with energy $\tilde{\Delta}$ and radiative linewidth Γ. The vectors $\hat{\mathbf{v}}_\pm$ correspond to projections of the transverse polarizations onto the transition dipole. The response of the lattice is maximized when $\mathbf{E}_{\text{in}} \propto \hat{\mathbf{v}}_-$, which corresponds to an elliptic polarization whose projection onto the xy plane is circular. The expression allows us to immediately read off the reflection and transmission coefficients:

$$r = -\frac{i\Gamma(\theta)/2}{\Delta_0 + \tilde{\Delta}(\theta, \phi) + i\gamma_{\text{nr}}/2 + i\Gamma(\theta)/2} \hat{\mathbf{v}}_+(\theta, \phi) \hat{\mathbf{v}}_-(\theta, \phi)^\dagger, \tag{4.45}$$

$$t = P_- - \frac{i\Gamma(\theta)/2}{\Delta_0 + \tilde{\Delta}(\theta, \phi) + i\gamma_{\text{nr}}/2 + i\Gamma(\theta)/2} \hat{\mathbf{v}}_-(\theta, \phi) \hat{\mathbf{v}}_-(\theta, \phi)^\dagger. \tag{4.46}$$

Both r and t should be thought of as 2×2 matrices acting on the subspaces of transverse polarizations. For a fixed incident polarization $\hat{\mathbf{e}}_{\text{in}}$, we may further compute the intensity reflection and transmission cofficients. They are given by

$$R = \frac{\Gamma(\theta)^2/4}{[\Delta_0 + \tilde{\Delta}(\theta, \phi)]^2 + [\gamma_{\text{nr}} + \Gamma(\theta)]^2/4} \left| \hat{\mathbf{v}}_-(\theta, \phi)^\dagger \hat{\mathbf{e}}_{\text{in}} \right|^2, \tag{4.47}$$

$$T = 1 - \frac{\Gamma(\theta)[\Gamma(\theta) + 2\gamma_{\mathrm{nr}}]/4}{[\Delta_0 + \tilde{\Delta}(\theta,\phi)]^2 + [\gamma_{\mathrm{nr}} + \Gamma(\theta)]^2/4} \left|\hat{\mathbf{v}}_-(\theta,\phi)^\dagger \hat{\mathbf{e}}_{\mathrm{in}}\right|^2 . \tag{4.48}$$

The intensity coefficients satisify $R + T = 1$ when $\gamma_{\mathrm{nr}} = 0$ as required.

In practice, we would like to infer the rotational symmetry of the lattice via the dependence of $\tilde{\Delta}$ on ϕ. Choosing the optimal polarization $\hat{\mathbf{e}}_{\mathrm{in}} = \hat{\mathbf{v}}_-(\theta,\phi)$, the maximum contrast in reflection for a fixed value of θ is given by

$$\Delta R = \frac{\Gamma^2}{4}\left[\frac{1}{(\Delta_0 + \tilde{\Delta}_{\mathrm{min}})^2 + \Gamma^2/4} - \frac{1}{(\Delta_0 + \tilde{\Delta}_{\mathrm{max}})^2 + \Gamma^2/4}\right] \tag{4.49}$$

where $\tilde{\Delta}_{\mathrm{min}} = \min_\phi \tilde{\Delta}(\theta,\phi)$ and similarly for $\tilde{\Delta}_{\mathrm{max}}$. For simplicity we set $\gamma_{\mathrm{nr}} = 0$, which implies that the contrast in transmission is equal to the contrast in reflection. We are free to choose Δ_0 to maximize the contrast. Writing $\Delta_0 = -(\tilde{\Delta}_{\mathrm{min}} + \tilde{\Delta}_{\mathrm{max}})/2 + \delta$, the contrast can be expressed as

$$\Delta R = \frac{\delta\bar{\Delta}/\Gamma^2}{(\delta^2/\Gamma^2 - \bar{\Delta}^2/\Gamma^2 + 1/4)^2 + \bar{\Delta}^2/\Gamma^2}, \tag{4.50}$$

where $\bar{\Delta} = (\tilde{\Delta}_{\mathrm{max}} - \tilde{\Delta}_{\mathrm{min}})/2$. In the limit $\bar{\Delta} \ll \Gamma$, the expression simplifies to

$$\Delta R \approx \frac{\delta\bar{\Delta}/\Gamma^2}{(\delta^2/\Gamma^2 + 1/4)^2} \tag{4.51}$$

It is easy to show that the contrast is maximized by choosing

$$\delta = \frac{1}{2\sqrt{3}}\Gamma, \tag{4.52}$$

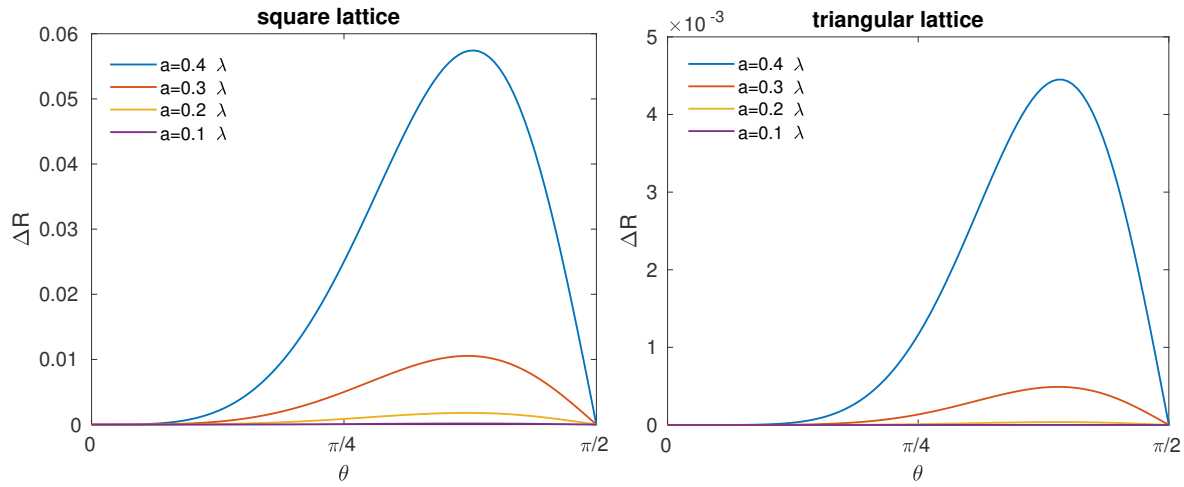

Figure 4.11: Reflection contrast according to Eq. (4.53) for a square and triangular lattice and various lattice constants a.

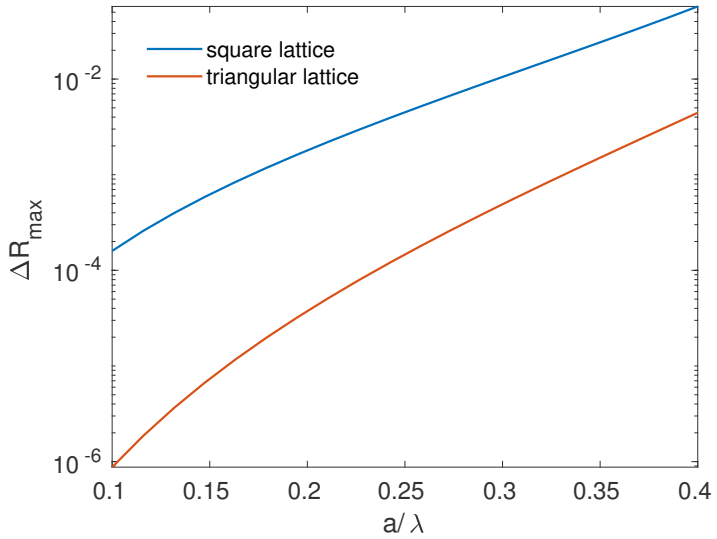

Figure 4.12: Maximum value of ΔR as a function of lattice constant.

yielding

$$\Delta R \approx \frac{3\sqrt{3}}{2}\frac{\bar{\Delta}}{\Gamma}. \tag{4.53}$$

The value of $\bar{\Delta}$ can be computed numerically. The results for a square and triangular lattice are plotted below.

As a final remark, we mention that by measuring the transmission coefficient for a component of the electric field that is neither parallel nor perpendicular to the incident field, it is possible to observe dispersive (asymmetric) line shapes. Such features could potentially enhance the sensitivity.

Chapter 5

Outlook

In this thesis, we have outlined several strategies for the implementation of scalable lattices for electrons and other quasiparticles in semiconductors. These theoretical proposals offer a fresh platform for controllable and scalable quantum systems in semiconductors. Furthermore, as we have discussed in Chapters 2-4, they may enable quantum simulations of many-body systems with long-range interactions. In the first part of this thesis, we have borrowed concepts from quantum optics and applied them to solid-state settings. In doing so, we have developed fruitful solid-state analogies of well-established AMO platforms, thereby finding quantum acoustical equivalents of optical lattices and ion Paul traps. In the second part of this thesis, we have studied how self-assembled electron lattices in two-dimensional semiconductors may be probed with tools from quantum optics. To this end, we have studied cooperative resonances of light scattered by quantum Wigner crystals. This may prove useful for future experiments, that aim at the observation of Wigner crystals in two-dimensional materials.

Finally, we conclude with possible future steps that go beyond the results presented in this thesis. For clarity, we will group them into two categories: (i) quantum acoustical systems and (ii) novel phenomena in two-dimensional materials.

Quantum acoustical systems

In quantum acoustics, fundamental sound-matter interactions at the quantum level are studied. Quantum acoustical systems bear strong similarities with quantum optical systems. However, there are also striking differences between the two that may be capitalized on in future research projects.

Acoustically defined traps and lattices.—As outlined in Chapter 2, one limitation for trapping quasiparticles in SAW standing wave lattices arises from their low effective mass and the ensuing instability of the time-averaged trap, a well-known phenomenon in the trapped-ion community. Future work may focus on developing systematic approaches to theoretically tackle these problems in order to render the realization of acoustic traps, lattices and related systems more realistic. This may enable a new class of experiments with well-controlled lattice systems of electrons, holes, trions or other semiconductor quasiparticles. One approach may consist in the investigation of acoustic traps and lattices

in quantum Hall systems, in which quasiparticles have very large effective masses and may therefore be more amenable to ponderomotive trapping. Since the lattice constant of a SAW-defined acoustic lattice matches well the expected magnetic localization length $l_\mathrm{B} = \sqrt{\hbar/(eB)}$ at magnetic field strengths $B < 1$ T, a filling factor of one of the lowest Landau level corresponds to a filling factor of the order of one in the acoustic lattice. Acoustically trapped electrons exposed to a magnetic field can be described by a minimal-coupling Hamiltonian of the form $H = (\mathbf{p} + e\mathbf{A})^2 + V_\mathrm{SAW}(t)$ with a time-dependent SAW driving field. Within a theoretical Floquet framework, one could analyze the impact of an external magnetic field and the appearance of a new energy scale, i.e. the cyclotron frequency $\omega_\mathrm{B} = eB/m$, on the stability of SAW-driven acoustic lattices.

Giant atoms.—Usually, when studying light-matter interactions in quantum optics and AMO systems, the wavelength of light exceeds the size of the atoms it interacts with by far, justifying the electric dipole approximation. On the contrary, the wavelength of surface-acoustic waves can easily exceed the size of superconducting qubits to which they can be coupled piezoelectrically. As has been pointed out before [93], this may give rise to interesting new physical effects, including non-exponential decay of a giant atom coupled to a waveguide [92]. This provides an exciting playground for the study of non-Markovian open quantum systems which are characterized by an information backflow from the environment to the system. While in quantum optics non-Markovianity is typically related to the structure of the environment, in the quantum acoustical setting its origin is due to the finite time it takes the sound (phonon) to propagate at speed v_s between different connection points, separated by a distance d, of the superconducting qubit to the waveguide. This time delay $\Delta t = d/v_\mathrm{s}$ may be of the same order or smaller than the relaxation time of the qubit and can be deterministically controlled by choosing the position of the connection points to the waveguide. The breakdown of Markovianity in the above sense may enable studies of new physical effects arising from these systems. One interesting direction is a thorough study of SAW waveguide-mediated interactions between N giant atoms in the non-Markovian regime. In contrast to previous work, memory effects in the open-system dynamics need to be taken into account and it is no longer possible to derive a Lindblad quantum master equation within the typically justified Born-Markov approximation. Moreover, the flexibility of the circuit design allows for unusual scenarios where superconducting transmon qubits are coupled at many connection points to the waveguide. In general, the properties of a system of coupled quantum emitters may differ significantly from those of single quantum emitters. This may give rise to subradiant and superradiant emission of light, where the decay rate of collective excitations is either reduced or enhanced due to mutual correlations. These collective effects find several key applications in quantum communication, metrology and quantum memories. In quantum acoustical systems where SAWs are coupled to multiple giant atoms in a waveguide or cavity QAD setting, it will be interesting to study cases where collective decay of multiple artificial atoms leads to subradiant and superradiant emission of sound. Giant atoms can also be coupled to microwave photons in transmission lines, yielding a waveguide-QED setup with giant atoms. In these setttings the Markov condition may hold, but the mere fact that these artificial atoms can be coupled to a waveguide at multiple connection points (which

are farther than a wavelength apart) leads to exotic behaviour such as decoherence-free interactions between two giant atoms [93]. In the future, the emergence of collective effects in these systems may be studied further, eventually taking into account the differences between real and artificial atoms. Another interesting extension of the typical quantum optics scenario would consist in the investigation of multi-level giant atoms coupled to waveguides.

Novel phenomena in two-dimensional materials

Two-dimensional materials such as (i) transition-metal dichalcogenides (TMDs) and (ii) graphene are prime candidates for the study of strongly correlated electrons. TMDs (i) have received a lot of attention lately and are becoming a main research focus in solid-state quantum optics and condensed-matter physics. Quasi-2D systems composed of bilayers of graphene (ii) have recently been demonstrated to possess a rich phase diagram that hosts unconventional superconducting phases [347, 348]. In the following, we will outline two possible research lines that aim at exploring novel phenomena in two-dimensional systems with analytical and numerical tools from quantum optics.

Multi-spin exchange Hamiltonians.—In physics, many-body interactions may arise from fundamental two-body interactions. In quantum information processing, many-body interactions are relevant in different areas, including quantum error correction, quantum simulation and quantum chemistry. However, the implementation of suitable higher-order many-body interactions is very challenging, given that the strength of these interactions should be comparable with and should be controlled independently from lower-order interactions. Various physical systems have been considered for the implementation of quantum many-body interactions, including trapped ions [349], cold atoms in optical lattices [350], polar molecules [351] and superconducting qubits [352]. It still remains a grand challenge to engineer higher-order many-body interactions in scalable quantum systems. The aim of a follow-up research project of Chapter 4 could be to propose and analyze a TMD-based system in which higher-order many-body interactions naturally occur. At low temperature, electronic systems are governed by spin-exchange interactions. Near the melting point of a two-dimensional Wigner crystal, the spin-exchange energy increases as well as the relative contribution of large loops involving higher-order many-body interactions. It has already been pointed out in the 1960s that this can give rise to the emergence of effective multi-spin exchange Hamiltonians [308]. The magnitude of the different higher-order contributions can be calculated within a path-integral formalism. At low densities, semiclassical WKB approximations enable the derivation of simple expressions for the exchange coupling strength. One may analyze in detail TMD-based Wigner crystals in which significant higher-order interactions between more than two spins could naturally occur.

Bilayer systems.—Recent breakthrough experiments with bilayer graphene have sparked a widespread interest in the study of crystal bilayers. Twisted bilayer graphene was shown to host superconductivity when the rotation angle between the two graphene layers is tuned to special *magic angles*, at which isolated and almost flat bands appear in the electronic band structure of the system. Since the first discovery of unconventional superconductivity and correlated insulating behaviour in twisted bilayer graphene, the underlying physical

phenomena leading to these unexpected results are being heavily debated. Very recently, similar correlated phenomena have been reported in twisted bilayer TMDs [353] and a proposal for cold-atom implementations of twisted-bilayer crystals has been put forward [354]. In the future, one may analyze optical signatures of twisted bilayer systems. Single layers of two-dimensional atomic arrays with sub-wavelength lattice spacings have been shown to display a strong optical response and even total reflection at certain *magic lattice constants* (see Chapter 4). An interesting question to ask in this context is how the optical response of a multi-layer system behaves, e.g. as a function of the twist angle and inter-layer separation. Transmission and reflection of such systems may be investigated numerically.

These ideas, together with the results presented in this thesis, are examples of the vast amount of interesting novel phenomena to be discovered at the interface of quantum optics, quantum information and solid-state physics.

Bibliography

[1] P. Delsing, A. N. Cleland, M. J. A. Schuetz, J. Knörzer, G. Giedke, J. I. Cirac, K. Srinivasan, M. Wu, K. C. Balram, C. Bäuerle, T. Meunier, C. J. B. Ford, P. V. Santos, E. Cerda-Méndez, H. Wang, H. J. Krenner, E. D. S. Nysten, M. Weiß, G. R. Nash, L. Thevenard, C. Gourdon, P. Rovillain, M. Marangolo, J.-Y. Duquesne, G. Fischerauer, W. Ruile, A. Reiner, B. Paschke, D. Denysenko, D. Volkmer, A. Wixforth, H. Bruus, M. Wiklund, J. Reboud, J. M. Cooper, Y. Fu, M. S. Brugger, F. Rehfeldt, and C. Westerhausen, *The 2019 surface acoustic waves roadmap*, J. Phys. D **52**, 353001 (2019).

[2] M. J. A. Schuetz, J. Knörzer, G. Giedke, L. M. K. Vandersypen, M. D. Lukin, and J. I. Cirac, *Acoustic Traps and Lattices for Electrons in Semiconductors*, Phys. Rev. X **7**, 041019 (2017).

[3] J. Knörzer, M. J. A. Schuetz, G. Giedke, H. Huebl, M. Weiler, M. D. Lukin, and J. I. Cirac, *Solid-state magnetic traps and lattices*, Phys. Rev. B **97**, 235451 (2018).

[4] J. Knörzer, M. J. A. Schuetz, G. Giedke, D. S. Wild, K. De Greve, R. Schmidt, M. D. Lukin, and J. I. Cirac, *Wigner crystals in two-dimensional transition-metal dichalcogenides: Spin physics and readout*, Phys. Rev. B **101**, 125101 (2020).

[5] P. Nalbach, J. Knörzer, and S. Ludwig, *Nonequilibrium Landau-Zener-Stueckelberg spectroscopy in a double quantum dot*, Phys. Rev. B **87**, 165425 (2013).

[6] S. Krönke, J. Knörzer, and P. Schmelcher, *Correlated quantum dynamics of a single atom collisionally coupled to an ultracold finite bosonic ensemble*, New J. Phys. **17**, 053001 (2015).

[7] J. Knörzer, C. Fey, H. R. Sadeghpour, and P. Schmelcher, *Control of multiple excited image states around segmented carbon nanotubes*, J. Chem. Phys. **143**, 204309 (2015).

[8] C. Fey, H. Jabusch, J. Knörzer, and P. Schmelcher, *Highly excited electronic image states of metallic nanorings*, J. Chem. Phys. **146**, 194704 (2017).

[9] M. Kremser, M. Brotons-Gisbert, J. Knörzer, J. Gückelhorn, M. Meyer, M. Barbone, A. V. Stier, B. D. Gerardot, K. Müller, and J. F. Finley, *Discrete Interactions*

between a few Interlayer Excitons Trapped at a $MoSe_2$-WSe_2 Heterointerface, npj 2D Mat. and Appl. **4**, 8 (2020).

[10] M. Planck, *Zur Theorie des Gesetez der Energieverteilung im Normalspectrum*, Verhandl. der Deutschen Physikal. Gesellsch. **2**, 237 (1900).

[11] A. Einstein, *Über einen die Erzeugung und Verwandlung des Lichtes betreffenden heuristischen Gesichtspunkt*, Ann. Phys. **17**, 132 (1905).

[12] A. M. Turing, *On computable numbers, with an application to the Entscheidungsproblem*, Proc. Lond. Math. Soc. **42**, 161 (1937).

[13] A. M. Turing, *Computing Machinery and Intelligence*, Mind **59**, 433 (1950).

[14] R. Landauer, *The physical nature of information*, Phys. Lett. A **217**, 188 (1996).

[15] J. P. Dowling, and G. J. Milburn, *Quantum technology: the second quantum revolution*, Phil. Trans. R. Soc. Lond. A **361**, 1655 (2003).

[16] A. Einstein, B. Podolsky, and N. Rosen, *Can Quantum-Mechanical Description of Physical Reality Be Considered Complete?*, Phys. Rev. **47**, 777 (1935).

[17] N. Gisin, and R. Thew, *Quantum communication*, Nat. Phot. **1**, 165 (2007).

[18] D. Gottesman, T. Jennewein, and S. Croke, *Longer-Baseline Telescopes Using Quantum Repeaters*, Phys. Rev. Lett. **109**, 070503 (2012).

[19] C. H. Bennett, and and G. Brassard, *Quantum cryptography: Public key distribution and coin tossing*, Proceedings of the IEEE International Conference on Computers, Systems, and Signal Processing, Bangalore, pp. 175 (1984).

[20] Y. Yu, F. Ma, X.-Y. Luo, B. Jing, P.-F. Sun, R.-Z. Fang, C.-W. Yang, H. Liu, M.-Y. Zheng, X.-P. Xie, W.-J. Zhang, L.-X. You, Z. Wang, T.-Y. Chen, Q. Zhang, X.-H. Bao, and J.-W. Pan, *Entanglement of two quantum memories via fibres over dozens of kilometres*, Nature **578**, 240 (2020).

[21] S. Wehner, D. Elkouss, and R. Hanson, *Quantum internet: A vision for the road ahead*, Science **362**, 303 (2018).

[22] H.-J. Briegel, W. Dür, J. I. Cirac, and P. Zoller, *Quantum Repeaters: The Role of Imperfect Local Operations in Quantum Communication*, Phys. Rev. Lett. **81**, 5932 (1998).

[23] M. K. Bhaskar, R. Riedinger, B. Machielse, D. S. Levonian, C. T. Nguyen, E. N. Knall, H. Park, D. Englund, M. Loncar, D. D. Sukachev, and M. D. Lukin, *Experimental demonstration of memory-enhanced quantum communication*, Nature **580**, 60 (2020).

[24] L. M. Duan, M. D. Lukin, J. I. Cirac, and P. Zoller, *Long-distance quantum communication with atomic ensembles and linears optics* Nature **414**, 413 (2001).

[25] B. P. Abbott, *et al.* (LIGO Scientific Collaboration and Virgo Collaboration), *Observation of Gravitational Waves from a Binary Black Hole Merger*, Phys. Rev. Lett. **116**, 061102 (2016).

[26] G. E. Marti, R. B. Hutson, A. Goban, S. L. Campbell, N. Poli, and J. Ye, *Imaging Optical Frequencies with* 100 μ*Hz Precision and* 1.1 μ*m Resolution*, Phys. Rev. Lett. **120**, 103201 (2018).

[27] S. Schreppler, N. Spethmann, N. Brahms, T. Bottler, M. Barrios, and D. M. Stamper-Kurn, *Optically measuring force near the standard quantum limit*, Science **344**, 1486 (2014).

[28] J. Chaste, A. Eichler, J. Moser, G. Ceballos, R. Rurali, and A. Bachtold, *A Nanomechanical Mass Sensor With Yoctogram Resolution*, Nature Nanotechnol. **7**, 301 (2012).

[29] W. Wasilewski, K. Jensen, H. Krauter, J. J. Renema, M. V. Balabas, and E. S. Polzik, *Quantum Noise Limited and Entanglement-Assisted Magnetometry*, Phys. Rev. Lett. **104**, 133601 (2010).

[30] V. Giovannetti, S. Lloyd, and L. Maccone, *Quantum-Enhanced Measurements: Beating the Standard Quantum Limit*, Science **306**, 1130 (2004).

[31] L. Pezzè, A. Smerzi, M. K. Oberthaler, R. Schmied, and P. Treutlein, *Quantum metrology with nonclassical states of atomic ensembles*, Rev. Mod. Phys. **90**, 035005 (2018).

[32] S. Slussarenko, M. M. Weston, H. M. Chrzanowski, L. K. Shalm, V. B. Verma, S. Woo Nam, and G. J. Pryde, *Unconditional violation of the shot-noise limit in photonic quantum metrology*, Nat. Photon. **11**, 700 (2017).

[33] F. Acernese *et al.* (Virgo Collaboration), *Increasing the Astrophysical Reach of the Advanced Virgo Detector via the Application of Squeezed Vacuum States of Light*, Phys. Rev. Lett. **123**, 231108 (2019).

[34] O. Hosten, N. J. Engelsen, R. Krishnakumar, and M. A. Kasevich, *Measurement noise 100 times lower than the quantum-projection limit using entangled atoms* Nature **529**, 505 (2016).

[35] D. Le Sage, K. Arai, D. R. Glenn, S. J. DeVience, L. M. Pham, L. Rahn-Lee, M. D. Lukin, A. Yacoby, A. Komeili, and R. L. Walsworth, *Optical magnetic imaging of living cells*, Nature **496**, 486 (2013).

[36] S. Rajendran, N. Zobrist, A. O. Sushkov, R. Walsworth, and M. D. Lukin, *A method for directional detection of dark matter using spectroscopy of crystal defects*, Phys. Rev. D **96**, 035009 (2017).

[37] P. Benioff, *The computer as a physical system: A microscopic quantum mechanical Hamiltonian model of computers as represented by Turing machines*, J. Stat. Phys. **22**, 563 (1980).

[38] D. Deutsch, *Quantum theory, the Church–Turing principle and the universal quantum computer*, Proc. R. Soc. Lond. A **400**, 97 (1985).

[39] D. P. DiVincenzo, *Two-bit gates are universal for quantum computation*, Phys. Rev. A **51**, 1015 (1995).

[40] T. Sleator, and H. Weinfurter, *Realizable Universal Quantum Logic Gates*, Phys. Rev. Lett. **74**, 4087 (1995).

[41] J. I. Cirac and P. Zoller, *Quantum Computations with Cold Trapped Ions*, Phys. Rev. Lett **74**, 4091 (1995).

[42] D. Loss, and D. P. DiVincenzo, *Quantum computation with quantum dots*, Phys. Rev. A **57**, 120 (1998).

[43] B. E. Kane, *A silicon-based nuclear spin quantum computer*, Nature **393**, 133 (1998).

[44] S. Asaad, V. Mourik, B. Joecker, M. A. I. Johnson, A. D. Baczewski, H. R. Firgau, M. T. Madzik, V. Schmitt, J. J. Pla, F. E. Hudson, K. M. Itoh, J. C. McCallum, A. S. Dzurak, A. Laucht, and A. Morello, *Coherent electrical control of a single high-spin nucleus in silicon*, Nature **579**, 205 (2020).

[45] Y. Nakamura, Y. A. Pashkin, and J. S. Tsai, *Coherent control of macroscopic quantum states in a single Cooper-pair box*, Nature **398**, 786 (1999).

[46] Y. Makhlin, G. Schön, and A. Shnirman, *Josephson-junction qubits with controlled couplings*, Nature **386**, 305 (1999).

[47] P. W. Shor, *Polynomial-Time Algorithms for Prime Factorization and Discrete Logarithms on a Quantum Computer*, SIAM J. Comput. **26**, 1484 (1997).

[48] L. K. Grover, *A fast quantum mechanical algorithm for database search*, Proceedings of the 28th Annual ACM Symposium on the Theory of Computing, pp. 212 (1996).

[49] A. W. Harrow, A. Hassidim, and S. Lloyd, *Quantum algorithm for solving linear systems of equations*, Phys. Rev. Lett. **103**, 150502 (2008).

[50] L. M. K. Vandersypen, M. Steffen, G. Breyta, C. S. Yannoni, M. H. Sherwood, and I. L. Chuang, *Experimental realization of Shor's quantum factoring algorithm using nuclear magnetic resonance*, Nature **414**, 883 (2001).

[51] E. Martin-Lopez, A. Laing, T. Lawson, R. Alvarez, X.-Q. Zhou, and J. L. O'Brien, *Experimental realization of Shor's quantum factoring algorithm using qubit recycling*, Nat. Photon. **6**, 773 (2012).

[52] J. Preskill, *Quantum Computing in the NISQ era and beyond*, Quantum **2**, 79 (2018).

[53] F. Arute, K. Arya, R. Babbush *et al.*, *Quantum supremacy using a programmable superconducting processor*, Nature **574**, 505 (2019).

[54] M. Tillmann, B. Dakic, R. Heilmann, S. Nolte, A. Szameit, and P. Walther, *Experimental boson sampling*, Nat. Photon. **7**, 540 (2013).

[55] R. Feynman, *Simulating Physics with Computers*, Int. J. Th. Phys. **21**, 467 (1982).

[56] Y. I. Manin, *Computable and Noncomputable* (in Russian), Sovetskoye Radio, Moscow (1980).

[57] J. I. Cirac and P. Zoller, *Goals and opportunities in quantum simulation*, Nat. Phys. **8**, 264 (2012).

[58] S. Somaroo, C. H. Tseng, T. F. Havel, R. Laflamme, and D. G. Cory, *Quantum Simulations on a Quantum Computer*, Phys. Rev. Lett. **82**, 5381 (1999).

[59] M. Greiner, O. Mandel, T. Esslinger, T. W. Hänsch, and I. Bloch, *Quantum phase transition from a superfluid to a Mott insulator in a gas of ultracold atoms*, Nature **415**, 39 (2002).

[60] H. Bernien, S. Schwartz, A. Keesling, H. Levine, A. Omran, H. Pichler, S. Choi, A. S. Zibrov, M. Endres, M. Greiner, V. Vuletić, and M. D. Lukin, *Probing many-body dynamics on a* 51*-atom quantum simulator*, Nature **551**, 579 (2017).

[61] H. Pichler, S.-T. Wang, L. Zhou, S. Choi, and M. D. Lukin, *Quantum Optimization for Maximum Independent Set Using Rydberg Atom Arrays*, Preprint available on *arXiv*:1808.10816 (2018).

[62] T. Hensgens, T. Fujita, L. Janssen, Xiao Li, C. J. Van Diepen, C. Reichl, W. Wegscheider, S. Das Sarma, and L. M. K. Vandersypen, *Quantum simulation of a Fermi-Hubbard model using a semiconductor quantum dot array*, Nature **548**, 73 (2017).

[63] J. P. Dehollain, U. Mukhopadhyay, V. P. Michal, Y. Wang, B. Wunsch, C. Reichl, W. Wegscheider, M. S. Rudner, E. Demler, and L. M. K. Vandersypen, *Nagaoka ferromagnetism observed in a quantum dot plaquette*, Nature **579**, 528 (2020).

[64] J. Argüello-Luengo, A. González-Tudela, T. Shi, P. Zoller, and J. I. Cirac, *Analogue quantum chemistry simulation*, Nature **574**, 215 (2019).

[65] C. Hempel, C. Maier, J. Romero, J. McClean, T. Monz, H. Shen, P. Jurcevic, B. P. Lanyon, P. Love, R. Babbush, A. Aspuru-Guzik, R. Blatt, and C. F. Roos, *Quantum Chemistry Calculations on a Trapped-Ion Quantum Simulator*, Phys. Rev. X **8**, 031022 (2018).

[66] G. Kurizki, P. Bertet, Y. Kubo, K. Mølmer, D. Petrosyan, P. Rabl, and J. Schmiedmayer, *Quantum technologies with hybrid systems*, PNAS **112**, 3866 (2015).

[67] D. Morgan, *Surface Acoustic Wave Filters* (Academic Press, Boston, 2007).

[68] S. Datta, *Surface Acoustic Wave Devices* (Prentice-Hall, Upper Saddle River, NJ, 1986).

[69] V. I. Alshits, A. N. Darinskii, and J. Lothe, *On the existence of surface waves in half-infinite anisotropic elastic media with piezoelectric piezomagnetic properties*, Wave Motion **16**, 265 (1992).

[70] V. I. Talyanskii, J. M. Shilton, M. Pepper, C. G. Smith, C. J. B. Ford, E. H. Linfield, D. A. Ritchie, and G. A. C. Jones, *Single-electron transport in a one-dimensional channel by high-frequency surface acoustic waves*, Phys. Rev. B **56**, 15180 (1997).

[71] J. Cunningham, V. I. Talyanskii, J. M. Shilton, M. Pepper, A. Kristensen, and P. E. Lindelof, *Single-electron acoustic charge transport on shallow-etched channels in a perpendicular magnetic field*, Phys. Rev. B **62**, 1564 (2000).

[72] S. Hermelin, S. Takada, M. Yamamoto, S. Tarucha, A. D. Wieck, L. Saminadayar, C. Bäuerle, and T. Meunier, *Electrons surfing on a sound wave as a platform for quantum optics with flying electrons*, Nature **477**, 435 (2011).

[73] R. P. G. McNeil, M. Kataoka, C. J. B. Ford, C. H. W. Barnes, D. Anderson, G. A. C. Jones, I. Farrer, and D. A. Ritchie, *On-demand single-electron transfer between distant quantum dots*, Nature **477**, 439 (2011).

[74] C. Bäuerle, D. C Glattli, T. Meunier, F. Portier, P. Roche, P. Roulleau, S. Takada, and X. Waintal, *Coherent control of single electrons: a review of current progress*, Rep. Prog. Phys. **81**, 056503 (2018).

[75] A. Bienfait, K. J. Satzinger, Y. P Zhong, H.-S. Chang, M.-H. Chou, C. R. Conner, É. Dumur, J. Grebel, G. A. Peairs, R. G. Povey, and A. N. Cleland, *Phonon-mediated quantum state transfer and remote qubit entanglement*, Science **364**, 368 (2019).

[76] C. Wiele, F. Haake, C. Rocke, and A. Wixforth, *Photon trains and lasing: The periodically pumped quantum dot*, Phys. Rev. A **58**, R2680(R) (1998).

[77] C. L. Foden, V. I. Talyanskii, G. J. Milburn, M. L. Leadbeater, and M. Pepper, *High-frequency acousto-electric single-photon source*, Phys. Rev. A **62**, 011803(R) (2000).

[78] B. Bertrand, S. Hermelin, S. Takada, M. Yamamoto, S. Tarucha, A. Ludwig, A. D. Wieck, C. Bäuerle, and T. Meunier, *Fast spin information transfer between distant quantum dots using individual electrons*, Nat. Nanotechn. **11**, 672 (2016).

[79] S. Takada, H. Edlbauer, H. V. Lepage, J. Wang, P.-A. Mortemousque, G. Georgiou, C. H. W. Barnes, C. J. B. Ford, M. Yuan, P. V. Santos, X. Waintal, A. Ludwig, A. D. Wieck, M. Urdampilleta, T. Meunier, and C. Bäuerle, *Sound-driven single-electron transfer in a circuit of coupled quantum rails*, Nat. Commun. **10**, 4557 (2019).

[80] R. Ito, S. Takada, A. Ludwig, A. D. Wieck, S. Tarucha, and M. Yamamoto, *Coherent beam splitting of flying electrons driven by a surface acoustic wave*, Preprint available on *arXiv*:2004.11553 (2020).

[81] M. J. A. Schuetz, E. M. Kessler, G. Giedke, L. M. K. Vandersypen, M. D. Lukin, and J. I. Cirac, *Universal Quantum Transducers Based on Surface Acoustic Waves*, Phys. Rev. X **5**, 031031 (2015).

[82] D. A. Golter, T. Oo, M. Amezcua, K. A. Stewart, and H. Wang, *Optomechanical Quantum Control of a Nitrogen-Vacancy Center in Diamond*, Phys. Rev. Lett **116**, 143602 (2016).

[83] D. A. Golter, T. Oo, M. Amezcua, I. Lekavicius, K. A. Stewart, and H. Wang, *Coupling a Surface Acoustic Wave to an Electron Spin in Diamond via a Dark State*, Phys. Rev. X **6**, 041060 (2016).

[84] Y.-I. Sohn, S. Meesala, B. Pingault, H. A. Atikian, J. Holzgrafe, M. Gündoğan, C. Stavrakas, M. J. Stanley, A. Sipahigil, J. Choi, M. Zhang, J. L. Pacheco, J. Abraham, E. Bielejec, M. D. Lukin, M. Atatüre, and M. Loncar , *Controlling the coherence of a diamond spin qubit through its strain environment*, Nat. Commun. **9**, 2012 (2018).

[85] M.-A. Lemonde, S. Meesala, A. Sipahigil, M. J. A. Schuetz, M. D. Lukin, M. Loncar, and P. Rabl, *Phonon networks with silicon-vacancy centers in diamond waveguides*, Phys. Rev. Lett. **120**, 213603 (2018).

[86] M. V. Gustafsson, P. V. Santos, G. Johansson, and P. Delsing, *Local probing of propagating acoustic waves in a gigahertz echo chamber*, Nat. Phys. **8**, 338 (2012).

[87] M. V. Gustafsson, T. Aref, A. F. Kockum, M. K. Ekström, G. Johansson, and P. Delsing, *Propagating phonons coupled to an artificial atom*, Science **346**, 207 (2014).

[88] R. Manenti, A. F. Kockum, A. Patterson, T. Behrle, J. Rahamim, G. Tancredi, F. Nori, and P. J. Leek, *Circuit quantum acoustodynamics with surface acoustic waves*, Nat. Commun. **8**, 975 (2017).

[89] A. N. Bolgar, J. I. Zotova, D. D. Kirichenko, I. S. Besedin, A. V. Semenov, R. S. Shaikhaidarov, and O. V. Astafiev, *Quantum Regime of a Two-Dimensional Phonon Cavity*, Phys. Rev. Lett. **120**, 223603 (2018).

[90] B. A. Moores, L. R. Sletten, J. J. Viennot, and K. W. Lehnert, *Cavity Quantum Acoustic Device in the Multimode Strong Coupling Regime*, Phys. Rev. Lett. **120**, 227701 (2018).

[91] K. J. Satzinger, Y. P. Zhong, H.-S. Chang, G. A. Peairs, A. Bienfait, Ming-Han Chou, A. Y. Cleland, C. R. Conner, É. Dumur, J. Grebel, I. Gutierrez, B. H. November, R. G. Povey, S. J. Whiteley, D. D. Awschalom, D. I. Schuster, and A. N. Cleland, *Quantum control of surface acoustic wave phonons*, Nature **563**, 661 (2018).

[92] G. Andersson, B. Suri, L. Guo, T. Aref, and P. Delsing, *Non-exponential decay of a giant artificial atom*, Nat. Phys. **15**, 1123 (2019).

[93] A. F. Kockum, *Quantum optics with giant atoms - the first five years*, Preprint available on *arXiv*:1912.13012 (2019).

[94] K. S. Novoselov, A. K. Geim, S. V. Morozov, D. Jiang, Y. Zhang, S. V. Dubonos, I. V. Grigorieva, and A. A. Firsov, *Electric Field Effect in Atomically Thin Carbon Films*, Science **306**, 666 (2004).

[95] A. K. Geim, *Random walk to graphene*, Nobel lecture 2010.

[96] A. Splendiani, L. Sun, Y. Zhang, T. Li, J. Kim, C.-Y. Chim, G. Galli, and F. Wang, *Emerging Photoluminescence in Monolayer MoS_2*, Nano Lett. **10**, 1271 (2010).

[97] P. Cudazzo, I. V. Tokatly, and R. Rubio, *Dielectric screening in two-dimensional insulators: Implications for excitonic and impurity states in graphane*, Phys. Rev. B **84**, 085406 (2011).

[98] Z. Jiang, Z. Liu, Y. Li, and W. Duan, *Scaling Universality between Band Gap and Exciton Binding Energy of Two-Dimensional Semiconductors*, Phys. Rev. Lett. **118**, 266401 (2017).

[99] G. Wang, A. Chernikov, M. M. Glazov, T. F. Heinz, X. Marie, T. Amand, and B. Urbaszek, *Colloquium: Excitons in atomically thin transition metal dichalcogenides*, Rev. Mod. Phys. **90**, 021001 (2018).

[100] T. Mueller, and E. Malic, *Exciton physics and device applications of two-dimensional transition metal dichalcogenide semiconductors*, npj 2D Mat. and Appl. **2**, 29 (2018).

[101] S. Manzeli, D. Ovchinnikov, D. Pasquier, O. V. Yazyev, and A. Kis, *2D transition metal dichalcogenides*, Nat. Rev. Mater. **2**, 17033 (2017).

[102] A. Ashkin, *History of optical trapping and manipulation of small-neutral particle, atoms, and molecules*, IEEE J. Sel. Top. Quantum Electron. **6**, 841 (2000).

[103] M. J. Lang and S. M. Block, *Laser-based optical tweezers*, Am. J. Phys. **71**, 201 (2003).

[104] M. H. Anderson, J. R. Ensher, M. R. Matthews, C. E. Wieman, and E. A. Cornell, *Observation of bose-einstein condensation in a dilute atomic vapor*, Science **269**, 198 (1995).

[105] C. C. Bradley, C. A. Sackett, J. J. Tollett, and R. G. Hulet, *Evidence of Bose-Einstein Condensation in an Atomic Gas with Attractive Interactions*, Phys. Rev. Lett. **75**, 1687 (1995).

[106] K. B. Davis, M.-O. Mewes, M. R. Andrews, N. J. van Druten, D. S. Durfee, D. M. Kurn, and W. Ketterle, *Bose-Einstein Condensation in a Gas of Sodium Atoms*, Phys. Rev. Lett. **75**, 3969 (1995).

[107] R. Blatt and C. F. Roos, *Quantum simulations with trapped ions*, Nat. Phys. **8**, 277 (2012).

[108] I. Bloch, J. Dalibard, W. Zwerger, *Many-body physics with ultracold gases*, Rev. Mod. Phys. **80**, 885 (2008).

[109] I. Bloch, J. Dalibard, and S. Nascimbène, *Quantum simulations with ultracold quantum gases*, Nat. Phys. **8**, 267 (2012).

[110] R. Hanson, L. P. Kouwenhoven, J. R. Petta, S. Tarucha, and L. M. K. Vandersypen, *Spins in few-electron quantum dots*, Rev. Mod. Phys. **79**, 1217 (2007).

[111] M. J. A. Schuetz, M. G. Moore, and C. Piermarocchi, *Trionic optical potential for electrons in semiconductors*, Nat. Phys. **6**, 919 (2010).

[112] J. Cunningham, V. I. Talyanskii, J. M. Shilton, M. Pepper, M. Y. Simmons, and D. A. Ritchie, *Single-electron acoustic charge transport by two counterpropagating surface acoustic wave beams*, Phys. Rev. B **60**, 4850 (1999).

[113] J. A. H. Stotz, R. Hey, P. V. Santos, and K. H. Ploog, *Coherent spin transport through dynamic quantum dots*, Nature Mat. **4**, 585 (2005).

[114] C. J. B. Ford, *Transporting and manipulating single electrons in surface-acoustic-wave minima*, Phys. Status Solidi B **254**, 1600658 (2017)

[115] M. M. de Lima and P. V. Santos, *Modulation of photonic structures by surface acoustic waves*, Rep. Prog. Phys. **68**, 1639 (2005).

[116] M. M. de Lima, F. Alsina, W. Seidel, and P. V. Santos, *Focusing of surface-acoustic-wave fields on (100) GaAs surfaces*, J. App. Phys. **94**, 7848 (2003).

[117] X. Ding, P. Li, S.-C. S. Lin, Z. S. Stratton, N. Nama, F. Guo, D. Slotcavage, X. Mao, J. Shi, F. Costanzoa, and T. J. Huang, *Surface acoustic wave microfluidics*, Lab Chip **13**, 3626 (2013).

[118] E. A. Cerda-Méndez, D. N. Krizhanovskii, M. Wouters, R. Bradley, K. Biermann, K. Guda, R. Hey, P. V. Santos, D. Sarkar, and M. S. Skolnick, *Polariton condensation in dynamic acoustic lattices*, Phys. Rev. Lett. **105**, 116402 (2010).

[119] I. V. Kukushkin, J. H. Smet, L. Höppel, U. Waizmann, M. Riek, W. Wegschneider, and K. von Klitzing, *Ultrahigh-frequency surface acoustic waves for finite wave-vector spectroscopy of two-dimensional electrons*, Appl. Phys. Lett. **85**, 4526 (2004).

[120] T. Byrnes, P. Recher, N. Y. Kim, S. Utsunomiya, and Y. Yamamoto, *Quantum Simulator for the Hubbard Model with Long-Range Coulomb Interactions Using Surface Acoustic Waves*, Phys. Rev. Lett. **99**, 016405 (2007).

[121] S. Büyükköse, B. Vratzov, D. Atac, J. van der Veen, P. V. Santos, and W.G. van der Wiel, *Ultrahigh-frequency surface acoustic wave transducers on $ZnO/SiO_2/Si$ using nanoimprint lithography*, Nanotechnology **23**, 315303 (2012).

[122] A. R. Hutson and D. L. White, *Elastic Wave Propagation in Piezoelectric Semiconductors*, J. Appl. Phys. **33**, 40 (1962).

[123] P. Bierbaum, *Interaction of ultrasonic surface waves with conduction electrons in thin metal films*, Appl. Phys. Lett. **21**, 595 (1972).

[124] A. Wixforth, J. P. Kotthaus, and G. Weimann, *Quantum Oscillations in the Surface-Acoustic-Wave Attenuation Caused by a Two-Dimensional Electron System*, Phys. Rev. Lett. **56**, 2104 (1986).

[125] A. Wixforth, J. Scriba, M. Wassermeier, J. P. Kotthaus, G. Weimann, and W. Schlapp, *Surface acoustic waves on $GaAs/Al_xGa_{1-x}As$ heterostructures*, Phys. Rev. B **40**, 7874 (1989).

[126] W. Paul, *Electromagnetic traps for charged and neutral particles*, Rev. Mod. Phys. **62**, 531 (1990).

[127] D. Leibfried, R. Blatt, C. Monroe, and D. Wineland, *Quantum dynamics of single trapped ions*, Phys. Rev. Mod. **75**, 281 (2003).

[128] S. Rahav, I. Gilary, and S. Fishman, *Time Independent Description of Rapidly Oscillating Potentials*, Phys. Rev. Lett. **91**, 110404 (2003).

[129] S. Rahav, I. Gilary, and S. Fishman, *Effective Hamiltonians for periodically driven systems*, Phys. Rev. A **68**, 013820 (2003).

[130] J. I. Cirac, L. J. Garay, R. Blatt, A. S. Parkins, and P. Zoller, *Laser cooling of trapped ions: The influence of micromotion*, Phys. Rev. A **49**, 421 (1994).

[131] S. Kohler, T. Dittrich, and P. Hänggi, *Floquet-Markovian description of the parametrically driven, dissipative harmonic quantum oscillator*, Phys. Rev. E **55**, 300 (1997).

[132] T. Fujisawa, T. H. Oosterkamp, W. G. van der Wiel, B. W. Broer, R. Aguado, S. Tarucha, and L. P. Kouwenhoven, *Spontaneous Emission Spectrum in Double Quantum Dot Devices*, Science **282**, 932 (1998).

[133] T. Fujisawa, D. G. Austing, Y. Tokura, Y. Hirayama, and S. Tarucha, *Allowed and forbidden transitions in artificial hydrogen and helium atoms*, Nature **419**, 278 (2002).

[134] T. Hayashi, T. Fujisawa, H. D. Cheong, Y. H. Jeong, and Y. Hirayama, *Coherent manipulation of electronic States in a double quantum dot*, Phys. Rev. Lett. **91**, 226804 (2003).

[135] J. R. Petta, A. C. Johnson, C. M. Marcus, M. P. Hanson, and A. C. Gossard, *Manipulation of a single charge in a double quantum dot*, Phys. Rev. Lett. **93**, 186802 (2004).

[136] P. Barthelemy and L. M. K. Vandersypen, *Quantum Dot Systems: a versatile platform for quantum simulations*, Ann. Phys. **525**, 808 (2013).

[137] V. Kornich, C. Kloeffel, and D. Loss, *Phonon-mediated decay of singlet-triplet qubits in double quantum dots*, Phys. Rev. B **89**, 085410 (2014).

[138] K. Wang, C. Payette, Y. Dovzhenko, P. W. Deelman, and J. R. Petta, *Charge Relaxation in a Single Electron Si/SiGe Double Quantum Dot*, Phys. Rev. Lett. **111**, 046801 (2013).

[139] J. G. Rodriguez-Madrid, G. F. Iriarte, J. Pedros, O. A. Williams, D. Brink, and F. Calle, *Super-High-Frequency SAW Resonators on AlN/Diamond*, IEEE Electron Device Lett. **33**, 495 (2012).

[140] M. Benetti, D. Cannata, F. Di Pietrantonio, and E. Verona, *Growth of AlN Piezoelectric Film on Diamond for High-Frequency Surface Acoustic Wave Devices*, IEEE Trans. Ultrason. Ferroelectr. Freq. Control **52**, 1806 (2005).

[141] M. B. Assouar, O. Elmazria, P. Kirsch, P. Alnot, V. Mortet, and C. Tiusan, *High-frequency surface acoustic wave devices based on AlN/diamond layered structure realized using e-beam lithography*, Journal of Applied Physics **101**, 114507 (2007).

[142] E. Glushkov, N. Glushkova, and C. Zhang, *Surface and pseudo-surface acoustic waves piezoelectrically excited in diamond-based structures*, Journal of Applied Physics **112**, 064911 (2012).

[143] M. Benetti, D. Cannata, F. Di Pietrantonio, V. I. Fedosov, and E. Verona, *Gigahertz-range electro-acoustic devices based on pseudo-surface-acoustic waves in AlN/diamond/Si structures*, Appl. Phys. Lett. **87**, 033504 (2005).

[144] R. H. Blick, M. L. Roukes, W. Wegscheider, and M. Bichler, *Freely suspended two-dimensional electron gases*, Physica B **249**, 784 (1998).

[145] COMSOL Multiphysics® v. 5.2. www.comsol.com. COMSOL AB, Stockholm, Sweden.

[146] In our Comsol simulations we have neglected the presence of the thin $Al_xGa_{1-x}As$ crystal layer with typically $x \approx 0.3$. As argued in Ref.[207], this treatment is approximately correct since the relevant material properties (elastic constants, densities, and dielectric constants) of $Al_xGa_{1-x}As$ and GaAs are very similar. The mode functions and speed of sound are largely defined by the elastic constants, which are roughly the same for both $Al_xGa_{1-x}As$ and pure GaAs; for example, the speed of the Rayleigh SAW mode for $Al_{0.3}Ga_{0.7}As$ is $v_s \approx 3010$m/s, which differs from that of pure GaAs by only $\sim 5\%$. Also, the piezoelectric coupling constants are rather similar, with $e_{14} \approx 0.15\text{C/m}^2$ for pure GaAs and $e_{14} \approx 0.145\text{C/m}^2$ for $Al_{0.3}Ga_{0.7}As$ [207].

[147] K. S. Novoselov, A. Mishchenko, A. Carvalho, and A. H. Castro Neto, *2D materials and van der Waals heterostructures*, Science **353**, aac9439 (2016).

[148] A. Kormányos, G. Burkard, M. Gmitra, J. Fabian, V. Zólyomi, N. D. Drummond, and V. Fal'ko, *$k \cdot p$ theory for two-dimensional transition metal dichalcogenide semiconductors*, 2D Mater. **2**, 022001 (2015)

[149] T. Eknapakul, P. D. C. King, M. Asakawa, P. Buaphet, R.-H. He, S.-K. Mo, H. Takagi, K. M. Shen, F. Baumberger, T. Sasagawa, S. Jungthawan, and W. Meevasana, *Electronic Structure of a Quasi-Freestanding MoS_2 Monolayer*, Nano Lett. **14**, 1312 (2014).

[150] K. F. Mak, K. He, C. Lee, G. H. Lee, J. Hone, T. F. Heinz, and J. Shan, *Tightly bound trions in monolayer MoS_2*, Nat. Mat. **12**, 207 (2013).

[151] J. S. Ross, S. Wu, H. Yu, N. J. Ghimire, A. M. Jones, G. Aivazian, J. Yan, D. G. Mandrus, D. Xiao, W. Yao, and X. Xu, *Electrical control of neutral and charged excitons in a monolayer semiconductor*, Nature Comm. **4**, 1474 (2013).

[152] P.H. Dawson and Y. Bingqi, *The second stability region of the quadrupole mass filter. I. Ion optical properties*, Int. J. Mass Spectrom. Ion Processes **54**, 25 (1983).

[153] P.H. Dawson and Y. Bingqi, *The second stability region of the quadrupole mass filter. II. Experimental results*, Int. J. Mass Spectrom. Ion Processes **54**, 41 (1983).

[154] F. J. R. Schülein, E. Zallo, P. Atkinson, O. G. Schmidt, R. Trotta, A. Rastelli, A. Wixforth, and H. J. Krenner, *Fourier synthesis of radiofrequency nanomechanical pulses with different shapes*, Nature Nanotechn. **10**, 512 (2015).

[155] G. C. Possa and L. F. Roncaratti, *Stability Diagrams for Paul Ion Traps Driven by Two Frequencies*, J. Phys. Chem. A **120**, 4915 (2016).

[156] Here, we restrict our discussion to the pseudopotential regime where $q^2 \ll 1$, as done in the major body of our work (apart from the discussion of exotic stability regions where the heating-related arguments should be contrasted with an increased temperature robustness).

[157] S. Furuta, C. H. W. Barnes, and C. J. L. Doran, *Single-qubit gates and measurements in the surface acoustic wave quantum computer*, Phys. Rev. B **70**, 205320 (2004).

[158] F. Martins, F. K. Malinowski, P. D. Nissen, E. Barnes, S. Fallahi, G. C. Gardner, M. J. Manfra, C. M. Marcus, and F. Kuemmeth, *Noise Suppression Using Symmetric Exchange Gates in Spin Qubits*, Phys. Rev. Lett. **116**, 116801 (2016).

[159] M. D. Reed, B. M. Maune, R. W. Andrews, M. G. Borselli, K. Eng, M. P. Jura, A. A. Kiselev, T. D. Ladd, S. T. Merkel, I. Milosavljevic, E. J. Pritchett, M. T. Rakher, R. S. Ross, A. E. Schmitz, A. Smith, J. A. Wright, M. F. Gyure, and A. T. Hunter, *Reduced Sensitivity to Charge Noise in Semiconductor Spin Qubits via Symmetric Operation*, Phys. Rev. Lett. **116**, 110402 (2016).

[160] T. A. Baart, T. Fujita, C. Reichl, W. Wegscheider, and L. M. K. Vandersypen, *Coherent spin-exchange via a quantum mediator*, Nature Nano. **12**, 26 (2017).

[161] C. Campbell, *Surface Acoustic Wave Devices for Mobile and Wireless Communications* (Academic Press, 1998).

[162] D. Jaksch, C. Bruder, J. I. Cirac, C. W. Gardiner, and P. Zoller, *Cold bosonic atoms in optical lattices*, Phys. Rev. Lett. **81**, 3108 (1998).

[163] W. Hofstetter, J. I. Cirac, P. Zoller, E. Demler, and M. D. Lukin, *High-temperature superfluidity of fermionic atoms in optical lattices*, Phys. Rev. Lett. **89**, 220407 (2002).

[164] P. W. Anderson, *Model for the Electronic Structure of Amorphous Semiconductors*, Phys. Rev. Lett. **34**, 953 (1975).

[165] A. Singha, M. Gibertini, B. Karmakar, S. Yuan, M. Polini, G. Vignale, M. I. Katsnelson, A. Pinczuk, L. N. Pfeiffer, K. W. West, and V. Pellegrini, *Two-Dimensional Mott-Hubbard Electrons in an Artificial Honeycomb Lattice*, Science **332**, 1176 (2011).

[166] T. Schlösser, K. Ensslin, J. P. Kotthaus, and M. Holland, *Internal structure of a Landau band induced by a lateral superlattice: a glimpse of Hofstadter's butterfly*, Europhys. Lett. **33**, 683 (1996).

[167] C. Albrecht, J. H. Smet, K. von Klitzing, D. Weiss, V. Umansky, and H. Schweizer, *Evidence of Hofstadters Fractal Energy Spectrum in the Quantized Hall Conductance*, Phys. Rev. Lett. **86**, 147 (2001).

[168] I. Kuljanishvili, C. Kayis, J. F. Harrison, C. Piermarocchi, T. A. Kaplan, S. H. Tessmer, L. N. Pfeiffer, and K. W. West, *Scanning-probe spectroscopy of semiconductor donor molecules*, Nat. Phys. **4**, 227 (2008).

[169] J. Martin, S. Ilani, B. Verdene, J. Smet, V. Umansky, D. Mahalu, D. Schuh, G. Abstreiter, and A. Yacoby, *Localization of Fractionally Charged Quasi-Particles*, Science **305**, 980 (2004).

[170] O. E. Dial, R. C. Ashoori, L. N. Pfeiffer, and K. W. West, *High-resolution spectroscopy of two-dimensional electron systems*, Nature **448**, 176 (2007).

[171] O. Gywat, H. J. Krenner, and J. Berezovsky, *Spins in optically active quantum dots*, Wiley-VCH (2010).

[172] A. Srivastava, M. Sidler, A. V. Allain, D. S. Lembke, A. Kis, and A. İmamoğlu, *Optically active quantum dots in monolayer WSe_2*, Nature Nano. **10**, 491 (2015).

[173] A. N. Vamivakas, Y. Zhao, C.-Y. Lu, and M. Atatüre, *Spin-resolved quantum-dot resonance fluorescence*, Nat. Phys. **5**, 198 (2009).

[174] M. Atatüre, J. Dreiser, A. Badolato, and A. İmamoğlu, *Observation of Faraday rotation from a single confined spin*, Nat. Phys. **3**, 101 (2007).

[175] J. Berezovsky, M. H. Mikkelsen, O. Gywat, N. G. Stoltz, L. A. Coldren, and D. D. Awschalom, *Nondestructive Optical Measurements of a Single Electron Spin in a Quantum Dot*, Science **314**, 1916 (2006).

[176] T. A. Baart, M. Shafiei, T. Fujita, C. Reichl, W. Wegscheider, and L. M. K. Vandersypen, *Single-spin CCD*, Nature Nano. **11**, 330 (2016).

[177] T. Byrnes, N. Kim, K. Kusudo, and Y. Yamamoto, *Quantum simulation of Fermi-Hubbard models in semiconductor quantum-dot arrays*, Phys. Rev. B **78**, 075320 (2008).

[178] Here, we take the mobility μ as our figure of merit, as it is one of the standard metrics to characterize the effect of disorder. Both long-range scattering and short-range scattering are reflected in the mobility and in fact the exact dependence of mobility on density often allows one to distinguish whether long-range or short-range scattering dominates. The main caveat about using mobility is that it is typically

measured in density ranges larger than those used in the present experiments. The same caveat, however, applies to the use of mobility for predicting quantum dot behaviour. Yet, empirically, for quantum dots defined in systems with relatively low mobility, such as Si/SiGe quantum wells, mobility is found to be a good predictor of the ability to realize well-behaved quantum dots, i.e. not suffering excessive disorder [205]. For this reason, and given that mobility has been measured across many systems, we refer to mobility as an indication of disorder.

[179] V. Umansky, R. de-Picciotto, and M. Heiblum, *Extremely high-mobility two dimensional electron gas: Evaluation of scattering mechanisms*, Appl. Phys. Lett. **71**, 683 (1997).

[180] D. Hofstadter, *Energy levels and wave functions of Bloch electrons in rational and irrational magnetic fields*, Phys. Rev. B **14**, 2239 (1976).

[181] A. Lagendijk, B. A. Van Tiggelen, and D. Wiersma, *Fifty years of Anderson localization*, Phys. Today **62**, 24 (2009).

[182] D. Belitz and T. R. Kirkpatrick, *The Anderson-Mott transition*, Rev. Mod. Phys. **66**, 261 (1994).

[183] D. Basko, I. Aleiner, and B. Altshuler, *Metal-insulator transition in a weakly interacting many-electron system with localized single-particle states*, Ann. Phys. **321**, 1126 (2006).

[184] K. Byczuk, W. Hofstetter, and D. Vollhardt, *Mott-Hubbard Transition versus Anderson Localization in Correlated Electron Systems with Disorder*, Phys. Rev. Lett. **94**, 056404 (2005).

[185] L. Fallani, J. E. Lye, V. Guarrera, C. Fort, and M. Inguscio, *Ultracold Atoms in a Disordered Crystal of Light: Towards a Bose Glass*, Phys. Rev. Lett. **98**, 130404 (2007).

[186] O. P. Sushkov and A.H. Castro Neto, *Topological Insulating States in Laterally Patterned Ordinary Semiconductors*, Phys. Rev. Lett. **110**, 186601 (2013).

[187] J. V. T. Buller, R. E. Balderas-Navarro, K. Biermann, E. A. Cerda-Mendez, and P. V. Santos, *Exciton-polariton gap soliton dynamics in moving acoustic square lattices*, Phys. Rev. B **94**, 125432 (2016).

[188] L. V. Butov, *Condensation and pattern formation in cold exciton gases in coupled quantum wells*, J. Phys. Condens. Matter **16**, R1577 (2004).

[189] A. T. Hammack, M. Griswold, L. V. Butov, L. E. Smallwood, A. L. Ivanov, and A. C. Gossard, *Trapping of Cold Excitons with Laser Light*, Phys. Rev. Lett. **96**, 227402 (2006).

[190] A. T. Hammack, L. V. Butov, L. Mouchliadis, A. L. Ivanov, and A. C. Gossard, *Kinetics of indirect excitons in an optically induced trap in GaAs quantum wells*, Phys. Rev. B **76**, 193308 (2007).

[191] S. Kumar, A. Kaczmarczyk, and B. D. Gerardot, *Strain-Induced Spatial and Spectral Isolation of Quantum Emitters in Mono- and Bilayer WSe_2*, Nano Lett. **15**, 7567 (2015).

[192] J.-X. Liu, D.-N. Fang, W.-Y. Wei, and X.-F. Zhao, *Love waves in layered piezoelectric/piezomagnetic structures*, J. Sound Vib. **315**, 146 (2008).

[193] Y. Pang, J.-X. Liu, Y.-S. Wang, and X.-F. Zhang, *Propagation of Rayleigh-type surface waves in a transversely isotropic piezoelectric layer on a piezomagnetic half-space*, J. Appl. Phys. **103**, 074901 (2008).

[194] M. Weiler, L. Dreher, C. Heeg, H. Huebl, R. Gross, M. S. Brandt, and S. T. B. Goennenwein, *Acoustically driven ferromagnetic resonance*, Phys. Rev. Lett. **106**, 117601 (2011).

[195] R. J. Glauber, in Laser Manipulation of Atoms and Ions, Proceedings of the International School of Physics "Enrico Fermi" Course 118, edited by E. Arimondo, W. D. Phillips, and F. Strumia (North-Holland, Amsterdam), p. 643 (1992).

[196] V. N. Golovach, A. Khaetskii, and D. Loss, *Phonon-Induced Decay of the Electron Spin in Quantum Dots*, Phys. Rev. Lett. **93**, 016601 (2004).

[197] H.-P. Breuer and F. Petruccione, *The Theory of Open Quantum Systems* (Oxford University Press, Oxford, 2002).

[198] R. J. Schnebele, M. Kataoka, C. J. B. Ford, C. H. W. Barnes, D. Anderson, G. A. C. Jones, I. Farrer, D. A. Ritchie, and M. Pepper, *Quantum-dot thermometry of electron heating by surface acoustic waves*, Appl. Phys. Lett. **89**, 122104 (2006).

[199] P. Utko, P. E. Lindelof, and K. Gloos, *Heating in single-electron pumps driven by surface acoustic waves*, Appl. Phys. Lett. **88**, 202113 (2006).

[200] R. Manenti, M. J. Peterer, A. Nersisyan, E. B. Magnusson, A. Patterson, and P. J. Leek, *Surface acoustic wave resonators in the quantum regime*, Phys. Rev. B **93**, 041411(R) (2016).

[201] W. Wu, Y. Li, F. Zhang, L. Lin, S. Niu, D. Chenet, X. Zhang, Y. Hao, T. F. Heinz, J. Hone, and Z. L. Wang, *Piezoelectricity of single-atomic-layer MoS2 for energy conversion and piezotronics*, Nature **514**, 470 (2014).

[202] M. K. Ekström, T. Aref, J. Runeson, J. Bjoerck, I. Bostroem, and P. Delsing, *Surface acoustic wave unidirectional transducers for quantum applications*, Appl. Phys. Lett. **110**, 073105 (2017).

[203] L. M. K. Vandersypen, H. Bluhm, J. S. Clarke, A. S. Dzurak, R. Ishihara, A. Morello, D. J. Reilly, L. R. Schreiber, and M. Veldhorst, *Interfacing spin qubits in quantum dots and donors - hot, dense and coherent*, npj Quant. Inf. **3**, 34 (2017).

[204] E. A. Chekhovich, M. N. Makhonin, A. I. Tartakovskii, A. Yacoby, H. Bluhm, K. C. Nowack, and L. M. K. Vandersypen, *Nuclear spin effects in semiconductor quantum dots*, Nat. Mater. **12**, 494 (2013).

[205] F. A. Zwanenburg, A. S. Dzurak, A. Morello, M. Y. Simmons, L. C. L. Hollenberg, G. Klimeck, S. Rogge, S. N. Coppersmith, and M. A. Eriksson, Silicon Quantum Electronics, *Silicon quantum electronics*, Rev. Mod. Phys. **85**, 961 (2013).

[206] M. Veldhorst, J. C. C. Hwang, C. H. Yang, A. W. Leenstra, B. de Ronde, J. P. Dehollain, J. T. Muhonen, F. E. Hudson, K. M. Itoh, A. Morello, and A. S. Dzurak, *An addressable quantum dot qubit with fault-tolerant control fidelity*, Nat. Nanotechnol. **9**, 981 (2014).

[207] S. H. Simon, *Coupling of surface acoustic waves to a two-dimensional electron gas*, Phys. Rev. B **54**, 13878 (1996).

[208] M. Lewenstein, A. Sanpera, V. Ahufinger, B. Damski, A. Sen De, and U. Sen, *Ultracold atomic gases in optical lattices: mimicking condensed matter physics and beyond*, Adv. Phys. **56**, 243 (2007).

[209] H. Lee, J. A. Johnson, M. Y. He, J. S. Speck, and P. M. Petroff, *Strain-engineered self-assembled semiconductor quantum dot lattices*, Appl. Phys. Lett. **78**, 105 (2001).

[210] M. Alloing, A. Lemaitre, E. Galopin, and F. Dubin, *Optically programmable excitonic traps*, Sci. Rep. **3**, 1578 (2013).

[211] C. Rocke, S. Zimmermann, A. Wixforth, J. P. Kotthaus, G. Böhm, and G. Weimann, *Acoustically Driven Storage of Light in a Quantum Well*, Phys. Rev. Lett. **78**, 4099 (1997).

[212] S. Zimmermann, A. Wixforth, J. P. Kotthaus, W. Wegscheider, M. Bichler, *A Semiconductor-Based Photonic Memory Cell*, Science **283**, 1292 (1999).

[213] R. Folman, P. Krüger, J, Schmiedmayer, J. Denschlag, and Carsten Henkel, *Microscopic atom optics: from wires to an atom chip*, Adv. in At. Mol. Opt. Physics **48**, 263 (2002).

[214] M. Keil, O. Amit, S. Zhou, D. Groswasser, Y. Japha, and R. Folman, *Fifteen Years of Cold Matter on the Atom Chip: Promise, Realizations, and Prospects*, J. Mod. Opt. **63**, 1840 (2016).

[215] A. André, D. Demille, J. M. Doyle, M. D. Lukin, S. E. Maxwell, P. Rabl, R. J. Schoelkopf, and P. Zoller, *A coherent all-electrical interface between polar molecules and mesoscopic superconducting resonators*, Nat. Phys. **2**, 636 (2006).

[216] S. Hou, B. Wei, L. Deng, and J. Yin, *Chip-based microtrap arrays for cold polar molecules*, Phys. Rev. A **96**, 063416 (2017).

[217] O. Romero-Isart, C. Navau, A. Sanchez, P. Zoller, and J. I. Cirac, *Superconducting Vortex Lattices for Ultracold Atoms*, Phys. Rev. Lett. **111**, 145304 (2013).

[218] J. Tejada, E. M. Chudnovsky, R. Zarzuela, N. Statuto, J. Calvo-de la Rosa, P. V. Santos, and A. Hernández-Mínguez, *Switching of magnetic moments of nanoparticles by surface acoustic waves*. Europhys. Lett. **118**, 37005 (2017).

[219] A. S. Salasyuk, A. V. Rudkovskaya, A. P. Danilov, B. A. Glavin, S. M. Kukhtaruk, M. Wang, A. W. Rushforth, P. A. Nekludova, S. V. Sokolov, A. A. Elistratov, D. R. Yakovlev, M. Bayer, A. V. Akimov, and A. V. Scherbakov, *Generation of a localized microwave magnetic field by coherent phonons in a ferromagnetic nanograting*, Phys. Rev. B **97**, 060404(R) (2018).

[220] R. Grimm, M. Weidemüller, Y. B. Ovchinnikov, *Optical dipole traps for neutral atoms*, Adv. Atom. Mol. Opt. Phys. **42**, 95 (2000).

[221] P. Redlinski, T. Wojtowicz, T. G. Rappoport, A. Libal, J. K. Furdyna, and B. Janko, *Zero- and one-dimensional magnetic traps for quasiparticles in diluted magnetic semiconductors*, Phys. Rev. B. **72**, 085209 (2005).

[222] M. Berciu, T. G. Rappoport, and B. Janko, *Manipulating spin and charge in magnetic semiconductors using superconducting vortices*, Nature **435**, 71 (2005).

[223] P. C. M. Christianen, F. Piazza, J. G. S. Lok, J. C. Maan, W. van der Vleuten, *Magnetic traps for excitons*, Physica B **249**, 624 (1998).

[224] A. Murayama and M. Sakuma, *Nanoscale magnet for semiconductor spintronics*, Appl. Phys. Lett. **88**, 122504 (2006).

[225] J. K. Furdyna, *Diluted magnetic semiconductors*, J. Appl. Phys. **64**, R29 (1998).

[226] S. Halm, P. E. Hohage, J. Nannen, E. Neshataeva, L. Schneider, G. Bacher, Y. H. Fan, J. Puls, and F. Henneberger, *Manipulation of spin states in a semiconductor by microscale magnets*, J. Phys. D: Appl. Phys. **41**, 164007 (2008).

[227] Y. S. Chen, S. Halm, E. Neshataeva, T. Kümmell, G. Bacher, M. Wiater, T. Wojtowicz, and G. Karczewski, *Local control of spin polarization in a semiconductor by microscale current loops*, Appl. Phys. Lett. **93**, 141902 (2008).

[228] J. Ruostekoski, G V. Dunne, and J. Javanainen, *Particle Number Fractionalization of an Atomic Fermi-Dirac Gas in an Optical Lattice*, Phys. Rev. Lett. **88**, 180401 (2002).

[229] D. Jaksch, and P. Zoller, *Creation of effective magnetic fields in optical lattices: the Hofstadter butterfly for cold neutral atoms*, New J. Phys. **5**, 56 (2003).

[230] J. Dalibard, F. Gerbier, G. Juzeliūnas, and P. Öhberg, *Colloquium: Artificial gauge potentials for neutral atoms*, Rev. Mod. Phys. **83**, 1523 (2011).

[231] N. Goldman,G. Juzeliūnas, P. Öhberg, and I. B. Spielman, *Light-induced gauge fields for ultracold atoms*, Rep. Prog. Phys. **77**, 126401 (2014).

[232] N. Goldman, J. C. Budich, and P. Zoller, *Topological quantum matter with ultracold gases in optical lattices*, Nat. Phys. **12**, 639 (2016).

[233] C. V. Sukumar, D. M. Brink, *Spin-flip transitions in a magnetic trap*, Phys. Rev. A **56**, 2451 (1997).

[234] K. A. Burrows, H. Perrin, and B. M. Garraway, *Nonadiabatic losses from radio-frequency-dressed cold-atom traps: Beyond the Landau-Zener model*, Phys. Rev. A **96**, 023429 (2017).

[235] S. Greschner, L. Santos, and T. Vekua, *Ultra-cold bosons in zig-zag optical lattices*, Phys. Rev. A **87**, 033609 (2013).

[236] A. Dhar, T. Mishra, R. V. Pai, S. Mukerjee, and B. P. Das, *Hard-core bosons in a zig-zag optical superlattice*, Phys. Rev. A **88**, 053625 (2013).

[237] In principle, screening could also affect other system parameters, like, e.g., the effective electron mass in the 2DEG; however, we do not expect this to play an important role since Coulomb drag effects [238] between an electron and its image charge should be negligible due to the high mobility of free electrons in the screening layer.

[238] B. N. Narozhny, and A. Levchenko, *Coulomb drag*, Rev. Mod. Phys. **88**, 025003 (2016).

[239] G. Tosi, F. A. Mohiyaddin, H. Huebl, and A. Morello, *Circuit-quantum electrodynamics with direct magnetic coupling to single-atom spin qubits in isotopically enriched ^{28}Si*, AIP Adv. **4**, 087122 (2014).

[240] B. Sarabi, P. Huang, and N. M. Zimmerman, *Possible Hundredfold Enhancement in the Direct Magnetic Coupling of a Single-Atom Electron Spin to a Circuit Resonator*, Phys. Rev. Appl. **11**, 014001 (2019).

[241] K. Ilin, D. Henrich, Y. Luck, Y. Liang, M. Siegel, and D. Yu. Vodolazov, *Critical current of Nb, NbN, and TaN thin-film bridges with and without geometrical nonuniformities in a magnetic field*, Phys. Rev. B **89**, 184511 (2014).

[242] When the setup is operated in the high-frequency ($\omega \sim$ GHz) regime, retardation effects of the propagating electromagnetic waves may become important, which can be described by the so-called *Jefimenkov equations* [270]. However, corrections to the Biot-Savart law will be of the order of $\sim d\omega/c$ where c denotes the speed of light. Even at ultra-high frequencies $\omega \sim (1-100)$ GHz and for typical distances $d \sim (0.1-1)$ μm, these corrections may safely be neglected and, in this quasistatic regime ($d\omega/c \ll 1$), the Biot-Savart law accurately describes the induced magnetic field due to the current density $\mathbf{J}$.

[243] L. Dreher, M. Weiler, M. Pernpeintner, H. Huebl, R. Gross, M. S. Brandt, and S. T. B. Goennenwein, *Surface acoustic wave driven ferromagnetic resonance in nickel thin films: Theory and experiment*, Phys. Rev. B **86**, 134415 (2012).

[244] L. Landau and E. Lifshitz. *On the Theory of the Dispersion of Magnetic Permeability in Ferromagnetic Bodies*. Phys. Z. Sowjetunion **8**, 153 (1935).

[245] T. Gilbert, *A phenomenological theory of damping in ferromagnetic materials*, IEEE Trans. Magn. **40**, 3443 (2004).

[246] B. Sherman, *Optical generation of high amplitude laser generated surface acoustic waves*, AIP Conf. Proc. **1511**, 337 (2013).

[247] M. A. W. Schoen, D. Thonig, M. L. Schneider, T. J. Silva, H. T. Nembach, O. Eriksson, O. Karis, and J. M. Shaw, *Ultra-low magnetic damping of a metallic ferromagnet*, Nat. Phys. **12**, 839 (2016).

[248] W. J. M. Naber, T. Fujisawa, H. W. Liu, and W. G. van der Wiel, *Surface-Acoustic-Wave-Induced Transport in a Double Quantum Dot*, Phys. Rev. Lett. **96**, 136807 (2006).

[249] Y.-Y. Liu, K. D. Petersson, J. Stehlik, J. M. Taylor, and J. R. Petta, *Photon Emission from a Cavity-Coupled Double Quantum Dot*, Phys. Rev. Lett. **113**, 036801 (2014).

[250] R. de Sousa, and S. Das Sarmas, *Gate control of spin dynamics in III-V semiconductor quantum dots*, Phys. Rev. B **68**, 155330 (2003).

[251] Note that, in the literature, the Rabi frequency is typically provided in the form $f_{\mathrm{Rabi}} = \Omega_0/(2\pi) \approx \Omega_0[\mu\mathrm{eV}] \times 240$ MHz.

[252] S. J. Koester, B. Brar, C. R. Bolognesi, E. J. Caine, A. Patlach, E. L. Hu, H. Kroemer, and M. J. Rooks, *Length dependence of quantized conductance in ballistic constrictions fabricated on InAs/AlSb quantum wells*, Phys. Rev. B **53**, 13063 (1996).

[253] C. H. Yang, M. J. Yang, K. A. Cheng, and J. C. Culbertson, *Characterization of one-dimensional quantum channels in InAs/AlSb*, Phys. Rev. B **66**, 115306 (2002).

[254] T. Koga, S. Faniel, T. Matsuura, S. Mineshige, Y. Sekine, and H. Sugiyama, *Determination of Spin-Orbit Coefficients and Phase Coherence Times in InGaAs/InAlAs Quantum Wells*. AIP Conf. Proc. **1416**, 38 (2011).

[255] A. Manchon, H. C. Koo, J. Nitta, S. M. Frolov, and R. A. Duine, *New perspectives for Rashba spin-orbit coupling*. Nat. Mat. **14**, 871 (2015).

[256] J. Singleton, *Band Theory And Electronic Properties Of Solids*, Oxford University Press, New York (2001).

[257] J. M. Elzerman, R. Hanson, L. H. Willems van Beveren, B. Witkamp, L. M. K. Vandersypen, and L. P. Kouwenhoven, *Single-shot read-out of an individual electron spin in a quantum dot*, Nature **430**, 431 (2004).

[258] S. Amasha, K. MacLean, I. P. Radu, D. M. Zumbühl, M. A. Kastner, M. P. Hanson, and A. C. Gossard, *Electrical Control of Spin Relaxation in a Quantum Dot*, Phys. Rev. Lett. **100**, 046803 (2008).

[259] A. V. Khaetskii, and Y. V. Nazarov, *Spin-flip transitions between Zeeman sublevels in semiconductor quantum dots*, Phys. Rev. B **64**, 125316 (2001).

[260] S. Nadj-Perge, S. M. Frolov, E. P. A. M. Bakkers, and L. P. Kouwenhoven, *Spin-orbit qubit in a semiconductor nanowire*, Nature **468**, 1084 (2010).

[261] J. W. G. van den Berg, S. Nadj-Perge, V. S. Pribiag, S. R. Plissard, E. P. A. M. Bakkers, S. M. Frolov, and L. P. Kouwenhoven, *Fast Spin-Orbit Qubit in an Indium Antimonide Nanowire*, Phys. Rev. Lett. **110**, 066806 (2013).

[262] N. Gemelke, E. Sarajlic, Y. Bidel, S. Hong, and S. Chu, *Parametric Amplification of Matter Waves in Periodically Translated Optical Lattices*, Phys. Rev. Lett. **95**, 170404 (2005).

[263] H. Lignier, C. Sias, D. Ciampini, Y. Singh, A. Zenesini, O. Morsch, and E. Arimondo, *Dynamical Control of Matter-Wave Tunneling in Periodic Potentials*, Phys. Rev. Lett. **99**, 220403 (2007).

[264] J. Struck, C. Ölschläger, R. Le Targat, P. Soltan-Panahi, A. Eckardt, M. Lewenstein, P. Windpassinger, and K. Sengstock, *Quantum Simulation of Frustrated Classical Magnetism in Triangular Optical Lattices*, Science **333**, 996 (2011).

[265] J. Struck, C. Ölschläger, M. Weinberg, P. Hauke, J. Simonet, A. Eckardt, M. Lewenstein, K. Sengstock, and P. Windpassinger, *Tunable Gauge Potential for Neutral and Spinless Particles in Driven Optical Lattices*, Phys. Rev. Lett. **108**, 225304 (2012).

[266] M. Łaçki, M. A. Baranov, H. Pichler, and P. Zoller, *Nanoscale Dark State Optical Potentials for Cold Atoms*, Phys. Rev. Lett. **117**, 233001 (2016).

[267] Y. Wang, S. Subhankar, P. Bienias, M. Laçki, T.-C. Tsui, M. A. Baranov, A. V. Gorshkov, P. Zoller, J. V. Porto, and S. L. Rolston, *Dark State Optical Lattice with a Subwavelength Spatial Structure*, Phys. Rev. Lett. **120**, 083601 (2018).

[268] J. L. Movilla and J. Planelles, *Two-dimensional Bloch electrons under strong magnetic modulation*, Phys. Rev. B **83**, 014410 (2011).

[269] M. Bukov, L. D'Alessio, and A. Polkovnikov, *Universal high-frequency behavior of periodically driven systems: from dynamical stabilization to Floquet engineering*, Adv. Phys. **64**, 139 (2015).

[270] J. D. Jackson, *Classical Electrodynamics*, Wiley, New York (1999).

[271] I. S. Gradshteyn and I. M. Ryzhik, *Table of Integrals, Series, and Products*, Academic Press, 6th ed. (2000).

[272] E. W. Weisstein, *Digamma function. From* MathWorld - *A Wolfram Web Resource*, URL http://mathworld.wolfram. com/DigammaFunction.html.

[273] J.-F. Robillard, O. Bou Matar, J. O. Vasseur, P. A. Deymier, M. Stippinger, A.-C. Hladky-Hennion, Y. Pennec, and B. Djafari-Rouhani, *Tunable magnetoelastic phononic crystals*, Appl. Phys. Lett. **95**, 124104 (2009).

[274] D. Trypogeorgos and C. J. Foot, *Cotrapping different species in ion traps using multiple radio frequencies*, Phys. Rev. A **94**, 023609 (2016).

[275] N. Leefer, K. Krimmel, W. Bertsche, D. Budker, J. Fajans, R. Folman, H. Häffner, and F. Schmidt-Kaler, *Investigation of two-frequency Paul traps for antihydrogen production*, Hyperfine Int. **238**, 12 (2017).

[276] E. Wigner, *On the interaction of electrons in metals*, Phys. Rev. **46**, 1002 (1934).

[277] E. E. Mendez, M. Heiblum, L. L. Chang, and L. Esaki, *High-magnetic-field transport in a dilute two-dimensional electron gas*, Phys. Rev. B **28**, 4886 (1983).

[278] E. Y. Andrei, G. Deville, D. C. Glattli, F. I. B. Williams, E. Paris, and B. Etienne, *Observation of a Magnetically Induced Wigner Solid*, Phys. Rev. Lett. **60**, 2765 (1988).

[279] I. Shapir, A. Hamo, S. Pecker, C. P. Moca, Ö. Legeza, G. Zarand, and S. Ilani, *Imaging the electronic Wigner crystal in one dimension*, Science **364**, 870 (2019).

[280] D. DiVincenzo, *The physical implementation of quantum computation*, Progr. Phys. **48**, 771 (2000).

[281] V. V. Deshpande and M. Bockrath, *Wigner crystal phases in confined carbon nanotubes*, Nat. Phys. **4**, 314 (2008).

[282] B. Antonio, A. Bayat, S. Kumar, M. Pepper, and S. Bose, *Self-Assembled Wigner Crystals as Mediators of Spin Currents and Quantum Information*, Phys. Rev. Lett. **115**, 216804 (2015).

[283] P. M. Platzman and M. I. Dykman, *Quantum Computing with Electrons Floating on Liquid Helium*, Science **284**, 1967 (1999).

[284] M. I. Dykman and P.M. Platzman, *Quantum computing using electrons floating on liquid helium*, Fortschr. Phys. **48**, 1095 (2000).

[285] D. Porras and J. I. Cirac, *Quantum manipulation of trapped ions in two-dimensional Coulomb crystals*, Phys. Rev. Lett. **96**, 250501 (2006).

[286] M. J. Biercuk, H. Uys, A. P. VanDevender, N. Shiga, W. M. Itano, and J. J. Bollinger, *High-fidelity quantum control using ion crystals in a Penning trap*, Quant. Info. Comp. **9**, 920 (2009).

[287] P. G. Silvestrov and P. Recher, *Wigner crystal phases in bilayer graphene*, Phys. Rev. B **95**, 075438 (2017).

[288] M. Zarenia, D. Neilson, B. Partoens, and F. M. Peeters, *Wigner crystallization in transition metal dichalcogenides: A new approach to correlation energy*, Phys. Rev. B **95**, 115438 (2017).

[289] E. C. Regan, D. Wang, C. Jin, M. Iqbal Bakti Utama, B. Gao, X. Wei, S. Zhao, W. Zhao, Z. Zhang, K. Yumigeta, M. Blei, J. D. Carlström, K. Watanabe, T. Taniguchi, S. Tongay, M. Crommie, A. Zettl, and F. Wang, *Mott and generalized Wigner crystal states in WSe_2/WS_2 moiré superlattices*, Nature **579**, 359 (2020).

[290] Y. Tang, L. Li, T. Li, Y. Xu, S. Liu, K. Barmak, K. Watanabe, T. Taniguchi, A. H. MacDonald, J. Shan, and K. F. Mak, *WSe_2/WS_2* moiré superlattices: a new Hubbard model simulator, Preprint available on *arXiv*:1910.08673 (2019).

[291] Y. Shimazaki, I. Schwartz, K. Watanabe, T. Taniguchi, M. Kroner, and A. İmamoğlu, *Strongly correlated electrons and hybrid excitons in a moiré heterostructure*, Nature **580**, 472 (2020).

[292] T. C. Berkelbach, M. S. Hybertsen, and D.R. Reichman, *Theory of neutral and charged excitons in monolayer transition metal dichalcogenides*, Phys. Rev. B **88**, 045318 (2013).

[293] A. Chernikov, T. C. Berkelbach, H. M. Hill, A. Rigosi, Y. Li, O. B. Aslan, D. R. Reichman, M. S. Hybertsen, and T. F. Heinz, *Exciton Binding Energy and Nonhydrogenic Rydberg Series in Monolayer WS_2*, Phys. Rev. Lett. **113**, 076802 (2014).

[294] S. Zeytinoglu, C. Roth, S. Huber, and A. İmamoğlu, *Atomically Thin Semiconductors as Nonlinear Mirrors*, Phys. Rev. A **96**, 031801(R) (2017).

[295] P. Back, S. Zeytinoglu, A. Ijaz, M. Kroner, and A. İmamoğlu, *Realization of an Electrically Tunable Narrow-Bandwidth Atomically Thin Mirror Using Monolayer $MoSe_2$*, Phys. Rev. Lett. **120**, 037401 (2018).

[296] G. Scuri, Y. Zhou, A. A. High, D. S. Wild, C. Shu, K. De Greve, L. A. Jauregui, T. Taniguchi, K. Watanabe, P. Kim, M. D. Lukin, and H. Park, *Large Excitonic Reflectivity of Monolayer $MoSe_2$ Encapsulated in Hexagonal Boron Nitride*, Phys. Rev. Lett. **120**, 037402 (2018).

[297] K. F. Mak, K. L. McGill, J. Park, and P. L. McEuen, *The valley Hall effect in MoS_2 transistors*, Science **344**, 1489 (2014).

[298] J. G. Roch, G. Froehlicher, N. Leisgang, P. Makk, K. Watanabe, T. Taniguchi, and R. J. Warburton, *Spin-polarized electrons in monolayer MoS_2*, Nat. Nanotechn. **14**, 432 (2019).

[299] A. Kumar, and P. K. Ahluwalia, *Tunable dielectric response of transition metals dichalcogenides MX_2 (M=Mo, W; X=S, Se, Te): Effect of quantum confinement*, Physica B: Cond. Mat. **407**, 4627 (2012).

[300] R. Roldán, A. Castellanos-Gomez, E. Cappelluti, and F. Guinea, *Strain engineering in semiconducting two-dimensional crystals*, J. Phys.: Cond. Matt. **27**, 313201 (2015).

[301] B. Amorim, A. Cortijo, F. de Juan, A.G. Grushin, F. Guinea, A. Gutierrez-Rubio, H. Ochoa, V. Parente, R. Roldán, P. San-Jose, J. Schiefele, M. Sturla, and M.A.H. Vozmediano, *Novel effects of strains in graphene and other two dimensional materials*, Phys. Rep. **617**, 1 (2016).

[302] K. Wang, K. De Greve, L. A. Jauregui, A. Sushko, A. High, Y. Zhou, G. Scuri, T. Taniguchi, K. Watanabe, M. D. Lukin, H. Park, and P. Kim, *Electrical control of charged carriers and excitons in atomically thin materials*, Nat. Nanotechnol. **13**, 128 (2018).

[303] L. V. Keldysh, *Coulomb interaction in thin semiconductor and semimetal films*, J. Exp. Th. Phys., **29**, 658 (1979).

[304] D. Rhodes, S. H. Chae, R. Ribeiro-Palau, and J. Hone, *Disorder in van der Waals heterostructures of 2D materials*, Nat. Mat. **18**, 541 (2019).

[305] J. Klein, M. Lorke, M. Florian, F. Sigger, J. Wierzbowski, J. Cerne, K. Müller, T. Taniguchi, K. Watanabe, U. Wurstbauer, M. Kaniber, M. Knap, R. Schmidt, J. J. Finley, and A. W. Holleitner, *Site-selectively generated photon emitters in monolayer MoS_2 via local helium ion irradiation*, Nat. Commun. **10**, 2755 (2019).

[306] P. Dey, L. Yang, C. Robert, G. Wang, B. Urbaszek, X. Marie, and S. A. Crooker, *Gate-Controlled Spin-Valley Locking of Resident Carriers in WSe_2 Monolayers*, Phys. Rev. Lett. **119**, 137401 (2017).

[307] A. Kormányos, V. Zólyomi, N. D. Drummond, and D. Burkard, *Spin-Orbit Coupling, Quantum Dots, and Qubits in Monolayer Transition Metal Dichalcogenides*, Phys. Rev. X **4**, 011034 (2014).

[308] D. J. Thouless, *Exchange in solid ^{3}He and the Heisenberg Hamiltonian*, Proc. Phys. Soc. London **86**, 893 (1965).

[309] N. D. Drummond and R. J. Needs, *Phase Diagram of the Low-Density Two-Dimensional Homogeneous Electron Gas*, Phys. Rev. Lett. **102**, 126402 (2009).

[310] Y. Wu, Q. Tong, G.-B. Lin, H. Yu, and W. Yao, *Spin-valley qubit in nanostructures of monolayer semiconductors: Optical control and hyperfine interaction*, Phys. Rev. B **93**, 045313 (2016).

[311] A. J. Pearce, and G. Burkard, *Electron spin relaxation in a transition-metal dichalcogenide quantum dot*, 2D Mater. **4**, 025114 (2017).

[312] R. Moessner, and S. L. Sondi, *Ising models of quantum frustration*, Phys. Rev. B **63**, 224401 (2001).

[313] R. J. Bettles, S. A. Gardiner, and C. S. Adams, *Enhanced Optical Cross Section via Collective Coupling of Atomic Dipoles in 2D Array*, Phys. Rev. Lett. **116**, 103602 (2016).

[314] E. Shahmoon, D. S. Wild, M. D. Lukin, and S. F. Yelin, *Cooperative Resonances in Light Scattering from Two-Dimensional Atomic Arrays*, Phys. Rev. Lett. **118**, 113601 (2017).

[315] D. G. Thomas, and J. J. Hopfield, *Bound Exciton Complexes*, Phys. Rev. Lett. **7**, 316 (1961).

[316] M. Sidler, P. Back, O. Cotlet, A. Srivastava, T. Fink, M. Kroner, E. Demler, and A. İmamoğlu, *Fermi polaron-polaritons in charge-tunable atomically thin semiconductors*, Nat. Phys. **13**, 255 (2017).

[317] L. Yang, N. A. Sinitsyn, W. Chen, J. Yuan, J. Zhang, J. Lou, and S. A. Crooker, *Long-lived nanosecond spin relaxation and spin coherence of electrons in monolayer MoS_2 and WS_2*, Nat. Phys. **11**, 830 (2015).

[318] A. Singh, G. Moody, K. Tran, M. E. Scott, V. Overbeck, G. Berghäuser, J. Schaibley, E. J. Seifert, D. Pleskot, N. M. Gabor, J. Yan, D. G. Mandrus, M. Richter, E. Malic, X. Xu, and X. Li, *Trion formation dynamics in monolayer transition metal dichalcogenides*, Phys. Rev. B **93**, 041401(R) (2016).

[319] E. Courtade, M. Semina, M. Manca, M. M. Glazov, C. Robert, F. Cadiz, G. Wang, T. Taniguchi, K. Watanabe, M. Pierre, W. Escoffier, E. L. Ivchenko, P. Renucci, X. Marie, T. Amand, and B. Urbaszek, *Charged excitons in monolayer WSe_2: Experiment and theory*, Phys. Rev. B **96**, 085302 (2017).

[320] D. Xiao, G.-B. Liu, W. Feng, X. Xu, and W. Yao, *Coupled Spin and Valley Physics in Monolayers of MoS_2 and Other Group-VI Dichalcogenides*, Phys. Rev. Lett. **108**, 196802 (2012).

[321] X. Xu, W. Yao, D. Xiao, and T. F. Heinz, *Spins and pseudospins in layered transition metal dichalcogenides*, Nat. Phys. **10**, 343 (2014).

[322] M. Born, and E. Wolf, *Principles of Optics: Electromagnetic Theory of Propagation, Interference and Diffraction of Light*, Cambridge University Press (1999).

[323] R. M. A. Azzam, and N. M. Bashara, *Ellipsometry and Polarized Light*, North-Holland Publishing Company, Amsterdam (1979).

[324] K. Voelker and S. Chakravarty, *Multiparticle ring exchange in the Wigner glass and its possible relevance to strongly interacting two-dimensional electron systems in the presence of disorder*, Phys. Rev. B **64**, 235125 (2001).

[325] K. A. Matveev, A. V. Andreev, and A. D. Klironomos, *Scattering of charge and spin excitations and equilibration of a one-dimensional Wigner crystal*, Phys. Rev. **90**, 035148 (2014).

[326] F. K. Malinowski, F. Martins, T. B. Smith, S. D. Bartlett, A. C. Doherty, P. D. Nissen, S. Fallahi, G. C. Gardner, M. J. Manfra, C. M. Marcus, and F. Kuemmeth, *Fast spin exchange across a multielectron mediator*, Nat. Commun. **10**, 1196 (2019).

[327] Y. Jiang, Z. Chen, Y. Han, P. Deb, H. Gao, S. Xie, P. Purohit, M. W. Tate, J. Park, S. M. Gruner, V. Elser, and D. A. Muller, *Electron ptychography of 2D materials to deep sub-angström resolution*, Nature **559**, 343 (2018).

[328] H. Yoo, R. Engelke, S. Carr, S. Fang, K. Zhang, P. Cazeaux, S. H. Sung, R. Hovden, A. W. Tsen, T. Taniguchi, K. Watanabe, G.-C. Yi, M. Kim, M. Luskin, E. B. Tadmor, E. Kaxiras, and P. Kim, *Atomic and electronic reconstruction at the van der Waals interface in twisted bilayer graphene*, Nat. Mat. **18**, 448 (2019).

[329] K. Agarwal, R. Schmidt, B. Halperin, V. Oganesyan, G. Zarand, M. D. Lukin, and E. Demler, *Magnetic noise spectroscopy as a probe of local electronic correlations in two-dimensional systems*, Phys. Rev. B **95**, 155107 (2017).

[330] T. H. Oosterkamp, T. Fujisawa, W. G. van der Wiel, K. Ishibashi, R. V. Hijman, S. Tarucha, and L. P. Kouwenhoven, *Microwave spectroscopy of a quantum-dot molecule*, Nature **395**, 873 (1998).

[331] A. R. Rezk, B. Carey, A. F. Chrimes, D. W. M. Lau, B. C. Gibson, C. Zheng, M. S. Fuhrer, L. Y. Yeo, and K. Kalantar-Zadeh, *Acoustically-Driven Trion and Exciton Modulation in Piezoelectric Two-Dimensional MoS_2*, Nano Lett. **16**, 849 (2016).

[332] Z. Hu, Z. Wu, C. Han, J. He, Z. Ni, and W. Chen, *Two-dimensional transition metal dichalcogenides: interface and defect engineering*, Chem. Soc. Rev. **47**, 3100 (2018).

[333] P. J. Clark, and F. C. Evans, *Distance to Nearest Neighbor as a Measure of Spatial Relationships in Populations*, Ecology **35**, 445 (1954).

[334] F. Lindemann, *The calculation of molecular vibration frequencies*, Z. Phys. **11**, 609 (1910).

[335] P. Nozières, and D. Pines, *Electron Interaction in Solids. General Formulation*, Phys. Rev. **109**, 741 (1958).

[336] R. M. White, *Quantum Theory of Magnetism*, Springer (2006).

[337] F. A. Rasmussen and K. S. Thygesen, *Computational 2D Materials Database: Electronic Structure of Transition-Metal Dichalcogenides and Oxides*, J. Phys. Chem. C **119**, 13169 (2015).

[338] O. Svelto, *Principles of Lasers*, Springer (2010).

[339] A. Thranhardt, C. Ell, G. Khitrova, and H. M. Gibbs, *Relation between dipole moment and radiative lifetime in interface fluctuation quantum dots*, Phys. Rev. B **65**, 035327 (2002).

[340] H.-L. Liu, C.-C. Shen, S.-H. Su, C.-L. Hsu, M.-Y. Li, and L.-J. Li, *Optical properties of monolayer transition metal dichalcogenides probed by spectroscopic ellipsometry*, Appl. Phys. Lett. **105**, 201905 (2014).

[341] H. H. Fang, B. Han, C. Robert, M. A. Semina, D. Lagarde, E. Courtade, T. Taniguchi, K. Watanabe, T. Amand, B. Urbaszek, M. M. Glazov, and X. Marie, *Control of the Exciton Radiative Lifetime in van der Waals Heterostructures*, Phys. Rev. Lett. **123**, 067401 (2019).

[342] Y.-M. He, G. Clark, J. R. Schaibley, Y. He, M.-C. Chen, Y.-J. Wei, X. Ding, Q. Zhang, W. Yao, X. Xu, C.-Y. Lu, and J.-W. Pan, *Single quantum emitters in monolayer semiconductors*, Nat. Nanotechn. **10**, 497 (2015).

[343] M. Koperski, K. Nogajewski, A. Arora, V. Cherkez, P. Mallet, J.-Y. Veuillen, J. Marcus, P. Kossacki, and M. Potemski, *Single photon emitters in exfoliated WSe_2 structures*, Nat. Nanotechn. **10**, 503 (2015).

[344] C. Chakraborty, L. Kinnischtzke, K. M. Goodfellow, R. Beams, and A. N. Vamivakas, *Voltage-controlled quantum light from an atomically thin semiconductor*, Nat. Nanotechn. **10**, 507 (2015).

[345] S. Ayari, A. Smiri, A. Hichri, S. Jaziri, and T. Amand, *Radiative lifetime of localized excitons in transition-metal dichalcogenides*, Phys. Rev. B **98**, 205430 (2018).

[346] L. Novotny and B. Hecht, *Principles of Nano-Optics*, University Press, Cambridge (2006).

[347] Y. Cao, V. Fatemi, S. Fang, K. Watanabe, T. Taniguchi, E. Kaxiras, and P. Jarillo-Herrero, *Unconventional Superconductivity in Magic-Angle Graphene Superlattices*, Nature **556**, 43 (2018).

[348] Y. Cao, V. Fatemi, A. Demir, S. Fang, S. L. Tomarken, J. Y. Luo, J. D. Sanchez-Yamagishi, K. Watanabe, T. Taniguchi, E. Kaxiras, R. C. Ashoori, and P. Jarillo-Herrero, *Correlated insulator behaviour at half-filling in magic-angle graphene superlattices*, Nature **556**, 80 (2018).

[349] A. Bermudez, D. Porras, and M. A. Martin-Delgado, *Competing many-body interactions in systems of trapped ions*, Phys. Rev. A **79**, 060303 (2009).

[350] J. K. Pachos, and E. Rico, *Effective three-body interactions in triangular optical lattices*, Phys. Rev. A **70**, 053620 (2004).

[351] H. P. Büchler, A. Micheli, and P. Zoller, *Three-body interactions with cold polar molecules*, Nat. Phys. **3**, 726 (2007).

[352] N. Chancellor, S. Zohren, and P. A. Warburton, *Circuit design for multi-body interactions in superconducting quantum annealing systems with applications to a scalable architecture*, npj Quant. Inf. **3**, 21 (2017).

[353] L. Wang, E.-M. Shih, A. Ghiotto, L. Xian, D. A. Rhodes, C. Tan, M. Claassen, D. M. Kennes, Y. Bai, B. Kim, K. Watanabe, T. Taniguchi, X. Zhu, J. Hone, A. Rubio, A. Pasupathy, and C. R. Dean, *Magic continuum in twisted bilayer WSe_2*, Preprint available on *arXiv*:1910.12147 (2019).

[354] A. González-Tudela and J. I. Cirac, *Cold atoms in twisted-bilayer optical potentials*, Phys. Rev. A **100**, 053604 (2019).

Acknowledgements

During the past years, I have been supported by many people, both scientifically and personally. On both counts, I am very glad that I've had the opportunity to learn from and work with my supervisor Ignacio Cirac. His scientific guidance and original thinking made my time as a Ph.D. student at MPQ a very exciting, insightful and highly enjoyable journey. I feel grateful for his invaluable support as a mentor, his kindness and the possibility to work in an inspiring environment, together with many great scientists from around the world.

I am thankful to Belén Paredes for her support as a co-supervisor, and for agreeing to act as a referee of my Ph.D. thesis.

Science is a joint effort, and much of this work would not have been possible without my collaborators. Luckily, I have had the pleasure to work together with Martin Schuetz, a great teacher whose structured way of thinking and working have contributed very much to my development during my Ph.D., both personally and as a scientist. It was great to have him as a close advisor and sparring partner.

Throughout my Ph.D., Géza Giedke shared with me his deep insights into various matters of physics, but also politics, philosophy and many other aspects of life. His scientific rigor and modesty set a great example for a young scientist, and I am deeply thankful for his hospitality and company during several visits in San Sebastián.

I would like to express my gratitude to Mikhail Lukin, who has kindly hosted me during several visits to Harvard, and whose deep physical intuition has been an integral part of the results presented in this thesis. Moreover, I would like to thank all my other collaborators for their support and hospitality during scientific visits, including Rainer Blatt, Jonathan Finley, Kristiaan de Greve, Philip Holz, Hans Huebl, Malte Kremser, Richard Schmidt, Lieven Vandersypen, Mathias Weiler, Dominik Wild, and Tao Shi.

During my time as a graduate student at MPQ, I have met great physicists, inspiring personalities, and close friends. I am fortunate to have met Manuel Rispler at MPQ, who became a close friend, and who kindly agreed to proofread parts of this thesis. To many bicycle tours to come. It was a great pleasure to meet Erez Zohar, whom I would like to thank for his moral support and friendship. I will remember our weekly movie nights, joint workshop organization, and refreshing conversations. For settling back in and for all future plans, I wish him and Na'ama all the best.

I would like to thank my office mates Miguel Bello, Arthur Christianen, Daniel González-Cuadra, Tommaso Guaita, Anna Hackenbroich, Ilya Kull, Xiaotong Ni, and Christoph

Sünderhauf, for creating a productive and enjoyable work environment. Patrick Emonts made our bike rides to MPQ both painful and pleasant, and I am glad that he taught me the basic principles of causality. During a significant part of my Ph.D., Alejandro González-Tudela was a core part of the quantum optics team at our group, and it was pleasant to have him around and great to discuss with him about physics. Köszönöm szépen, András Molnar, for showing us around Budapest and bringing joy to many occasions. Cosimo Rusconi combines a great sense of humour, an infectious passion for physics and a cheerful disposition. I would like to thank him for carefully proofreading parts of this thesis. Eduardo Sánchez-Burillo is a great roommate, and our chess meetings became an integral part of Friday's lunch routine. Tao Shi is an amazing and inspiring physicist, and I am glad to be able to work with him.

It was a pleasure to get to know Javier Argüello-Luengo, Mari-Carmen Bañuls, Julian Bender, Asli Cebe, Yue Chang, Henrik Dreyer, Alessandro Farace, Ivan Glasser, Andrew Goldsborough, Caroline de Groot, Giacomo Giudice, Johannes Kofler, Ivan Kukuljan, Nicola Pancotti, Vanessa Paulisch, Martí Perarnau-Llobet, Julian Roos, Norbert Schuch, David Stephen, and all other members of the MPQ theory division. In particular, I am very grateful for the kind assistance of Andrea Kluth and Regina Jasny, who have supported me in many bureaucratic endeavors and beyond.

Thanks to Samuel Markson, for his humour and friendship, and for always giving me shelter in Boston.

Special thanks to my family, who always support me. It is encouraging to know that I can always count on you.

Finally, I would like to thank Bernadette for her continuous support, for her passion, and for sharing with me her contagious sense of humor.

Funding from the Max Planck Society, the Nanosystems Initiative Munich, and the Max Planck Harvard Research Center for Quantum Optics is gratefully acknowledged.